

# Advanced laboratory-based photoelectron spectroscopies on metal and oxide surfaces

## Habilitationsschrift

zur Erlangung des akademischen Grades

Dr. rer. nat. habil.

vorgelegt der

Naturwissenschaftlichen Fakultät II - Chemie, Physik und Mathematik  
der Martin-Luther-Universität Halle-Wittenberg

von

Herrn Dr. rer. nat. Cheng-Tien Chiang

geb. am 26. Juni 1984 in Taipeh, Taiwan

Gutachter

1. Prof. Dr. Wolf Widdra
2. Prof. Dr. Claus Michael Schneider
3. Prof. Dr. Uwe Bovensiepen

Halle (Saale), verteidigt am 17. Dezember 2019,

Probevorlesung am 30. Januar 2020



# Contents

<b>1</b>	<b>Introduction</b>	<b>1</b>
1.1	Photoelectron spectroscopy on solids . . . . .	3
1.2	Double photoemission . . . . .	4
1.3	High-order harmonic generation . . . . .	6
<b>2</b>	<b>Photoelectron spectroscopy experiments</b>	<b>9</b>
2.1	Chambers and lasers for high-order harmonics . . . . .	9
2.2	Angle-resolved photoelectron spectrometers . . . . .	10
2.2.1	Electrostatic time-of-flight spectrometer . . . . .	10
2.2.2	Momentum microscope with hemispherical analyzers . . . . .	11
2.3	Analysis of photoelectron pairs . . . . .	11
<b>3</b>	<b>Selected results</b>	<b>13</b>
3.1	High-order harmonic generation light sources at megahertz repetition rates	13
3.2	Time-of-flight photoelectron spectroscopy using high-order harmonics . . .	18
3.3	Double photoemission of metal and oxide surfaces . . . . .	24
3.4	Angular distribution of photoelectrons and photoelectron pairs . . . . .	31
<b>4</b>	<b>Summary and outlook</b>	<b>39</b>
<b>5</b>	<b>Original publications</b>	<b>41</b>
5.1	High-order harmonic generation at 4 MHz as a light source for time-of-flight photoelectron spectroscopy . . . . .	42
5.2	Efficient and tunable high-order harmonic light sources for photoelectron spectroscopy at surfaces . . . . .	46
5.3	Boosting laboratory photoelectron spectroscopy by megahertz high-order harmonics . . . . .	53
5.4	Atomic line emission and high-order harmonic generation in argon driven by 4-MHz sub- $\mu$ J laser pulses . . . . .	61
5.5	Angle-resolved photoelectron spectroscopy at surfaces with high-order harmonic generation . . . . .	66
5.6	SiO <sub>2</sub> /Si(001) studied by time-resolved valence band photoemission at MHz repetition rates: Linear and nonlinear excitation of surface photovoltage . .	77

5.7	Electron pair emission detected by time-of-flight spectrometers: recent progress . . . . .	83
5.8	Band-resolved double photoemission spectroscopy on correlated valence electron pairs in metals . . . . .	87
5.9	Extended energy range analysis for angle-resolved time-of-flight photoelectron spectroscopy . . . . .	93
<b>References</b>		<b>99</b>



# 1 Introduction

Since the discovery of the photoelectric effects, photoelectron spectroscopy (PES) has evolved into the most powerful method to analyze the electronic band structure of condensed matter [1–4]. In comparison to earlier experimental access to the electronic states such as optical absorption [5–9] and the de Haas-van Alphen effect [10–14], PES offers the unique possibility to directly analyze the energy, momentum, and spin of the electrons in solids [15–22]. Therefore, there has been tremendous progress in the development of advanced PES by improving the light source, the energy analyzer, as well as the spin detector. In strong contrast to PES experiments at synchrotron facilities with an extremely widely tunable photon energy range at high photon flux, earlier laboratory PES experiments have been severely restricted by the limited choices of available photon energies from discharge lamps [23–25]. This situation has been changed by the application of laser-based light sources to laboratory PES experiments [26, 27]. Especially due to the discovery of high-order harmonic generation (HHG) a few decades ago [28–30], laser-based vacuum-ultraviolet light sources in laboratory with a tunable photon energy range have become available. These laser-based HHG light sources have provided laboratory PES experiments the possibilities to explore the full energy and momentum phase space of the electronic band structure in solids with sub-femtosecond time resolution [31–39].

However, earlier HHG-based PES experiments have been impeded by the low repetition rates of high-power lasers below few kilohertz [27, 34], which lead to the degradation of the energy and momentum resolution by the space-charge effects [40, 41]. This barrier is surmounted in the Habilitation work presented here. By specifically designing an HHG setup aiming at a two to three orders-of-magnitude higher repetition rate into the megahertz range, the MHz HHG light sources in this work allow efficient laboratory PES experiments to study the electronic structure and dynamics at surfaces (Chap. 3.1-3.2).

Besides the development of modern light sources for PES, the electron spectrometers in PES have been revolutionized by the implementation of the time-of-flight analysis [42–46] as well as by the invention of the momentum microscopy [4, 47–49]. The time-of-flight (ToF) analysis of photoelectrons is combined in the framework of this Habilitation work to the MHz HHG light source (Chap. 3.2). Due to the inherent time structure of the pulsed laser that drives HHG, all the detected photoelectrons can be assigned by their flight time from the solid surface under investigation to the electron detector. Together

with the hit position provided by the two-dimensional electron detector, the kinetic energy of the photoelectrons and their two momentum components parallel to the solid surface can be retrieved. This ToF technique is in strong contrast to PES experiments using a hemispherical energy analyzer which selectively filters only a narrow energy or momentum range. Instead, in the ToF-PES a wide angular and energy range of photoelectrons can be simultaneously detected. In this Habilitation work the HHG-based ToF-PES is developed aiming at double photoemission spectroscopy on pairs of correlated electrons in solids. Due to the higher energy resolution of this unique combination than most of the earlier DPE experiments, the signatures of band-dependent electron pairs from Ag and Cu are observed for the first time (Chap. 3.3).

As an alternative modern PES method besides the ToF technique, all photoelectrons from the valence bands of solids can be mapped directly in the reciprocal space by the momentum microscopy. In collaboration with Dr. Christian Tusche using the momentum microscopy, the full valence band electronic structure of the monolayer-thick BaTiO<sub>3</sub>-derived oxide quasicrystal is investigated [50, 51] (Chap. 3.4). By using the symmetry analysis over the whole momentum space, the energy-momentum dispersion of the oxygen 2*p* valence bands can be clearly identified and distinguished from the underlying highly dispersive Pt valence bands. In addition, the signatures of occupied Ti 3*d* states are observed at the Fermi level, which imply an important role of the Ti 3*d* states to the formation mechanism of the oxide quasicrystal [52, 53].

The Habilitation work presented here is organized as the following. In Chap. 1, the fundamental concepts of HHG, PES and the more advanced DPE are introduced. In Chap. 2 the experimental setups are briefly described. In Chap. 3 the selected results are presented, which are summarized in Chap. 4 and can be found in the original publications in Chap. 5. In addition, an overview of the photoemission methods and the materials studied in this work is provided in Tab. 1.1.

		photoemission methods		
		ARPES	DPE	tr-PES
materials	Ag(001)	Chap. 3.2	Chap. 3.3-3.4	
	Cu(111)	Chap. 3.2	Chap. 3.3	
	Pt(111)	Chap. 3.4		
	SiO <sub>2</sub> /Si(001)	✓		Chap. 3.2
	NiO/Ag(001)	✓	Chap. 3.3	
	CoO/Ag(001)	✓	Chap. 3.3	
	BaTiO <sub>3</sub> -derived OQC/Pt(111)	Chap. 3.4		✓

Table 1.1: Overview of photoelectron spectroscopy (PES) methods and materials studied in this Habilitation work. ARPES: angle-resolved PES; DPE: double photoemission; tr-PES: time-resolved PES; OQC: oxide quasicrystal. Here the methodological difference between conventional ARPES and the momentum microscopy is neglected [47, 48]. Symbol ✓ indicates the experiments performed in the framework of this Habilitation work, but not presented here.

## 1.1 Photoelectron spectroscopy on solids

In photoelectron spectroscopy (PES), an incident electromagnetic wave with a photon energy  $h\nu$  excites the solids. As a consequence of this photoexcitation, electrons are emitted from the solid surfaces. These photoelectrons are collected and can be analyzed with energy, angular and spin resolution. Theoretically, the photoelectrons can be represented by the corresponding current distribution which indicates the number of photoelectrons emitted along a certain direction in space within a given time interval [54–56]. The number of emitted photoelectrons can be formulated as [17, 57, 58]:

$$I(E_k, \vec{k}_{\parallel}) \propto |\langle \Psi_f | \Delta | \Psi_i \rangle|^2 \delta(\varepsilon_f - \varepsilon_i - h\nu) \quad (1.1)$$

with  $E_k$  as the kinetic energy of the photoelectron, and  $\vec{k}_{\parallel}$  is its momentum parallel to the solid surface.  $\Psi_i$  is the initial state wave function of the solid at the energy  $\varepsilon_i$ , and  $\Psi_f$  describes the final state wave function of the whole system at the energy  $\varepsilon_f$  including the solid with the photo-hole as well as the outgoing photoelectron at  $E_k$ . The energy conservation is described by  $\delta(\varepsilon_f - \varepsilon_i - h\nu)$ . The operator  $\Delta$  represents the interaction between the incident light and the solid, and its leading order is proportional to the scalar product of the vector potential of the incident light and the canonical momentum operator [54, 55, 59]. For PES at the low photon energy in the vacuum-ultraviolet range as presented in this Habilitation work, the linear momentum of the incident photon as well as the recoil effect can be neglected [60–64].

Conventionally, Eqn. (1.1) is further simplified by the sudden-approximation which neglects the interaction between the photoelectron and the solid including the photo-hole. As a result, Eqn. (1.1) can be rewritten by [58, 59]:

$$I(E_k, \vec{k}_{\parallel}) \propto \sum_i |\langle \psi_f | \Delta | \psi_i \rangle|^2 A(E_f - h\nu) \quad (1.2)$$

with  $A(E_f - h\nu)$  as the spectral function that describes the photo-hole in the solid at the energy  $E_f - h\nu$ . Here the off-diagonal parts of  $A(E_f - h\nu)$  have been neglected. The one-electron wave function  $\psi_i$  represents the initial state at the energy  $E_i$  and the crystal momentum  $\vec{k}_i$ . The final state  $\psi_f$  is the time-reversed low-energy electron diffraction (LEED) state at  $E_f$  that carries the photoelectron away from the surface [65, 66], and  $E_f = E_k + \Phi$  with  $\Phi$  as the surface work function. In the limit of non-interacting electrons in the solid,  $A(E_f - h\nu)$  is proportional to  $\delta(E_f - E_i - h\nu)$  which describes the energy conservation [56, 59]. In analogy, the momentum conservation for the components parallel to the surface including umklapp processes follows as  $\vec{k}_{\parallel} = \vec{k}_{i,\parallel} + \vec{g}_{\parallel}$ . Here  $\vec{k}_{i,\parallel}$  represents the components of  $\vec{k}_i$  parallel to the surface, and  $\vec{g}_{\parallel}$  is the reciprocal lattice vector of the surface [15, 67, 68]. In the above description the spin of the photoelectron can be included, which will add an additional condition given by the total angular momentum conservation in the photoemission process.

## 1.2 Double photoemission

In double photoemission (DPE) spectroscopy on solids, a pair of photoelectrons is emitted upon photoexcitation. In contrast to the well-established DPE experiments of atoms and molecules in the gas phase [76–84] as well as DPE from core-levels of solids [85–88], DPE on the valence band structure of solids has been less frequently studied. Similar experiments to the valence DPE spectroscopy are the CVV Auger coincidence photoelectron spectroscopy [89–93], where a pair of valence electrons is emitted as triggered by the photoemission process of a core electron. Pioneering DPE spectroscopy experiments on the valence electrons in solids have been performed by Prof. Jürgen Kirschner and Dr. Frank O. Schumann [70–74, 94, 95], where a variety of differently designed spectrometers were applied. An overview of the earlier valence band DPE experiments is shown in Fig. 1.1 as summarized by the solid angle acceptance and the energy resolution of the spectrometer. As can be seen in Fig. 1.1, the laser-based laboratory DPE experiments in this Habilitation work have only a slightly larger angular acceptance but a factor of two lower energy resolution than the first synchrotron experiments by Herrmann *et al.* [71]. However, the DPE experiments in this Habilitation work provide a much longer available measurement time in laboratory than at synchrotron

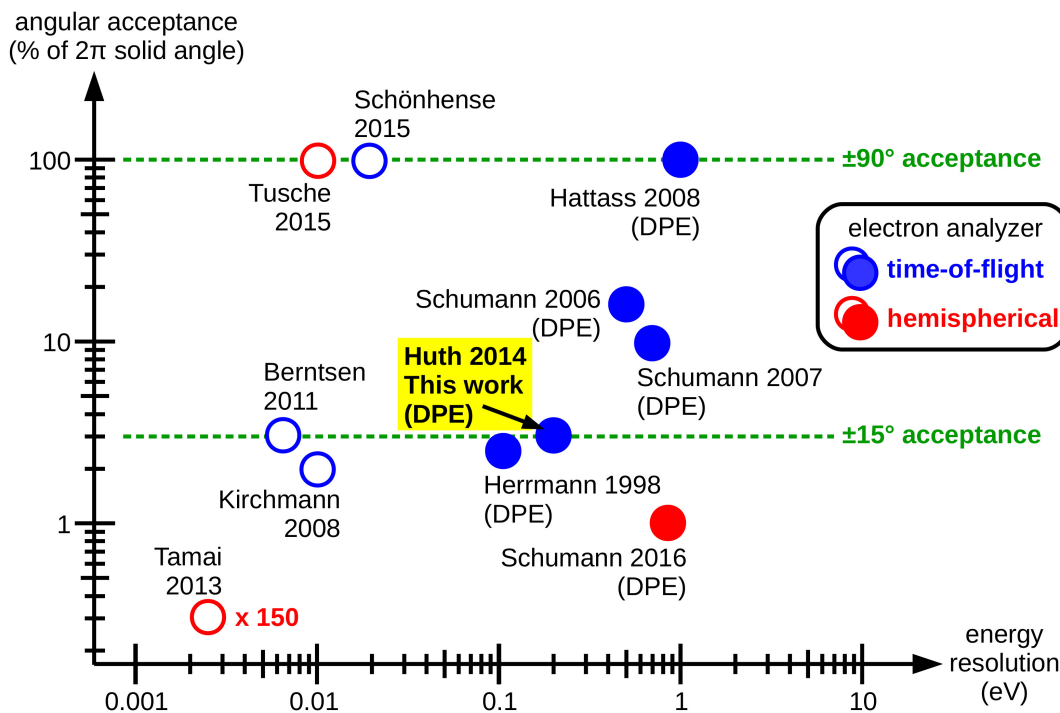


Figure 1.1: Energy resolution and angular acceptance of photoelectron spectrometers used in single photoemission (open symbols) and double photoemission (DPE, filled symbols) experiments on valence band electronic structure of solids. The values are estimated from the literature for hemispherical [47, 69, 70] and time-of-flight analyzers [4, 43, 44, 71–74]. The setup used in this Habilitation work is marked ([C5.7] in Tab. 5.1) and presented in Chap. 2.2.1 in more detail. For clarity, the angular acceptance of the high-resolution experiments by Tamai *et al.* is multiplied by 150 [69, 75].

facilities, which is critically important for sufficient statistics of counting the photoelectron pairs in the energy- and angle-resolved DPE measurements as will be shown in Chap. 3.3-3.4.

The theoretical description of the DPE process on the valence bands of solids has been discussed in detail by Prof. Jamal Berakdar, and the intensity of the photoemitted electron pairs can be given similarly as for single photoemission process in Eqn. (1.1) [96]:

$$I(E_{k,1}, \vec{k}_{\parallel,1}, E_{k,2}, \vec{k}_{\parallel,2}) \propto |\langle \Psi_f | \Delta | \Psi_i \rangle|^2 \delta(\varepsilon_f - \varepsilon_i - h\nu) \quad (1.3)$$

with the energy of the photoelectrons in the pair as given by  $E_{k,1,2}$  and their momentum parallel to the surface by  $\vec{k}_{\parallel,1,2}$ . The energies  $\varepsilon_{i,f}$  are defined similarly as in Eqn. (1.1), whereas the final state  $\Psi_f$  at  $\varepsilon_f$  includes the two photo-holes in the solid and the two outgoing photoelectrons. In strong contrast to the single photoemission process in Chap. 1.1, the operator  $\Delta$  here contains the canonical momentum operators for both electrons in the pair. It can be written more explicitly as  $\Delta = \Delta_1 + \Delta_2$ , with each of the  $\Delta_{1,2}$  containing only one canonical momentum operator for the individual electron nominally labeled as 1 and 2 in the pair. The Eqn. (1.3) can be approximated by [97–99]:

$$I(E_{k,1}, \vec{k}_{\parallel,1}, E_{k,2}, \vec{k}_{\parallel,2}) \propto \langle \psi_f^{(2)} | \Delta A^{(2)}(E_f - h\nu) \Delta^\dagger | \psi_f^{(2)} \rangle \quad (1.4)$$

with  $A^{(2)}(E_f - h\nu)$  as the two-particle spectral function for two photo-holes in the solids at the sum energy of  $E_f - h\nu$ . The final state  $\psi_f^{(2)}$  is the time-reversed LEED state for two correlated electrons at a sum energy of  $E_f$  [97], which can be related to  $E_{k,1,2}$  by  $E_f = E_{k,1} + E_{k,2} + \Phi_{DPE}$ . Here  $\Phi_{DPE}$  indicates the minimal energy required for the emission of electron pairs in the DPE process, which does not necessarily equal twice of the work function  $\Phi$  for the single photoemission process. By assuming an infinite lifetime of the two-electron states in the solid, Eqn. (1.4) can be simplified as [97]:

$$I(E_{k,1}, \vec{k}_{\parallel,1}, E_{k,2}, \vec{k}_{\parallel,2}) \propto \sum_i \left| \langle \psi_f^{(2)} | \Delta | \psi_i^{(2)} \rangle \right|^2 \delta(E_f - E_i - h\nu) \quad (1.5)$$

with the two-electron initial state  $\psi_i^{(2)}$  at the sum energy  $E_i$  in the solid. The comparison between Eqn. (1.5) for DPE and Eqn. (1.2) for single photoemission indicates that DPE could be viewed as a direct tool to map the energy and momentum distribution of two-electron states in solids, similar as the well-established angle-resolved PES for the single electron band structure.

### 1.3 High-order harmonic generation

In high-order harmonic generation (HHG), the frequency of the incident light is converted into a much higher frequency by a generation medium [28, 29]. HHG processes have been studied in detail in the gas phase medium [30, 100–102], and recently HHG in solids has been investigated [103–105]. In the classical single atom picture of HHG, the intense electric field of the incident light distorts the atomic potential, and the electrons in the atom can escape the parent atom in the tunnel ionization process [106, 107]. This tunnel ionization process is mainly governed by the strength of the electric field ( $E$ ) in comparison to the ionization potential ( $I_p$ ) for the electrons. After the tunneling process, the electron is accelerated in the electric field of incident light to a high kinetic energy [108, 109]. From this ponderomotive acceleration, the maximum kinetic energy that the electron can gain is [30, 101, 108, 109]:

$$U_p = \frac{e^2 E^2}{4m\omega^2} = c_0 I \lambda^2 \quad (1.6)$$

with  $E$  and  $\omega$  as the magnitude of the electric field of the incident light and its angular frequency.  $I$  and  $\lambda$  are the corresponding intensity and wavelength, and  $e$  and  $m$  are the charge and the rest mass of an electron. The constant  $c_0$  has a value of  $9.3 \times 10^{-14}$  when  $U_p$ ,  $I$ , and  $\lambda$  are given in units of eV, W/cm<sup>2</sup>, and  $\mu\text{m}$  [30, 100]. Since the electric field of the incident light oscillates at the angular frequency  $\omega$ , the ponderomotive motion of the electron can lead to recombination or recollision of the electron with the parent atom. In the recombination process, the ponderomotive energy  $U_p$  can be released by the emission of a high energy photon, whose maximal energy follows as [110–112]:

$$h\nu_{max} \approx I_p + 3.17U_p \quad (1.7)$$

with  $h\nu_{max}$  as the maximum photon energy from the HHG process. In the above simplified picture, the efficiency of HHG is mainly determined by the tunneling process and depends critically on  $E$  and  $I_p$ . In the quantum mechanical picture, the interference between the recolliding electron wave function with the ground state wave function in the atom leads to an oscillating electric dipole that emits the high photon energy coherently [102, 112, 113]. In addition to the above single atom response, the coherent superposition of the emitted light within the generation medium plays an important role for the efficiency of HHG. The condition for the coherent superposition is conventionally called as the phase-matching condition [114, 115], which describes the phase-sensitive addition of the generated light. The phase-matching condition has been investigated in conventional HHG experiments using high power lasers at kHz repetition rates with a pulse energy above few mJ [113, 116–120]. This phase-matching condition becomes distinctly different when driving the HHG with a much lower laser pulse energy at few  $\mu\text{J}$  [121–123]. There, a tight-focusing geometry must be applied in order to reach a sufficient strength of the electric field  $E$  in the generation medium. As a result, a much higher density of the gas medium is needed [124].

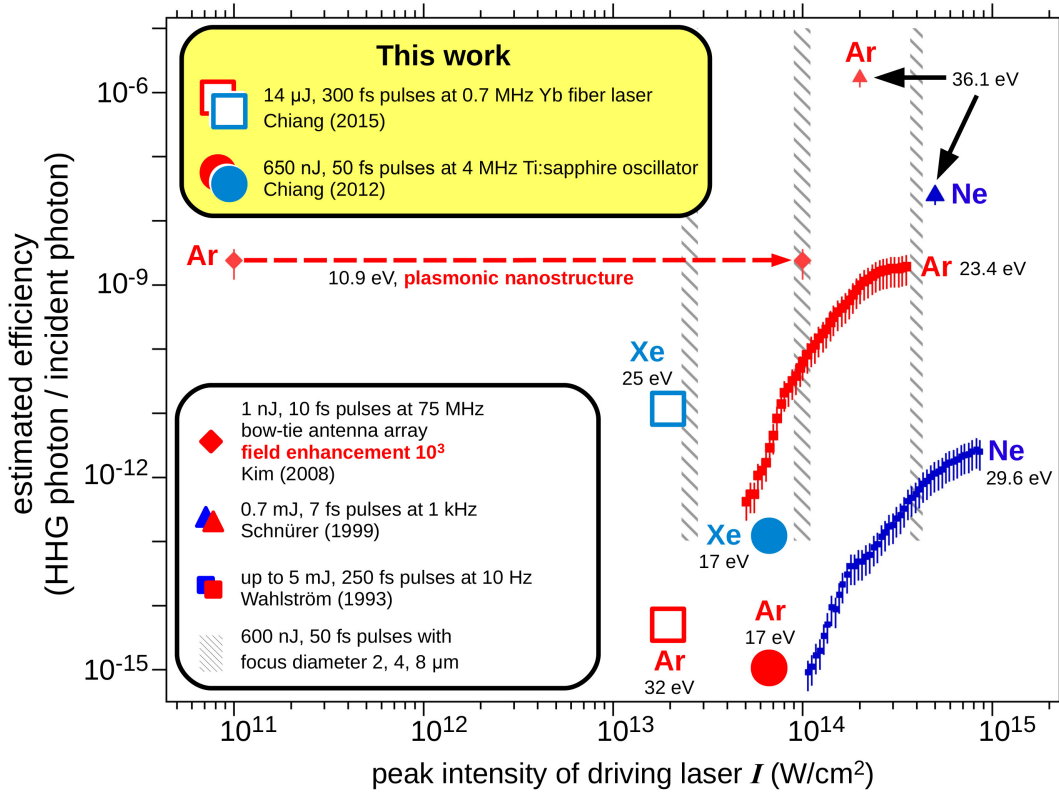


Figure 1.2: Efficiency of HHG estimated from literature [125–127], with the generated photon energies as indicated. For comparison, the efficiency of HHG presented in this Habilitation work from [C5.1,5.3] in Tab. 5.1 and from Chap. 3.1 is shown. The hatched areas illustrate intensity regions at different focus size of the same incident light.

To provide examples of the efficiency of HHG, selected literature values are summarized in Fig. 1.2.

As can be seen in Fig. 1.2 by the data from Wahlström *et al.* [125] with variable pulse energies and gas mediums, the efficiency of HHG depends highly nonlinearly on the incident laser intensity  $I$ . This nonlinear dependence has imposed a tremendous barrier to drive HHG by ultrafast lasers at a high repetition rate above MHz, which is conventionally connected to a pulse energy below  $100 \mu\text{J}$  due to the limited average laser power of around 100 W. As indicated by the red dashed arrow in Fig. 1.2, there was an impressive proposal of using the field enhancement of plasmonic nanostructures to increase the efficiency of HHG [127]. A similar approach has been pursued in the beginning of this Habilitation work. However, under the high electric field strength of the incident laser pulses, only the destruction of nanostructure could be observed together with the second- and third-order harmonics. These observations are consistent with later experiments which asked for a more robust design of nanostructure-assisted HHG [104, 128–132].

In Fig. 1.2 the efficiency of HHG presented in this Habilitation work is also compared with the literature values. Due to the much lower laser pulse energy at few  $\mu\text{J}$ , the efficiency is much lower than the earlier HHG experiments. However, as will be shown in Chap. 3.1–3.2, the HHG setup constructed in this Habilitation work can allow efficient



photoemission experiments due to the orders-of-magnitude higher repetition rates than conventional HHG setups at several Hz to few kHz. The implementation of MHz HHG as a light source for photoelectron spectroscopy has also been developed worldwide more recently with a much more intricate setup including an enhancement cavity [31, 133, 134] or a newly designed laser system [135, 136]. Meanwhile, there are other designs of MHz HHG setups for optical experiments together with the further developments of high power laser architecture [137–139].



# 2 Photoelectron spectroscopy experiments

In this chapter the experimental setups are introduced shortly. More details of the high-order harmonic generation (HHG) can also be found in Chap. 3.1 as well as in the publications [C5.1-5.4] in Tab. 5.1. The time-of-flight (ToF) spectrometer used in this Habilitation work has been described by the group of Prof. Oscar Tjernberg in Ref. [44], and its underlying concepts are comparable to other ToF photoelectron spectrometers [43, 46, 140, 141]. Based on a pair of the ToF spectrometers combined with coincidence electronics, the double photoemission (DPE) setup has been developed in collaboration with Dr. Michael Huth and Dr. Frank O. Schumann in the former group of Prof. Jürgen Kirschner at the Max Planck Institute of Microstructure Physics as published in [C5.7]. The momentum microscope was designed and constructed by Dr. Christian Tusche [47]. In the following some more specific details about these experimental setups are provided.

## 2.1 Chambers and lasers for high-order harmonics

Within the framework of this Habilitation work, two generation chambers of the high-order harmonics have been used. The first chamber was designed by Ralf Kulla in the group of Prof. Wolf Widdra and used for the first high-order harmonic generation (HHG) experiment in Halle in the Master thesis of Dr. Alexander Blättermann from 2011 to 2012 as published in [C5.4]. The second generation chamber was specifically constructed for a compact geometry of HHG in collaboration with Steffen Helmbach and Ralf Kulla in 2013 and has been described in the publication [C5.2]. In this second HHG chamber there are two particularly important features. Firstly, the positioning of the gas jet for HHG is adjusted by a tripod instead of a conventional  $x$ - $y$ - $z$  stage. The former allows a shorter length of the gas pipeline within the generation chamber and a more stable alignment of the gas jet with the  $10\ \mu\text{m}$  focus of the incident laser. Secondly, the position of the gas jet together with the laser focus is placed intentionally asymmetrically away from the center of the chamber. Consequently the distance from the laser focus, where HHG occurs, to the exit port of the chamber towards the monochromator is shorter. This shorter distance provides available space for a gate valve that separates the HHG chamber from the following monochromator and the photoemission chamber. The generated harmonics

are selected by a commercial monochromator with a toroidal grating having a groove density of  $1200 \text{ mm}^{-1}$ , which was originally designed for He-I and He-II radiations from a helium discharge lamp for laboratory photoemission experiments [142].

In this Habilitation work two very different laser systems have been used to drive HHG. The first one is a long-cavity Ti-sapphire laser which operates at a constant repetition rate of 4 MHz with a central wavelength of around 800 nm and a pulse energy of 650 nJ. The second laser is the high-power Yb-fiber-based amplifier system with a variable repetition rate from 0.2 to 25 MHz, a central wavelength of 1040 nm, and a higher pulse energy up to  $40 \mu\text{J}$  [143]. Despite that the fiber laser has a much higher pulse energy, its pulse width of around 300 fs is much longer than the 50 fs pulse duration of the Ti-sapphire laser. As a result, a higher pulse energy above few  $\mu\text{J}$  is necessarily required when driving HHG by the fiber laser. Nevertheless, the fiber laser has a better long-term stability which allows the continuous operation of HHG up to 10 days. This non-stop operation is of critical importance for the long acquisition time of double photoemission experiments with sufficient statistics as shown in Chap. 3.3.

## 2.2 Angle-resolved photoelectron spectrometers

The photoelectron spectroscopy (PES) presented in this Habilitation work includes the application of the time-of-flight spectrometer [44, 144] as well as the momentum microscopy with a pair of hemispherical energy analyzers [47, 48]. These spectrometers are described briefly in the following.

### 2.2.1 Electrostatic time-of-flight spectrometer

In the time-of-flight (ToF) photoelectron spectroscopy, the energy ( $E$ ) and the emission angles ( $\theta$ ,  $\phi$ ) of photoelectrons are analyzed according to their flight time ( $t$ ) from the sample surface to the detector as well as by their hit position ( $\vec{r}$ ) on the two-dimensional (2D) detector. Such time-of-flight technique has been applied to PES and photoelectron microscopy since several decades [42, 145–150]. With the modern developments of electron optics as well as the 2D detectors based on multichannel plates [43, 151], ToF spectrometer nowadays can offer parallel detection of photoelectrons with a high energy and a high angular resolution comparable to conventional hemispherical energy analyzers [4, 44–46, 140, 141]. However, a prerequisite for ToF spectroscopy is the well-defined timing in order to assign the ToF to each individual photoelectron event. This well-defined timing has limited the application of ToF spectroscopy at synchrotron facilities, where the repetition rate of light can be too high to allow for an unambiguous ToF assignment [152, 153]. In strong contrast, laboratory laser-based HHG light sources at repetition rates between kHz to few MHz can be ideally combined with the ToF analysis.

The ToF spectrometers used in this Habilitation work [144] have an electrostatic lens system comparable to the entrance lenses of hemispherical electron analyzers [44, 45, 150].

Instead of using the chromatic dispersion in the imaging properties of the hemispherical analyzer to measure the energy and emission angles of the photoelectrons, in the ToF spectrometer the ToF ( $t$ ) as well as the hit position ( $\vec{r}$ ) of photoelectrons are measured by the 2D delay-line detector [140, 151]. The transformation from the measured  $t$  and  $\vec{r}$  coordinates to the  $E$ ,  $\theta$ , and  $\phi$  emission coordinates follows the known electron-optical imaging properties of the spectrometer. These properties have been simulated in advance by the model of the electron lens system provided from the manufacturer [154]. Examples of the mapping from  $(t, \vec{r})$  to  $(E, \theta, \phi)$  can be found in the publication [C5.9] in Tab. 5.1. The nominal solid angle acceptance of the ToF spectrometer is within a cone of  $\pm 15^\circ$ , whereas the standard available energy range is  $\pm 10\%$  of the pass energy setting centered at the given kinetic energy setting [44].

### 2.2.2 Momentum microscope with hemispherical analyzers

In the photoemission experiments on the BaTiO<sub>3</sub>-derived quasicrystal presented in this Habilitation work in Chap. 3.4, the momentum microscope developed by Dr. Christian Tusche in the former department of Prof. Jürgen Kirschner at the Max Planck Institute of Microstructure Physics was applied [47]. In this specific version of the momentum microscope, a pair of hemispherical energy analyzers is used as an energy filter and images of the momentum distribution of photoelectrons were measured sequentially at each individual energy. The momentum mapping of the photoelectron distribution was achieved by imaging the photoelectron distribution at the back-focal plane of an electron extractor lens with high-voltage, and this momentum imaging has been demonstrated in earlier experiments using commercial photoemission electron microscopes [48, 49]. In the experiments presented here, a helium discharge lamp with its unpolarized He-I radiation at 21.2 eV was used as an excitation light source [47, 155], and the photoelectrons emitted in all directions from the surface were collected. All the experiments with the momentum microscope were performed at room temperature in collaboration with Dr. Martin Ellguth, Dr. Florian O. Schumann, and Dr. Christian Tusche.

## 2.3 Analysis of photoelectron pairs

In the double photoemission (DPE) experiments, pairs of photoelectrons are detected and analyzed with energy and angular resolution. Specifically for the DPE experiments presented in this Habilitation work, a pair of time-of-flight (ToF) spectrometers are combined with the high-order harmonic generation (HHG) light source as shown in Fig. 2.1 from the publication [C5.7]. This unique combination allows the parallel detection of photoelectron pairs in a wide energy range as presented in Chap. 3.3 and in [C5.7, 5.8]. The ToF spectrometer is described in Chap. 2.2.1, and its measurement settings for the DPE experiments have been discussed in detail in [C5.9] as well as in the Dissertation of Dr. Andreas Trüttschler [156]. In the following, a short summary of this ToF and

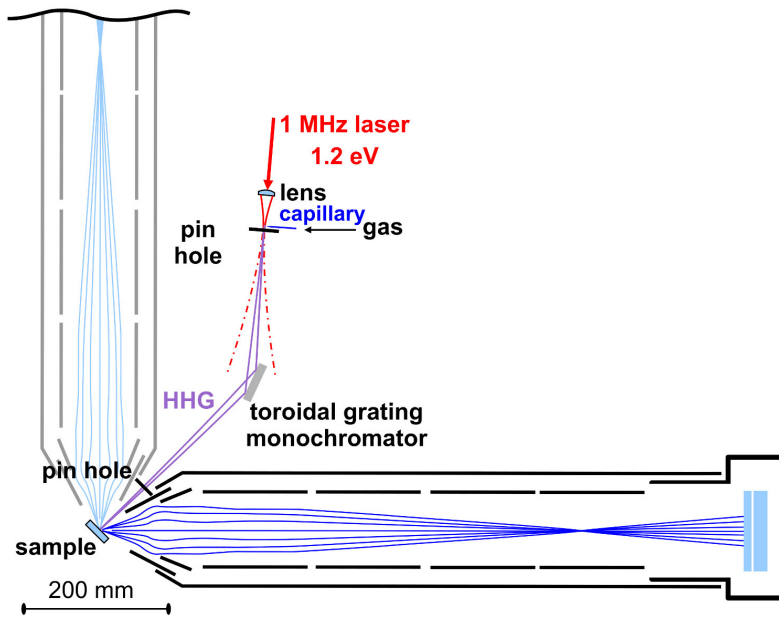


Figure 2.1: DPE setup with two time-of-flight spectrometers [44, 144] in combination with the high-order harmonic generation (HHG) light source presented in Chap. 3.1. For DPE experiments, the repetition rate of HHG is set as either 0.7 or 1.0 MHz. Reprinted from [C5.7] with the permission of AIP Publishing.

HHG-based DPE setup will be provided.

As is shown in Fig. 2.1, two ToF-spectrometers are oriented towards the sample surface at angles of  $\pm 45^\circ$ . Between the ToF spectrometers the HHG light source is mounted facing to the sample surface with a normal incidence geometry. With this specific geometry, the incident polarization of light is defined as *p*- or *s*-polarization if its electric field is parallel or perpendicular to the plane spanned by the two ToF spectrometers. The photoelectrons emitted from the sample surface within  $\pm 15^\circ$  relative to each of the spectrometer axes are guided by the electron optics as schematically shown by the electron trajectories in Fig. 2.1 (blue curves). All the DPE experiments presented in this Habilitation work were measured at room temperature, and the nominal kinetic and pass energy settings of the spectrometer were  $E_{kin} = 8 \text{ eV}$  and  $E_{pass} = 60 \text{ eV}$ .

In the delay-line detector (DLD) at the end of the ToF spectrometer, each individual photoelectron is detected as one electrical pulse at the multichannel plate (MCP) as well as two pulses at each of the two orthogonally oriented delay-lines. The pulse from the MCP is amplified and sent to the coincidence electronics. If the two MCP pulses of a photoelectron pairs simultaneously arrive at the coincidence electronics within a time window of around 150 ns relative to each other, the coincidence condition is fulfilled. Then the output of the coincidence electronics will trigger a digitizer to measure the wave forms of the pulses from the delay-lines. During the DPE experiments, these wave forms are analyzed in real time by a computer program written by Prof. Jürgen Kirschner and Dr. Michael Huth specifically for the evaluation of electron pairs (LabVIEW, National Instruments). According to these analyses, the hit position on the DLD of each of the photoelectrons within the pair is retrieved. The ToF of each photoelectron event is measured according to the relative time delay between the electrical pulse from the MCP and the pulse from a reference photodiode that is connected to the driving laser of HHG.

# 3 Selected results

In this chapter the results of this Habilitation work are presented, which include the construction of high-order harmonic generation light sources in Chap. 3.1 and the combination with photoemission experiments in Chap. 3.2. In Chap. 3.3 these experiments are further extended for electron pair coincidence detection, and in Chap. 3.4 the angular distributions of photoelectrons are presented. Publications derived from these experiments can be found in Chap. 5.

## 3.1 High-order harmonic generation light sources at megahertz repetition rates

For photoelectron spectroscopy (PES) as a general tool to characterize the electronic structure of materials, its combination with light sources of a tunable photon energy and a controllable polarization is important. Such combinations have been realized at synchrotron radiation facilities and provided rich insights into the electronic states of solids by the selective excitations of photoelectrons [16, 17, 157, 158]. Recently, by using high-order harmonic generation (HHG) of femtosecond laser pulses, laboratory light sources with a wide photon energy range have become available. In the following the HHG light sources at megahertz repetition rates developed in the context of this Habilitation work for PES applications are summarized. Details of the setup can be found in publications

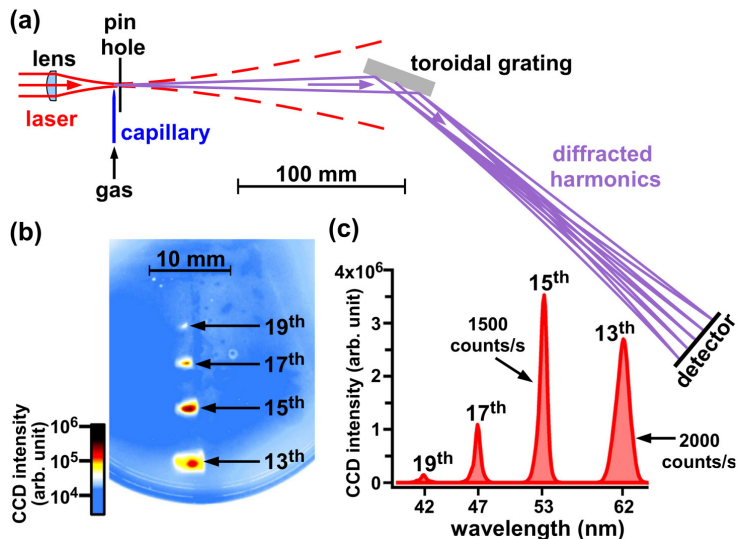


Figure 3.1: (a) Overview of the HHG setup. (b) Raw image of harmonics on the detector in (a) from an argon jet driven by 650 nJ, 50 fs laser pulses at 800 nm. (c) Background-subtracted line profile from (b) with estimated photon flux. Reprinted from [C5.1] with the permission of AIP Publishing.

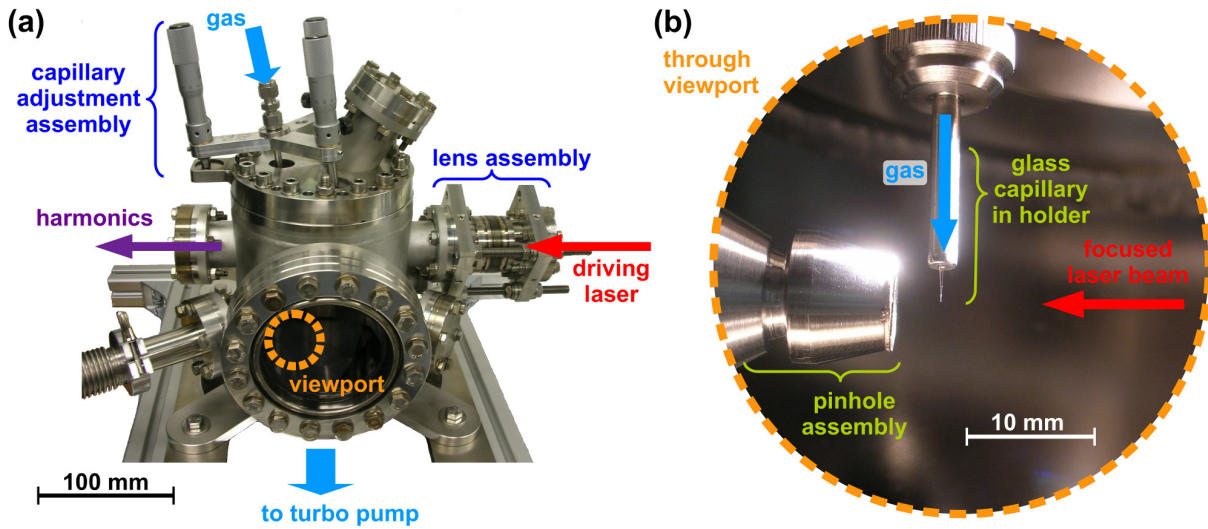


Figure 3.2: (a) Compact design of generation chamber and (b) magnified view near the gas jet. Reprinted from [C5.2].

[C5.1] to [C5.4] in Tab. 5.1. In Fig. 3.1(a) the setup is schematically shown, which consists of a focusing lens for the driving laser, a gas jet produced from a glass capillary, a toroidal monochromator grating, and a Chevron double channelplate detector. In strong contrast to conventional HHG setups at low repetition rates [28–30], this design adapts the tight-focusing geometry with a lens of a short focal length of only 50 mm. The tight-focusing geometry allows a small focus radius of few  $\mu\text{m}$  of the driving laser, and it aims at a sufficiently high laser peak irradiance for HHG of around  $10^{13} \text{ W/cm}^2$  when using  $\mu\text{J}$  laser pulses at megahertz repetition rates [121, 159, 160]. Details of the generation chamber are displayed in Fig. 3.2(a) with a magnified view near the capillary in Fig. 3.2(b). The capillary in Fig. 3.2(b) has an opening of only 20 to 30  $\mu\text{m}$  in order to reduce the gas pressure in the generation chamber down to  $10^{-2}$  mbar when pumping with a 700 l/s turbomolecular pump, despite a high backing pressure of the gas jet up to 10 bar. The pinhole with a diameter of about 150  $\mu\text{m}$  is located next to the capillary. It blocks most of the driving laser beam after its focus point close to the end of the capillary and helps to reduce the pressure in the monochromator chamber down to  $10^{-8}$  mbar. Meanwhile, this pinhole allows the generated harmonics with a smaller divergence to pass to the monochromator. The simplified diagram for the gas handling can be found in Fig. 3.3, where an additional gas-recycling system consisting of a compressor ( $C$ ) and a storage reservoir ( $B_2$ ) is also shown. The gas recycling system allows for the application of expensive gases such as xenon in double photoemission experiments with an extensive measurement time up to 10 days (Chap. 3.3).

The generated harmonics are directly characterized by the channelplate detector with a phosphor screen positioned at the exit of the monochromator as shown in Fig. 3.1(a), with an example of the raw image on the detector captured by a CCD camera in Fig. 3.1(b). There, the well-separated spectral features on the detector can be clearly seen as displayed by the corresponding line profile in Fig. 3.1(c), and they indicate a



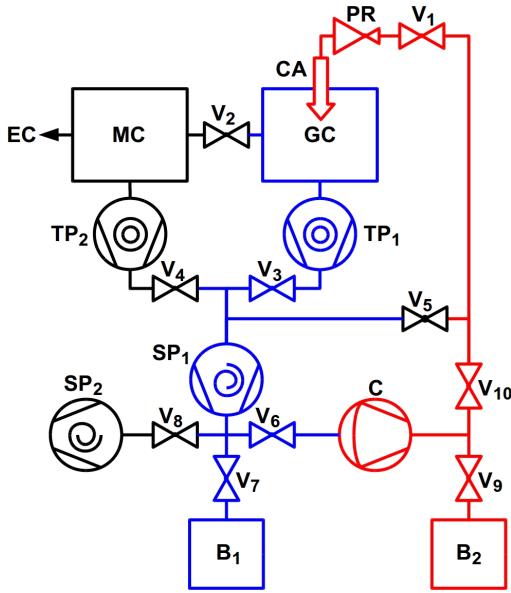


Figure 3.3: Pumping and gas recycling systems of HHG. GC: generation chamber for the harmonics with gas jet from a glass capillary (CA); MC: monochromator chamber; EC: photoemission experiment chamber; TP<sub>1,2</sub>: turbo pumps; SP<sub>1,2</sub>: scroll pumps; B<sub>1,2</sub>: gas reservoirs; C: compressor; V<sub>1-10</sub>: valves; PR: pressure regulator. Reprinted from [C5.2].

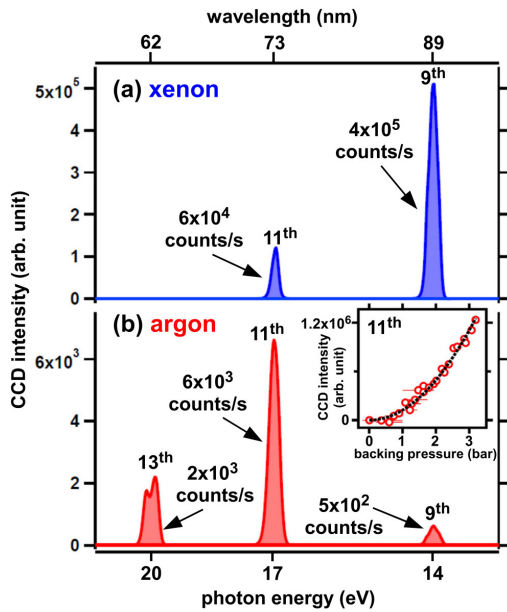


Figure 3.4: High-order harmonics generated from the (a) xenon and (b) argon gas jets using the setup in Fig. 3.1(a) driven by 50 fs pulses with a pulse energy of 650 nJ at 4 MHz repetition rate and a central wavelength around 800 nm. Inset in (b) shows the quadratic pressure dependent intensity of the 11th harmonic. Reprinted from [C5.1] with the permission of AIP Publishing.

discrete wavelength distribution of odd-order harmonics generated from argon. The spectrum of harmonics strongly depends on the generation medium, and this dependence can be seen in Fig. 3.4 when comparing the harmonics from xenon and argon jets with the same driving laser pulses. This dependence on the gas species can be understood by the different ionization potential  $I_p$  in argon and xenon ( $I_p^{Ar} = 15.8$  eV,  $I_p^{Xe} = 12.1$  eV [161, 162]). Because  $I_p^{Ar} > I_p^{Xe}$ , the tunnel ionization process as the first step of HHG has a higher probability in xenon than in argon. As a result, the harmonics generated from xenon have a higher photon flux [107, 163–165]. In addition, as shown in the inset of Fig. 3.4(b), the photon flux of the 11th harmonic from argon depends quadratically on the backing pressure of the gas jet, indicating a constructive summation of the electric field of the harmonics generated from individual atoms in the jet [111, 163, 166]. This observation is in agreement with previous theoretical predictions and experiments [121, 124], where gas jets of few  $\mu\text{m}$  diameter with a high backing pressure above 2 bar have been suggested for the phase-matching condition. The small diameter of the gas jet can further help to

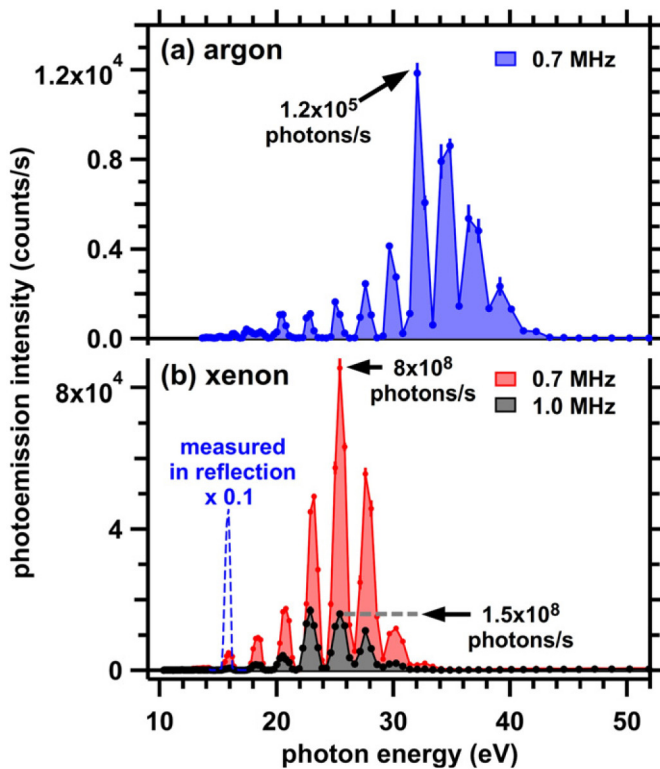


Figure 3.5: High-order harmonics generated from the (a) argon and (b) xenon gas jets using the setup in Fig. 3.1(a) driven by 300 fs pulses with a pulse energy of 10 and  $14 \mu\text{J}$  at repetition rates of 1 and 0.7 MHz, respectively. The central wavelength is around 1040 nm. Reprinted from [C5.3] under the terms of the Creative Commons Attribution 3.0 licence.

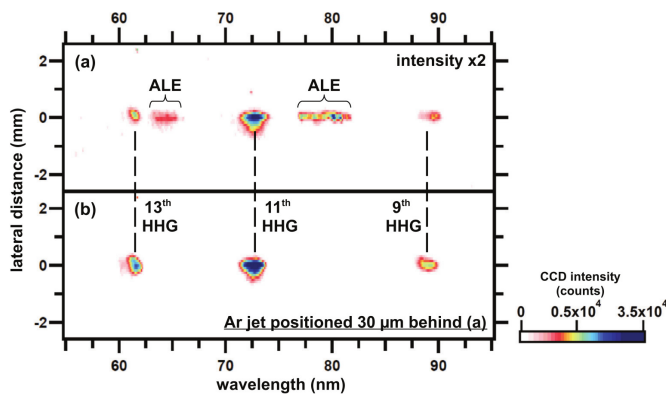


Figure 3.6: (a) Coexistence of harmonics and atomic line emission (ALE) driven by the same laser pulses as in Fig. 3.4. In (b) the gas jet is positioned  $30 \mu\text{m}$  after (a). From [C5.4], copyright (2014) by the American Physical Society.

minimize the absorption of the harmonics by the gas jet itself [124, 126, 167].

Moreover, the maximum photon energy of the harmonics strongly depends on the gas medium and the electric field strength of the driving laser [107, 112, 163]. As can be seen in Fig. 3.1(b) and Fig. 3.4(a), the highest order of the harmonics generated from argon is 19 (29.5 eV) and from xenon is 11 (17.0 eV) when driven by the 650 nJ laser pulses. With a much higher pulse energy up to  $14 \mu\text{J}$  as shown in Fig. 3.5, the harmonic spectra from argon and xenon can be extended up to 40 and 32 eV due to the higher ponderomotive acceleration of electronic motion driven by the electric field in the second step of HHG [107, 112, 168]. Besides the odd-order harmonics, additional spectral features can be observed between the harmonics as shown in Fig. 3.6(a) when the argon gas jet is directly positioned in the laser focus. These additional spectral features are assigned to the atomic line emission (ALE) from neutral argon atoms and singly ionized argon ions according to their characteristic photon energies. Due to an improved phase-matching condition for the harmonics in the laser beam slightly after the focus [121, 160], the intensity of the harmonics becomes enhanced in Fig. 3.6(b) when the gas jet is positioned about  $30 \mu\text{m}$



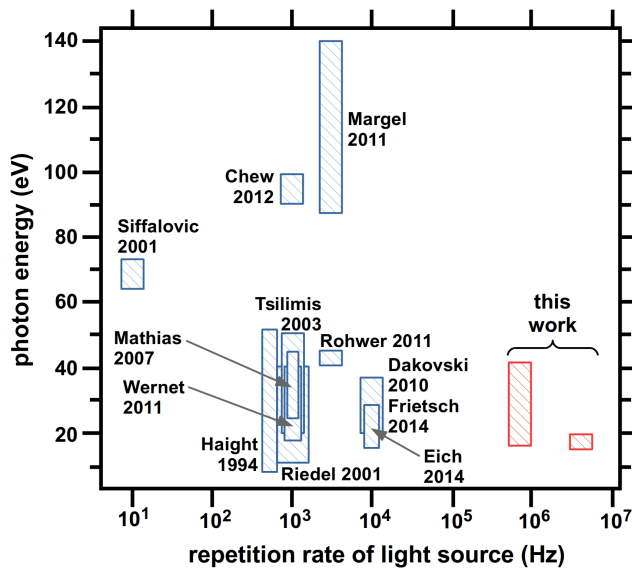


Figure 3.7: Overview of photon energy range and repetition rate of high-order harmonic light sources for PES at surfaces [27, 32, 34–36, 169–175]. Reprinted from [C5.2].

after the laser focus. Meanwhile, the ALE gets significantly suppressed possibly due to the reduced ionization probability with the lower laser field strength away from the focus.

The harmonic spectra in Fig. 3.4 and Fig. 3.5 cover the photon energy range significantly higher than the typical work function of metal surfaces ( $< 6$  eV) [176, 177] as well as the band gap of oxides ( $< 9$  eV) [178–180]. Therefore these HHG light sources are suitable for studying the valence electronic structure of metal and oxide surfaces. In Fig. 3.7 an overview of the photon energy range of existing HHG light sources for photoelectron spectroscopy (PES) is shown. At a low repetition rate of 3 kHz, previous HHG light source can cover a much higher photon energy range beyond 100 eV for photoemission on core level of adsorbates [171]. As a trade-off for the two to three orders-of-magnitude higher repetition rates of the HHG setups presented in this chapter, the driving lasers at the MHz repetition rates unavoidably have a lower pulse energy than those at the kHz repetition rates [181]. This lower pulse energy consequently leads to a lower photon energy of the harmonics. However, as will become clear in Chap. 3.2 and Chap. 3.3, the MHz repetition rates of the HHG light source is an essential property which allows efficient PES and the double photoemission experiments at surfaces.

## 3.2 Time-of-flight photoelectron spectroscopy using high-order harmonics

In combination with the megahertz high-order harmonic generation (HHG) light source presented in Chap. 3.1, efficient laboratory photoelectron spectroscopy (PES) with a tunable photon energy can be performed. In this chapter the HHG-based PES experiments using the time-of-flight (ToF) technique are summarized from publications [C5.1], [C5.2], [C5.3], [C5.5], and [C5.6] in Tab. 5.1. The harmonics at MHz repetition rates from the HHG chamber in Fig. 3.2 are combined with a commercial ToF electron spectrometer [44, 144], where the energy and momentum distribution of photoelectrons are retrieved from their ToF and hit positions on the two-dimensional delay-line detector. As will be shown in this chapter, the tunable photon energy and polarization as well as the temporal structure of the HHG light source at megahertz repetition rate can offer an efficient mapping of valence band structure of solids in PES.

The importance of the MHz repetition rate of the HHG light source is shown in Fig. 3.8. There the literature values for the emitted and detected rate of photoelectrons as a function of the repetition rate of HHG light sources [32–34, 36, 37], synchrotron radiation

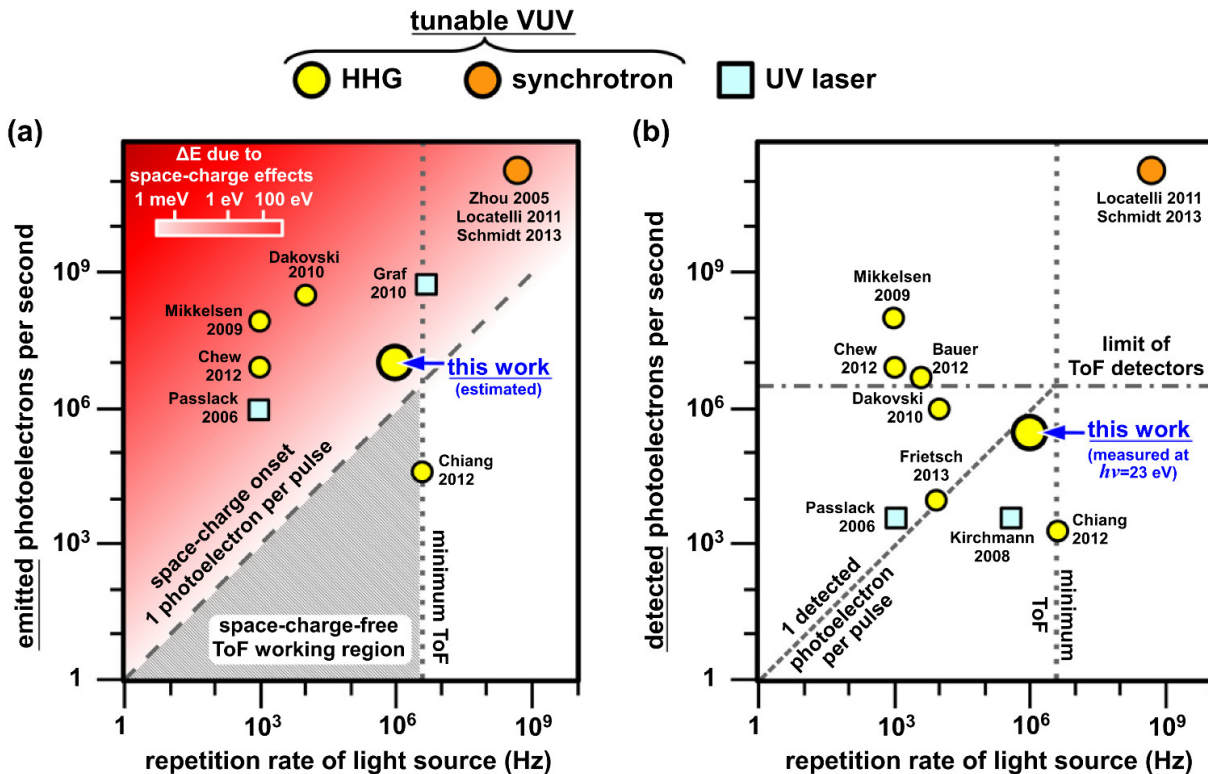


Figure 3.8: Overview of high-order harmonics and other light sources for photoelectron spectroscopy (PES) ([32–34, 36, 37, 40, 43, 182–185] and [C5.1,5.3]). In (a) and (b) the total emission rate and the detection rate of photoelectrons are shown as a function of the repetition rate of the light sources, respectively. Reprinted from [C5.3] under the terms of the Creative Commons Attribution 3.0 licence. Similar plot is also presented in the literature published later [133].

[182–184], as well as ultraviolet lasers [40, 43, 185] are summarized. An important limitation for these PES experiments is indicated by the dashed diagonal line in Fig. 3.8(a) at one photoelectron emitted per light pulse. This limit originates from the onset of the space-charge effects due to the Coulomb repulsion between photoelectrons in vacuum [186, 187]. The quantitative influence of the space-charge effects can be estimated by the resultant energy broadening in the photoelectron spectrum by the background color in Fig. 3.8(a) according to a model calculation [41]. As one can clearly see in Fig. 3.8(a), the space-charge effects can cause a significant energy broadening in the photoelectron spectra when the PES experiments are operating at higher photoemission rates further above the space-charge onset. Therefore, for reasonable electron counting statistics in PES experiments with only negligible space-charge effects, conventional synchrotron-based experiments are performed at high repetition rates above 100 MHz [182–184]. The MHz repetition rate is much higher than the few kHz of conventional HHG light sources [32–34, 36, 37]. As a consequence, most HHG-based PES experiments at kHz can not fully use the available photon flux, which otherwise will cause significant energy and momentum broadening in the photoelectron spectra [32, 34]. By using the HHG light sources at MHz developed in this Habilitation work (Chap. 3.1), more efficient HHG-based PES experiments can be performed due to the much higher repetition rates.

To efficiently collect the photoelectrons, the ToF electron spectrometer is used and its advantage for a wide energy [146, 188] and angular detection range [4, 43, 44, 140, 141] will be discussed later. In the combination of MHz HHG with the ToF electron spectrometer, there are additional limitations besides the space-charge effects. Due to the detection of photoelectrons according to their ToF, the photoelectrons need to be unambiguously assigned to each of the excitation light pulses. This assignment requires a minimum time interval between successive excitation light pulses, which generally depends on the settings of the electron lens system in the ToF spectrometer and the energy distribution of the photoelectrons. A typical minimal time interval can be estimated as 200 to 300 ns by considering the ToF dispersion and resolution of the spectrometer [C5.3]. The corresponding upper bound of the repetition rate of the light source is at around 4 MHz as indicated by the vertical dotted lines in Fig. 3.8(a,b), which could be extended above 10 MHz for specific cases [133, 153]. The detection of photoelectrons can impose another limit due to the maximal count rate that is allowed for the detector. For the chevron detector used in this work with double microchannel plates, a typical maximum count rate is 3 MHz as indicated by the horizontal dashed-dotted line in Fig. 3.8(b) [44].

Considering the above conditions given by the space-charge effect, the ToF dispersion as well as the detector capability, the space-charge-free operation conditions for ToF-PES is shown by the hatched triangular region in Fig. 3.8(a). The HHG-based PES setup developed in this work is located close to the top corner of the optimal condition and represents efficient PES experiments. The space-charge-free PES can be demonstrated in Fig. 3.9 with the photoelectron spectra from Ag(001) measured at an average detected

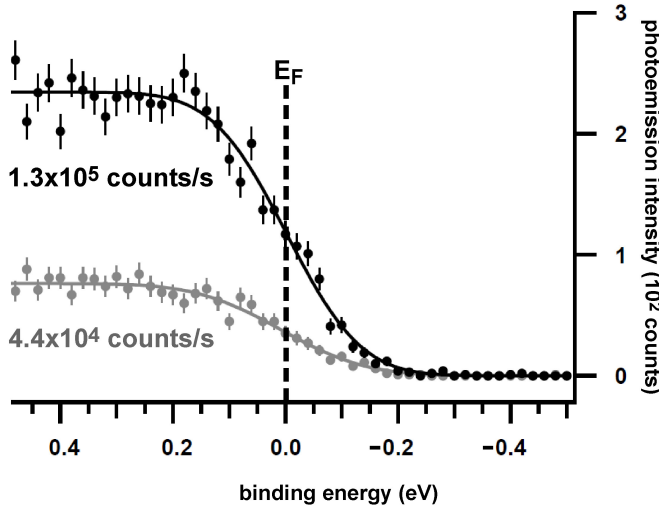


Figure 3.9: Photoelectron spectra near the Fermi level ( $E_F$ ) from Ag(001) with a photon energy  $h\nu = 22.7$  eV at 1 MHz and an acquisition time of 10 sec. Reprinted from [C5.3] under the terms of the Creative Commons Attribution 3.0 licence.

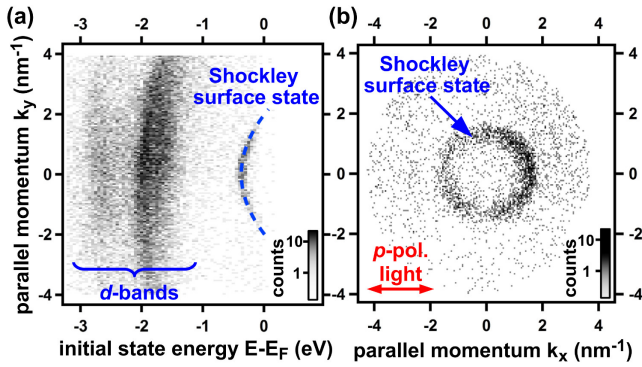


Figure 3.10: (a) Energy-momentum and (b) two-dimensional momentum distribution of photoelectrons from Cu(111) excited by  $h\nu = 14$  eV. (b) is for photoelectrons from 0.1 eV below  $E_F$ . Reprinted from [C5.1] with the permission of AIP Publishing.

count rate of 0.1 and 0.04 electrons/pulse using HHG at 1 MHz. Despite the about factor of 2 different count rates in these measurements, in these spectra the photoemission features of the Fermi level ( $E_F$ ) have comparable energies within 10 meV. Therefore a significant influence of the space-charge effects can be excluded.

The combination of the ToF spectrometer with the MHz HHG light source not only allows for a high count rate of detected photoelectron events, but also for the simultaneous measurement of the two momentum coordinates of photoelectrons parallel to the sample surface  $\vec{k}_{\parallel} = (k_x, k_y)$  [4, 43, 44, 140, 141]. As shown in Fig. 3.10(a) for photoelectrons from the Cu(111) surface, the well-known Shockley surface state with its parabolic energy-momentum  $E-k_{\parallel}$  dispersion can be identified (dashed) [69, 189]. This characteristic dispersion results in a circular pattern of the two-dimensional  $k_x$ - $k_y$  momentum distribution in Fig. 3.10(b) for photoelectrons coming from the proximity of  $E_F$ . The higher photoemission intensity from the Shockley surface state at  $k_x > 0$  than at  $k_x < 0$  in Fig. 3.10(b) can be attributed to the linear dichroism in angular distribution of photoelectrons [153, 190, 191]. Here the linear dichroism occurs due to the symmetry-breaking caused by the linear  $p$ -polarization of light, and it can be more clearly demonstrated on the fourfold symmetric Ag(001) surface with both  $p$ - and  $s$ -polarized light as shown in Fig. 3.11(c-f). In Fig. 3.11(c), the  $E-\vec{k}_{\parallel}$  distribution of photoelectrons with their momentum  $\vec{k}_{\parallel}$  perpendicular to the electric field of the  $s$ -polarized light is shown, and mainly a flat dispersion of the Ag  $d$  band is observed. This observation is comparable to Fig. 3.11(f) for  $p$ -polarized light, whereas both the polarization of light

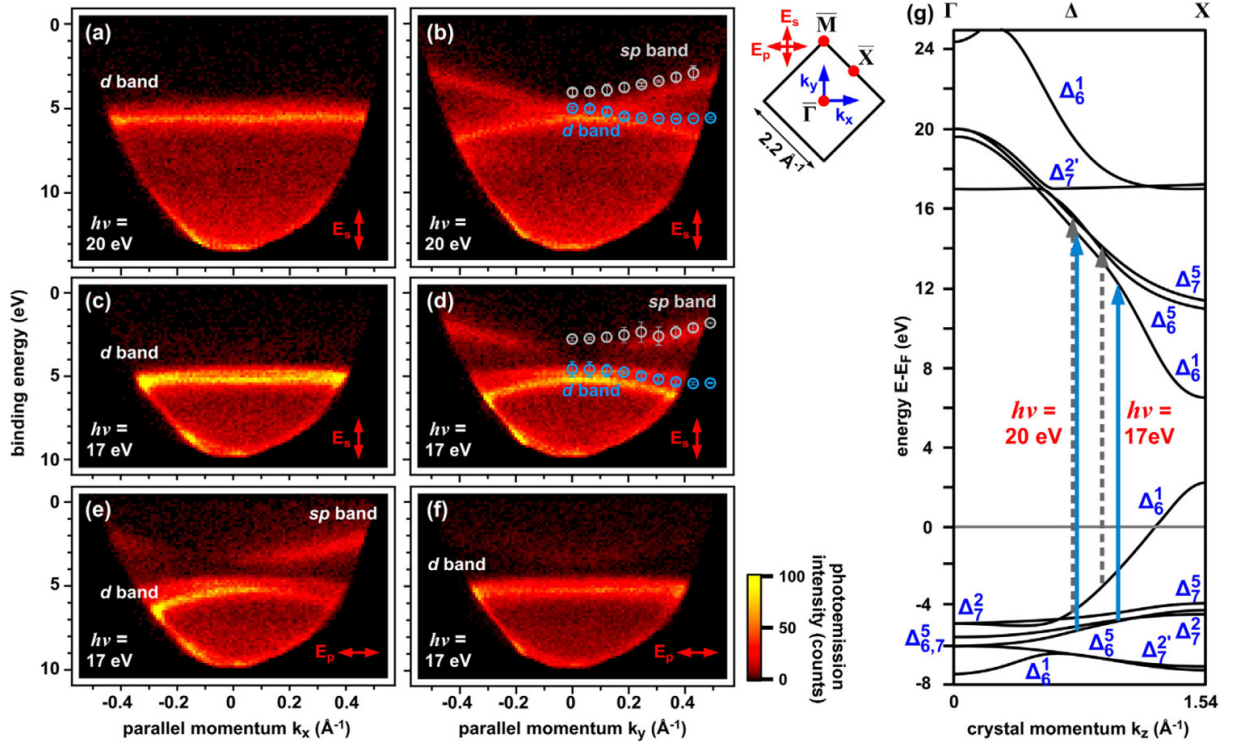


Figure 3.11: Energy- and momentum distribution of photoelectrons from Ag(001) excited by (a,b)  $h\nu = 20$  eV and (c-f)  $h\nu = 17$  eV. (a-d) and (e,f) are measured with  $s$ - and  $p$ -polarized light, respectively. (g) indicates the  $h\nu$ -dependent optical transitions in the band structure of Ag [192], and they can be estimated by an empirical band structure modeling as shown in (b,d) by the circles [193]. Reprinted from [C5.2].

and the momentum direction  $\vec{k}_{\parallel}$  of the photoelectrons are rotated by  $90^\circ$ . Similarly, for photoelectrons with their momentum  $\vec{k}_{\parallel}$  aligned parallel to the light electric field, their distributions in Fig. 3.11(d,e) for  $p$ - and  $s$ -polarized light are comparable and show both the dispersion of the  $sp$  and the  $d$  bands. According to these observations, the  $\vec{k}_{\parallel}$  momentum distribution of photoelectrons is locked to the polarization of light and is rotated by  $90^\circ$  when going from the  $s$ -polarized light (Fig. 3.11(c,d)) to the  $p$ -polarized light (Fig. 3.11(e,f)). In addition, the intensity asymmetry between the positive and negative momentum directions in Fig. 3.11(e) with  $p$ -polarized light is in contrast to the symmetric distribution in Fig. 3.11(d) with  $s$ -polarized light. Since this asymmetry is absent for  $s$ -polarized light, its origin can be related to the electric field component perpendicular to the surface due to the  $45^\circ$  angle of light incidence.

In addition to the tunable linear polarization of light, the HHG light source offers another advantage to disentangle different bands in the electronic structure of solids by its tunable photon energy. As can be seen in the comparison between Fig. 3.11(a,b) and Fig. 3.11(c,d), there are clear changes in the photoelectron spectra when going from the photon energy  $h\nu = 20$  eV to 17 eV with the same  $s$ -polarization of light. For both photon energies the less dispersive  $d$  band is observed at a comparable energy near 5 eV below  $E_F$  along the  $k_x$  direction in Fig. 3.11(a,c). However, along the  $k_y$  direction the dispersive  $sp$  band appears further separated in energy from the  $d$  band in Fig. 3.11(d) at  $h\nu = 17$  eV



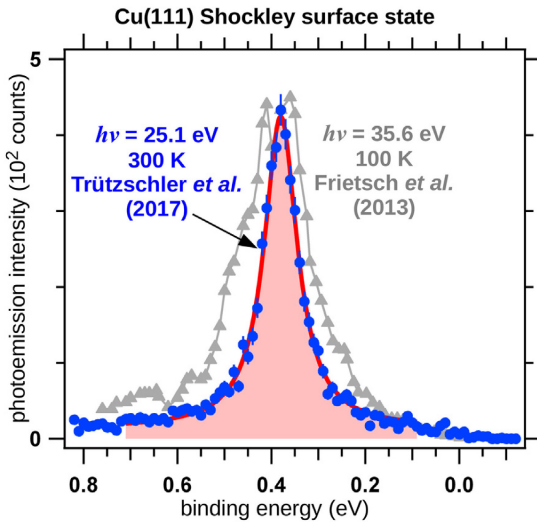


Figure 3.12: Photoelectron spectra from Cu(111) excited by  $h\nu = 25.1$  eV at 0.7 MHz (blue [156]) in comparison with literature by  $h\nu = 35.6$  eV at 10 kHz (gray [32]). Red curve is a fit with the Lorentzian function with a full-width-at-half-maximum of 86 meV. Reprinted from [C5.5]. Copyright (2018), with permission from Elsevier.

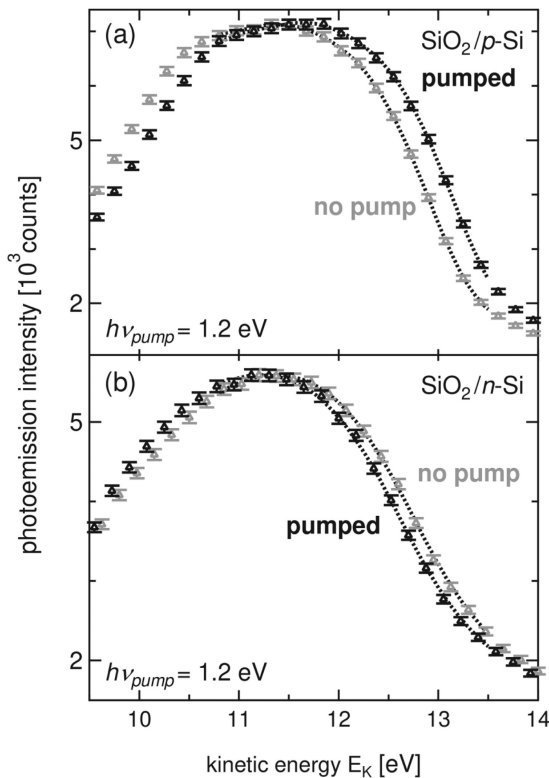


Figure 3.13: Photoelectron spectra of  $O_{2p}$  non-bonding states at  $SiO_2/Si(001)$  measured using  $h\nu_{probe} = 22.6$  eV at 0.7 MHz with (a)  $p$ - and (b)  $n$ -doped Si. Black (gray) curves are spectra with (without) additional excitation  $h\nu_{pump} = 1.2$  eV that triggers the surface photovoltage effect. Reprinted from [C5.6] with permission. Copyright (2019) American Vacuum Society.

than in Fig. 3.11(b) at  $h\nu = 20$  eV. This observation can be understood by the bulk band structure in Fig. 3.11(g) along the momentum direction  $k_z$  perpendicular to the surface, where the arrows indicate the optical transitions at  $h\nu = 17$  and 20 eV. As one can clearly see in Fig. 3.11(g), there is a larger energy difference between the  $sp$  and  $d$  bands initial states in the optical transitions at  $h\nu = 17$  eV as compared to that at  $h\nu = 20$  eV. This  $h\nu$ -dependent probing of the electronic bands in the three-dimensional momentum space has been widely applied at synchrotron facilities [157, 158, 194], which becomes available in laboratory when using the HHG light sources. The advantage of the tunable photon energy of the HHG light source will be further explored in Chap. 3.3 for spectroscopy on photoelectron pairs.

Last but not least, the temporal pulse structure of the HHG light source allows for time-resolved PES experiments on the femtosecond to picosecond time scale [26, 38, 195–

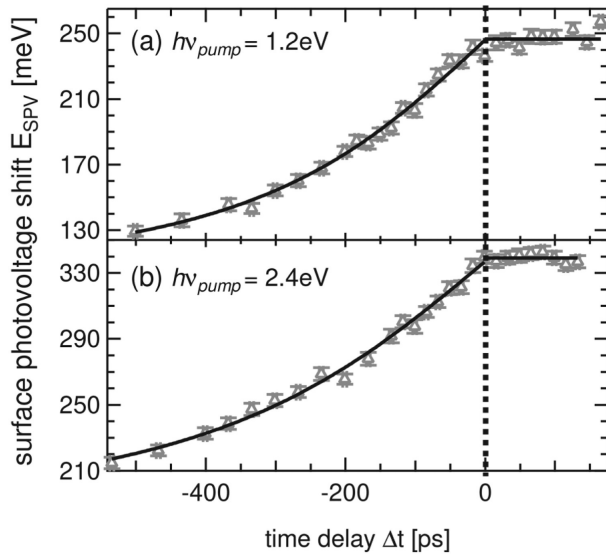


Figure 3.14: Surface photovoltage effect as a function of pump-probe delay triggered by  $h\nu_{pump}$  of (a) 1.2 eV and (b) 2.4 eV with an excitation density of 53 and  $2 \mu\text{J}/\text{cm}^2$ , respectively. The photoelectrons are excited by the probe with the high-order harmonic at  $h\nu_{probe} = 22.6 \text{ eV}$ . Reprinted from [C5.6] with permission. Copyright (2019) American Vacuum Society.

[197]. As an estimation for the intrinsic pulse duration of the HHG light source, the energy bandwidth of the harmonics is retrieved from the photoelectron spectrum on Cu(111) in Fig. 3.12 (blue circles). There the Shockley surface state appears as a dominant peak with a full-width-at-half-maximum of 86 meV, including its intrinsic lifetime corresponding to a linewidth of 56 meV at 300 K due to electron-phonon scattering [198]. As a result, the bandwidth of the harmonic at  $h\nu = 25.1 \text{ eV}$  can be estimated as 65 meV and the lower bound of its temporal duration is about 10 fs. Both of these values depend only weakly on  $h\nu$  [156]. As preliminary time-resolved HHG-based PES experiments at MHz repetition rates, SiO<sub>2</sub>/Si(001) interfaces are investigated by using the high-order harmonic with a photon energy  $h\nu_{probe} = 22.6 \text{ eV}$  in combination with an additional optical excitation at  $h\nu_{pump} = 1.2 \text{ eV}$  as shown in Fig. 3.13. The photoelectron spectra are shifted in energy when the optical excitation  $h\nu_{pump}$  is present, and the shift has a polarity which depends on the doping of the underlying Si(001) substrate. Due to this characteristic doping dependence, the observed  $h\nu_{pump}$ -induced shift can be assigned to the surface photovoltage (SPV) effect, where charge carriers excited by  $h\nu_{pump}$  compensate the electrostatic bending of the valence and conduction bands of Si in the proximity of the SiO<sub>2</sub>/Si(001) interface [199, 200]. In the time-resolved PES experiments shown in Fig. 3.14, the SPV shift in the photoelectron spectra can be observed as a function of the time delay between  $h\nu_{pump}$  and  $h\nu_{probe}$  [201, 202]. The temporal resolution of the HHG setup is limited to 2 ps by the pulse stretching of the single toroidal grating in the monochromator (Chap. 3.1) [39, 203], which can be compensated by a subsequent grating for an improved time resolution down to several fs [204, 205].

### 3.3 Double photoemission of metal and oxide surfaces

To probe the electron-electron interaction in solids, double photoemission (DPE) spectroscopy has a tremendous potential since both of the two interacting electrons can be directly measured [94, 96, 206]. In this chapter the DPE experiments on Ag(001), Cu(111) as well as NiO and CoO films using the high-order harmonic generation (HHG) light source of Chap. 3.1 in combination with the photoemission setup in Chap. 3.2 are summarized. The setup as well as the preliminary DPE results on NiO are published in [C5.7] in Tab. 5.1. With the HHG-based DPE experiments on Ag and Cu surfaces, for the first time the band-dependent electron pair emission processes could be resolved and the results are published in [C5.8] in Tab. 5.1. Most of the DPE experiments in this chapter were performed by Dr. Andreas Trüttschler in the framework of his dissertation [156].

The principal sketch of the DPE experimental setup is shown in the inset of Fig. 3.15(a), consisting of two nominally identical time-of-flight spectrometers [44, 144] and the HHG light source presented in Chap. 3.1 in the middle. The detection of photoelectron pairs is indicated by the coincidence AND logic gate (&) and the more detailed description can be found in Chap. 2.3. The raw data of the DPE spectrum measured on Ag(001) with a photon energy  $h\nu = 32.3$  eV are shown in Fig. 3.15(a), with two energy axes for the two electrons within a detected electron pair ( $E_{1,2}$ ). As will be shown in the following, this two-dimensional (2D) representation of the DPE spectrum allows a direct analysis of the band-dependent energy distribution of electron pairs.

To examine the photoelectron pairs more precisely, the 2D spectrum in Fig. 3.15(a) is analyzed as a function of the total energy of two electrons within an electron pair:  $E_{sum} = E_1 + E_2$ . The  $E_{sum}$  direction is shown by the green arrow in Fig. 3.15(a) along the diagonal of the 2D energy spectrum. The line profile of the electron pair distribution in Fig. 3.15(a) along  $E_{sum}$  is shown in Fig. 3.15(b) (red solid circles). In addition, in Fig. 3.15(b) the background signal from an independent control experiment is shown (bg, empty circles), which allows the estimation of accidental electron pair events triggered

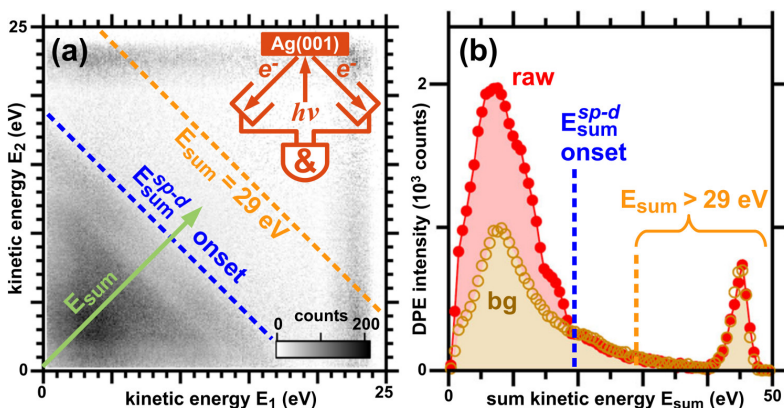


Figure 3.15: (a) Raw DPE spectrum measured on Ag(001) with a photon energy  $h\nu = 32.3$  eV and  $s$ -polarization. (b) Line profiles along the sum energy ( $E_{sum}$ ) direction from (a) and from accidental events as background (bg). From [C5.8], copyright (2017) by the American Physical Society.



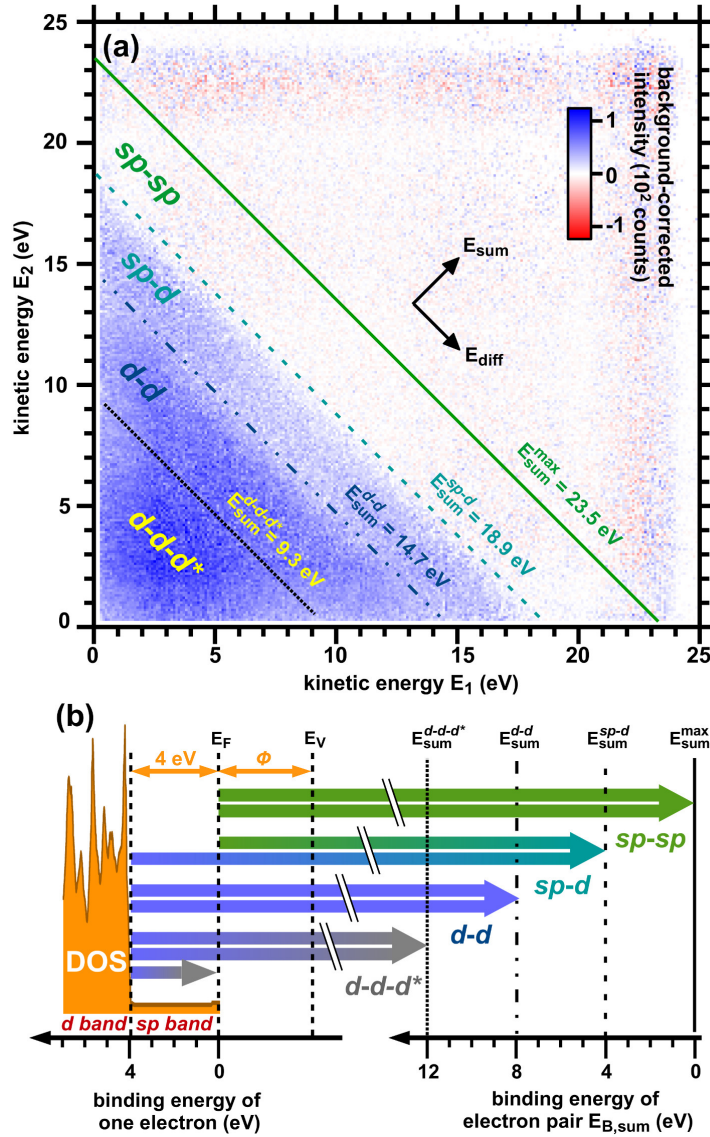


Figure 3.16: (a) Background-subtracted 2D DPE spectrum of Ag(001) with *s*-polarized light at  $h\nu = 32.3$  eV. (b) Schematics of DPE processes with the density of states (DOS) of Ag from Ref. [208]. Adapted from [C5.8], copyright (2017) by the American Physical Society.

by two independent photons within one light pulse [207]. As one can clearly see in Fig. 3.15(b), there is a significant number of photoelectron pairs below a well-defined total energy of the electron pairs as labeled by  $E_{sum}^{sp-d}$ . The position of  $E_{sum}^{sp-d}$  is also indicated in Fig. 3.15(a) (blue dashed), and it has a characteristic 45° orientation relative to the individual energy axis  $E_1$  and  $E_2$ .

The background-subtracted DPE spectrum from Fig. 3.15(a) is shown in Fig. 3.16(a), and two more features can be identified as indicated by the dashed-dotted and the dotted lines of  $E_{sum}^{d-d}$  and  $E_{sum}^{d-d-d^*}$  which are 45° orientated relative to the  $E_1$  and  $E_2$  axes. For comparison, the density of states of Ag is displayed in Fig. 3.16(b) (DOS, filled) [208]. As can be explained by the schematics in Fig. 3.16(b), these three diagonal features  $E_{sum}^{sp-d}$ ,  $E_{sum}^{d-d}$  and  $E_{sum}^{d-d-d^*}$  result from emission processes of electron pairs participated by 1, 2, and 3 Ag *d* electrons. Taking the dashed line for  $E_{sum}^{sp-d}$  in Fig. 3.16(a) and (b) as an example, it marks the maximal energy of an electron pair consisting of one *sp*- and one *d*-electron. For the excitation of the *sp* electron at the Fermi level ( $E_F$ ) and its emission into vacuum, a minimal amount of energy of the Ag(001) work function  $\Phi_{Ag} \approx 4.4$  eV

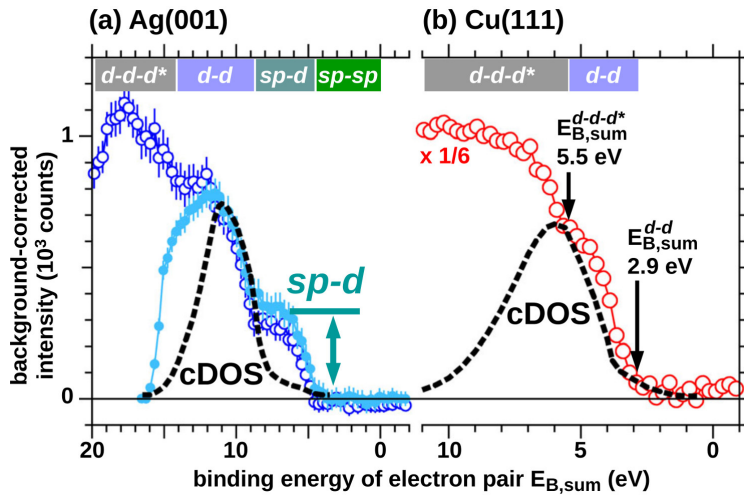


Figure 3.17: Comparison of DPE spectra on (a) Ag(001) and (b) Cu(111) with the self-convoluted DOS from Ref. [213] (cDOS). Empty and solid circles are measured with  $h\nu = 32.3$  and  $25.1$  eV. From [C5.8], copyright (2017) by the American Physical Society.

is required [209]. For the  $d$  electron, an additional amount of energy to overcome the minimal binding energy of the Ag  $4d$  bands  $E_{B,Ad} \approx 4$  eV is needed, which can also be seen in Fig. 3.16(b) [208]. As a result,  $E_{sum}^{sp-d} = h\nu - 2\Phi_{Ag} - E_{B,Ad} \approx 19.5$  eV, which reasonably agrees with the observed  $E_{sum}^{sp-d}$  at 18.9 eV in Fig. 3.16(a). The slight deviation of less than 0.6 eV between the expected and the observed values of  $E_{sum}^{sp-d}$  could serve as an upper bound for the modification of the electronic structure due to the presence of two photo-holes locally [210, 211]. Similarly, both  $E_{sum}^{d-d}$  and  $E_{sum}^{d-d-d^*}$  can be explained by the transitions in Fig. 3.16(b) and ascribed to the maximal energies of  $d-d$  photoelectron pairs as well as their associated shake-up satellite with an additional neutral  $d^*$  excitation. The  $d^*$  excitation promotes a  $d$  electron up to  $E_F$  which does not leave the surface, and it is in analogy to the shake-up process in the core-level photoelectron spectroscopy [212].

In addition to the quantitative connection between the maximum energies of electron pairs and the number of participating  $d$  electrons, the magnitude of the DPE signals can be compared with the density of states. In Fig. 3.17(a) the DPE  $E_{sum}$  spectra measured on Ag(001) with  $h\nu = 32.3$  and  $25.1$  eV are shown, and the assignment of electron pairs according to Fig. 3.16(b) is labeled on the upper scale. More importantly, the self-convoluted DOS of Ag from Ref. [213] is shown in Fig. 3.17(a) (cDOS), which provides an estimation for the relative amount of  $sp-d$  and  $d-d$  electron pairs from Ag [214–217]. This estimation based on the cDOS is derived from the theoretical model proposed by M. Cini and G. A. Sawatzky for correlated electrons with weak interaction [218, 219], and it was originally applied to explain Auger electron emission processes participated by two valence electrons. As can be seen in Fig. 3.17(a), the cDOS can describe the observed onsets of  $d-d$  and  $sp-d$  electron pairs from Ag. However, the amount of the detected  $sp-d$  electron pairs is about a factor of three higher than that in the cDOS. This observation on Ag is in strong contrast to Cu as shown in Fig. 3.17(b), where no significant  $sp-d$  electron pairs can be found in the experimental result as well as in the cDOS. The observed  $sp-d$  electron pairs in Ag and their absence in Cu can be attributed to the characteristic interaction between the  $sp$  and  $d$  electrons in these metals. Due to the larger volume fraction and the higher polarizability of the Ag  $4d$  electrons than the Cu  $3d$  electrons

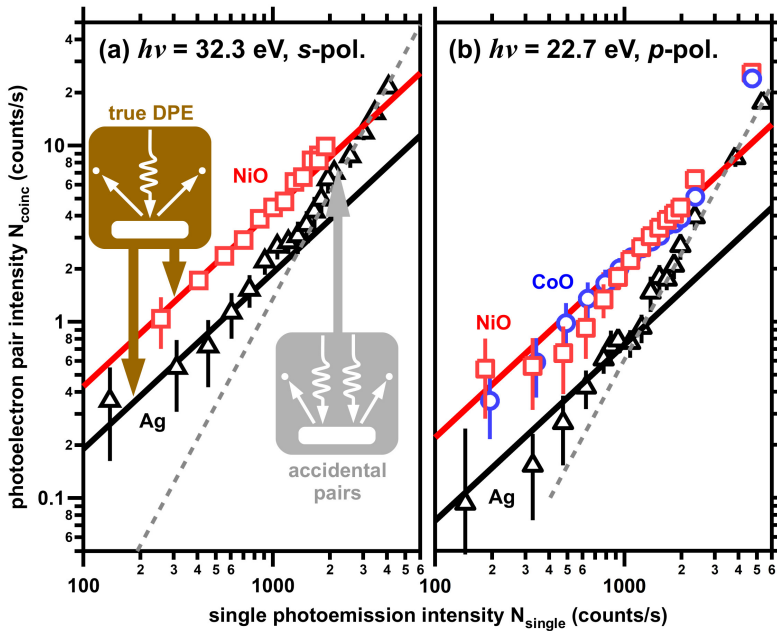


Figure 3.18: Count rate of detected photoelectron pairs from Ag, NiO and CoO using (a)  $h\nu = 32.3$  eV with  $s$ -polarization and (b)  $h\nu = 22.7$  eV with  $p$ -polarization as functions of the single photoemission count rate. True and accidental coincidence events with a slope of 1 and 2 are indicated by the solid and dashed lines. Adapted from [156].

[220, 221], the interaction between the  $sp$  and  $d$  electrons in Ag could be stronger than that in Cu. Consequently, the DPE matrix element for the  $sp$ - $d$  pairs from Ag may have a larger magnitude and lead to a higher DPE intensity than on Cu [222].

The electron-electron interaction does not only play an important role in DPE from different electronic states in the same material as discussed above for Ag and Cu, but can also lead to a material-dependent DPE intensity [70, 223]. In order to provide experimental possibilities to compare the strength of electron-electron interaction between different materials, in this work the following DPE experiments on NiO and CoO were performed in comparison with the metals Ag and Cu. Due to the sizable onsite Coulomb repulsion between electrons in the Ni and Co  $3d$  orbitals of around 8 eV, both NiO and CoO are commonly classified as the prototypes of strongly correlated materials [224–230].

In Fig. 3.18, the DPE experiments on the 3 nm NiO films grown on Ag(001) are compared with Ag(001). The DPE count rate on NiO at  $h\nu = 32.3$  eV with  $s$ -polarization is shown in Fig. 3.18(a) by the red squares ( $N_{coinc}$ ) as a function of the single photoemission intensity ( $N_{single}$ ). On this double logarithmic plot a dominant linear dependence of  $\log(N_{coinc})$  as a function of  $\log(N_{single})$  can be seen, which indicates a relation of  $N_{coinc} \propto N_{single}^q$  with a well-defined exponent  $q$ . These data can be reasonably described by  $q \approx 1$  with a ratio of  $T_{NiO} = N_{coinc}/N_{single} = 0.43 \pm 0.04\%$  as drawn by the solid line. For comparison, DPE count rate on Ag(001) under the same experimental conditions is shown in Fig. 3.18(a) (black triangles) with a transition from  $q \approx 1$  with a ratio of  $T_{Ag} = 0.19 \pm 0.08\%$  (solid line) to a quadratic dependence  $q \approx 2$  (dashed line). The regions at low  $N_{coinc}$  and  $N_{single}$  with  $q \approx 1$  belongs to true double photoemission events, where a single incident photon excites a correlated electron pair [96, 222]. In contrast, at a higher photon flux and consequently with a higher  $N_{single}$ , the region with  $q \approx 2$  dominates and contains mainly accidental coincidence events where two photons excite two uncorrelated electrons. By comparing  $T_{NiO}$  with  $T_{Ag}$  under the same single photoemission rate, on NiO

an about two times higher DPE intensity is detected than on Ag.

To examine whether the higher DPE intensity on NiO than Ag as revealed by  $T_{NiO} > T_{Ag}$  in Fig. 3.18(a) is a general phenomenon, in Fig. 3.18(b) we compare DPE experiments at a different photon energy  $h\nu = 22.7$  eV with  $p$ -polarized light. There, the ratio for true DPE events on NiO and Ag are  $T_{NiO} = 0.22 \pm 0.07\%$  and  $T_{Ag} = 0.08 \pm 0.03\%$ . Therefore  $T_{NiO} > T_{Ag}$  still holds at this lower  $h\nu$  with a different light polarization. In addition, the DPE intensity from 3 nm CoO films grown on Ag(001) is also shown in Fig. 3.18(b) with  $T_{CoO} = 0.20 \pm 0.03\%$ , which is very comparable to  $T_{NiO}$ . In Fig. 3.19 we summarize the results measured with different  $h\nu$  and light polarization. Here two general trends can be clearly seen. Firstly, the higher the  $h\nu$  is, the more electron pairs are emitted in comparison to the increase in the single photoemission events (solid lines). Secondly,  $T_{NiO} \approx T_{CoO} \geq T_{Ag}$  is valid in this  $h\nu$  range and signify a possible connection between the DPE intensity and the stronger electron-electron interaction in NiO and CoO than in Ag [70]. On NiO the DPE intensity becomes significantly higher than Ag at increasing  $h\nu$ , especially when  $h\nu$  becomes sufficient to excite electron pairs consisting of one electron from the oxygen  $2s$  state and one from the NiO valence band ( $h\nu \geq h\nu_{NiO,d-O_{2s}}$ , dashed-dotted line).

The photoelectron pairs from NiO and CoO can be analyzed similarly as for Ag in

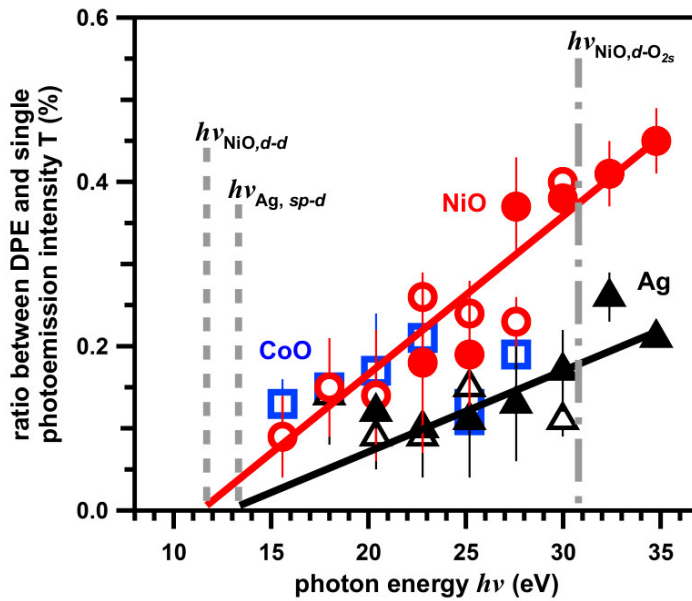


Figure 3.19: Ratio between DPE and single photoemission count rates  $T$  measured on Ag(001), 3 nm NiO and CoO films at  $h\nu = 15$  to 35 eV with  $p$ - (open symbols) and  $s$ -polarized light (filled symbols). Dashed lines: minimal  $h\nu$  for DPE of the  $sp-d$  photoelectron pairs from Ag ( $h\nu_{Ag,sp-d}$ ), and for DPE on NiO from the valence bands ( $h\nu_{NiO,d-d} = 2E_{B,VBM} + 2\Phi_{NiO}$ ). Dashed-dotted line: minimal  $h\nu$  for pairs with one electron from the  $O_{2s}$  level and one from the valence bands of NiO ( $h\nu_{NiO,d-O_{2s}} = E_{B,O_{2s}} + E_{B,VBM} + 2\Phi_{NiO}$ ). Literature values for NiO: work function:  $\Phi_{NiO} = 4.4$  eV [231, 232], binding energy of the valence band maximum:  $E_{B,VBM} \approx 1.5$  eV [233, 234], binding energy of  $O_{2s}$ :  $E_{B,O_{2s}} \approx 20.5$  eV [235, 236]. Solid lines are guide for the eye. Adapted from [156].



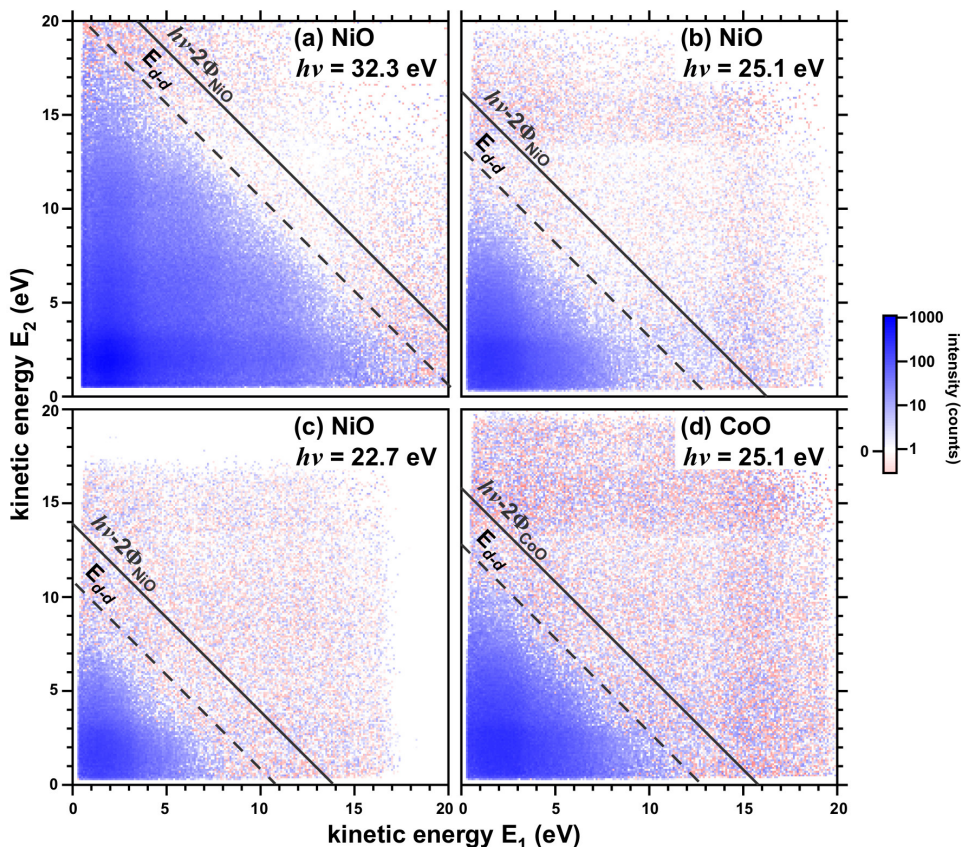


Figure 3.20: 2D DPE spectra on NiO/Ag(001) measured with (a)  $h\nu = 32.3$  eV, (b)  $h\nu = 25.1$  eV, (c)  $h\nu = 22.7$  eV, and (d) DPE on CoO/Ag(001) with  $h\nu = 25.1$  eV. Data in (a), (b) and (d) are measured with  $s$ -polarized light, and (c) with  $p$ -polarization. Solid lines: highest possible sum kinetic energy at  $h\nu - 2\Phi_{\text{NiO,CoO}}$ ; Dashed lines: expected onset of DPE signals of  $d$  electrons from the valence band maximum at  $E_{d-d} = h\nu - h\nu_{d-d} = h\nu - 2\Phi_{\text{NiO,CoO}} - 2E_{B,VBM}$ ; Work functions of NiO and CoO:  $\Phi_{\text{NiO}} = 4.4$  eV and  $\Phi_{\text{CoO}} = 4.6$  eV [231, 232, 237]; Binding energies of the valence band maximum of NiO and CoO are  $E_{B,VBM} \approx 1.5$  eV [233, 234, 238]. Adapted from [156].

Fig. 3.16 with respect to the energy of the individual electron  $E_{1,2}$  within an pair. In Fig. 3.20 the two-dimensional DPE spectra measured at various  $h\nu$  on NiO as well as DPE on CoO are shown, where the accidental coincidence events have been subtracted. There the DPE signals are observed mainly in the triangular region below a sum energy  $E_{d-d}$ , which indicates the highest kinetic energy of the electron pairs consisting of two  $d$  electrons from the valence band maximum. This onset will be discussed later with the sum energy spectrum. In addition, between  $E_{1,2} = 0$  to 3 eV in Fig. 3.20 there are features parallel to the  $E_{1,2}$  axes, which could be attributed to the final states consisting of the high-lying unoccupied  $4sp$  states derived from the Ni and Co ions in these oxides [239, 240].

In Fig. 3.21 the sum energy spectra of electron pairs from NiO and CoO are shown as a function of the binding energy of the electron pairs. Instead of the step-like features observed in Ag and Cu in Fig. 3.17, on NiO and CoO the DPE intensity increases rapidly toward higher binding energies. This observation is ascribed to the possibility of low

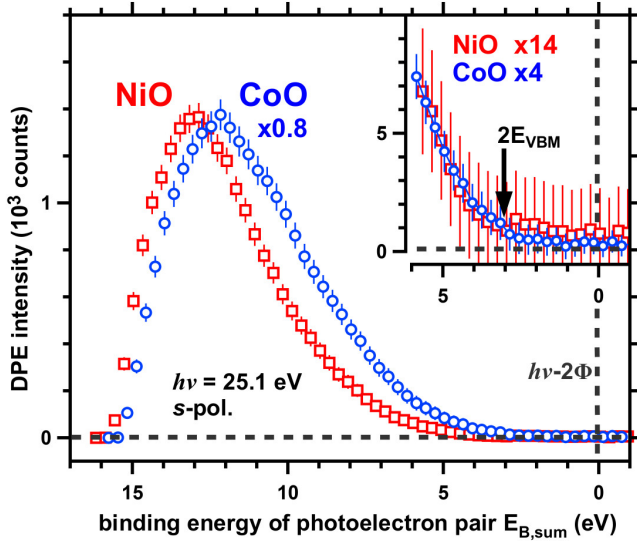


Figure 3.21: Sum energy spectra of NiO and CoO from Fig. 3.20(b,d) integrated over an energy region of  $E_{diff} = E_1 - E_2 = \pm 20$  eV. Inset shows the onset of the DPE signals at a binding energy for photoelectron pairs at about  $2E_{B,VBM} = 3.0$  eV (arrow [233, 234, 238]). Adapted from [156].

energy excitations of  $d$  electrons in NiO [241–245] and CoO [242, 243, 246, 247], which require only an amount of energy above 0.6 eV that is much smaller than the minimal binding energy of the  $d$  electrons in Cu and Ag (2 and 4 eV). Consequently, the phase space for electron pairs with multiple  $d$  excitations in NiO and CoO can increase more rapidly toward higher binding energies as compared to Ag and Cu. A closer look at the onset of the DPE signals is shown in the inset of Fig. 3.21, where the expected emission of two  $d$  electrons as a pair from the valence band maximum is indicated ( $2E_{VBM}$ ), and it corresponds to the  $E_{d-d}$  onset in the 2D spectra in Fig. 3.20. The binding energy of the valence band maximum  $E_{VBM}$  in NiO and CoO is about 1.5 eV [233, 234, 238]. In conventional photoelectron spectroscopy,  $E_{VBM}$  is related to a Zhang-Rice state in theory, which is formed by the initial excitation of a single  $d$  electron followed by the filling and screening of neighboring  $2p$  electrons at oxygen ions [234, 248–253]. The indications of the DPE onset at  $2E_{VBM}$  in Fig. 3.21 imply that a pair of Zhang-Rice states is generated in the DPE process, and there is a non-vanishing interaction between them [254].

### 3.4 Angular distribution of photoelectrons and photoelectron pairs

The photoelectrons emitted from solids have specific angular distributions that are connected to their energy- and momentum-dependent band occupation [15]. In the traditional angle-resolved photoelectron spectroscopy (ARPES), the energy-momentum dispersion  $E(\vec{k})$  of the electronic structure of solids can be traced by the transformation from the measured kinetic energy ( $E_k$ ) and two-dimensional (2D) angular coordinates ( $\theta, \phi$ ) to the binding energy ( $E_B$ ) and the 2D momentum coordinates parallel to the surface ( $k_x, k_y$ ) [16, 17]. In this chapter the angular distribution of photoelectrons from the BaTiO<sub>3</sub>-derived oxide quasicrystal (OQC) as well as photoelectron pairs from Ag(001) are presented. The former experiments were performed in collaboration with Dr. Christian Tusche using the newly built momentum microscope with a direct imaging of photoelectron momentum distribution at the back-focal plane of the electron optics [47, 48]. The latter double photoemission (DPE) experiments on photoelectron

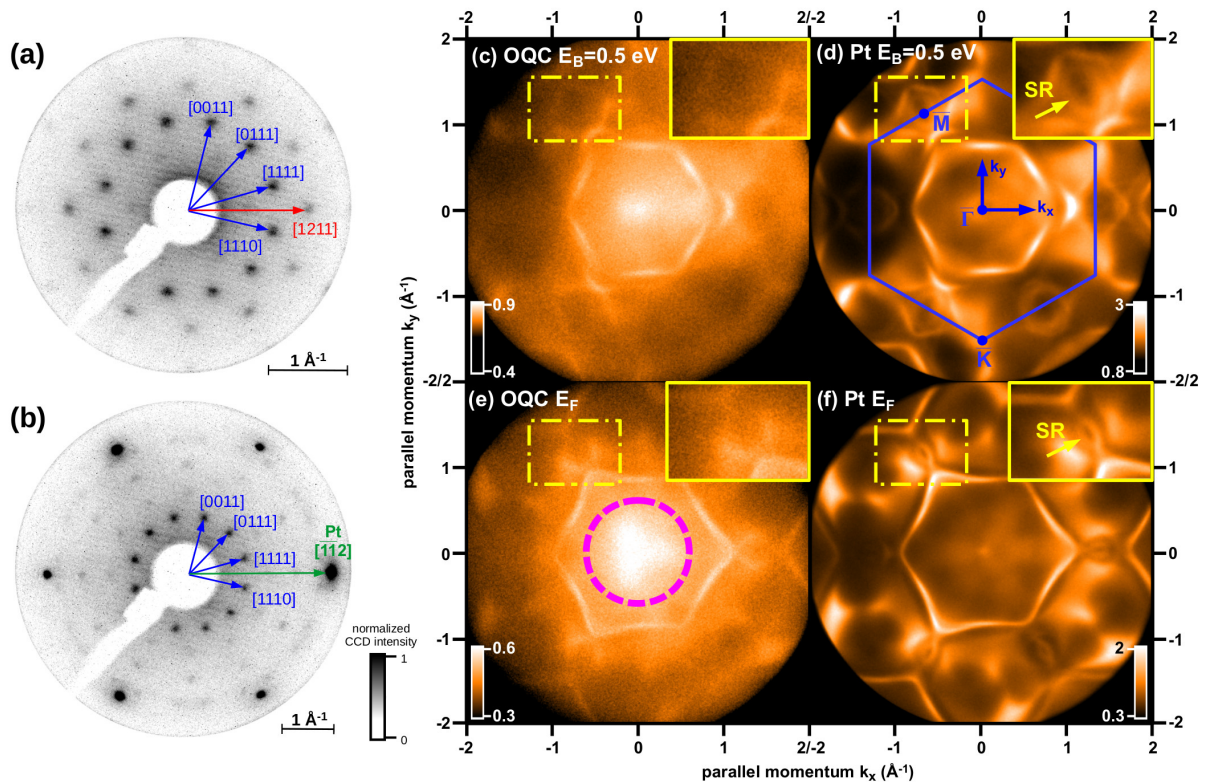


Figure 3.22: (a,b) Low energy electron diffraction (LEED) patterns on the OQC at (a) 28 and (b) 66 eV. The intensity is normalized by the [0011] spot. (c-f) 2D momentum maps of photoelectrons from (c,e) the OQC and (d,f) Pt(111). (c,d) are measured at the binding energy  $E_B = 0.5$  eV, and (e,f) at the Fermi level ( $E_F$ ). The color scales are in  $10^4$  CCD counts. Magnified views near the Pt  $\bar{M}$  point (yellow) show the Pt surface resonance (SR) in (d,f), which is absent on the OQC in (c,e). In (d) the  $k_{x,y}$  directions and the surface Brillouin zone of Pt(111) are marked (blue). The circle in (e) indicates the occupation of the Ti  $3d$  states.

pairs were performed using the time-of-flight spectrometers presented in Chap. 3.2 and Chap. 3.3 in the framework of the Dissertation of Dr. Andreas Trützschler [156]. The preparatory works for the angle-resolved DPE experiments have been published in [C5.9] in Tab. 5.1, and the results of momentum microscopy on the OQC have been submitted for publication.

The OQCs have been discovered recently in ultrathin films of BaTiO<sub>3</sub> and SrTiO<sub>3</sub> on Pt(111) [50, 255]. The dodecagonal BaTiO<sub>3</sub>-based OQC was formed by dewetting-wetting processes [50, 51], and its signature appears in the low energy electron diffraction (LEED) as the characteristic 12-fold patterns as shown in Fig. 3.22(a,b). On the BaTiO<sub>3</sub>-derived OQC the energy and momentum distributions of photoelectrons were measured by the momentum microscope at 300 K using the excitation of the He-I radiation with a photon energy of  $h\nu = 21.2$  eV [47, 155]. The 2D momentum  $k_x$ - $k_y$  distribution close to the Fermi level ( $E_F$ ) are shown in Fig. 3.22(c,e) for the OQC. The identical measurements on Pt(111) are displayed in Fig. 3.22(d,f) for comparison. On the OQC the dominant features in Fig. 3.22(c,e) can be related to the Pt 5d bulk bands in Fig. 3.22(d,f) [256–259] due to the monolayer thickness of the OQC. However, there are two significant differences between Fig. 3.22(c,e) and Fig. 3.22(d,f). Firstly, the Pt surface resonance (SR) [256, 258–260], which can be better seen near the Pt  $\bar{M}$  point in the insets of Fig. 3.22(d,f), is suppressed in Fig. 3.22(c,e) due to the presence of the OQC on top of the Pt(111). This suppression is attributed to the sensitivity of surface resonance to the modification of the surface potential [261, 262].

Secondly, in Fig. 3.22(e) the photoemission intensity distribution on the OQC from  $E_F$  in the momentum region around the  $\bar{\Gamma}$  point is marked (circle). Within this specific momentum region, the photoemission intensity on the OQC is much higher than that of the Pt(111) in Fig. 3.22(f). This intensity increase on the OQC can be related to the occupation of the Ti 3d states near  $E_F$  [263, 264]. The amount of occupation can be estimated by the area density of the Ti atoms in the OQC of about  $2.5 \times 10^{14}$  cm<sup>-2</sup> and by the assumption of a Ti 3d<sup>1</sup> configuration according to the Ti<sup>3+</sup> feature in the earlier x-ray photoelectron spectroscopy [50]. The corresponding Fermi wave vector is  $0.6 \text{ \AA}^{-1}$  as indicated by the dashed circle in Fig. 3.22(e), which reasonably explains the observed momentum region on the OQC with a higher photoemission intensity. Due to the broad momentum distribution of the Ti 3d states in Fig. 3.22(e), the precise energy-momentum dispersion  $E(\vec{k})$  could not be observed, and it will be examined in further studies at synchrotron facilities with resonant photoemission spectroscopy [265–267]. Since the formation of quasicrystals is conventionally ascribed to the opening of band gaps at  $E_F$  [52, 53, 268–271], the observed signature of the Ti 3d states at  $E_F$  in this work may imply an alternative formation mechanism of the OQC [52, 53].

To reveal the electronic dispersion  $E(\vec{k})$  of the OQC, in Fig. 3.23(a,c) the 2D slices of the energy-momentum distributions of photoelectrons are shown in comparison with that of the Pt in Fig. 3.23(b,d). As can be seen in Fig. 3.23(a), there are features at  $E_B \approx 4$



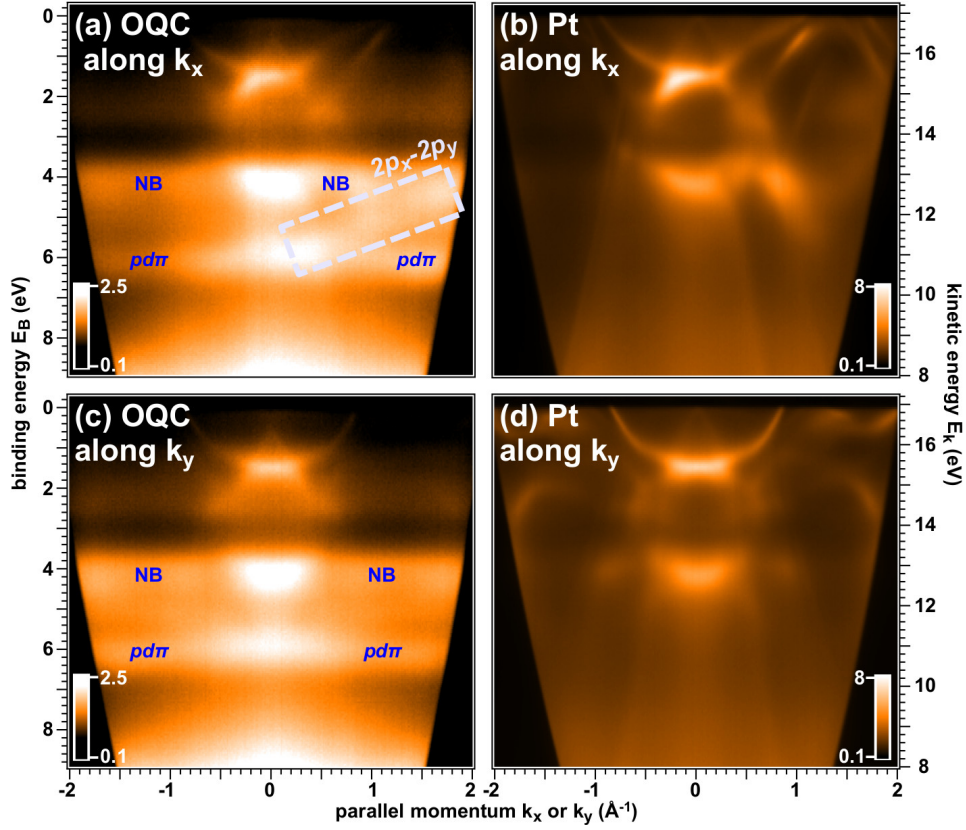


Figure 3.23: Energy-momentum distribution of photoelectrons from (a,c) the OQC and (b,d) Pt(111) along the  $k_{x,y}$  directions as indicated in Fig. 3.22(d). In (a) the dispersive oxygen-derived electronic state  $2p_x-2p_x$  is marked. NB: Non-bonding O- $2p$  state;  $pd\pi$ :  $\pi$ -bonding state with Ti- $3d$  and O- $2p$  orbitals [272]. Color scales in  $10^4$  CCD counts.

and 6 eV on the OQC with a high intensity but a flat  $E(\vec{k})$  dispersion. These electronic states can be assigned to the non-bonding (NB) state of the oxygen  $2p$  orbitals as well as the  $\pi$ -bonding state of the Ti- $3d$  and O- $2p$  orbitals ( $pd\pi$ ) [272–275]. Moreover, there is a dispersive feature between the NB and the  $pd\pi$  states, which is marked in Fig. 3.23(a) as  $2p_x-2p_y$  whose notation will become clear in the discussion later. Since the  $2p_x-2p_y$  state appears more dominantly in Fig. 3.23(a) on the  $+k_x$  side than on the  $-k_x$  side, its dispersion can be more clearly disentangled from the nearby NB and  $pd\pi$  states when the photoemission intensity is decomposed into components according to the distribution on the 2D  $k_x-k_y$  plane. A possible choice of such symmetry-based decomposition can be formulated as:

$$I(k_x, k_y, E_B) = \sum_{n=0}^{\infty} I_n(k_r, E_B) \cos(2\pi n\phi + \phi_0) \quad (3.1)$$

with the azimuthal angle for the photoelectron distribution on the  $k_x-k_y$  plane as given by  $\phi = \tan^{-1}(k_y/k_x)$ , and the magnitude of the parallel momentum as  $k_r = \sqrt{k_x^2 + k_y^2}$ . The non-negative integer  $n$  describes the intensity variation along  $\phi$ , and  $n=0$  represents the isotropic part of the photoelectron azimuthal angular distribution. Likewise,  $n=1, 2$  and  $3$  indicate the unidirectional, two- and three-fold azimuthal angular distributions. The additional parameter  $\phi_0$  is an offset, which specifies the azimuthal rotation angle

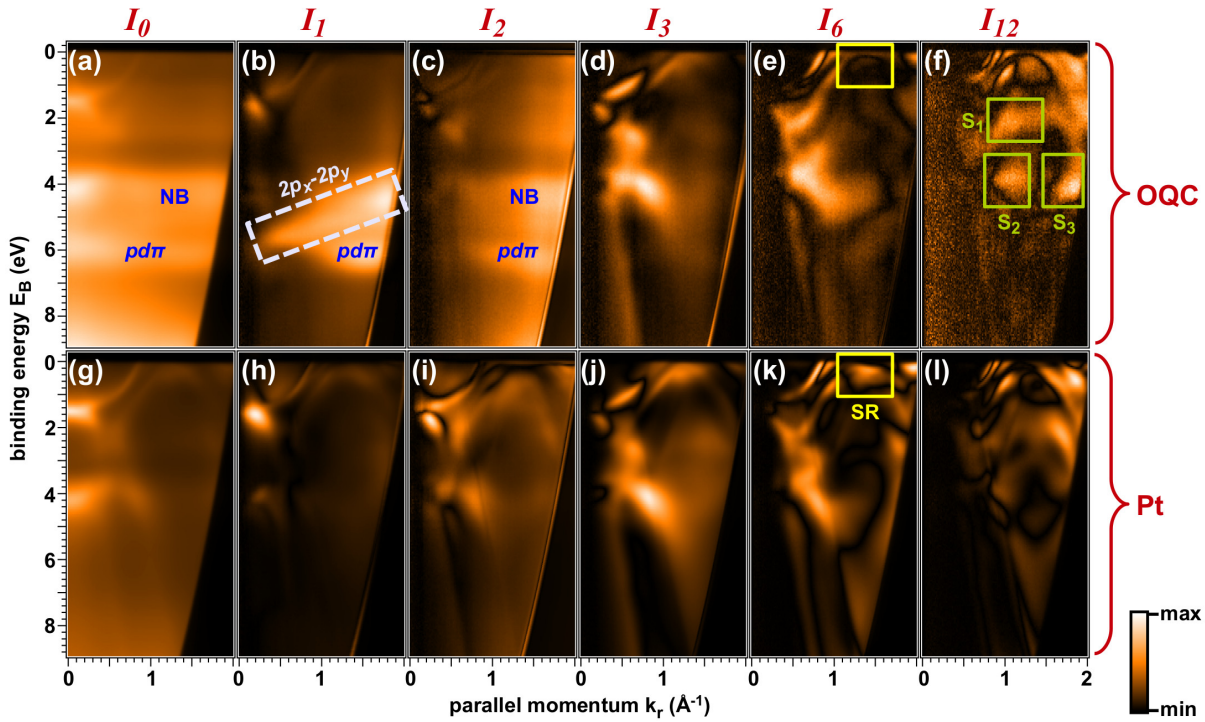


Figure 3.24: Dominant parts of the symmetry-adapted photoemission intensity  $I_n(k_r, E_B)$  with  $n = 0, 1, 2, 3, 6$  and  $12$ . (a-f) for the OQC and (g-l) for Pt(111). The SR indicates the surface resonance of Pt(111) at  $\bar{M}$  points in (k), and it is quenched in (e) on the OQC. In (f), the  $S_{1,2,3}$  indicate more pronounced twelve-fold features on the OQC. The minimum/maximum color scales are: (a) 0.1/2.6 (b) 0/0.4 (c) 0/0.2 (d) 0/0.1 (e) 0/0.06 (f) 0/0.02 (g) 0.2/7.3 (h) 0/1.6 (i) 0/0.5 (j) 0/1.3 (k) 0/0.6 (l) 0/0.3 in  $10^4$  CCD counts.

at each combination of  $n$ ,  $k_r$  and  $E_B$ . A similar decomposition was used in early works to identify the valence band photoemission spectra of metals with element- and orbital-specificity [276, 277]. In Fig. 3.24(a-f) the main components  $I_n(k_r, E_B)$  of the OQC are shown, which are compared with the same components of the Pt(111) in Fig. 3.24(g-l).

As can be seen in Fig. 3.24, there are significant differences between the OQC and Pt in the isotropic  $I_0$ , the unidirectional  $I_1$ , as well as the two-fold  $I_2$  components. In contrast, on the OQC the multiples of the three-fold symmetry  $I_{3,6,12}$  are very comparable to that of the Pt. The very similar  $I_{3,6,12}$  of the OQC and Pt indicate that on the OQC, there is a significant amount of photoelectrons from the Pt transmitting through the ultrathin OQC layer. In addition, there are few regions in  $I_{12}$  as marked by  $S_{1,2,3}$  in Fig. 3.24(f) which appear stronger on the OQC than on the Pt. Since these regions are energetically close to the intense features of Pt at  $E_B \approx 2$  and  $4$  eV, they are tentatively ascribed to photoelectrons from Pt undergoing unklapp scattering processes at the twelve-fold atomic potential of the OQC [68]. These twelve-fold features are twenty times weaker in intensity than the unidirectional component  $I_1$  of the OQC in Fig. 3.24(b), where the clear dispersion of the  $2p_x-2p_y$  state can be identified.

In Fig. 3.25(a) the  $I_1$  spectra are displayed in detail, and the observed dispersion of the  $2p_x-2p_y$  and  $pd\pi$  states are summarized in Fig. 3.25(b). In addition, the NB and  $pd\pi$  states from Fig. 3.23(a,c) are summarized with the established oxygen  $O_{2p}$  valence band

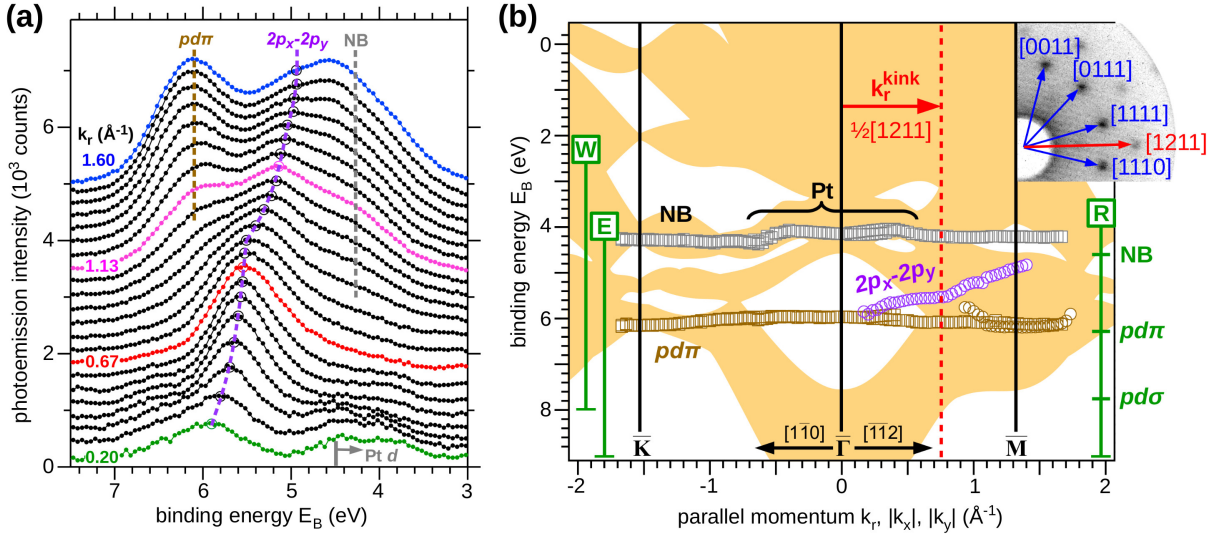


Figure 3.25: (a)  $I_1(k_r, E_B)$  spectra from Fig. 3.24(b), with the bottom of the bulk Pt  $d$  bands along  $\Lambda$  indicated [278]. Curves are shifted vertically by 150 counts, and dashed lines and circles are guide to the eye. (b) Energy-momentum dispersion of oxygen-derived valence bands of the OQC. Circles indicate  $2p_x-2p_y$  and  $pd\pi$  states in  $I_1(k_r, E_B)$  from Fig. 3.24(b), and squares for the NB and  $pd\pi$  states in Fig. 3.23(a,c). R, W, and E mark regions of the  $O_{2p}$  bands on BaTiO<sub>3</sub> crystals and films together with the Ti<sub>3d</sub>- $O_{2p}$   $pd\sigma$  bonding bands in literature [272, 279, 280]. In addition, Pt bulk transitions are indicated [278]. The filled area indicates the surface-projected bands on Pt(111) [260]. Inset shows the LEED pattern of OQC at 28 eV with the associated wave vector  $q_{[1211]} = 2k_r^{kink}$  for the kink in the dispersion of the  $2p_x-2p_y$  state.

regions from the early works on BaTiO<sub>3</sub> crystals and thin films (R,W,E [272, 279, 280]). Since the  $2p_x-2p_y$  state is located in the known energy-momentum regions of the oxygen-derived valence bands of BaTiO<sub>3</sub>, its main character is assigned to the  $O_{2p}$  orbitals, and a possible mixture of the Ti-3d orbitals is less than 10% [281]. Moreover, the  $2p_x-2p_y$  state can be ascribed to  $O_{2p}$  orbitals in the  $x-y$  surface plane according to its dominant angular distribution  $I_1$  in Fig. 3.24(b), which is in strong contrast to the NB and  $pd\pi$  states mainly in the isotropic  $I_0$  and two-fold  $I_2$  components. This assignment is supported by photoemission model calculations, which predict a larger unidirectional intensity asymmetry for atomic  $p$  orbital oriented in the surface [282, 283]. This relationship between the orbital orientation and the photoelectron angular distribution is the origin of intensity asymmetry (dichroism) in photoelectron angular distribution [153, 190, 191, 284]. More importantly, in Fig. 3.25(b) a kink in the dispersion of the  $2p_x-2p_y$  state is visible at  $k_r^{kink}$ . The momentum coordinate  $k_r^{kink}$  can be related to the diffraction spot at  $q_{[1211]}$  in the LEED pattern in the inset of Fig. 3.25(b) by  $2k_r^{kink} = q_{[1211]} \approx 1.5 \text{ \AA}^{-1}$  [50, 285, 286]. Therefore the observed kink may signify the influence of the atomic potential of the OQC to the electronic structure, which is in analogy to the band gap opening at Brillouin zone boundaries in periodic systems as well as the folding of electronic bands in metallic quasicrystals [287–291].

The angle-resolved analysis of the photoelectron distribution can provide insight not



only into the single-electron band structure as shown by the above example on BaTiO<sub>3</sub>-derived OQC, but it can also be extended to analyze electron pairs from the double photoemission (DPE) processes as presented in Chap. 3.3. One of the ultimate goals of angle-resolved DPE is to experimentally measure the extension of the exchange and correlation holes in momentum space [72–74, 292–294]. The theoretical concepts of the exchange and correlation holes have been regarded as fundamental for the understanding of electron-electron interaction since the birth of solid state physics [295–298], and they remain at the frontier of research even up to today [299–306]. The second goal for angle-resolved DPE is to explore the characteristic energy-momentum dispersion relation of electronic states consisting of two electrons. Such an energy dispersion of two-electron states has been postulated to explain the spectral width of Auger processes participated by two valence electrons [216], and it has been addressed recently in more detail in theory [307–309]. In the following, the development toward angle-resolved DPE experiments using the high-order harmonic generation setup in Chap. 3.1 in combination with the angle-resolved time-of-flight (ToF) spectroscopy in Chap. 3.2 is presented. As an example, the angle-resolved DPE experiments on Ag(001) with a photon energy  $h\nu = 32.3$  eV and *s*-polarization will be shown.

The two-dimensional (2D) angular distribution of electron pairs in DPE from Ag(001) is shown in Fig. 3.26. The distribution of one electron in the pair is displayed in Fig. 3.26(a), and the other electron in the pair detected in coincidence is shown in Fig. 3.26(b). Besides the slightly higher intensity in the middle at  $\theta_{x,1} = -45^\circ$  for the electron 1 and at  $\theta_{x,2} = 45^\circ$  for the electron 2 due to a better transmission of the electron optics along the spectrometer axis, their angular distributions are broad and smooth as shown by the line profiles in Fig. 3.26(c,d) (black). For comparison, the distributions of

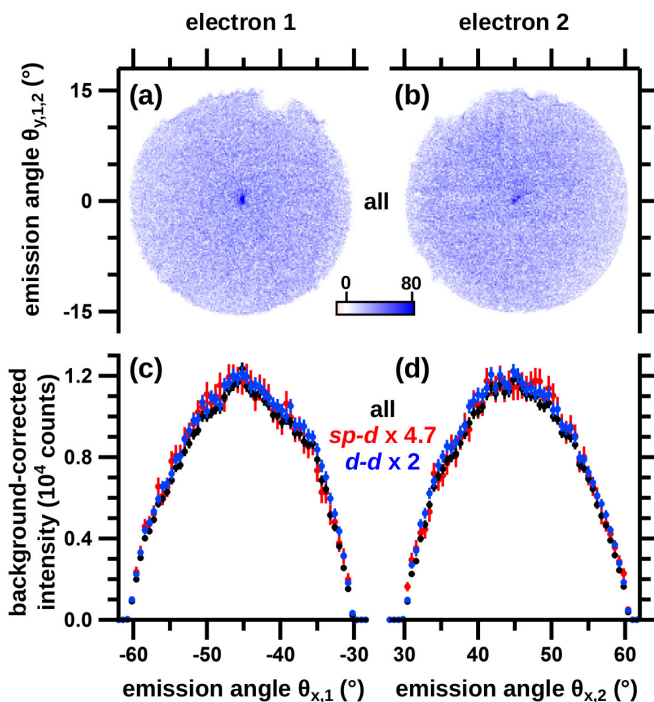


Figure 3.26: DPE on Ag(001) with  $h\nu = 32.3$  eV and *s*-polarization. (a,b) 2D angular distributions of electron 1 and 2 in the electron pairs detected by the two ToF-spectrometers in coincidence. In (c,d) the 2D distributions in (a,b) are integrated over the angle  $\theta_{y,1}$  and  $\theta_{y,2}$  (all), and compared with the *sp-d* and the *d-d* electron pairs selected according to their sum energy range ( $E_{sum}$ ) in Fig. 3.16(a). Color scale in (a,b) in counts. Adapted from [156].

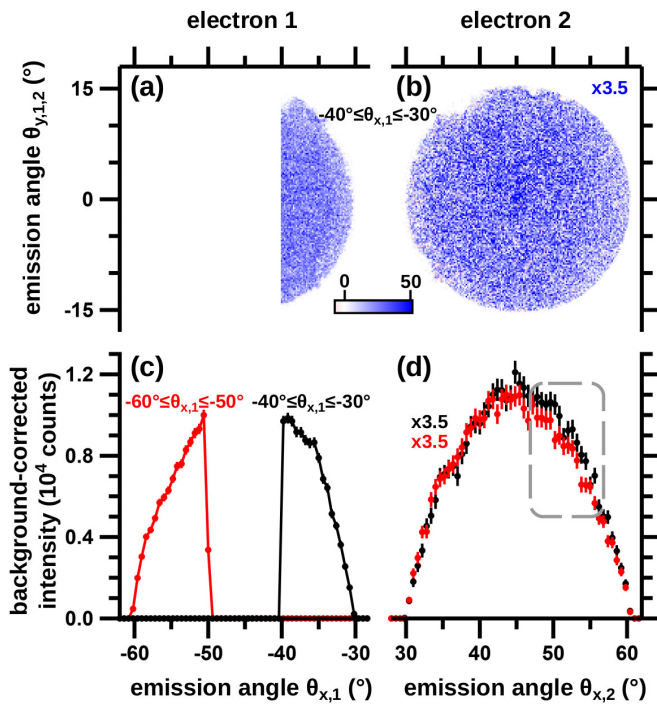


Figure 3.27: DPE on Ag(001) with  $h\nu = 32.3$  eV and  $s$ -polarization. (a,b) 2D angular distribution of electron pairs with a selected emission angle  $\theta_{x,1}$  for the electron 1 between  $-30^\circ$  and  $-40^\circ$ . In (c,d) the 2D distributions in (a,b) are integrated over the angle  $\theta_{y,1}$  and  $\theta_{y,2}$  (black), and compared with pairs selected by the condition  $-60^\circ \leq \theta_{x,1} \leq -50^\circ$  (red). Color scale for (a,b) in counts, and (b,d) are enhanced by a factor of 3.5.

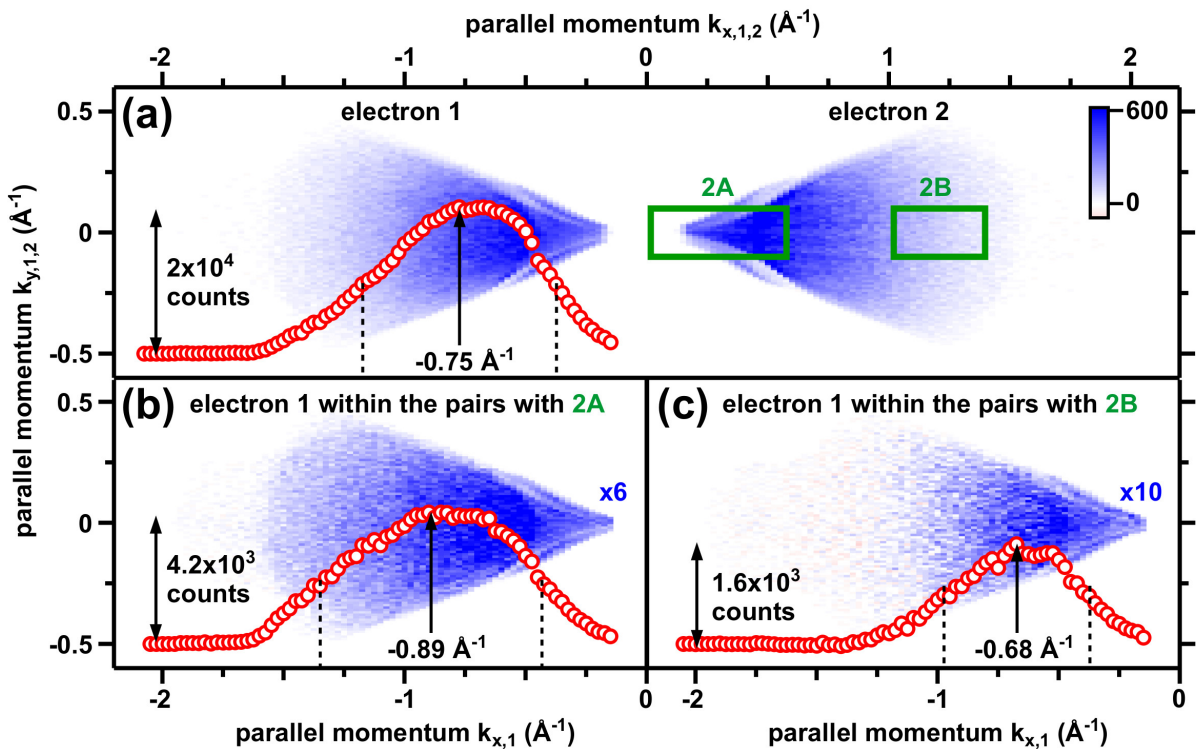


Figure 3.28: (a) 2D momentum distribution of electron pairs on Ag(001) measured with  $h\nu = 32.3$  eV and  $s$ -polarization. (b) The distribution of electron 1 in the same pairs as the electron 2 selected in the marked momentum region 2A in (a). (c) The distribution of electron 1 in the same pairs as the electron 2 selected by the region 2B in (a). The red circles display the distribution of electron 1 integrated over the momentum component  $k_{y,1}$ . Vertical dashed lines as well as the arrows mark the left- and right edges of the integrated distribution as well as their middle points. Color scale for (a-c) is shown in (a) in counts, with the intensity in (b) and (c) enhanced by a factor of 6 and 10, respectively. Adapted from [156].

electron pairs consisting of one  $sp$  and one  $d$  electron ( $sp-d$ ) as well as the pairs with two  $d$  electrons ( $d-d$ ) are also shown in Fig. 3.26(c,d)(red,blue). There, the angular distributions of  $sp-d$ ,  $d-d$  as well as the energy-integrated electron pairs are comparable up to a scaling factor. This observation indicates that the angular distribution of electron pairs from Ag(001) is independent of their sum energy within the detected angular range, and it is in strong contrast to single photoemission processes on Ag as shown in Fig. 3.11.

The angular distribution of electron pairs can be examined more closely by selecting the angular or momentum coordinates of one of the electron within the pairs. In Fig. 3.27(a,b) the distributions of pairs with one electron in  $-40^\circ \leq \theta_{x,1} \leq -30^\circ$  are shown, and their integrated line profiles are displayed in Fig. 3.27(c,d) (black). For comparison, a selection of the electron 1 further away from the electron 2 is demonstrated by choosing the angular range  $-60^\circ \leq \theta_{x,1} \leq -50^\circ$ , and its line profiles in Fig. 3.27(c,d) (red) show only a marginal decrease in the range of  $48^\circ \leq \theta_{x,2} \leq 55^\circ$  (dashed region). However, this slight decrease of DPE intensity would be consistent with the early DPE studies on Cu(111) with a larger angular acceptance but an order-of-magnitude lower energy resolution [73, 74], where the angular distribution of one electron follows that of the other electron in the same pair. A similar result can be observed in the momentum space in Fig. 3.28 when the angular coordinates are transformed to the corresponding momentum components parallel to the surface. In Fig. 3.28(a) the momentum distribution of the electron pairs without any restriction is shown. For comparison, Fig. 3.28(b,c) display the momentum distributions of one electron in the pair with an additional condition given by the momentum selection of the other electron at 2A and 2B in Fig. 3.28(a). As can be clearly seen by the relative shift along  $k_{x,1}$  between the distributions in Fig. 3.28(b,c), the momentum of the two electrons in the pair are correlated with each other. For the future DPE experiments, such a momentum analysis of photoelectron pairs would be important for studies of the momentum-dependent electron pairing in superconductors [21].

## 4 Summary and outlook

In this Habilitation work, the electronic structure at the surface of transition metals and their oxides is studied by laboratory photoelectron spectroscopy (PES) with advanced methods. These methods include the application of a novel light source based on high-order harmonic generation (HHG) at megahertz repetition rates (Chap. 3.1), the combination of the HHG light source with time-of-flight photoelectron spectroscopy (Chap. 3.2), as well as their implementation in the energy- and angle-resolved double photoemission (DPE) spectroscopy (Chap. 3.3-3.4). Moreover, the electronic structure of the oxide quasicrystal was directly imaged in the momentum space by the momentum microscopy (Chap. 3.4).

For the HHG-based PES experiments, a compact generation chamber for the harmonics using the tight-focusing geometry was designed. This specific geometry allows the production of high-order harmonics driven by  $\mu\text{J}$  laser pulses at a repetition rate from 0.2 to 1.0 MHz. The high repetition rates provide a unique opportunity for laboratory PES without limitation from the space-charge effects, which have imposed a severe barrier for earlier HHG-based PES at few kHz repetition rates. Therefore, the HHG setup presented in this Habilitation work benchmarks the development towards an efficient laboratory vacuum-ultraviolet light source for photoelectron-based techniques such as PES and photoelectron microscopy [C5.1-5.5].

The well-defined temporal pulse structure of the HHG light source is ideal for the application of the time-of-flight electron spectroscopy, which allows to simultaneously measure the energy and the two momentum components of individual photoelectrons. In this work, by using the tunable photon energy range of the HHG light source from 14 to 42 eV, the energy-momentum electronic dispersion of Ag(001) is shown [C5.2,5.3]. Specifically the role of the three-dimensional momentum components as well as the characteristic dependence on the light polarization are demonstrated. More importantly, the femtosecond pulse duration of the high-order harmonics provides an inherent temporal resolution in the HHG-based PES experiments, which enables the study of electron dynamics in photon-pump, photoelectron-probe experiments. As a prototypical system the dynamics at the  $\text{SiO}_2/\text{Si}(001)$  interfaces upon nonlinear photoexcitation is studied [C5.6].

In combination with a pair of time-of-flight spectrometers, the HHG light source is implemented in DPE experiments to reveal the electron-electron interaction in metals

and oxides [C5.7,5.8]. This particular combination provides a high energy resolution, and consequently the signatures of band-dependent DPE spectra on Ag(001) and Cu(111) can be discovered for the first time by this Habilitation work. The clear indications of electron pairs from Ag consisting of one *sp* electron and one *d* electron (*sp-d* pair) as well as two electrons from the *d* bands (*d-d* pair) are in strong contrast to DPE on the strongly correlated systems NiO and CoO. On NiO and CoO the DPE intensity is higher than that on Ag and Cu, which is consistent with a stronger electron-electron interaction in these oxides. In addition, the DPE spectra on NiO and CoO show a continuously increasing intensity towards higher binding energies of the electron pairs. This observation can be explained by the smaller amount of energy required to excite a *d* electron in these oxides than in Ag and Cu, which leads to a rapidly expanding phase space of electron pairs when the number of participating *d* electrons increases.

In order to gain more insights into the electronic structure of metal and oxide surfaces, the angular and momentum distributions of photoelectrons and photoelectron pairs are examined by the momentum microscopy as well as by the angle-resolved DPE analysis [C5.9]. The former is demonstrated on the BaTiO<sub>3</sub>-derived oxide quasicrystal grown on the Pt(111) surface. By decomposing the momentum distribution of photoelectrons according to their azimuthal symmetry, three different oxygen-derived valence bands are clearly identified from the dispersive features of the underlying Pt. In addition, signatures of Ti 3*d* states are observed at the Fermi level, which imply a Ti 3*d*<sup>1</sup> occupation that is compatible with previous x-ray photoelectron spectroscopy experiments.

In analogy to the single photoemission processes, in DPE the angular and momentum distributions of photoelectron pairs can be resolved. In strong contrast to the clear angle-dependent features in single photoemission processes, the angle-resolved analysis of DPE experiments on Ag(001) indicates broad angular distributions of both photoelectrons in the pairs. Within the detected angular range, these distributions are independent of the total energy of the electron pairs. By selecting a given momentum range of one of the electrons in the pair, the momentum distribution of the other electron in the same pair is influenced accordingly. This observation agrees with earlier DPE experiments having a lower energy resolution but a much larger angular acceptance, and indicates that the two electrons in the same pair are correlated in the momentum space.

By using the femtosecond duration of the high-order harmonics, it will become possible to investigate the dynamics of electron pairs in time-resolved pump-probe DPE experiments [309]. In these experiments, the temporal response of electron pairs to the collective excitations in solids could be studied directly. In addition, the MHz HHG allows DPE experiments using the recently developed time-of-flight momentum microscopy [4], where the photoelectron pairs can be detected with full solid angle acceptance. With this unique experiment in the future, the electron-electron interaction in solids could be explored with two orders-of-magnitude higher efficiency than the DPE experiments presented in this Habilitation work.



# 5 Original publications

In this chapter the publications in Tab. 5.1 as results of this Habilitation work are attached.

notation	citation	page
[C5.1]	High-order harmonic generation at 4 MHz as a light source for time-of-flight photoemission spectroscopy, Appl. Phys. Lett. <b>101</b> , 071116 (2012). Reprinted with the permission of AIP Publishing.	42
[C5.2]	Efficient and tunable high-order harmonic light sources for photoelectron spectroscopy at surfaces, J. Electron Spectrosc. Relat. Phenomena, <b>200</b> , 15 (2015).	46
[C5.3]	Boosting laboratory photoelectron spectroscopy by megahertz high-order harmonics, New J. Phys. <b>17</b> , 013035 (2015). Under the terms of the Creative Commons Attribution 3.0 licence.	53
[C5.4]	Atomic line emission and high-order harmonic generation in argon driven by 4 MHz sub- $\mu$ J laser pulses, Phys. Rev. A <b>89</b> , 043404 (2014). Copyright by the American Physical Society.	61
[C5.5]	Angle-resolved photoelectron spectroscopy at surfaces with high-order harmonic generation, Reference module in chemistry, molecular sciences and chemical engineering, Encyclopedia of Interfacial Chemistry, 28-38, edited by K. Wandelt, ISBN:978-0-12-409547-2. Copyright (2018), with permission from Elsevier.	66
[C5.6]	SiO <sub>2</sub> /Si(001) studied by time-resolved valence band photoemission at MHz repetition rates: Linear and nonlinear excitation of surface photovoltage, J. Vac. Sci. Technol. A <b>37</b> , 021101 (2019). Reprinted with permission. Copyright (2019) American Vacuum Society.	77
[C5.7]	Electron pair emission detected by time-of-flight spectrometers: recent progress, App. Phys. Lett. <b>104</b> , 061602 (2014). Reprinted with the permission of AIP Publishing.	83
[C5.8]	Band-resolved double photoemission spectroscopy on correlated valence electron pairs in metals, Phys. Rev. Lett. <b>118</b> , 136401 (2017). Copyright by the American Physical Society.	87
[C5.9]	Extended energy range analysis for angle-resolved time-of-flight photoelectron spectroscopy, J. Appl. Phys. <b>124</b> , 164504 (2018). Reprinted with the permission of AIP Publishing and under the terms of the Creative Commons Attribution 4.0 licence.	93

Table 5.1: Publications derived from this Habilitation work.

## High-order harmonic generation at 4 MHz as a light source for time-of-flight photoemission spectroscopy

Cheng-Tien Chiang,<sup>1,2</sup> Alexander Blättermann,<sup>2</sup> Michael Huth,<sup>1</sup> Jürgen Kirschner,<sup>1</sup> and Wolf Widdra<sup>1,2,a)</sup>

<sup>1</sup>Max Planck Institute of Microstructure Physics, Weinberg 2, D-06120 Halle, Germany

<sup>2</sup>Institute of Physics, Martin-Luther-Universität Halle-Wittenberg, Von-Danckelmann-Platz 3, D-06120 Halle(Saale), Germany

(Received 8 June 2012; accepted 2 August 2012; published online 16 August 2012)

We demonstrate high-order harmonic generation (HHG) at 4 MHz driven by a long-cavity femtosecond laser oscillator. The laser output is used directly in a tight focusing geometry, where the harmonics are generated from a gas jet with high backing pressure. The harmonic light source is applied to time-of-flight photoemission spectroscopy, and the characteristic electronic structure of Cu(111) is measured. Our results suggest a straightforward design of high-order harmonic generation at megahertz repetition rate and pave the way for applications in electron spectroscopy and microscopy. © 2012 American Institute of Physics. [<http://dx.doi.org/10.1063/1.4746264>]

The strong electric field in intense laser pulses can liberate bound electrons via tunnel ionization, accelerate free electrons in oscillatory pondermotive motion, and control electron-atom scattering for emission of high energy photons.<sup>1</sup> Coherent quantum mechanical combination of these three pathways leads to the high-order harmonic generation (HHG), whereby attosecond pulses of vacuum-ultraviolet and soft x-ray light can be produced in a laboratory setup.<sup>2–5</sup> Due to the ultrashort temporal duration and the widely tunable photon energy range of HHG-based light sources, their applications in electron microscopy and spectroscopy have great potential for studies of ultrafast electron dynamics in atomic, molecular, and condensed matter systems.<sup>6–9</sup>

Despite the long-term development of HHG since more than two decades, the design of HHG setups is still in rapid evolution.<sup>10–12</sup> Conventional HHG experiments are driven by amplified laser pulses at kilohertz frequency and can provide high photon energy up to several hundred electronvolts with moderate intensity. However, the statistics of experiments are limited by the rather low repetition rates, which result in a long acquisition time for applications in spectroscopy<sup>13–16</sup> and microscopy.<sup>17,18</sup> Especially, for photoelectron-based techniques, the overall counting rate is limited by the laser repetition rate due to energy and momentum broadening by space-charge effects.<sup>19–22</sup>

To increase the repetition rate of HHG, the driving laser with a typical average power of several watts needs to deliver more light pulses per unit time.<sup>10</sup> Consequently, the electric field strength decreases, and the HHG efficiency is dramatically reduced. Recently, three different approaches have been demonstrated in order to boost the repetition rate of HHG. Vernaleken *et al.*<sup>23</sup> and Hädrich *et al.*<sup>24</sup> used high power fiber-based lasers and amplifiers. They are able to generate the 17th harmonic at 20.8 MHz repetition rate using a sophisticated laser system with 20 W output power. Alternatively, to avoid using complex amplifier systems, Kim *et al.* used optically excited plasmons in microstructures to enhance the driving electric field.<sup>25,26</sup> Although they reported

HHG up to 80 MHz, this approach and these results are currently under critical debate due to damages in the microstructures caused by the intense field.<sup>27</sup> The third approach is to generate harmonics inside the cavity of a resonator, either external to or implemented in the driving laser.<sup>28,29</sup> With additional efforts optimizing the output coupler for harmonics, Cingöz *et al.*<sup>30</sup> generated harmonics up to the 23rd order at 154 MHz and used their comb structure to characterize the line width of atomic transitions.

In this Letter, we report a more compact setup for HHG at megahertz repetition rate. We use directly the output of a Ti-sapphire laser at 4 MHz to generate harmonics up to 19th order from an Ar gas jet. With the generated light, we demonstrate a proof-of-principle application in the time-of-flight photoelectron spectroscopy. Our results provide a straightforward method for HHG at high repetition rate and pave the way to HHG-based electron microscopy and spectroscopy.

We use a long-cavity Ti-sapphire laser to drive the HHG.<sup>31</sup> The laser has a repetition rate of 4 MHz with a pulse width of 50 fs and an average power of 2.6 W centered around 800 nm. The long laser cavity is folded in restricted space by using a Herriott cell. After passing through a pair of prisms for control of pulse width, the laser beam is expanded to a diameter of about 15 mm and then focused by an achromatic lens into a gas jet in the generation chamber. The setup is shown in Fig. 1(a). The focal length of the lens is 50 mm and the laser focus has a diameter of 5  $\mu\text{m}$ . The gas jet of Ar or Xe is produced by a glass capillary with a 30  $\mu\text{m}$  circular opening.<sup>32</sup> With a 3 bar backing pressure of the gas jet, the pressure inside the generation chamber rises to  $6 \times 10^{-3}$  mbar, with a partial pressure of residual gas below  $1 \times 10^{-7}$  mbar.

After the harmonics are generated in the gas jet, they pass through a pin hole with a diameter of 200  $\mu\text{m}$ , which separates the generation from the monochromator chamber. The monochromator chamber is differentially pumped and has a pressure below  $2 \times 10^{-7}$  mbar during HHG experiments. As shown schematically in Fig. 1(a), the generated high-order harmonics are diffracted by a toroidal grating in the monochromator chamber<sup>33</sup> and focused on the detector, which consists of two stacked channelplates and a phosphor

<sup>a)</sup>Electronic mail: wolf.widdra@physik.uni-halle.de.

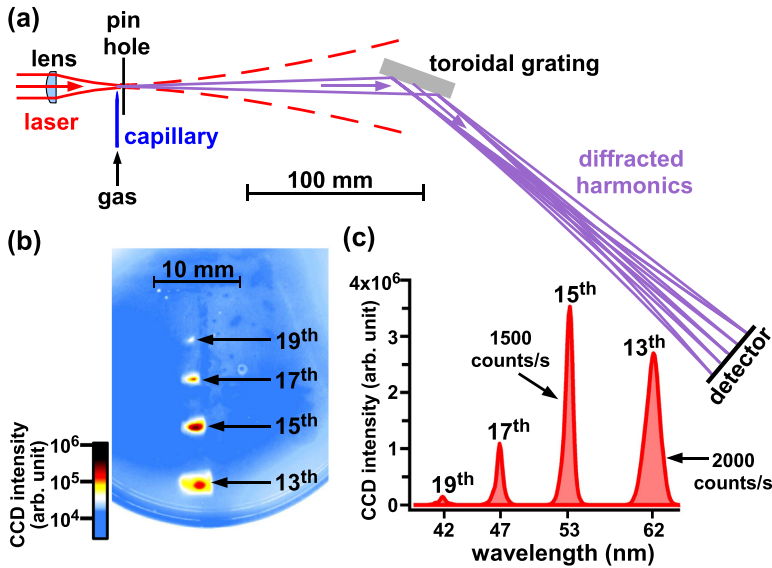
071116-2 Chiang *et al.*Appl. Phys. Lett. **101**, 071116 (2012)

FIG. 1. (a) Geometry of the setup. Incident laser is linearly *s*-polarized with respect to the grating. (b) Image of the diffracted harmonics on the detector. The Ar gas jet has a backing pressure of 3.5 bar. (c) Line profile of the harmonics in (b) along the wavelength dispersive direction. The intensity of each harmonic is integrated laterally and the background is removed.

screen.<sup>34</sup> The fluorescence from the phosphor screen is measured by a CCD camera, which can be operated in an event-counting mode for calibration of the count rate of HHG photons. In Fig. 1(b), the image of the diffracted harmonics generated from Ar is shown. The HHG spectrum with estimated count rate is presented in Fig. 1(c).

The harmonics can be tuned by using different gases. In Fig. 2, we compare the HHG spectra from Xe and Ar. The

spectra were measured with identical geometry and a backing pressure of 3 bar. The intensity of the 9th and 11th harmonics from Xe are about 800 and 10 times more intense than from Ar, respectively. In contrast to HHG from Ar, the harmonics from Xe are limited to the 11th order. The observed difference between HHG in Ar and in Xe is consistent with the known dependence of the ionization potential.<sup>35</sup> With the same driving electric field, the probability of tunnel ionization is higher in Xe due to its lower ionization potential as compared to Ar, explaining the higher HHG intensity from Xe. The lower cutoff energy in the HHG spectrum from Xe can as well be explained, since the energy of the electron before recombination and photon generation scales with the ionization potential.

In addition to the features in the HHG spectra that can be interpreted qualitatively by the microscopic response of a single atom, the macroscopic generation of harmonic radiation relies on the coherent buildup of the electric field generated inside the laser-gas interaction volume.<sup>5,12,36</sup> Ideally, the HHG intensity reaches its maximum when the generated harmonics from all gas atoms in the laser focus can be constructively summed up. The constructive superposition requires a constant phase difference between the driving and the generated electric fields in space and time and is called phase-matching condition. In experiments, increasing the repetition rate while keeping the same intensity in the laser focus usually requires a tighter focusing. The tighter focusing geometry deteriorates the phase-matching condition due to a space-dependent Gouy phase.<sup>37</sup> In addition, the number of gas atoms in the interaction volume decreases rapidly as the focus size decreases. Heyl *et al.* have proposed to increase the gas jet pressure and to use the optical dispersion of gases to compensate for the Gouy phase.<sup>11</sup> Moreover, the number of gas atoms in the jet rises with increasing pressure. In our setup with tight focusing, we use a backing pressure up to several bars as shown in the inset of Fig. 2(b) for the 11th harmonic from the Ar jet. The intensity of the 11th

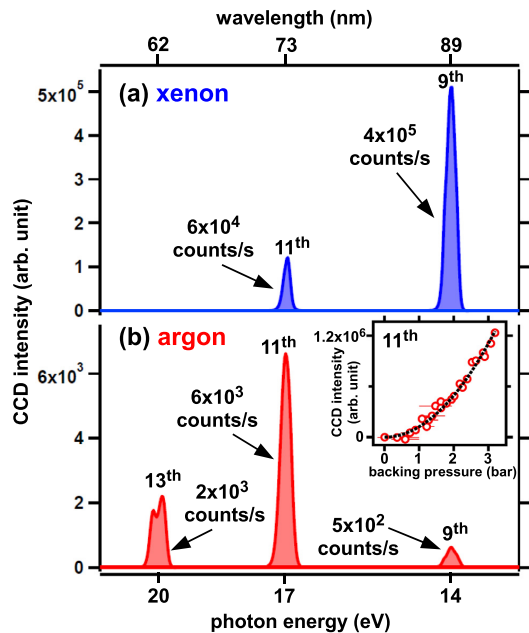


FIG. 2. Spectra of high-order harmonics generated within (a) Xe and (b) Ar jets. In both cases, the backing pressure of the gas jet is 3 bar. In the inset of (b), the backing pressure dependence of the 11th harmonic from the Ar jet is shown.

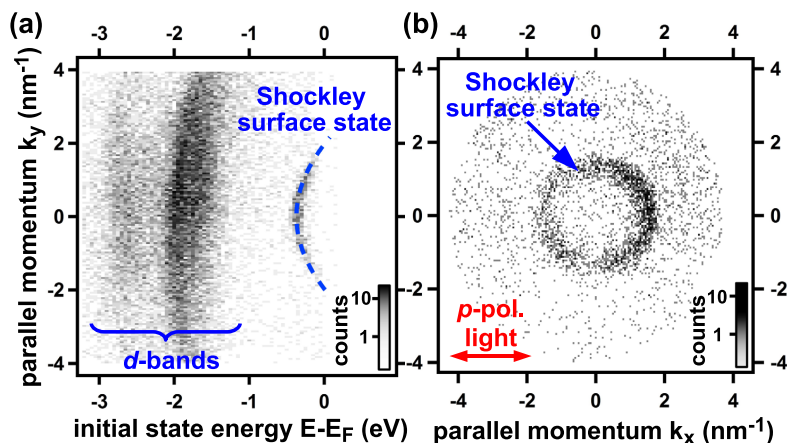


FIG. 3. (a) Photoemission spectra from Cu(111) along the  $\bar{\Gamma}\bar{K}$  direction. The dispersion of the Shockley surface state is observed (dashed curve).<sup>40,41</sup> (b) Momentum distribution of photoelectrons coming from 0.1 eV below the Fermi level. This measurement was done with the 9th harmonic in Xe with photon energy about 14 eV. The harmonic is linearly *p*-polarized with a projection onto the sample surface as indicated by the arrow.

harmonic increases quadratically with the backing pressure (dashed curve), implying a constant phase-matching condition up to 3 bar.<sup>11</sup> Note that our capillary with small opening makes it possible to operate at this pressure range with limited pumping speed. Additionally, the distribution of gas produced by the capillary is more local than in typical gas cells, minimizing the reabsorption of generated harmonics.<sup>11</sup> Since we did not observe a saturated nor a super quadratic backing pressure dependence of HHG, the backing pressure for optimal phase-matching condition is estimated to be above 3 bar.

We use the generated harmonics as an excitation source for time-of-flight photoemission spectroscopy. Therefore, the channelplate detector in Fig. 1(a) is replaced by a Cu(111) sample located in an ultrahigh vacuum chamber. Additionally, a pin hole with a diameter of 1.5 mm is used to filter the chosen harmonic and to separate the monochromator and the photoemission chambers. This results in an additional rare gas background pressure in the photoemission chamber below  $2 \times 10^{-9}$  mbar during the operation of HHG. The Cu(111) sample surface is cleaned by standard sputtering and annealing procedure and is checked by low-energy electron diffraction. Photoelectrons are collected by an electrostatic time-of-flight spectrometer,<sup>38,39</sup> which is mounted at  $45^\circ$  with respect to the incident HHG light. The sample is positioned in normal emission geometry. The time-of-flight of photoelectrons are referenced to the time at which HHG pulses excite the sample surface.

Figure 3 shows valence band photoemission data for a photon energy of 14 eV (9th harmonic from a Xe jet) with an acquisition time of 42 min. All photoelectrons with photoemission angles between  $\pm 15^\circ$  were recorded simultaneously. From the three dimensional data set with respect to photoelectron energy and momenta parallel to the sample surface, two-dimensional cuts are shown in Figs. 3(a) and 3(b). In Fig. 3(a), in the energy range from 3 eV below the Fermi level ( $E_F$ ) up to  $E_F$ , the distribution of photoelectrons having a wave vector within  $\pm 4 \text{ nm}^{-1}$  parallel to  $\bar{\Gamma}\bar{K}$  in the surface Brillouin zone is shown. Near  $E_F$ , we observed the characteristic dispersion of the Shockley surface state on Cu(111) surface, which can be described by a parabolic dispersion with an effective mass of 0.4 times the electron mass and a binding energy of 0.37 eV (blue dashed curve).<sup>40,41</sup> At lower energies

around 2 eV below  $E_F$ , we observed less dispersive features with higher photoemission intensity. These features are attributed to photoemission from copper *d*-bands with lower dispersion and a higher density of states. In Fig. 3(b), we show the momentum distribution of photoelectrons from 0.1 eV below  $E_F$ . The circular feature corresponds to photoemission from the Shockley surface state with two-dimensional free-electron-like dispersion.

To summarize, we demonstrate the HHG at 4 MHz repetition rate by directly using the output of a Ti-sapphire laser oscillator. The generation relies on a tight focusing of the laser light into a gas jet with high backing pressure. Moreover, we use the HHG light for time-of-flight photoemission spectroscopy and measure the characteristic electronic structure of the Cu(111) surface. Our results suggest a straightforward method to increase the repetition rate of HHG, providing a basis of efficient applications to photoelectron spectroscopies and microscopy.

The authors thank J. Gddde and C. Heyl for fruitful discussions. Support from R. Kulla, K. Duncker, M. Kiel, R. Neumann, and M. Schrder is gratefully acknowledged. M.H. would like to thank financial support by the DFG through SFB 762.

<sup>1</sup>P. B. Corkum, *Phys. Today* **64**, 36 (2011).

<sup>2</sup>M. Ferray, A. L'Huillier, X. F. Li, L. A. Lompre, G. Mainfray, and C. Manus, *J. Phys. B* **21**, L31 (1988).

<sup>3</sup>P. B. Corkum, *Phys. Rev. Lett.* **71**, 1994 (1993).

<sup>4</sup>F. Krausz and M. Ivanov, *Rev. Mod. Phys.* **81**, 163 (2009).

<sup>5</sup>T. Popmintchev, M.-C. Chen, P. Arpin, M. M. Murnane, and H. C. Kapteyn, *Nature Photon.* **4**, 822 (2010).

<sup>6</sup>M. Nisoli and G. Sansone, *Prog. Quantum Electron.* **33**, 17 (2009).

<sup>7</sup>J. Itatani, J. Levesque, D. Zeidler, H. Niikura, H. Pepin, J. C. Kieffer, P. B. Corkum, and D. M. Villeneuve, *Nature (London)* **432**, 867 (2004).

<sup>8</sup>A. L. Cavalieri, N. Mller, T. Uphues, V. S. Yakovlev, A. Baltuska, B. Horvath, B. Schmidt, L. Blumel, R. Holzwarth, S. Hendel, M. Drescher, U. Kleineberg, P. M. Echenique, R. Kienberger, F. Krausz, and U. Heinzmann, *Nature (London)* **449**, 1029 (2007).

<sup>9</sup>T. Haarlammer and H. Zacharias, *Curr. Opin. Solid State Mater. Sci.* **13**, 13 (2009).

<sup>10</sup>T. Sdmeyer, S. V. Marchese, S. Hashimoto, C. R. E. Baer, G. Gingras, B. Witzel, and U. Keller, *Nature Photon.* **2**, 599 (2008).

<sup>11</sup>C. M. Heyl, J. Gddde, A. L'Huillier, and U. Hfer, *J. Phys. B* **45**, 074020 (2012).

<sup>12</sup>C. Winterfeldt, C. Spielmann, and G. Gerber, *Rev. Mod. Phys.* **80**, 117 (2008).

- <sup>13</sup>P. Wernet, J. Gaudin, K. Godehusen, O. Schwarzkopf, and W. Eberhardt, *Rev. Sci. Instrum.* **82**, 063114 (2011).
- <sup>14</sup>E. Magerl, S. Neppel, A. L. Cavaliere, E. M. Bothschafter, M. Stanislowski, T. Uphues, M. Hofstetter, U. Kleineberg, J. V. Barth, D. Menzel, F. Krausz, R. Ernstorfer, R. Kienberger, and P. Feulner, *Rev. Sci. Instrum.* **82**, 063104 (2011).
- <sup>15</sup>G. L. Dakovski, Y. Li, T. Durakiewicz, and G. Rodriguez, *Rev. Sci. Instrum.* **81**, 073108 (2010).
- <sup>16</sup>S. Mathias, L. Miaja-Avila, M. M. Murnane, H. Kapteyn, M. Aeschlimann, and M. Bauer, *Rev. Sci. Instrum.* **78**, 083105 (2007).
- <sup>17</sup>S. H. Chew, F. Sussmann, C. Spath, A. Wirth, J. Schmidt, S. Zharebtsov, A. Guggenmos, A. Oelsner, N. Weber, J. Kapaldo, A. Gliserin, M. I. Stockman, M. F. Kling, and U. Kleineberg, *Appl. Phys. Lett.* **100**, 051904 (2012).
- <sup>18</sup>A. Mikkelsen, J. Schwenke, T. Fordell, G. Luo, K. Klunder, E. Hilner, N. Anttu, A. A. Zakharov, E. Lundgren, J. Mauritsson, J. N. Andersen, H. Q. Xu, and A. L'Huillier, *Rev. Sci. Instrum.* **80**, 123703 (2009).
- <sup>19</sup>J. Graf, S. Hellmann, C. Jozwiak, C. L. Smallwood, Z. Hussain, R. A. Kaindl, L. Kipp, K. Rossnagel, and A. Lanzara, *J. Appl. Phys.* **107**, 014912 (2010).
- <sup>20</sup>S. Passlack, S. Mathias, O. Andreyev, D. Mittnacht, M. Aeschlimann, and M. Bauer, *J. Appl. Phys.* **100**, 024912 (2006).
- <sup>21</sup>A. Locatelli, T. O. Menteş, M. Á. Niño, and E. Bauer, *Ultramicroscopy* **111**, 1447 (2011).
- <sup>22</sup>X. Zhou, B. Wannberg, W. Yang, V. Brouet, Z. Sun, J. Douglas, D. Desseau, Z. Hussain, and Z.-X. Shen, *J. Electron Spectrosc. Relat. Phenom.* **142**, 27 (2005).
- <sup>23</sup>A. Vernaleken, J. Weitenberg, T. Sartorius, P. Russbuehdt, W. Schneider, S. L. Stebbings, M. F. Kling, P. Hommelhoff, H.-D. Hoffmann, R. Poprawe, F. Krausz, T. W. Hänsch, and T. Udem, *Opt. Lett.* **36**, 3428 (2011).
- <sup>24</sup>S. Hädrich, M. Krebs, J. Rothhardt, H. Carstens, S. Demmler, J. Limpert, and A. Tünnermann, *Opt. Express* **19**, 19374 (2011).
- <sup>25</sup>S. Kim, J. Jin, Y.-J. Kim, I.-Y. Park, Y. Kim, and S.-W. Kim, *Nature (London)* **453**, 757 (2008).
- <sup>26</sup>I.-Y. Park, S. Kim, J. Choi, D.-H. Lee, Y.-J. Kim, M. F. Kling, M. I. Stockman, and S.-W. Kim, *Nature Photon.* **5**, 677 (2011).
- <sup>27</sup>M. Sivis, M. Duwe, B. Abel, and C. Ropers, *Nature (London)* **485**, E1 (2012).
- <sup>28</sup>C. Gohle, T. Udem, M. Herrmann, J. Rauschenberger, R. Holzwarth, H. A. Schuessler, F. Krausz, and T. W. Hänsch, *Nature (London)* **436**, 234 (2005).
- <sup>29</sup>E. Seres, J. Seres, and C. Spielmann, *Opt. Express* **20**, 6185 (2012).
- <sup>30</sup>A. Cingöz, D. C. Yost, T. K. Allison, A. Ruehl, M. E. Fermann, I. Hartl, and J. Ye, *Nature (London)* **482**, 68 (2012).
- <sup>31</sup>Femtosource scientific XL 650, Femtolasers Produktions GmbH, Vienna, Austria.
- <sup>32</sup>Micropipette made from borosilicate glass, Hilgenberg GmbH, Malsfeld, Germany.
- <sup>33</sup>MBS M-1 VUV monochromator, 1200 lines/mm, MB Scientific AB, Uppsala, Sweden.
- <sup>34</sup>BOS-40-6 beam observation system, Beam Imaging Solutions, Longmont, USA.
- <sup>35</sup>M. Lewenstein, P. Balcou, M. Y. Ivanov, A. L'Huillier, and P. B. Corkum, *Phys. Rev. A* **49**, 2117 (1994).
- <sup>36</sup>P. Balcou and A. L'Huillier, *Phys. Rev. A* **47**, 1447 (1993).
- <sup>37</sup>F. Lindner, W. Stremme, M. G. Schätzel, F. Grasbon, G. G. Paulus, H. Walther, R. Hartmann, and L. Strüder, *Phys. Rev. A* **68**, 013814 (2003).
- <sup>38</sup>Themis 1000, SPECS Surface Nano Analysis GmbH, Berlin, Germany.
- <sup>39</sup>M. H. Berntsen, O. Gotberg, and O. Tjernberg, *Rev. Sci. Instrum.* **82**, 095113 (2011).
- <sup>40</sup>A. A. Ünal, C. Tusche, S. Ouazi, S. Wedekind, C.-T. Chiang, A. Winkelmann, D. Sander, J. Henk, and J. Kirschnner, *Phys. Rev. B* **84**, 073107 (2011).
- <sup>41</sup>F. Reinert, G. Nicolay, S. Schmidt, D. Ehm, and S. Hüfner, *Phys. Rev. B* **63**, 115415 (2001).



Contents lists available at ScienceDirect

## Journal of Electron Spectroscopy and Related Phenomena

journal homepage: [www.elsevier.com/locate/elspec](http://www.elsevier.com/locate/elspec)

# Efficient and tunable high-order harmonic light sources for photoelectron spectroscopy at surfaces



Cheng-Tien Chiang<sup>a,b</sup>, Michael Huth<sup>a</sup>, Andreas Trützscher<sup>a,b</sup>, Frank O. Schumann<sup>a</sup>,  
Jürgen Kirschner<sup>a,b</sup>, Wolf Widdra<sup>b,a,\*</sup>

<sup>a</sup> Max-Planck-Institut für Mikrostrukturphysik, Weinberg 2, D-06120 Halle(Saale), Germany

<sup>b</sup> Institute of Physics, Martin-Luther-Universität Halle-Wittenberg, Von-Danckelmann-Platz 3, D-06120 Halle(Saale), Germany

### ARTICLE INFO

**Article history:**  
Available online 13 April 2015

**Keywords:**  
High-order harmonic generation  
Photoelectron spectroscopy  
Ag(001)

### ABSTRACT

With the recent progress in high-order harmonic generation (HHG) using femtosecond lasers, laboratory photoelectron spectroscopy with an ultrafast, widely tunable vacuum-ultraviolet light source has become available. Despite the well-established technique of HHG-based photoemission experiments at kilohertz repetition rates, the efficiency of these setups can be intrinsically limited by the space-charge effects. Here we present recent developments of compact HHG light sources for photoelectron spectroscopy at high repetition rates up to megahertz, and examples for angle-resolved photoemission experiments are demonstrated.

© 2015 Elsevier B.V. All rights reserved.

## 1. Introduction

Photoelectron spectroscopy (PES) has evolved into a powerful method to explore the electronic structure of materials. With the rapidly growing interest in material science with emphasis on the novel electronic properties, further development of modern PES and its light sources is strongly motivated [1,2]. To map the electronic structure in general, photoemission experiments can be performed using polarized light with a widely tunable photon energy range. Conventional light sources are the synchrotron radiation and laboratory discharge lamps. Recently, with the development of high-order harmonic generation (HHG) from gases using femtosecond lasers, HHG-based laboratory PES has allowed characterization of electronic systems on the sub-femtosecond time scale [3–6].

In the earlier development of HHG light sources, the repetition rate of HHG was limited at a few hertz due to the necessary high pulse energy of several mJ using picosecond lasers [19,20]. By using Ti:sapphire femtosecond lasers Linder and Heyl et al. later demonstrated HHG at 100 kHz with  $\mu$ J laser pulses [21,22]. Details of the development of HHG light sources have been reviewed

elsewhere [23–26]. The higher repetition rate of HHG light sources is of crucial importance for photoemission experiments on solids because of the space-charge effects. The space-charge effects result from the Coulomb repulsion between photoelectrons from the same light pulse. They impose a margin on the number of emitted photoelectrons per pulse, beyond which an energy and momentum broadening in photoemission spectra can occur [27]. As we summarize in Fig. 1, conventional HHG-based PES setups mainly work at few kHz, therefore the space-charge effects can limit the photoemission intensity to several thousands photoelectrons per second.

To further increase the efficiency of HHG-based PES, it becomes necessary to extend the repetition rate of HHG light sources into the megahertz range. As already demonstrated in several elegant optical experiments, MHz HHG can be achieved by using high power laser systems working simply at MHz, or by additional enhancements such as a resonant cavity or plasmonic nanostructures [28–33]. In addition to these approaches, we demonstrate HHG at MHz using a more compact setup and drive HHG directly by a Ti:sapphire long cavity oscillator [34] or by a compact Yb-fiber laser system. For PES with HHG excitation, the combination with time-of-flight (ToF) electron spectrometers has been proven to be highly efficient [35,36]. Detailed comparison of the absolute photoemission intensity and efficiency of experiments have been addressed before [36] and in this paper we present examples with tunable photon energy and light polarization as well as discuss the new extensive development.

\* Corresponding author at: Institute of Physics, Martin-Luther-Universität Halle-Wittenberg, Von-Danckelmann-Platz 3, D-06120 Halle(Saale), Germany.  
Tel.: +49 345 552 5360; fax: +49 345 552 7160.

E-mail address: [wolf.widdra@physikuni-halle.de](mailto:wolf.widdra@physikuni-halle.de) (W. Widdra).



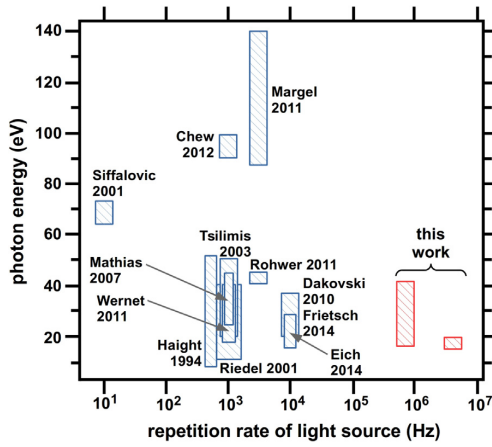


**Fig. 1.** Overview of HHG-based PES setups highlighted by their photon energy range and repetition rate [7–18]. For clarity, the overlapping kHz [9–12] as well as 10 kHz experiments are shown with different width [16–18].

## 2. Photoelectron spectroscopy experiments

To demonstrate the tunability of megahertz HHG light sources for laboratory PES, we choose photoemission experiments on a Ag(001) surface as an example. Photoemission spectra from this surface have been well-documented using synchrotron radiation and the details can be explained by the band structure [40,41]. For photon energies below 23 eV, the harmonics are driven by

a Ti:sapphire long cavity laser working at 4 MHz with a photon energy of 1.5 eV, a pulse energy of 650 nJ and a pulse duration of 50 fs [42]. For a wider photon energy range from 18 to 40 eV the harmonics are driven by an Yb-fiber laser system at 0.7 MHz with a photon energy of 1.2 eV, a pulse energy of 14  $\mu$ J, and a pulse duration of 300 fs [43]. The output of one of these lasers is focused into an Ar or Xe gas jet in a vacuum chamber and the generated harmonics are selected and focused on the Ag(001) surface using a commercial monochromator designed for He discharge lamps [44]. The photoelectrons are collected by a time-of-flight (ToF) spectrometer and their energy ( $E$ ) as well as the two momentum components parallel to the surface ( $k_x$ ,  $k_y$ ) are analyzed [35,45]. Details of the HHG and the PES setups have been described in previous publications [36,46,47].

The photoemission spectra measured with  $p$ - and  $s$ -polarized harmonics are shown in Fig. 2 for photon energies  $h\nu = 17$  and 20 eV driven by the Ti:sapphire laser. From the three-dimensional energy and momentum distribution  $I(E, k_x, k_y)$  of photoelectrons down to a binding energy of more than 10 eV, we present in Fig. 2 the two-dimensional slices  $I(E, k_x)$  and  $I(E, k_y)$ . Using the  $s$ -polarized light at 17 and 20 eV, we observe a different distribution of photoelectrons along the  $k_x$  and  $k_y$  directions when comparing Fig. 2a with Fig. 2b, as well as Fig. 2c with Fig. 2d. The flat  $E - k_x$  dispersion in Fig. 2a and Fig. 2c at the binding energy of around 5 eV is attributed to the Ag  $d$  band. At comparable binding energies in the  $E - k_y$  dispersion in Fig. 2b and Fig. 2d, the  $d$  band exhibits a slightly downward dispersion. The upward dispersive band at around 2 to 3 eV is assigned to the Ag  $sp$  band. These assignments are based on the theoretical band structure in Fig. 2g [37] and the observed dispersion can be qualitatively described by the empirical band structure as shown by the circles in Fig. 2b and Fig. 2d [38,39].

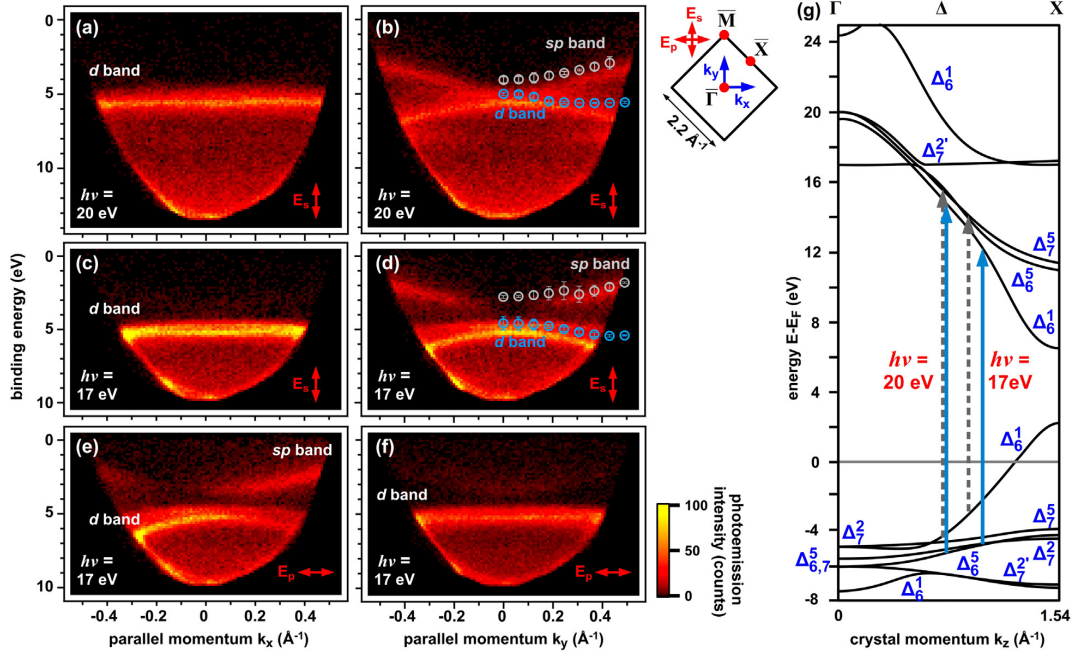


**Fig. 2.** (a)–(e) Angle-resolved photoemission spectra measured on the Ag(001) surface along the momentum directions  $k_x$  and  $k_y$  as indicated by the surface Brillouin zone. The photon energy used is  $h\nu = 20$  eV for (a) and (b), and  $h\nu = 17$  eV for (c)–(f). The incident light is  $s$ - and  $p$ -polarized for (a)–(d) and (e)–(f), respectively. The spectra are integrated over  $\Delta k = 0.1 \text{ \AA}^{-1}$  perpendicular to the respective momentum direction. The electric field of the  $s$ -polarization of light is parallel to  $k_y$  and the  $p$ -polarization has a component in the Ag(001) surface parallel to  $k_x$ . The relative orientation between the light polarization and the momentum directions of photoelectrons is shown in the inset with the surface Brillouin zone. Possible transitions for  $h\nu = 17$  and 20 eV are indicated in a comparison with theoretical band structure of Ag from Eckardt et al. in (g) [37] and estimated by an empirical band structure at selected momenta [38,39] in (b,d).

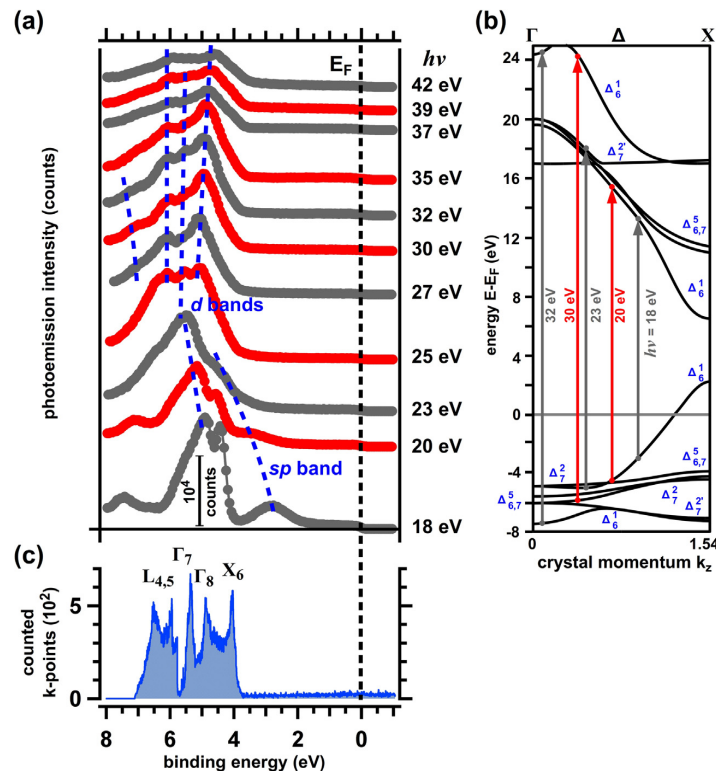


**Fig. 3.** (a) Photon energy dependent photoemission spectra measured on the Ag(001) surface. The photoelectrons emitted within  $\pm 15^\circ$  from the surface normal are integrated. For clarity, the spectra are shifted vertically. (b) The theoretical bulk band structure of Ag with possible transitions indicated at various photon energies [37]. (c) Calculated density of states of Ag using empirical band structure [38,48]. Selected high symmetry points are marked.

By going from *s*- to *p*-polarized light at the same photon energy  $h\nu = 17$  eV, we observe a significant change in the distribution of photoelectrons as seen in the comparison of Fig. 2c,d and Fig. 2e,f. With *s*-polarized light we observe only the *d* band along the  $k_x$  direction (Fig. 2c), and both the *sp* and the *d* bands along the  $k_y$  direction (Fig. 2d). In strong contrast, with *p*-polarized light we observe both the *sp* and the *d* bands along the  $k_x$  direction (Fig. 2e), but mainly only the *d* band along the  $k_y$  direction (Fig. 2f). The observation indicates that photoelectrons with momentum parallel to the polarization of light are emitted in optical transitions from both the *sp* and *d* bands, whereas photoelectrons with momentum perpendicular to the light polarization are mainly emitted in transitions from the *d* band. As the polarization of light is rotated from *s* to *p*, the distribution of photoelectrons is rotated accordingly due to the optical selection rules [49].

The wide tunability in photon energy of HHG-based PES is further demonstrated in Fig. 3a by the angle-integrated photoemission spectra. The photon energy dependence can be qualitatively explained by the band structure in Fig. 3b and by the density of states (DOS) in Fig. 3c [38,48]. At  $h\nu = 18$  eV, a resonant transition takes place between the occupied and unoccupied *sp* bands where no significant feature in the DOS appears. As  $h\nu$  is increased, transitions can occur between the occupied *d* and unoccupied bands and the dominant photoemission signal from the *d* bands is due to their high DOS at 4–7 eV below the Fermi level. At around  $h\nu = 32$  eV, a resonant transition may occur at the bottom of the *sp* band and this is indicated in Fig. 3a at a binding energy of about 7 eV.

### 3. Further developments

In contrast to the well-established kHz HHG setups for time-resolved PES as summarized in Fig. 1, an efficient and space-charge free MHz HHG setup with reduced complexity can be operated by an individual user for long-term measurements. In this section we introduce the design of a compact generation chamber and a gas-recycling system. The latter is of high importance for long-term experiments due to the costs for rare gases as xenon. In addition, we demonstrate a proof-of-principle long-term operation of the setup. At the end of this section the pulse duration and the bandwidth of the harmonics are discussed.

#### 3.1. Compact generation chamber

The megahertz HHG setup follows a tight-focusing geometry for phase-matching conditions at high backing pressure [26]. In order to suppress mechanical vibrations as well as to be user-friendly, the ideal generation chamber should have a minimal size, which is only limited by the front flange of the vacuum pump with a sufficient pumping speed. Here a turbo pump with a nominal pumping speed of 700 l/s and a front flange with an inner diameter of 150 mm is used [50]. Therefore the generation chamber has about the same inner diameter. In Fig. 4a a photograph of the generation chamber is shown and in Fig. 4b the 30  $\mu\text{m}$  glass capillary [51] for the gas jet can be seen. The laser beam is focused into the gas jet by the lens assembly which consists of an achromatic lens sealing the chamber [52] and a bellows allowing mechanical adjustment. The glass



18

C.-T. Chiang et al. / Journal of Electron Spectroscopy and Related Phenomena 200 (2015) 15–21

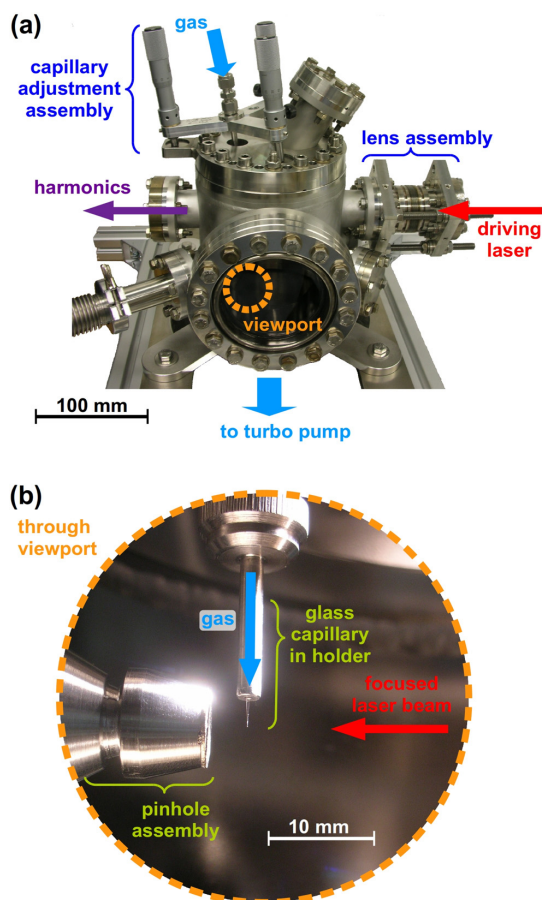


**Fig. 4.** Photographs of the generation chamber for the harmonics (a), with the glass capillary and the pinhole assembly visible through the viewport as in (b).

capillary in Fig. 4b is mounted in a holder on the top flange of the generation chamber in Fig. 4a. Its position can be adjusted by the tripod via three micrometer screws. Behind the gas jet, a  $150\ \mu\text{m}$  pin hole blocks the fundamental driving laser beam and reduces the gas loading in the monochromator chamber thereafter [44].

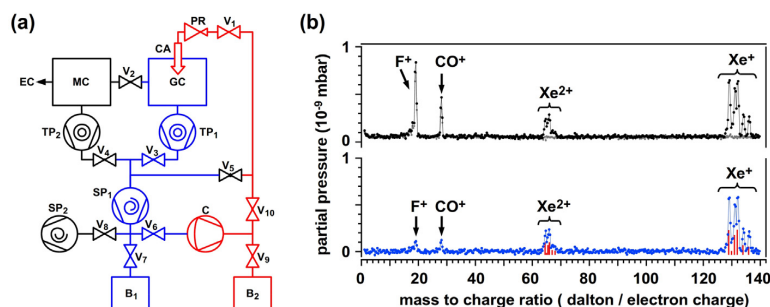


**Fig. 5.** (a) Simplified flow diagram of the gas-recycling system with high (red) and low (blue) pressure region indicated. GC: generation chamber for the harmonics with gas jet from a glass capillary (CA); MC: monochromator chamber; EC: photoemission experiment chamber; TP<sub>1,2</sub>: turbo pumps; SP<sub>1,2</sub>: scroll pumps; B<sub>1,2</sub>: gas reservoirs; C: compressor; V<sub>1...10</sub>: valves; PR: pressure regulator. (b) Mass spectra of residual gas in the photoemission experiment chamber with (black) and without (gray) using Xe in GC. The difference spectrum is shown in the lower panel together with the relative natural abundance of Xe isotopes (red bars) [53]. (For interpretation of the references to color in this figure legend, the reader is referred to the web version of this article.)

### 3.2. Gas-recycling system

The HHG spectrum strongly depends on the generation gas medium [20,23,25]. For higher photon energies gases with higher ionization potential such as He, Ne or Ar are used. On the other hand, HHG from gases with lower ionization potential, e.g. Xe and Kr, can lead to several orders of magnitude higher photon flux at lower photon energies. Due to the cost of Xe and Kr in a long-term HHG experiment, it is necessary to recycle the gas from the generation chamber and to compress it to the backing pressure for the gas jet. In Fig. 5a, a simplified gas flow diagram of our recycling system for Xe is presented. The gas jet with a backing pressure of 5 bar is injected into the generation chamber (GC) by the capillary (CA). During the HHG operation, the background pressure of Xe is about  $10^{-2}$  mbar in GC and 1 bar after the scroll pump (SP<sub>1</sub>). From the gas reservoir (B<sub>1</sub>), the recycled gas can be further compressed by a dry membrane compressor (C) up to 10 bar and stored in an expansion tank (B<sub>2</sub>). From there the gas is fed to the pressure regulator (PR) for regulation of the backing pressure of the gas jet. For maintenance the recycling systems can be divided into several parts by the valves (V<sub>1...10</sub>) and the gas is stored in B<sub>1</sub> and B<sub>2</sub>.

During the operation of the recycling system with Xe, we characterize the recycled gas by a quadrupole mass spectrometer in the experiment chamber (EC) behind the monochromator chamber (MC). In Fig. 5b the black (gray) mass spectrum in the upper panel is measured during (without) the operation of the recycling system about a week after its installation. The gray spectrum shows the residual gas of CO in EC, and the F<sup>+</sup> signal can be attributed to the outgassing of the mass spectrometer itself (electron stimulated desorption). The difference of these two spectra is displayed in the lower panel, showing dominantly the signals of singly and doubly ionized Xe. For comparison the red vertical bars indicate the signals estimated by the relative natural abundance of Xe isotopes [53]. With this gas-recycling system the HHG setup has been operated with the same xenon loading for more than 6 months. For longer operation we observed CO in the residual gas, which could be suppressed by installing an additional adsorption pump in the recycling system.

### 3.3. Long-term operation

By using the compact generation chamber in combination with the Xe recycling system, we demonstrate the proof-of-principle for a long-term operation of HHG-based photoemission using the Yb-fiber laser. In Fig. 6a,c the count rate of photoelectrons excited by

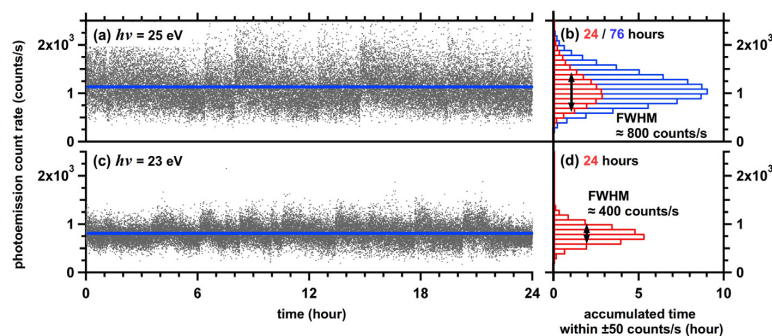


**Fig. 6.** Photoemission count rate in 24-hour-long measurements with the HHG light source for photon energies (a,b) 25 eV and (c,d) 23 eV. Each data point in (a,c) is measured for about 2.5 s and the average count rate is indicated by the blue horizontal lines at 1100 and 800 counts/s for (a) and (c), respectively. In (b,d) the histograms (red) of the data in (a,c) are shown with their full-width-at-half-maximum (FWHM). In (b) an additional histogram (blue) is taken from a longer measurement for 76 h. (For interpretation of the references to color in this figure legend, the reader is referred to the web version of this article.)

the HHG light source is shown for two independent experiments lasting 24 h. These experiments were performed in conventional laboratory condition without active temperature regulation and the laboratory temperature varied about  $\pm 0.5^\circ\text{C}$  around  $22^\circ\text{C}$  during these days. In order to compensate the influence of the temperature variation on the fiber laser, we actively changed the pulse compressor settings inside the fiber laser and minimized the output pulse duration. In Fig. 6b,d the histograms of the photoelectron count rate in Fig. 6a,c are displayed and the full-width-at-half-maximum (FWHM) is estimated. In addition we show in Fig. 6b a histogram from a longer measurement for 76 h. By comparing the histograms in Fig. 6b we see that the operation of the HHG light source can be extended to several days without additional degradation of its stability.

For a quantitative estimation, we derive the ratio of the FWHM to the average count rate from the histograms in Fig. 6b,d and obtain values of about 0.8 and 0.5 for 25 and 23 eV, respectively. The larger variation for 25 eV could be attributed to its higher harmonic order and a consequently more sensitive generation condition. For comparison, Leitner et al. characterized the shot-to-shot intensity distribution of their HHG setup for a photon energy range from 17 to 27 eV at a repetition rate of 3 kHz, and the FWHM variation amounts to 0.53 of the average intensity [54]. A much smaller FWHM intensity fluctuation of about 0.08 has been demonstrated in a short measurement with 430 shots using a 10 Hz HHG setup at 33 eV for seeding the sFLASH beam line [55]. The stability of our HHG light could be further improved by reducing the temperature variation in the laboratory and by additional damping of the mechanical vibration from the vacuum pumps.

### 3.4. Bandwidth and pulse duration

Due to the ultimate pulse duration down to a few hundreds of attoseconds, HHG light sources have great potential for time-resolved PES [3,4,6]. To get a train of these short pulses, the harmonics need to be selected and compressed properly after the generation. Moreover, much effort is required in order to single out an isolated sub-femtosecond pulse and to precisely characterize its pulse duration. Details of the available approaches have been reviewed recently [6,57]. Here we estimate the lower limit for the pulse duration of the harmonics according to their bandwidth in photon energy.

The bandwidth of the harmonics can be quantitatively estimated in photoemission experiments. In Fig. 7a we present the width of the Fermi-edge in the photoemission spectra in Fig. 3a. These values (red circles) represent the total energy resolution in the photoemission experiments and they include the energy resolution of the

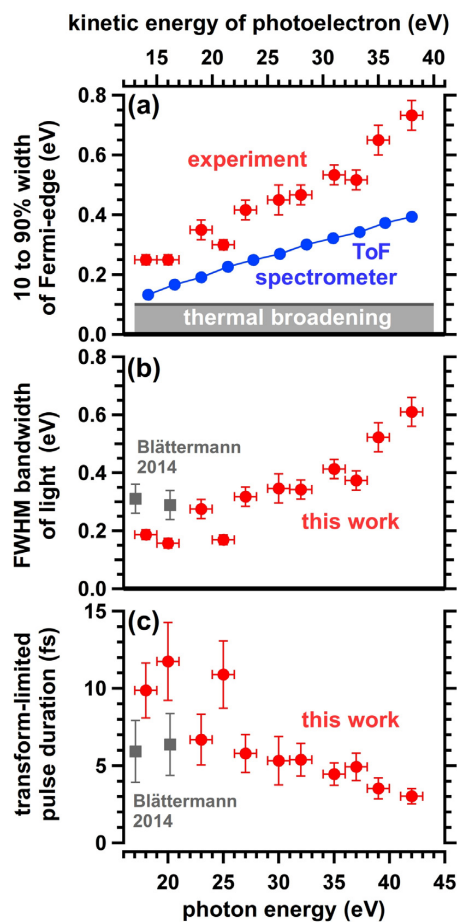


**Fig. 7.** (a) Red data points are the measured 10–90% width of the Fermi-edge in photoemission spectra in Fig. 2a at the kinetic energies of photoelectrons shown by the top scale and photon energies by the bottom scale. Blue data points are the simulated energy resolution of the ToF spectrometer settings using a conservative estimation of the time resolution of 300 ps for the electronics [47,56]. Gray area indicates the 100 meV thermal broadening at 300 K. (b) Red points show the full-width-at-half-maximum bandwidth of light estimated from data in (a). For comparison, gray squares show the directly measured bandwidth from our previous publication [34]. (c) The transform-limited pulse width (full-width-at-half-maximum, FWHM) estimated from the bandwidth in (b).

ToF electron spectrometer (blue circles), the thermal broadening at 300 K (gray area), as well as the bandwidth of the harmonics. From these data, we estimate the bandwidth of the harmonics in Fig. 7b. In addition, we extract the bandwidth of low energy harmonics driven by the Ti:sapphire laser from a direct measurement published previously (gray squares) [34].

From the bandwidth in Fig. 7b, we estimate the transform-limited pulse duration of a single harmonic pulse in Fig. 7c. The estimated pulse duration ranges from about 3 to 10 fs for photon energies from 40 to 17 eV. In our setup, we use a monochromator grating after the generation in order to select a single harmonic as well as to focus it onto the sample. In this diffraction process, the pulse width is stretched to about 2 ps [58]. However this temporal stretching might be compressed by a second identical grating or other designs [59,60]. In addition to the duration of a single isolated pulse, the duration of the pulse train of the harmonics can be estimated by the pulse duration of the driving lasers, which corresponds to about 50 and 300 fs for Ti:sapphire and Yb-fiber laser, respectively. In order to achieve a better time-resolution, further development to compress either the driving laser or the harmonics is required.

#### 4. Summary

To summarize, light sources based on high-order harmonic generation (HHG) provide a unique opportunity to perform laboratory photoelectron spectroscopy (PES) using linearly polarized light with a wide photon energy range of more than 20 eV. By using the harmonics generated from lasers with megahertz repetition rates ranging from Ti:sapphire oscillators to Yb-based fiber lasers, efficient and space-charge free photoemission experiments are nowadays possible that last for many days without interruption. Here we demonstrate such photon-energy and polarization dependent PES experiments on an Ag(001) surface. The developments of the compact generation setup, the recycling system for the gases as well as the long-term operation of the HHG light source are presented. In addition, the bandwidth of the harmonics is estimated from the energy broadening in the photoelectron spectra and the lower limit of the pulse duration is given. These modern developments should provide an efficient way for laboratory PES and microscopy as well as for time-resolved experiments in the future.

#### Acknowledgements

We thank C. Heyl, J. GÜdde, K. Duncker, and M. Kiel for fruitful discussions at the initial stage of our experiments, A. Blättermann for the first HHG experiments using the Ti:sapphire laser. An excellent technical support by R. Kulla, S. Helmbach, M. Schröder, R. Neumann, and F. Weiß is gratefully acknowledged. We also thank for financial support from SFB 762.

#### Appendix A. Supplementary Data

Supplementary data associated with this article can be found, in the online version, at <http://dx.doi.org/10.1016/j.elspec.2015.04.001>

#### References

- [1] W. Schattke, M. Van Hove (Eds.), *Solid State Photoemission and Related Methods*, Wiley-VCH, Berlin, 2003.
- [2] S. Suga, A. Sekiyama, *Photoelectron Spectroscopy: Bulk and Surface Electronic Structures*, Springer-Verlag, Berlin Heidelberg, 2014.
- [3] A.L. Cavalieri, N. Müller, T. Uphues, V.S. Yakovlev, A. Baltuska, B. Horvath, B. Schmidt, L. Blumel, R. Holzwarth, S. Hendel, M. Drescher, U. Kleineberg, P.M. Echenique, R. Kienberger, F. Krausz, U. Heinzmann, *Nature* 449 (2007) 1029–1032.
- [4] F. Krausz, M. Ivanov, *Rev. Mod. Phys.* 81 (2009) 163–234.
- [5] T. Haarlammert, H. Zacharias, *Curr. Opin. Solid State Mater. Sci.* 13 (2009) 13–27.
- [6] L. Plaja, R. Torres, A. Zair (Eds.), *Attosecond Physics: Attosecond Measurements and Control of Physical Systems*, Springer-Verlag, Berlin Heidelberg, 2013.
- [7] P. Siffalovic, M. Drescher, M. Spieweck, T. Wiesenath, Y.C. Lim, R. Weidner, A. Elizarov, U. Heinzmann, *Rev. Sci. Instrum.* 72 (2001) 30–35.
- [8] R. Haight, D.R. Peale, *Rev. Sci. Instrum.* 65 (1994) 1853–1857.
- [9] D. Riedel, J.L. Hernandez-Pozos, R.E. Palmer, S. Baggott, K.W. Kolasinski, J.S. Foord, *Rev. Sci. Instrum.* 72 (2001) 1977–1983.
- [10] G. Tsilimis, J. Kutzner, H. Zacharias, *Surf. Sci.* 528 (2003) 171–176.
- [11] S. Mathias, L. Mijsa-Avila, M.M. Murnane, H. Kapteyn, M. Aeschlimann, M. Bauer, *Rev. Sci. Instrum.* 78 (2007) 083105.
- [12] P. Wernet, J. Gaudin, K. Godehusen, O. Schwarzkopf, W. Eberhardt, *Rev. Sci. Instrum.* 82 (2011) 063114.
- [13] S.H. Chew, F. Süßmann, C. Späth, A. Wirth, J. Schmidt, S. Zherebtsov, A. Guggenmos, A. Oelsner, N. Weber, J. Kapaldo, A. Gliserin, M.I. Stockman, M.F. Kling, U. Kleineberg, *Appl. Phys. Lett.* 100 (2012) 051904.
- [14] E. Magerl, S. Neppel, A.L. Cavalieri, E.M. Bothschafter, M. Stanislowski, T. Uphues, M. Hofstetter, U. Kleineberg, J.V. Barth, D. Menzel, F. Krausz, R. Ernstorfer, R. Kienberger, P. Feulner, *Rev. Sci. Instrum.* 82 (2011) 063104.
- [15] T. Rohwer, S. Hellmann, M. Wiesenmayer, C. Sohr, A. Stange, B. Slomski, A. Carr, Y. Liu, L.M. Avila, M. Kallane, S. Mathias, L. Kipp, K. Rossnagel, M. Bauer, *Nature* 471 (2011) 490–493.
- [16] G.L. Dakovski, Y. Li, T. Durakiewicz, G. Rodriguez, *Rev. Sci. Instrum.* 81 (2010) 073108.
- [17] B. Frietsch, R. Carley, K. Döbrich, C. Gahl, M. Teichmann, O. Schwarzkopf, P. Wernet, M. Weinelt, *Rev. Sci. Instrum.* 84 (2013) 075106.
- [18] S. Eich, A. Stange, A. Carr, J. Urbancic, T. Popmintchev, M. Wiesenmayer, K. Jansen, A. Ruffing, S. Jakobs, T. Rohwer, S. Hellmann, C. Chen, P. Matyba, L. Kipp, K. Rossnagel, M. Bauer, M. Murnane, H. Kapteyn, S. Mathias, M. Aeschlimann, *J. Electron Spectrosc. Relat. Phenomena* 195 (2014) 231–236.
- [19] A. McPherson, G. Gibson, H. Jara, U. Johann, T.S. Luk, I.A. McIntyre, K. Boyer, C.K. Rhodes, *J. Opt. Soc. Am. B* 4 (1987) 595.
- [20] M. Ferray, A. L'Huillier, X.F. Li, L.A. Lompre, G. Mainfray, C. Manus, *J. Phys. B: Atomic Mol. Opt. Phys.* 21 (1988) L31.
- [21] F. Lindner, W. Stremme, M. Schätzel, F. Grasbon, G. Paulus, H. Walther, R. Hartmann, L. Strüder, *Phys. Rev. A* 68 (2003) 013814.
- [22] C. Heyl, J. GÜdde, U. Höfer, A. L'Huillier, *Phys. Rev. Lett.* 107 (2011) 033903.
- [23] C. Winterfeldt, C. Spielmann, G. Gerber, *Rev. Mod. Phys.* 80 (2008) 117–140.
- [24] T. Brabec (Ed.), *Strong Field Laser Physics*, Springer-Verlag, Berlin Heidelberg, 2009.
- [25] T. Popmintchev, M.-C. Chen, P. Arpin, M.M. Murnane, H.C. Kapteyn, *Nat. Photon* 4 (2010) 822–832.
- [26] C.M. Heyl, J. GÜdde, A. L'Huillier, U. Höfer, *J. Phys. B: Atomic Mol. Opt. Phys.* 45 (2012) 074020.
- [27] S. Hellmann, K. Rossnagel, M. Marczyński-Bühlow, L. Kipp, *Phys. Rev. B* 79 (2009) 035402.
- [28] S. Hädrich, A. Klenke, J. Rothhardt, M. Krebs, A. Hoffmann, O. Pronin, V. Pervak, J. Limpert, A. Tünnermann, *Nat. Photon* 8 (2014) 779–783.
- [29] C. Benko, T.K. Allison, A. Cingoz, L. Hua, F. Labaye, D.C. Yost, J. Ye, *Nat. Photon* 8 (2013) 530–536.
- [30] I. Pupez, S. Holzberger, T. Eidam, H. Carstens, D. Esser, J. Weitenberg, P. Ruzsbuldt, J. Rauschenberger, J. Limpert, T. Udem, A. Tünnermann, T.W. Hänsch, A. Apolonski, F. Krausz, E. Fill, *Nat. Photon* 7 (2013) 608–612.
- [31] M. Sivils, M. Duwe, B. Abel, C. Ropers, *Nature* 485 (2012) E1–E3.
- [32] M.B. Raschke, *Annalen der Physik* 525 (2013) A40–A42.
- [33] N. Pfullmann, M. Noack, J. Cardoso de Andrade, S. Rausch, T. Nagy, C. Reinhardt, V. Knittel, R. Bratschitsch, A. Leitenstorfer, D. Akemeier, A. Httten, M. Kovacev, U. Morgner, *Annalen der Physik* 526 (2014) 119–134.
- [34] A. Blättermann, C.-T. Chiang, W. Widdra, *Phys. Rev. A* 89 (2014) 043404.
- [35] M.H. Berntsen, O. Gotberg, O. Tjernberg, *Rev. Sci. Instrum.* 82 (2011) 095113.
- [36] C.-T. Chiang, M. Huth, A. Trüttschler, M. Kiel, F.O. Schumann, J. Kirschner, W. Widdra, *N. J. Phys.* 17 (2015) 013035.
- [37] H. Eckardt, L. Fritsche, J. Noffke, *J. Phys. F: Met. Phys.* 14 (1984) 97.
- [38] R. Benbow, N. Smith, *Phys. Rev. B* 27 (1983) 3144–3151.
- [39] In the two-dimensional cut  $\Gamma X W K W X$  of the fcc bulk Brillouin zone, the energy bands of Ag are calculated at 507 points using the empirical Hamitonian in Ref. [38], 2014.
- [40] U. König, P. Weinberger, J. Redinger, H. Erschbaumer, A.J. Freeman, *Phys. Rev. B* 39 (1989) 7492–7499.
- [41] S.C. Wu, C.K.C. Lok, J. Sokolov, J. Quinn, Y.S. Li, D. Tian, F. Jona, *J. Phys.: Condens. Matter* 1 (1989) 4795.
- [42] Femtosource scientific XL650, 2011. Femtolasers Produktions GmbH, Vienna, Austria.
- [43] Impulse, ytterbium-fiber laser system, 2013. Clark-MXR, Inc., Dexter, USA.
- [44] MBS M-1 VUV monochromator, 2012. 1200 lines/mm, MB Scientific AB, Uppsala, Sweden.
- [45] Themis 1000, 2010. SPECS Surface Nano Analysis GmbH, Berlin, Germany.
- [46] C.-T. Chiang, A. Blättermann, M. Huth, J. Kirschner, W. Widdra, *Appl. Phys. Lett.* 101 (2012) 071116.
- [47] M. Huth, C.-T. Chiang, A. Trüttschler, F.O. Schumann, J. Kirschner, W. Widdra, *Appl. Phys. Lett.* 104 (2014) 061602.

- [48] In the irreducible  $1/48$  part of the Brillouin zone (BZ), the 42 energy bands of  $\text{Ag}$  are calculated at 11760 points using the Hamiltonian in Ref. [38]. The DOS is estimated by a histogram with a 10 meV width of bins, and its apparent dip near 6 eV may be due to the limited sampling points in the BZ, 2014.
- [49] W. Eberhardt, F.J. Himpsel, *Phys. Rev. B* 21 (1980) 5572–5576.
- [50] HiPace 700, 2011. Pfeiffer Vacuum GmbH, Asslar, Germany.
- [51] Micropipette made from borosilicate glass, 2013. Hilgenberg GmbH, Malsfeld, Germany.
- [52] Achromatic doublet, AC254-050-B, 2013. Thorlabs Inc., Newton, USA.
- [53] J.E. Sansonetti, W.C. Martin, *J. Phys. Chem. Ref. Data* 34 (2005) 1559–2259.
- [54] T. Leitner, A.A. Sorokin, J. Gaudin, H. Kaser, U. Kroth, K. Tiedtke, M. Richter, P. Wernet, *N. J. Phys.* 13 (2011) 093003.
- [55] T. Maltezopoulos, M. Mittenzwey, A. Azima, J. Bödewadt, H. Dachraoui, M. Rehders, C. Lechner, M. Schulz, M. Wieland, T. Laarmann, J. Roßbach, M. Drescher, *Appl. Phys. B* 115 (2014) 45–54.
- [56] Charged particle trajectory simulation program SIMION, 2012. Scientific Instrument Services, Inc., Ringoes, USA.
- [57] M. Chini, K. Zhao, Z. Chang, *Nat. Photon* 8 (2014) 178–186.
- [58] M. Bauer, *J. Phys. D: Appl. Phys.* 38 (2005) R253.
- [59] H. Igarashi, A. Makida, M. Ito, T. Sekikawa, *Opt. Express* 20 (2012) 3725–3732.
- [60] L. Poletto, P. Miotti, F. Frassetto, C. Spezzani, C. Grazioli, M. Coreno, B. Ressel, D. Gauthier, R. Ivanov, A. Ciavardini, M. de Simone, S. Stagira, G.D. Ninno, *Appl. Opt.* 53 (2014) 5879–5888.



## PAPER

## Boosting laboratory photoelectron spectroscopy by megahertz high-order harmonics

## OPEN ACCESS

## RECEIVED

15 September 2014

## ACCEPTED FOR PUBLICATION

10 December 2014

## PUBLISHED

20 January 2015

Content from this work  
may be used under the  
terms of the [Creative  
Commons Attribution 3.0  
licence](#).

Any further distribution of  
this work must maintain  
attribution to the author  
(s) and the title of the  
work, journal citation and  
DOI.

Cheng-Tien Chiang<sup>1,2</sup>, Michael Huth<sup>1</sup>, Andreas Trützscher<sup>1,2</sup>, Mario Kiel<sup>2</sup>, Frank O Schumann<sup>1</sup>,  
Jürgen Kirschner<sup>1,2</sup> and Wolf Widdra<sup>2,1</sup><sup>1</sup> Max Planck Institute of Microstructure Physics, Weinberg 2, 06120 Halle, Germany<sup>2</sup> Institute of Physics, Martin-Luther-Universität Halle-Wittenberg, Von-Danckelmann-Platz 3, D-06120 Halle(Saale), GermanyE-mail: [wolf.widdra@physik.uni-halle.de](mailto:wolf.widdra@physik.uni-halle.de)**Keywords:** photoelectron spectroscopy, high-order harmonic generation, electronic structure**Abstract**

Since the discovery of the photoelectric effect, photoelectron spectroscopy has evolved into the most powerful technique for studying the electronic structure of materials. Moreover, the recent combination of photoelectron experiments with attosecond light sources using high-order harmonic generation (HHG) allows direct observation of electron dynamics in real time. However, the efficiency of these experiments is greatly limited by space-charge effects at typically low repetition rates of photoexcitation. Here, we demonstrate HHG-based laboratory photoemission experiments at a photoelectron count rate of  $1 \times 10^5$  electrons/s and characterize the main features of the electronic band structure of Ag(001) within several seconds without significant degradation by the space-charge effects. The combination of a compact HHG light source at megahertz repetition rates with the efficient collection of photoelectrons using time-of-flight spectroscopy may allow rapid investigation of electronic bands in a flexible laboratory environment and pave the way for an efficient design of attosecond spectroscopy and microscopy.

**1. Introduction**

Photoelectron spectroscopy (PES) has provided tremendous insight into fundamental physics and material science. By analyzing the energy, the momentum, as well as the spin of photoelectrons, a complete picture of electronic structure and related properties of materials can be uncovered. Because of this abundant information, the development of advanced PES has remained one of the pioneering research topics for many decades.

Until today, the evolution of angle-resolved photoelectron spectroscopy (ARPES) can be categorized into two groups. The first group focuses on the improvement of electron spectrometers for a better energy and momentum resolution and a higher detection efficiency. In conventional spectrometers based on a hemispherical energy analyzer, only one momentum component of the photoelectron can be analyzed simultaneously with the energy ( $k_x, E$ ). Therefore, the acquisition speed for a three-dimensional data set of the photoemission intensity  $I(k_x, k_y, E)$  is often limited by the sequential data acquisition with rotation of the sample or the spectrometer in between. This issue is solved by using an imaging spectrometer to record the two-dimensional momentum distribution of photoelectrons  $I(k_x, k_y)$  simultaneously [1–5]. With the recent development of time-of-flight (ToF) spectrometers, band mapping using ARPES is pushed to much higher efficiency since hundreds of energy channels within several eV are measured in parallel together with the two-dimensional momentum distribution ( $k_x, k_y$ ) [6–11].

The second group of modern ARPES is the establishment of new excitation light sources. Traditional light sources in the laboratory are discharge lamps with sufficient intensity but only at few photon energies. In strong contrast, the synchrotron radiation light sources cover a wide photon energy range with high brilliance and high energy resolution. Although ARPES with these two types of light sources is well established, there are difficulties applying them to ToF-based experiments. For ToF spectroscopy, the discharge lamps are not suitable due to the absence of a well-defined time structure. On the other hand, for synchrotron radiation, it is necessary to use the



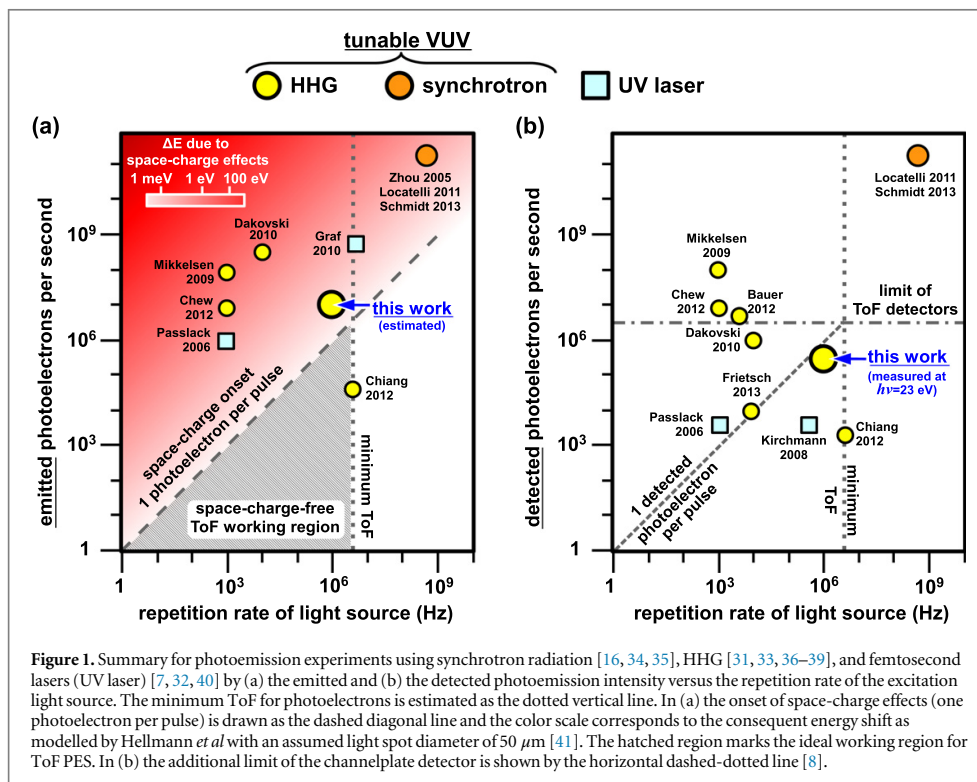


**Figure 1.** Summary for photoemission experiments using synchrotron radiation [16, 34, 35], HHG [31, 33, 36–39], and femtosecond lasers (UV laser) [7, 32, 40] by (a) the emitted and (b) the detected photoemission intensity versus the repetition rate of the excitation light source. The minimum ToF for photoelectrons is estimated as the dotted vertical line. In (a) the onset of space-charge effects (one photoelectron per pulse) is drawn as the dashed diagonal line and the color scale corresponds to the consequent energy shift as modelled by Hellmann *et al* with an assumed light spot diameter of 50  $\mu\text{m}$  [41]. The hatched region marks the ideal working region for ToF PES. In (b) the additional limit of the channelplate detector is shown by the horizontal dashed-dotted line [8].

limited beam time of single-bunch or chopper-assisted modes at a reduced repetition rate (see later discussion) [6, 12–17].

An ideal laboratory light source for ToF-based ARPES is the femtosecond laser, whose applications to photoemission experiments have revealed atom and electron dynamics at the femtosecond time scale [18–22]. With recent progress of laser physics in high-order harmonic generation (HHG) of vacuum-ultraviolet (VUV) light [23–25], HHG light sources allow laboratory ARPES experiments with a wide photon energy range at attosecond time resolution [26, 27]. Nevertheless, the existing HHG light sources work mostly at several kilohertz repetition rate and the optical architecture becomes demanding when going to megahertz [28–30]. As a consequence of these low repetition rates, the space-charge effects between photoelectrons emitted from one light pulse limit significantly the efficiency of HHG-based photoemission experiments [31–33].

In order to boost the acquisition speed of laboratory ARPES in a space-charge-free condition, application of a HHG light source at high repetition rates is essential. To summarize this issue and to analyze available approaches, figure 1(a) displays the rate of photoemitted electrons as a function of the repetition rate of the light source. Different symbols mark available literature data for experiments using light sources such as high-order harmonic generation (HHG) [31, 33, 36–39], femtosecond lasers (UV laser) [7, 32, 40], and synchrotron radiation [16, 34, 35], for which space-charge effects have been observed and quantified. The diagonal dashed line represents the condition of one photoelectron emitted per light pulse that corresponds to the onset of space-charge effects. Above this line, photoemission spectra can be broadened in energy as well as in momentum due to the repulsive Coulomb interaction between electrons that are photoexcited within the light pulse duration. The theoretically estimated strength of space-charge effects is represented by the resultant energy shift ( $\Delta E$ ) of characteristic features in a modeled spectrum [41] and encoded as the red background color in figure 1(a). As is evident from this diagram, efficient photoemission experiments require as high as possible repetition rates to avoid space-charge broadening. There are, however, additional physical limitations due to the electron spectrometers or the detectors. For ToF PES, there is a necessary minimum time interval between light pulses in order to avoid temporal overlap between photoelectrons from successive light pulses. For an energy spectrum with 800 independent data points with a typical 300 ps time resolution of electronics, the minimum time interval is 240 ns and corresponds to an upper limit for the repetition rate at around 4 MHz. This limit is indicated by the vertical dotted line in figure 1. As a consequence, the working region for ToF spectroscopy without space-charge broadening is limited, as marked by the hatched region in figure 1(a). As one can clearly see, the optimal



condition for ToF photoemission experiments corresponds to highest possible repetition rate with about 1 to 10 photoelectrons per pulse. However, so far, all HHG light sources for PES or microscopy are working at substantially lower repetition rates (see symbols in figure 1(a)).

From a practical point of view, it is also instructive to consider the number of detected photoelectrons at a given repetition rate. In general, the ratio between emitted and detected photoelectrons depends strongly on the type of analyzer. It can be also varied by the trade-off between analyzer transmission and energy or momentum resolution. In principle, the maximum acceptance is provided by combining an electron energy analyzer with the objective lens of a photoelectron emission microscope (PEEM) to collect all photoelectrons emitted in the full  $2\pi$  solid angle above the sample surface [4, 5, 10]. Figure 1(b) shows a similar plot as in figure 1(a), but with the vertical axis replaced by the detected count rate of photoelectrons. For imaging detectors, there exists generally an upper limit for the detected count rate to avoid permanent damage. In the case of channelplate-based delay-line-detectors (DLD), a conservative estimation of maximum allowed count rate is about  $3 \times 10^6$  counts/s [8] and is shown by the horizontal line in figure 1(b) (dashed-dotted).

In this paper, we report on laboratory ARPES experiments with a ToF spectrometer close to the optimal condition using a megahertz HHG light source. HHG ARPES at 1 MHz repetition rate with a *detected* photoelectron count rate of  $10^5$  electrons/s benchmarks the efficiency, as indicated in figure 1. As an example, we discuss the photoemission experiments from a Ag(001) surface with linearly polarized light. It shows the twofold photoelectron momentum patterns owing to the symmetry-breaking of incident light polarization. Based on the high repetition rate, we are able to analyze  $10^6$  photoelectrons within one-quarter the Brillouin zone in a 10 second measurement and to identify the clear signal of the *d* band complex ranging from 4 to 6 eV below the Fermi level ( $E_F$ ).

## 2. Experimental setup

To perform ToF-based ARPES, we use a home-built HHG setup as the pulsed excitation light source [39]. The high-order harmonics are driven by a compact turn-key operation ytterbium-fiber laser system (Impulse, Clark-MXR, Inc., USA), delivering a photon energy of 1.2 eV and pulses with intensity full-width-at-half-maximum (FWHM) of 300 fs. In the present experiments, we used pulse energies of 10 and 14  $\mu$ J at repetition rates of 1 and 0.7 MHz, respectively. The light pulses are focused into a gas jet in a vacuum chamber and the generated VUV is separated and focused onto the sample in the photoemission chamber by a standard toroidal diffraction grating (MB Scientific, Sweden). Details of the HHG generation and selection are described in [39]. The harmonic spectrum can be measured by turning the toroidal grating gradually while recording the count rate at the channelplates in the DLD of the ToF spectrometer.

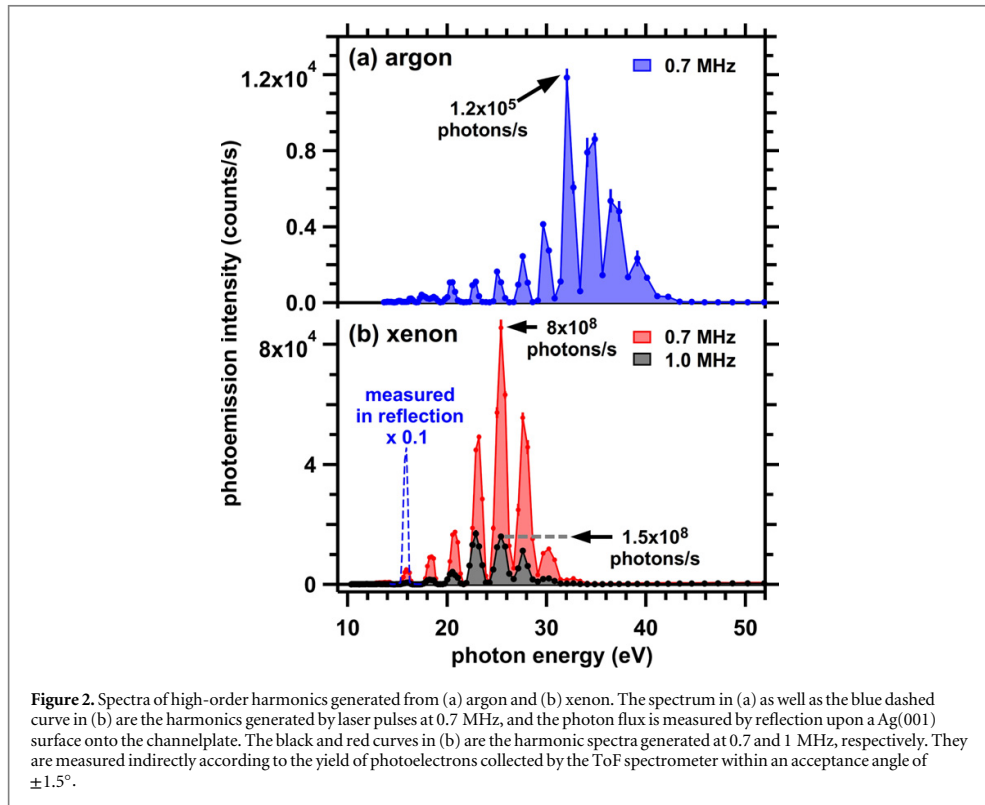
The photoelectrons are collected by a commercial ToF spectrometer with a  $\pm 15^\circ$  acceptance angle (Themis 1000, SPECS, Germany [8]). The ToF of photoelectrons is determined by the time difference between reference light pulses from the laser and the arrival time on the detector. The hit-position on the DLD is measured using time-to-digital converters. The reference time pulses from the laser are calibrated using the reflection of HHG light pulses from the sample. From the measured ToF of photoelectron and its hit position on the DLD, the kinetic energy and the emission angle of the photoelectron are derived using a conversion matrix from model calculations of the electron trajectory in the ToF spectrometer [42].

## 3. Results

### 3.1. HHG at MHz repetition rate

For an argon gas jet as generation medium, the HHG spectrum as back reflected from a Ag(001) crystal is shown in figure 2(a). Under these conditions, the photons are reflected at an angle of  $22.5^\circ$  onto the chevron channelplate in the DLD of the ToF spectrometer. The absolute photon flux is estimated by using the reflectivity of silver at 32 eV ( $\approx 0.1$  [43]) together with the detection efficiency of the channelplate ( $\approx 0.1$  [44]). The maximum photon flux from argon is located at a photon energy around 32 eV with a value of  $1.2 \times 10^5$  photons/s, which is less than one photon per laser pulse at this high repetition rate of 0.7 MHz. In total, the generated HHG spectrum covers the energy range from 20 to 40 eV with argon as the generation medium.

The HHG photon flux can be greatly enhanced by using xenon as the generation medium. In figure 2(b), the HHG spectra from xenon driven at 0.7 and 1 MHz are displayed. Due to the high photon flux generated from xenon, these spectra have to be measured indirectly according to the number of photoelectrons entering the ToF spectrometer within an acceptance angle of  $\pm 1.5^\circ$ , corresponding to about 0.03% of the full  $2\pi$  solid angle above the sample surface. A reflection measurement, as completed for argon, can only be performed for photon energy near 16 eV with moderate photon flux and is shown by the blue dashed curve. The photon flux at 16 eV from xenon is estimated to be  $4.6 \times 10^7$  photons/s or 66 photons/pulse at 0.7 MHz. At the maximum of the spectrum

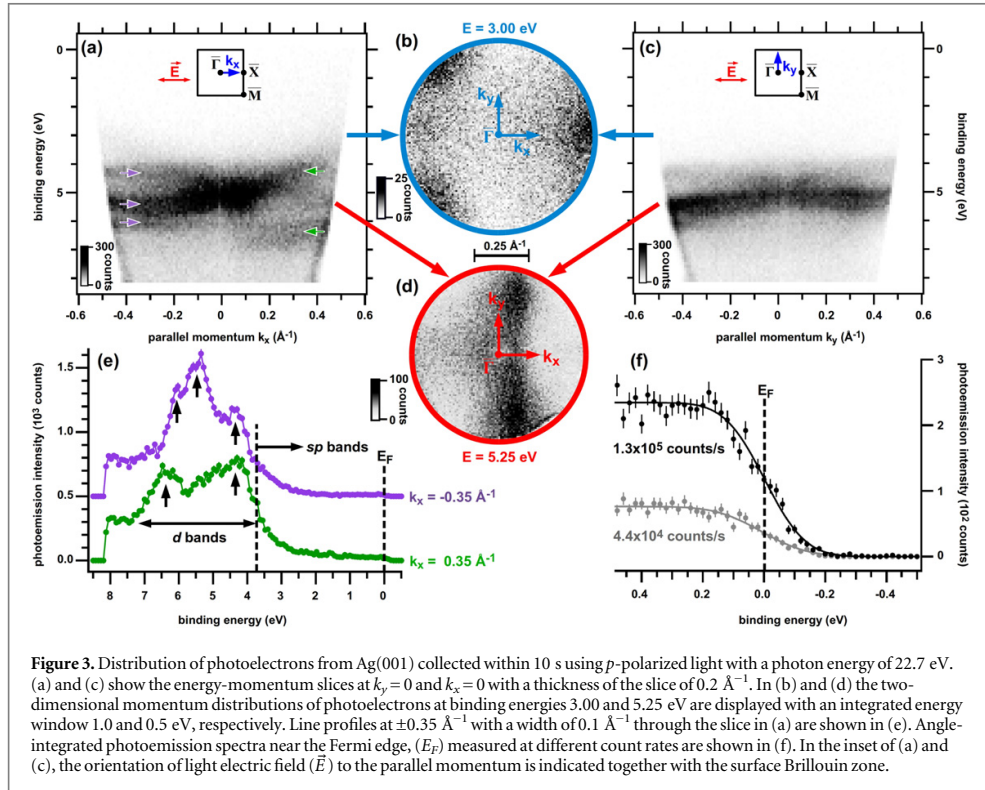


around 25 eV, the photon flux is estimated to be  $8 \times 10^8$  photons/s (1100 photons/pulse). Switching to 1 MHz leads to lower photon flux because of a lower pulse energy setting of the pumping laser. The maximum photon flux at 1 MHz is around  $1.5 \times 10^8$  (150 photons/pulse) at the photon energy of 22.7 eV. Note that the HHG intensity is more than three orders of magnitude higher than in our previous HHG study where a laser oscillator at 4 MHz was used [39]. Using xenon, the available photon energies are lower than using argon and range from 14 to 32 eV. Below 14 eV, the transmission of the toroidal grating, which is optimized for 40 eV, drops significantly [45].

According to the results in figure 2(b), we can estimate the total yield of photoelectrons. At the maximum of the spectrum for a photon energy of 25 eV at 0.7 MHz, we measured around  $8 \times 10^4$  electrons/s emitted into 0.03% of the  $2\pi$  full hemisphere. This small solid angle of detection was set by turning off all the electron lenses of the ToF spectrometer and was intentionally used to avoid damage of the detector at high count rates. As a rough estimation, a simple scaling up to the full  $2\pi$  hemisphere leads to a photoelectron yield of  $2 \times 10^8$  electrons/s emitted from the sample at 0.7 MHz, which corresponds to around 300 electrons/pulse. About  $5 \times 10^7$  electrons/s emitted from the sample is estimated from experiments at 1 MHz, and this emission intensity is marginally above the space-charge onset of one electron/pulse. The ratio of the estimated number of photoelectrons to the number of incident photons per second is about 0.25. This value is a factor of three higher than the known photoemission yield [46, 47] and can be ascribed to the emission angle and light polarization dependence that are neglected in the estimation. In figure 1(a) we show the conservative estimation of the total yield of photoelectrons at around  $1 \times 10^7$  electrons/s at 1 MHz, which is close to the optimal condition in the ToF working region.

### 3.2. Fast ToF photoemission experiments

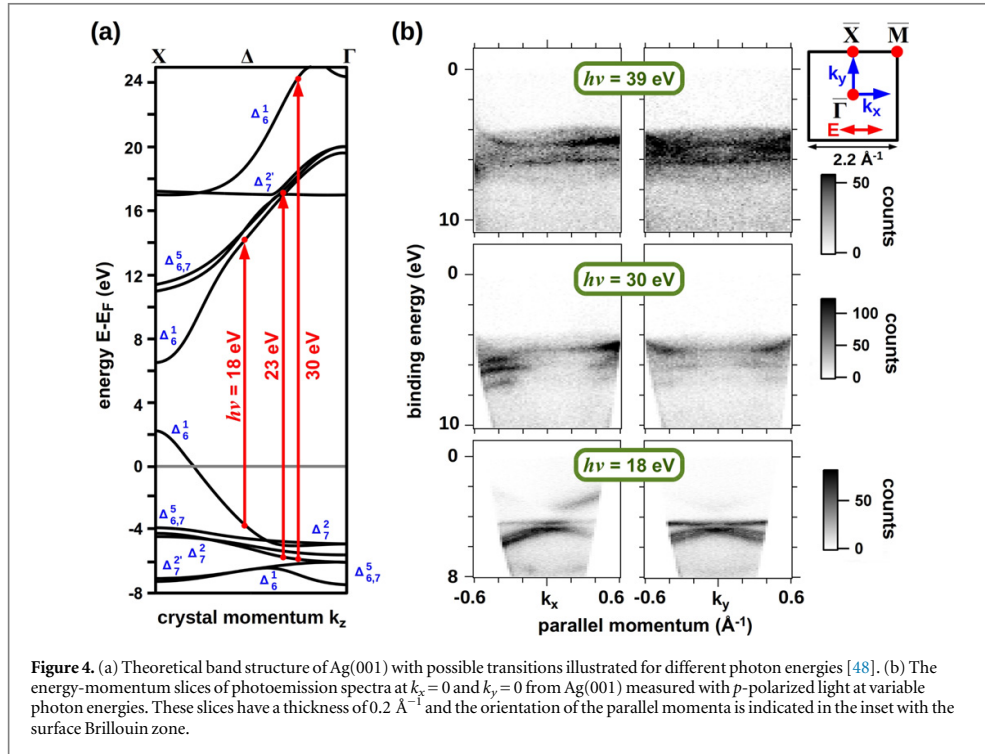
To demonstrate the efficiency of our present setup, we present a fast photoemission measurement from Ag(001) at 1 MHz with a photon energy of 22.7 eV. The angle of incidence of light is  $45^\circ$  and the light is *p*-polarized. In figure 3, we show the data from a single measurement with an acquisition time of 10 s and nominal kinetic and pass energy setting as 16 and 60 eV, respectively. Within this short time, we *detected* a total number of  $3 \times 10^6$  photoelectrons and this count rate is indicated in figure 1(b) for comparison with other photoemission experiments. The photoelectrons are analyzed according to their ToF and hit positions on the DLD in the spectrometer. This analysis yields the three-dimensional photoemission intensity as a function of energy (*E*) and



momentum components ( $k_x, k_y$ ) parallel to the surface  $I(k_x, k_y, E)$ . The two-dimensional slices of the photoemission intensity with energy versus momentum are shown in figures 3(a) and (c),  $I(k_x, E)$  and  $I(k_y, E)$ , respectively. In figure 3(e), we depicted the line profiles  $I(E)$  at fixed  $k_x = \pm 0.35 \text{ \AA}^{-1}$  from figure 3(a). Clear features of the *d* bands from 4 to 7 eV below the Fermi energy ( $E_F$ ) with high intensity are observed and the weak intensity above 4 eV is attributed to the *sp* bands. The cutoff at 8 eV is due to the limit of the electron lens system in the ToF spectrometer at the chosen setting.

Closer inspection of the dispersion of the photoemission features in figure 3(a) reveals a clear asymmetry between the positive and negative  $k_x$  sides. As indicated by the arrows in figures 3(a) and (e), on the negative side of  $k_x$  we observed three branches of *d* bands, whereas on the positive side, only two branches can be seen. This asymmetry in photoemission pattern can be further identified in the momentum distribution of photoelectrons  $I(k_x, k_y)$ , as shown in figures 3(b) and (d) for different energies. The momentum distribution has a mirror symmetry with respect to the  $k_x$  axis but no mirror symmetry about the  $k_y$  axis. This observation can be explained by the experimental geometry as defined by the Ag(001) surface with fourfold symmetry and by the linearly polarized incident light within the optical plane on which the  $k_x$  axis is located. The linear polarization of light is  $45^\circ$  tilted from the surface normal and simultaneously has a component parallel to the  $k_x$  momentum direction, as well as another component perpendicular to the surface. These two electric field components can cause interference in the matrix element of photoemission and result in an asymmetric distribution of photoelectrons [49, 50]. As a consequence, breaking the original fourfold symmetry with the incident off-normal light leads to a twofold pattern, which has only mirror-symmetry about the  $k_x$  axis in our case. The appearance of the threefold pattern in figure 3(b) can be considered as a special case of a mirror-symmetric pattern with respect to the  $k_x$  axis at this specific binding energy.

To check whether space-charge effects have an influence on the present experiments, we follow the well-established method in the literature and compare the Fermi-edge in photoemission spectra measured with different count rates [34, 40]. In figure 3(f), we show the angle-integrated photoemission spectra near the Fermi energy ( $E_F$ ) measured with  $1.3 \times 10^5$  and  $4.4 \times 10^4$  electrons/s and the fits with a step function convoluted by a Gaussian function. From the fit, the position of the Fermi edge in these two spectra can be evaluated and their difference is less than 10 meV. We therefore exclude significant space-charge effects much higher than 10 meV, which is in accordance with our expectation for the MHz high repetition rates, as discussed in figure 1. The full-width-at-half-maximum (FWHM) of the Gaussian functions in the fits is around 250 meV. By taking into



account the thermal broadening of the Fermi–Dirac distribution that corresponds to a FWHM of around 100 meV at 300 K, we estimate the energy resolution in the present experiments as 230 meV. This value is larger than that in our previous measurements on the surface state of Cu(111) surfaces using a lower photon energy [39]. As included in the energy resolution, about 180 meV can be attributed to the bandwidth of the HHG light source at a photon energy of 22.7 eV, whereas the other 150 meV comes from the energy resolution of the ToF spectrometer for the present lens setting of a 12 eV energy window. This estimated bandwidth of the harmonics corresponds to a transform-limited pulse duration of about 9 fs from generation, which is subsequently stretched by the monochromator grating to about 2 ps.

The features of electronic bands observed in photoemission spectra in figure 3 can be qualitatively interpreted by the band structure of Ag(001), as shown in figure 4(a) [48]. With a photon energy close to 23 eV, the dominant photoemission signals come from the resonance between Ag  $d$  and unoccupied  $sp$  bands. Similar transitions from the  $d$  bands can also take place at higher photon energies of 30 and 39 eV as observed in figure 4(b). In addition, at a lower photon energy of 18 eV, a resonance between  $sp$  bands occurs and photoemission signals from the Ag  $sp$  bands with stronger dispersion along the momentum direction  $k_x$  is observed, as shown in the lowest panel of figure 4(b).

#### 4. Discussion

In the following, we compare the efficiency of the MHz HHG setup with photoemission experiments with discharge lamps in the laboratory, as well as at synchrotron radiation facilities. Our quantitative comparison is based on the detected photoemission count rate according to the spectrometer acceptance and the space-charge limit.

##### 4.1. Comparison with laboratory experiments using discharge lamps

In conventional laboratory photoemission experiments using a hemispherical energy analyzer in combination with a discharge lamp, the sequential azimuthal rotation of the sample is necessary for a three-dimensional  $I(k_x, k_y, E)$  data set. Based on the 180 min measurement by Reinert *et al* with an angular acceptance of  $\pm 7^\circ$  and a high-energy resolution of 3.5 meV, we estimate an acquisition time of 10 min for a measurement with comparable momentum range and energy resolution to our results in figure 3 [51]. This longer acquisition time than our present HHG-based experiments can be attributed to an order of magnitude lower photoemission

intensity from the surface states and the slow subsequent sample rotation in their experiments. Using the PEEM-based spectrometer to collect all emitted photoelectrons, a three-dimensional data set  $I(k_x, k_y, E)$  typically takes 0.5 to 1 h [4, 5]. A comparable measurement using our present setup requires a 30 times longer acquisition time than for the data in figure 3 and the total measurement time is about 5 min. Therefore, our setup is more efficient than these laboratory experiments using a laboratory discharge lamp either with a hemispherical energy analyzer or a PEEM-based spectrometer.

Despite the lower efficiency of these laboratory ARPES experiments using a discharge lamp, they may be advantageous due to the high-energy resolution coming from the narrow width of the ionization lines. On the other hand, the HHG-based ToF experiments provide a more simple control over the polarization of light as well as the possibilities for time-resolved pump-probe experiments.

#### 4.2. Comparison with experiments using synchrotron radiation

In comparison to laboratory light sources such as discharge lamps or HHG, synchrotron radiation can provide significantly higher photon flux at a higher repetition rate, as indicated in figure 1. Therefore, synchrotron-based ARPES experiments can be generally more efficient than our laboratory HHG-based ARPES experiments. In order to compare the relative efficiency, in the following, we discuss the space-charge-limited ARPES experiments using synchrotron in the normal operation mode in combination with a hemispherical energy analyzer, as well as in the single-bunch mode with a ToF spectrometer.

For experiments with a hemispherical energy analyzer, we estimate the acquisition time of space-charge-limited synchrotron ARPES experiments using a count rate of 200 photoelectrons per pulse near the onset of space-charge effects ( $\Delta E = 1.4$  meV) at a 500 MHz repetition rate [34]. Assuming this count rate as the maximum intensity in experiments and an isotropic distribution of photoelectrons, there are  $10^{11}$  electrons/s emitted from the sample and  $3 \times 10^9$  electrons/s within the  $\pm 15^\circ$  emission angle enter the hemispherical energy analyzer. To acquire a two-dimensional momentum distribution with a range and a resolution comparable to our results in figure 3, experiments with the hemispherical energy analyzer need to include 240 steps within the  $180^\circ$  azimuthal sample rotation. Therefore, the effective count rate for measuring a three-dimensional data set  $I(k_x, k_y, E)$  is reduced by a factor of 1/240 and ends up at  $1 \times 10^7$  electrons/s. This count rate is about two orders of magnitude higher than that in our HHG-ToF experiments and proves that the synchrotron-based experiment with a hemispherical energy analyzer is more efficient. The higher efficiency of synchrotron ARPES experiments is directly related to their two orders of magnitude higher repetition rate than our HHG light source and this aspect was overlooked in an earlier comparison in [11].

In strong contrast to ARPES using the hemispherical energy analyzer, experiments with a ToF spectrometer require a reduced repetition rate of the synchrotron radiation [6, 17]. The single-bunch mode at several synchrotron facilities operates at a repetition rate in the range from 1.25 MHz at BESSY [16, 17] and NSLS [12], to 3 MHz at ALS [15] and 5 MHz at ESRF [14]. Despite the much more intense light from synchrotron than in our laboratory HHG setup, the detected photoelectron count rate would not be significantly higher beyond  $10^6$  counts/s due to the limit of the imaging detectors. Therefore, we estimate a conservative maximum count rate of synchrotron-based ToF PES of around  $10^6$  counts/s, which can be reached using our laboratory HHG-based experiments.

## 5. Summary

To summarize, we demonstrate efficient laboratory-based ARPES using HHG from a fiber laser at megahertz repetition rate in combination with ToF spectroscopy. Count rates as high as  $1 \times 10^5$  electrons/s within a 3% portion of the full  $2\pi$  solid angle are *detected* and *analyzed*. The presented efficiency significantly improves conventional laboratory ARPES experiments using discharge lamps or laser-based HHG light sources at kHz repetition rates. Our results provide a guide for efficient and flexible laboratory-based band-mapping experiments that are important for general studies in material science. Such HHG light sources at high repetition rates might pave the way for compact ultrafast time-resolved multi-dimensional PES and microscopy, where thousands of photoelectron spectra at different pump-probe delays are required [52, 53].

## Acknowledgments

Technical support from R Kulla, R Neumann, F Weiß, K Sklarek, and H Menge as well as financial support from the DFG through SFB 762 are gratefully acknowledged.



## References

- [1] Eastman D, Donelon J, Hien N and Himpfel F 1980 *Nucl. Instrum. Methods* **172** 327–36
- [2] Clarke A, Jennings G and Willis R F 1987 *Rev. Sci. Instrum.* **58** 1439–44
- [3] Düttemeyer T, Quitmann C, Kitz M, Dornemann K, Johansson L S O and Reihl B 2001 *Rev. Sci. Instrum.* **72** 2638
- [4] Krömker B, Escher M, Funnemann D, Hartung D, Engelhard H and Kirschner J 2008 *Rev. Sci. Instrum.* **79** 053702
- [5] Tromp R M, Fujikawa Y, Hannon J B, Ellis A W, Berghaus A and Schaff O 2009 *J. Phys.: Condens. Matter.* **21** 314007
- [6] Schicketz M, Oelsner A, Morais J, Mergel V, Schmidt-Böcking H and Schönhense G 2001 *Proc. 7th Int. Conf. on Synchrotron Radiation Instrumentation Nucl. Instrum. Methods Phys. Res. A* **467468** 1519–22 ISSN 0168-9002
- [7] Kirchmann P, Rettig L, Nandi D, Lipowski U, Wolf M and Bovensiepen U 2008 *Appl. Phys. A* **91** 211–7
- [8] Bernsten M H, Gotberg O and Tjernberg O 2011 *Rev. Sci. Instrum.* **82** 095113
- [9] Öhrwall G et al 2011 *J. Electron Spectrosc. Relat. Phenom.* **183** 125–31
- [10] Schönhense G 2014 *Johannes Gutenberg Universität Mainz, post-deadline talk at DPG Frühjahrstagung in Dresden* unpublished
- [11] Ovsyannikov R, Karlsson P, Lundqvist M, Lupulescu C, Eberhardt W, Föhlisch A, Svensson S and Mårtensson N 2013 *J. Electron Spectrosc. Relat. Phenom.* **191** 92–103
- [12] Wehlitz R, Pibida L S, Levin J C and Sellin I A 1999 *Rev. Sci. Instrum.* **70** 1978–82
- [13] Hattass M, Jalowy T, Czasch A, Weber T, Jahnke T, Schossler S, Schmidt L P, Jagutzki O, Dorner R and Schmidt-Böcking H 2004 *Rev. Sci. Instrum.* **75** 2373–8
- [14] Moreschini L, Ghiringhelli G, Larsson K, Veit U and Brookes N B 2008 *Rev. Sci. Instrum.* **79** 033905
- [15] Jozwiak C, Graf J, Lebedev G, Andresen N, Schmid A K, Fedorov A V, Gabaly F E, Wan W, Lanzara A and Hussain Z 2010 *Rev. Sci. Instrum.* **81** 053904
- [16] Schmidt T, Sala A, Marchetto H, Umbach E and Freund H J 2013 *Ultramicroscopy* **126** 23–32
- [17] Hollack K et al 2014 *Nat. Commun.* **5** 4010
- [18] Höfer U, Shumay I L, Reu C, Thomann U, Wallauer W and Fauster T 1997 *Science* **277** 1480–2
- [19] Aeschlimann M, Burgermeister R, Pawlik S, Bauer M, Oberli D and Weber W 1998 *Proc. Seventh International Conference on Electron Spectroscopy J. Electron Spectrosc. Relat. Phenom.* **8891** 179–83
- [20] Petek H, Weida M J, Nagano H and Ogawa S 2000 *Science* **288** 1402–4
- [21] Weinelt M 2002 *J. Phys.: Condens. Matter.* **14** R1099
- [22] Rettig L, Cortés R, Thirupathiah S, Gegenwart P, Jeevan H S, Wolf M, Fink J and Bovensiepen U 2012 *Phys. Rev. Lett.* **108** 097002
- [23] Winterfeldt C, Spielmann C and Gerber G 2008 *Rev. Mod. Phys.* **80** 117–40
- [24] Popmintchev T, Chen M C, Arpin P, Murnane M M and Kapteyn H C 2010 *Nat. Photon.* **4** 822–32
- [25] Hädrich S, Klenke A, Rothhardt J, Krebs M, Hoffmann A, Pronin O, Pervak V, Limpert J and Tünnemann A 2014 *Nat. Photonics* **8** 779
- [26] Cavalieri A L et al 2007 *Nature* **449** 1029–32
- [27] Krausz F and Ivanov M 2009 *Rev. Mod. Phys.* **81** 163–234
- [28] Seres E, Seres J and Spielmann C 2012 *Opt. Express* **20** 6185–90
- [29] Cingöz A, Yost D C, Allison T K, Ruelh A, Fermann M E, Hartl I and Ye J 2012 *Nature* **482** 68–71
- [30] Pupeza I et al 2013 *Nat. Photon.* **7** 608–12
- [31] Chew S H et al 2012 *Appl. Phys. Lett.* **100** 051904
- [32] Passlack S, Mathias S, Andreyev O, Mittnacht D, Aeschlimann M and Bauer M 2006 *J. Appl. Phys.* **100** 024912
- [33] Dakovski G L, Li Y, Durakiewicz T and Rodriguez G 2010 *Rev. Sci. Instrum.* **81** 073108
- [34] Zhou X, Wannberg B, Yang W, Brouet V, Sun Z, Douglas J, Dessau D, Hussain Z and Shen Z X 2005 *J. Electron Spectrosc. Relat. Phenom.* **142** 27–38
- [35] Locatelli A, Mentş T O, Ángel Niño M and Bauer E 2011 *Ultramicroscopy* **111** 1447–54
- [36] Mikkelsen A et al 2009 *Rev. Sci. Instrum.* **80** 123703
- [37] Bauer M and Rohde G 2012 *Christian-Albrechts-Universität zu Kiel, private communications*
- [38] Frietsch B, Carley R, Dbrich K, Gahl C, Teichmann M, Schwarzkopf O, Wernet P and Weinelt M 2013 *Rev. Sci. Instrum.* **84** 075106
- [39] Chiang C T, Blättermann A, Huth M, Kirschner J and Widdra W 2012 *Appl. Phys. Lett.* **101** 071116
- [40] Graf J, Hellmann S, Jozwiak C, Smallwood C L, Hussain Z, Kaindl R A, Kipp L, Rossnagel K and Lanzara A 2010 *J. Appl. Phys.* **107** 014912
- [41] Hellmann S, Rossnagel K, Marczyński-Bühlow M and Kipp L 2009 *Phys. Rev. B* **79** 035402
- [42] Huth M, Chiang C T, Trützscher A, Schumann F O, Kirschner J and Widdra W 2014 *Recent Prog. Appl. Phys. Lett.* **107** 061602
- [43] Lynch D W and Hunter W R 1985 Comments on the optical constants of metals and an introduction to the data for several metals *Handbook of Optical Constants of Solids (Academic Press handbook series vol 1)* ed E D Palik (Boston: Academic Press) pp 350–7 <http://sciencedirect.com/science/article/pii/B9780125444156500157>
- [44] Martin C and Bowyer S 1982 *Appl. Opt.* **21** 4206–7
- [45] Estimated by the numerical program REFLEC. See: Schäfers F and Krumrey M 1996 *BESSY Technischer Bericht* **201** 1 REFLEC — a program to calculate VUV/X-ray optical elements and synchrotron radiation beamlines
- [46] Cairns R B and Samson J A R 1966 *J. Opt. Soc. Am.* **56** 1568–73
- [47] Saloman E 1980 *Nucl. Instrum. Methods* **172** 79–87
- [48] Eckardt H, Fritsche L and Noffke J 1984 *J. Phys. F: Met. Phys.* **14** 97
- [49] Únal A A, Winkelmann A, Tusche C, Bisio F, Ellguth M, Chiang C T, Henk J and Kirschner J 2012 *Phys. Rev. B* **86** 125447
- [50] Venus D 1994 *Phys. Rev. B* **49** 8821
- [51] Reinert F, Nicolay G, Schmidt S, Ehm D and Hüfner S 2001 *Phys. Rev. B* **63** 115415
- [52] Okino T, Furukawa Y, Shimizu T, Nabekawa Y, Yamanouchi K and Midorikawa K 2014 *J. Phys. B: At. Mol. Opt. Phys.* **47** 124007
- [53] Cui X, Wang C, Argondizzo A, Garrett-Roe S, Gumhalter B and Petek H 2014 *Nat. Phys.* **10** 505–9



PHYSICAL REVIEW A **89**, 043404 (2014)

## Atomic line emission and high-order harmonic generation in argon driven by 4-MHz sub- $\mu$ J laser pulses

Alexander Blättermann,<sup>1,2,\*</sup> Cheng-Tien Chiang,<sup>2,1</sup> and Wolf Widdra<sup>1,2,†</sup><sup>1</sup>*Institute of Physics, Martin-Luther-Universität Halle-Wittenberg, Von-Danckelmann-Platz 3, D-06120, Halle (Saale), Germany*<sup>2</sup>*Max Planck Institute of Microstructure Physics, Weinberg 2, 06120 Halle, Germany*

(Received 31 October 2013; published 3 April 2014)

We report on the coexistence of atomic line emission (ALE) and high-order harmonic generation (HHG) from argon with experimental conditions bridging the multiphoton and tunnel ionization regimes. Driven by sub- $\mu$ J femtosecond laser pulses in tight-focusing geometry, characteristic spectra of ALE from highly excited neutral argon as well as from singly ionized argon are detected in the presence of the harmonics. The results are discussed with respect to the electronic structure of argon and the phase-matching condition of the HHG process.

DOI: 10.1103/PhysRevA.89.043404

PACS number(s): 42.65.Ky, 42.65.Re

### I. INTRODUCTION

High-order harmonic generation (HHG) is a process in which strong laser pulses with low photon energy, down to the midinfrared region, are converted into bursts of high-energy radiation ranging from the extreme ultraviolet up to hard x ray [1,2]. The celebrated combination of HHG-based light sources with varieties of spectroscopy and microscopy methods allows ultimate time resolution in experiments and real-time observation of ultrafast electron dynamics in general [3]. In the simplified picture of the HHG process, a strong electric field, more than several V/Å, from a driving laser is required to trigger tunnel ionization [4]. This marks a HHG threshold at incident laser peak intensity around  $10^{13}$  W/cm<sup>2</sup>. The demand to build a HHG source of the highest possible repetition rate requires therefore detailed knowledge of the onset of the tunnel ionization regime. It has been reported that the threshold intensity for HHG could be greatly reduced by several orders of magnitude using field enhancement in plasmonic nanostructures [5,6]. However, the first exciting results demonstrated by Kim *et al.* [5] could not be reproduced by other groups and the observed emission of vacuum-ultraviolet light was later identified as atomic line emission (ALE) [7,8].

The ALE is usually dominated by the HHG signals when the process is driven by mJ laser pulses from amplified laser systems at low repetition rate [2]. The recent observation of ALE driven by a weak laser field [7,8] signifies more than a technical issue of discriminating ALE from HHG features when they have comparable intensity. From the fundamental physical point of view, the observation is relevant to the transition region between multiphoton and tunnel ionization regimes where the ac-Stark shift and resonances can take place [9–11]. This transition occurs when the Keldysh parameter  $\gamma$ , the ratio of the time scale for tunnel ionization to the period of the incident laser field [12], is close to unity. In a simplified picture, tunnel ionization needs to compete with the oscillating optical electric field, since at a high frequency

the field switches its direction earlier, before the electron tunnels through the dynamically distorted ionization potential. At high field strength and low frequency,  $\gamma < 1$ , the tunnel ionization dominates, corresponding to experiments showing dominant HHG spectra. At lower field strength and higher frequency,  $\gamma$  goes beyond unity and multiphoton ionization from weakly perturbed atomic states comes into play, leading to the emission of characteristic ALE spectra.

In this paper, we investigate for  $\gamma \approx 1$  the coexistence of ALE and HHG from an argon jet driven by femtosecond laser pulses of 650 nJ at 4 MHz repetition rate. In strong contrast to previous studies [8], which showed only either dominant HHG features driven by mJ pulses at several kHz repetition rate or ALE driven by nJ pulses at MHz, we observe the clear coexistence of ALE and HHG processes under otherwise identical experimental conditions. By comparing the ALE spectra with the electronic structure of argon atoms, we assign the ALE features to emission from highly excited neutral argon atoms and singly charged argon ions. The simultaneous observation of ALE and HHG and the understanding of their relative intensities might be important for the development of low-power, but high repetition rate, HHG sources which operate just above the transition regime for  $\gamma \approx 1$ . As a tool, the observation of ALE might allow one to locate the crossing condition of the  $\mu$ m gas jet and the  $\mu$ m laser focus when the optimal HHG conditions are not yet met. But more essentially, the clear separation of both effects is necessary to assign the HHG radiation under threshold conditions.

HHG sources with MHz repetition rates are essential for the design of laser-based vacuum-ultraviolet light source in electron-based spectroscopy and microscopy, where repetition rate significantly beyond traditional kHz Ti:sapphire amplifier systems [13,14] is necessary. By far, as an alternative to our approach using a sub- $\mu$ J laser oscillator at MHz, HHG experiments at this high repetition rate require either intricate high-power fiber laser systems [15–18] or an additional complex resonant cavity for field enhancement [19–21].

### II. EXPERIMENTAL SETUP

In Fig. 1(a), an overview of the setup is shown. To drive HHG, we used the output of a Ti:sapphire oscillator with its cavity extended by a Herriott-type multipass cell [22,23]. The

\*Present address: Max Planck Institute for Nuclear Physics, Saupfercheckweg 1, 69117 Heidelberg, Germany; alexander.blaettermann@mpi-hd.mpg.de

†Corresponding author: wolf.widdra@physik.uni-halle.de

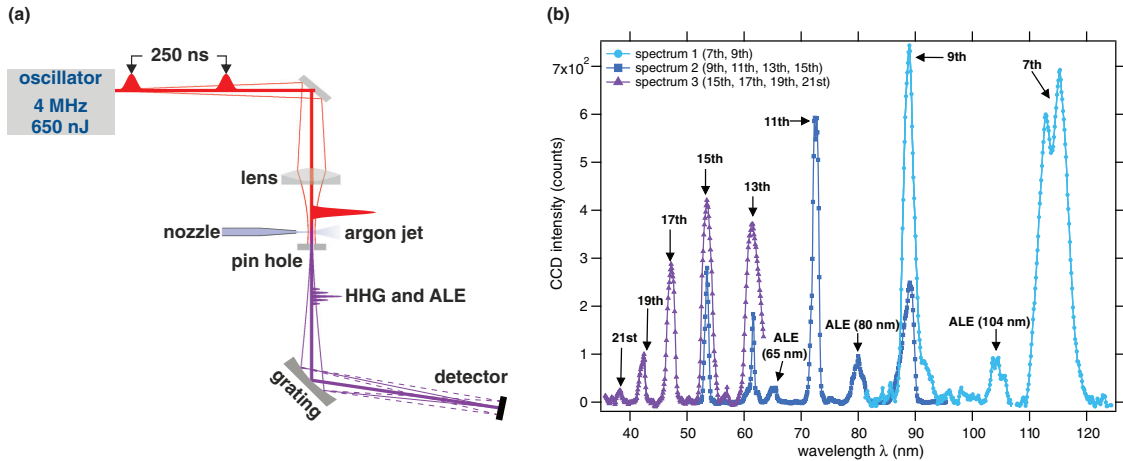


FIG. 1. (Color online) (a) Setup of experiments. (b) Spectra of the generated radiation from argon, measured for 7.5 s for spectra 1 and 2, and 60 s for spectrum 3. The three spectra are measured with different diffraction angles by which the grating is rotated. A smooth background was subtracted from the spectra. The order of the harmonics and the atomic lines (ALE) with their wavelength are indicated.

laser output has a central wavelength around 800 nm, and a pulse energy of 650 nJ with 50 fs pulse duration at 4 MHz repetition rate. An achromatic lens focuses the laser beam into an argon gas jet emerging from a glass capillary with 30  $\mu\text{m}$  orifice and a backing pressure of 3 to 4 bar. The focal length is about 50 mm, which results in a beam-waist diameter of around 5  $\mu\text{m}$ . These focus parameters are in strong contrast to the conventional HHG setups using amplified laser systems with  $\mu\text{J}$  to mJ pulse energy, in which a sufficient intensity can still be provided by a much larger focus size. In our case, the peak intensity at the focus is estimated to be  $7 \times 10^{13} \text{ W/cm}^2$ . The emitted vacuum-ultraviolet light is diffracted and focused onto an imaging detector by a toroidal grating. Due to the diffraction geometry, the longest wavelength that can be observed is around 120 nm and a wide spectral range can be detected upon rotation of the grating. The diffracted HHG pulses are stretched to a temporal width of 1 to 2 ps according to the line density of the grating and the estimated beam-spot size on the grating. Details of the setup are described elsewhere [24].

### III. RESULTS

Figure 1(b) shows spectra of vacuum-ultraviolet light generated from an argon jet with a backing pressure of 4 bar. In the spectra, the harmonics of the driving laser field are indicated by their harmonic order and the additional features are attributed to atomic lines (ALE) of argon. The photon flux is estimated to be  $2 \times 10^4$  photons/s for the 13th harmonic with an assumed 10% efficiency of the detector. This flux is about 4 orders of magnitude lower than that of a conventional HHG setup driven by amplifier laser systems [14].

By using the cutoff in the HHG spectra as a reference, we can estimate the Keldysh parameter  $\gamma$  in our experiment as the following. The HHG spectra extend up to the 17th harmonic and show a cutoff around the 19th harmonic with a photon energy of 29.5 eV ( $E_{\text{cutoff}}$ ). According to the empirical cutoff law of HHG [25], the ponderomotive energy ( $U_p$ ) of electrons

in the laser field can be estimated by  $E_{\text{cutoff}} = I_p + 3.17U_p$ . Here,  $I_p$  is the ionization potential of the neutral argon atom of 15.8 eV.  $U_p$  is estimated to be 4.3 eV and the peak intensity at the laser focus is estimated to be around  $7.3 \times 10^{13} \text{ W/cm}^2$ . This peak intensity is in reasonable agreement with our estimation by the focus spot size. From these, we estimate the Keldysh parameter  $\gamma \approx 1.4$ , which is in the transition region between the multiphoton and tunnel ionization regimes.

As a crosscheck for the assignment of ALE and HHG, we used xenon instead of argon as the generation medium, and harmonics up to the 13th order were observed with higher intensity, whereas the ALE features at 65, 80, and 104 nm wavelength were not observed (data not shown). This suggests that the assigned ALE features are related to the characteristic electronic structure of argon atoms and ions.

The detailed spectrally resolved structure of the ALE is shown in Fig. 2. Figures 2(a) and 2(b) display the two-dimensional diffraction pattern and Fig. 2(c) shows the corresponding line profiles. In the presented spectral range, the 9th, 11th, and 13th harmonics dominate, but additional features appear at about 64 and 80 nm, which we resolve with high resolution. In Fig. 2(b), the diffraction pattern of the generated radiation is measured under identical conditions, except for a reduced exposure time as in Fig. 2(a), and the argon gas jet is displaced by about 30  $\mu\text{m}$  away from the lens along the light propagation axis. As clearly shown by the comparison between the line profiles in Fig. 2(c), the intensity of the 11th harmonic was about tripled from Figs. 2(a) to 2(b), whereas the ALE features completely vanish. This observation shows directly the very different generation conditions for ALE and HHG.

### IV. DISCUSSION

In general, the identification of specific ALE transitions simultaneously in HHG experiments is not straightforward

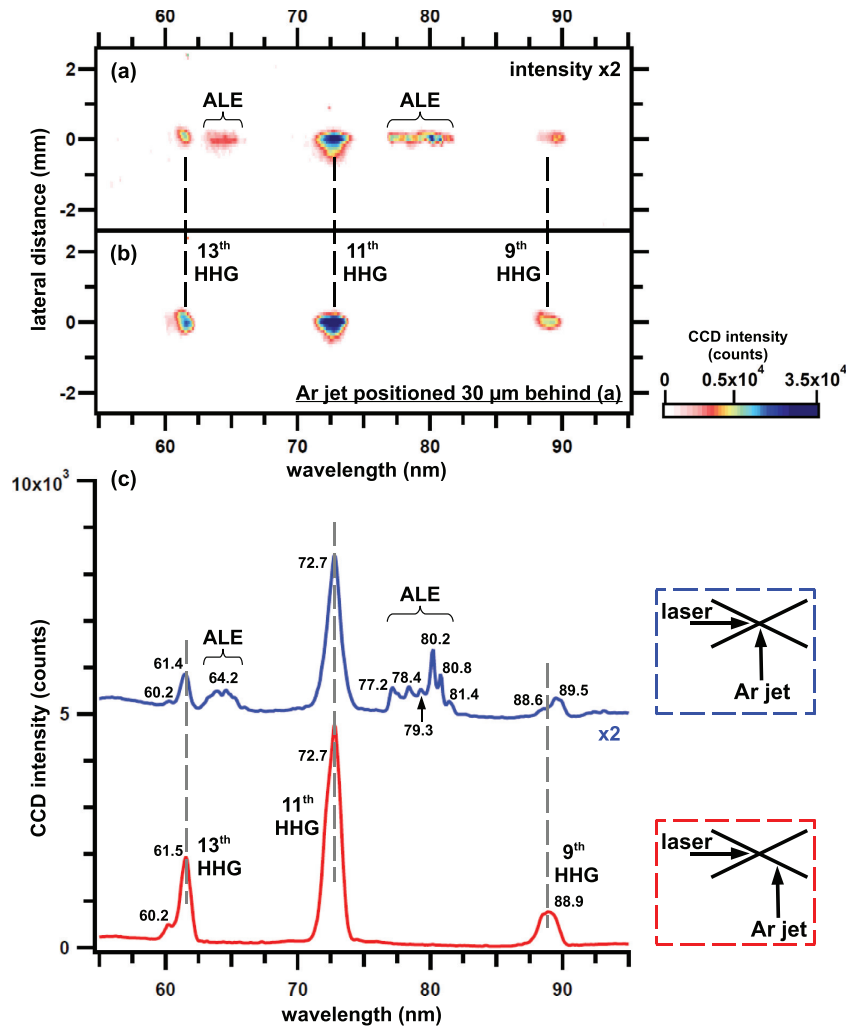


FIG. 2. (Color online) (a),(b) The diffraction patterns of generated vacuum-ultraviolet radiation for two different argon jet positions. In (a), the argon jet is positioned 30  $\mu\text{m}$  closer toward the incident laser beam than in (b). (c) The averaged line profiles from (a), blue curve, and (b), red curve. A constant background in the line profile is subtracted. For clarity, the blue curve is vertically shifted. The exposure time for image (a) and (b) is 22 and 11 s, respectively, and a factor 2 should be taken into account when comparing their absolute intensity.

because of the abundance of possible transitions [7] as well as laser-intensity-dependent Stark shifts of the characteristic atomic lines [9–11]. Moreover, the HHG spectra can depend on the generation geometry and the driving laser-pulse energy. It has been shown that different electron trajectories can lead to splittings of the odd harmonic spectral features; however, at sub- $\mu\text{J}$  pulse energies in tight-focusing geometry, significant splittings are absent according to the detailed study by Heyl *et al.* [26]. For comparison with the experimental spectra, we show in Fig. 3 the atomic transitions of neutral argon reported in the literature summarized by the Grotrian diagram [27–30]. Here the excited atomic levels of neutral argon are indicated with their energies relative to the ground-state  $[\text{Ne}]3s^23p^6$  electronic configuration. Selected optical transitions from

these excited states to the ground state are sketched and labeled with the emitted wavelength ( $\lambda$ ).

Comparing the observed vacuum-ultraviolet spectra in Fig. 1(b) with the energy diagram in Fig. 3(a), we can assign the ALE features near 80 and 104 nm to atomic transitions in neutral argon atoms. The ALE feature near 104 nm agrees well with the transitions from the excited states  $[\text{Ne}]3s^23p^54s^1$  at about 12 eV ( $\lambda = 104.8, 106.7$  nm) to the ground state. These transitions were also observed in Ref. [8] when argon is driven by mJ laser pulses at 1 kHz. Furthermore, the feature near 80 nm with fine-scale spectra features revealed in Fig. 2(c) can be related to transitions from highly excited states near the ionization threshold ( $I_p$ ), i.e.,  $[\text{Ne}]3s^23p^5ns^1$  with  $n \geq 6$  and  $[\text{Ne}]3s^23p^5nd^1$  with  $n \geq 4$ , to the ground state.

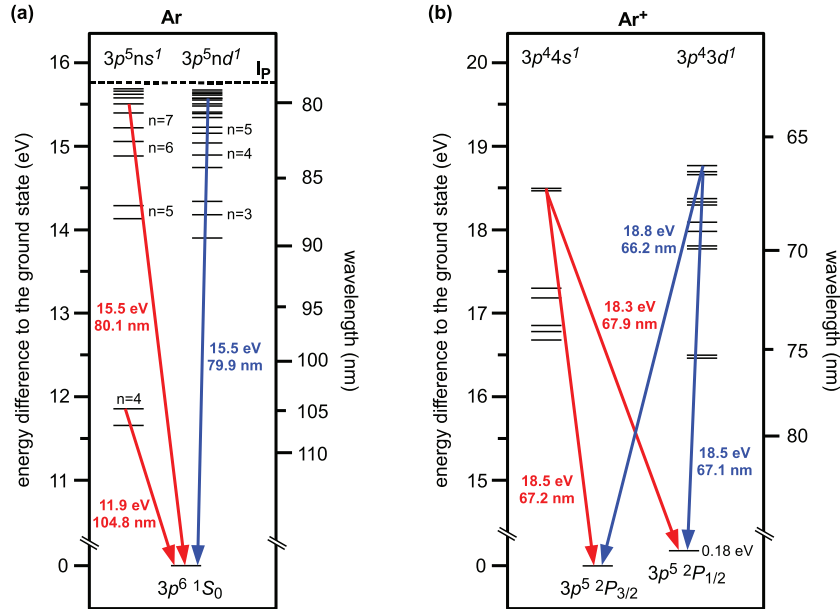


FIG. 3. (Color online) The relevant Grotrian diagrams of (a) a neutral argon atom [27–29] and (b) a singly ionized argon ion [28,30] for the observed atomic emission lines. Excited states are shown with the energy (left axis) and emitted wavelength (right axis) in an optical transition to the ground states. Examples for dipole allowed transitions are indicated by the arrows labeled with the wavelength of emitted radiation. In (a), the ionization energy ( $I_p$ ) for a singly charged ion is marked by the dashed line.

A closer look at the fine-scale spectra feature near 80 nm in Fig. 2(c) reveals its extension down to 77.2 nm. This value is smaller than the corresponding value of the ionization potential ( $I_p$ ) of 78.8 nm. Since all the  $[\text{Ne}]3s^23p^5ns^1$  and  $[\text{Ne}]3s^23p^5nd^1$  bound states must be located below  $I_p$  in the argon atom in a field-free environment, we tentatively attribute this deviation to the dynamic Stark effect due to the strong driving laser field. In analogy, comparing the weak ALE feature near 65 nm in Fig. 2(c) with Fig. 3(b), we could assign this feature to transitions of singly charged argon ions from the energetically higher states  $[\text{Ne}]3s^23p^44s^1$  or  $[\text{Ne}]3s^23p^43d^1$  to the  $[\text{Ne}]3s^23p^5$  ground state with wavelength in the range of 66 to 70 nm. According to the experiments of Ackermann *et al.*, the Stark shift depends linearly on the laser intensity with a slope of about 5 meV per  $10^{12}$  W/cm<sup>2</sup> for the  $[\text{Ne}]3s^23p^54s^1$  to  $[\text{Ne}]3s^23p^5$  transition driven by a laser at around 500 nm [11]. In our case, this would result in a shift of about 350 meV, which is in good agreement with the experimentally obtained values of the transitions near 104 nm shifted by about 2 nm. In highly excited states, electrons are even more affected by the driving laser field and the energy shift may be even comparable to the ponderomotive energy ( $U_p$ ) [31].

In our experiments, we could not precisely quantify the magnitude of the Stark shift due to a possible experimental error in the relative wavelength determination of the ALE features. Due to the different directional characteristics of HHG and ALE, a small deviation could result from the different illumination of the diffraction grating. The harmonics will follow the fundamental driving laser beam, whereas the ALE is isotropic. From the observed ALE feature at 104 nm

in Fig. 1(b) and the expected transition from  $[\text{Ne}]3s^23p^54s^1$  at 104.8 nm and 106.7 nm, we can estimate an upper limit of the error of around 2 nm. This size of error can occur when there is a misalignment of around 0.1 mm near the optical axis between the driving laser and the optical components.

After identifying the specific ALE features, we now discuss their dependence on the argon jet position with respect to the laser focus. The atomic transitions are incoherent single-atom processes and the phase difference between emitters does not play any role in ALE. Therefore, it is expected that ALE is most efficient where the excitation is strongest, namely, when the argon jet is placed directly in the laser focus. This simple consideration neglects the dynamic Stark effect, which can shift atomic levels into multiphoton resonance with the incident laser [11]. In contrast, HHG is based on the laser-induced atomic nonlinear polarization and the coherent superposition of the emitted waves from single atoms in the generation medium, i.e., the argon gas jet. As a result of the phase mismatch due to focusing, optical dispersion in the gas, and intrinsic atomic polarization phase shift, the optimized gas jet position is located slightly behind the laser focus [32,33]. In our experiments with sub- $\mu\text{J}$  pulse energy and tight-focusing geometry, the compensation of the Gouy phase of the focused laser beam by the neutral gas optical dispersion plays an important role [13,14]. As an estimation, the optimal condition for HHG is calculated by numerical simulation of the propagation of the laser-induced polarization and the electric field using the paraxial Helmholtz equation and Green's function method. We estimate an optimum position for the 11th harmonic at about 36  $\mu\text{m}$  behind the laser focus.

According to this value, together with the observed 30  $\mu\text{m}$  shift between the argon jet position for experiments shown in Figs. 2(a) and 2(b), we confirm that the optimum gas jet position for ALE is at the laser focus, as schematically shown in the inset beside Fig. 2(c). This is also consistent with our observation that there exists only one position for maximal ALE intensity when scanning the gas jet position along the laser propagation direction.

### V. SUMMARY

To summarize, we observe the coexistence of characteristic atomic line emission (ALE) and high-order harmonic generation (HHG) from argon excited by tightly focused sub- $\mu\text{J}$  laser pulses at 4 MHz repetition rate. By this, we provide a detailed study of HHG in a rare gas jet at the transition from multiphoton to tunnel ionization regimes ( $\gamma \approx 1$ ). The identified ALE features are assigned to transitions in neutral argon atoms from the optically excited  $3p^5 4s$  state and

higher excited states near the ionization threshold to the  $3p^6$  ground state. In addition, there are weak ALE features attributed to transitions in singly charged argon ions from the excited  $3p^4 4s^1$  or  $3p^4 3d^1$  states to the  $3p^5$  ground state. The simultaneously observed HHG spectra extend up to the 21st order with a photon energy of about 32 eV. Due to the phase-matching condition involved in HHG, the relative weighting of harmonics and atomic lines can be controlled by the gas jet positioning with respect to the incident laser focus. We demonstrate a straightforward way to identify and control the contributions of ALE relative to HHG by positioning the gas media relative to the laser focus, which could be important for the design of HHG experiments where the contribution of ALE should be minimized [5–8].

### ACKNOWLEDGMENTS

Technical support from R. Kulla, M. Kiel, and M. Schröder, as well as support and fruitful discussion with F. O. Schumann and J. Kirschner, are gratefully acknowledged.

- 
- [1] A. McPherson, G. Gibson, H. Jara, U. Johann, T. S. Luk, I. A. McIntyre, K. Boyer, and C. K. Rhodes, *J. Opt. Soc. Am. B* **4**, 595 (1987).
- [2] X. F. Li, A. L'Huillier, M. Ferray, L. A. Lompré, and G. Mainfray, *Phys. Rev. A* **39**, 5751 (1989).
- [3] F. Krausz and M. Ivanov, *Rev. Mod. Phys.* **81**, 163 (2009).
- [4] P. B. Corkum, *Phys. Rev. Lett.* **71**, 1994 (1993).
- [5] S. Kim, J. Jin, Y.-J. Kim, I.-Y. Park, Y. Kim, and S.-W. Kim, *Nature (London)* **453**, 757 (2008).
- [6] I.-Y. Park, S. Kim, J. Choi, D.-H. Lee, Y.-J. Kim, M. F. Kling, M. I. Stockman, and S.-W. Kim, *Nat. Photon.* **5**, 677 (2011).
- [7] M. Siviš, M. Duwe, B. Abel, and C. Ropers, *Nature (London)* **485**, E1 (2012).
- [8] M. Siviš, M. Duwe, B. Abel, and C. Ropers, *Nat. Phys.* **9**, 304 (2013).
- [9] E. Mevel, P. Breger, R. Trainham, G. Petite, P. Agostini, A. Migus, J.-P. Chambaret, and A. Antonetti, *Phys. Rev. Lett.* **70**, 406 (1993).
- [10] R. M. Potvliege and S. Vučič, *Phys. Rev. A* **74**, 023412 (2006).
- [11] P. Ackermann, H. Münch, and T. Halfmann, *Opt. Express* **20**, 13824 (2012).
- [12] L. V. Keldysh, *Zh. Eksp. Teor. Fiz.* **47**, 1945 (1965) [*JETP* **20**, 1307 (1965)].
- [13] F. Lindner, W. Stremme, M. G. Schätzel, F. Grasbon, G. G. Paulus, H. Walther, R. Hartmann, and L. Strüder, *Phys. Rev. A* **68**, 013814 (2003).
- [14] C. M. Heyl, J. Güdde, A. L'Huillier, and U. Höfer, *J. Phys. B* **45**, 074020 (2012).
- [15] F. J. Furch, S. Birkner, F. Kelkensberg, A. Giree, A. Anderson, C. P. Schulz, and M. J. J. Vrakking, *Opt. Express* **21**, 22671 (2013).
- [16] A. Thai, M. Hemmer, P. K. Bates, O. Chalus, and J. Biegert, *Opt. Lett.* **36**, 3918 (2011).
- [17] J. Boulet, Y. Zaouter, J. Limpert, S. Petit, Y. Mairesse, B. Fabre, J. Higuët, E. Mével, E. Constant, and E. Cormier, *Opt. Lett.* **34**, 1489 (2009).
- [18] A. Vernaleken, J. Weitenberg, T. Sartorius, P. Russbuedt, W. Schneider, S. L. Stebbings, M. F. Kling, P. Hommelhoff, H.-D. Hoffmann, R. Poprawe, F. Krausz, T. W. Hänsch, and T. Udem, *Opt. Lett.* **36**, 3428 (2011).
- [19] E. Seres, J. Seres, and C. Spielmann, *Opt. Express* **20**, 6185 (2012).
- [20] A. Cingöz, D. C. Yost, T. K. Allison, A. Ruehl, M. E. Fermann, I. Hartl, and J. Ye, *Nature (London)* **482**, 68 (2012).
- [21] I. Pupeza, S. H. amd T. Eidam, H. Carstens, D. E. aned J. Weitenberg, P. Rußbüldt, J. Rauschenberger, J. Limpert, T. Udem, A. Tünnermann, T. W. Hänsche, A. Apolonski, F. Krausz, and E. Fill, *Nat. Photon.* **7**, 608 (2013).
- [22] Femtsource scientific XL 650, Femtolasers Produktions GmbH, Vienna, Austria (2011).
- [23] D. Herriott and H. J. Schulte, *Appl. Opt.* **4**, 883 (1965).
- [24] C.-T. Chiang, A. Blättermann, M. Huth, J. Kirschner, and W. Widdra, *Appl. Phys. Lett.* **101**, 071116 (2012).
- [25] A. L'Huillier, M. Lewenstein, P. Salières, P. Balcou, M. Y. Ivanov, J. Larsson, and C. G. Wahlström, *Phys. Rev. A* **48**, R3433 (1993).
- [26] C. M. Heyl, J. Güdde, U. Höfer, and A. L'Huillier, *Phys. Rev. Lett.* **107**, 033903 (2011).
- [27] H. Beutler, *Z. Phys.* **93**, 177 (1935).
- [28] J. E. Sansonetti and W. C. Martin, *J. Phys. Chem. Ref. Data* **34**, 1559 (2005).
- [29] L. Minnhagen, *J. Opt. Soc. Am.* **63**, 1185 (1973).
- [30] L. Minnhagen, *J. Opt. Soc. Am.* **61**, 1257 (1971).
- [31] A. L'Huillier, L. A. Lompré, D. Normand, X. Tang, and P. Lambropoulos, *J. Opt. Soc. Am. B* **6**, 1790 (1989).
- [32] C. Winterfeldt, C. Spielmann, and G. Gerber, *Rev. Mod. Phys.* **80**, 117 (2008).
- [33] P. Balcou and A. L'Huillier, *Phys. Rev. A* **47**, 1447 (1993).

## Angle-Resolved Photoelectron Spectroscopy at Surfaces With High-Order Harmonic Generation

**C-T Chiang**, Martin-Luther-Universität Halle-Wittenberg, Halle, Germany; and Max-Planck-Institut für Mikrostrukturphysik, Halle, Germany

© 2018 Elsevier Inc. All rights reserved.

<b>Introduction</b>	<b>28</b>
<b>Experimental Development</b>	<b>28</b>
Overview	28
Photon Energy Range	29
Energy and Time Resolution	29
Photon Flux and Repetition Rate	30
Band Mapping	30
<b>Theory for Time-Dependent Photoemission Processes</b>	<b>31</b>
<b>Surfaces Investigated by HHG-Based PES</b>	<b>31</b>
Adsorbates	32
Two-Dimensional and Layered Materials	32
Metals	32
Semiconductors	33
Oxides and Strongly Correlated Materials	34
<b>Summary</b>	<b>34</b>
<b>Acknowledgments</b>	<b>34</b>
<b>References</b>	<b>35</b>
<b>Further Reading</b>	<b>38</b>

### Glossary

**High-order harmonic generation (HHG)** Production of high multiples of incident photon energy of a driving laser field, usually in the vacuum-ultraviolet range of the electromagnetic wave spectrum.

**Photoelectron spectroscopy (PES)** Spectroscopy of electrons ejected from a material due to an incident photon.

### Introduction

Photoelectron spectroscopy (PES) has provided fundamental information on physical and chemical properties at surfaces and interfaces.<sup>1,2</sup> Among the immense varieties of PES experiments, PES using high-order harmonic generation (HHG) as a light source allows spectroscopy in a laboratory with a widely tunable photon energy, variable polarization of light, and attosecond to femto-second time resolution. Therefore, HHG-based PES has been developed over more than two decades to study dynamical processes at surfaces and interfaces.<sup>3–5</sup> In this article we provide an overview of HHG-based PES experiments on surfaces and interfaces. In Section “**Experimental Development**” we outline the key ingredients of HHG-based PES setups, and in Section “**Theory for Time-Dependent Photoemission Processes**” a short reminder of theoretical concepts with emphasis on electron dynamics is given. In Section “**Surfaces Investigated by HHG-Based PES**” we summarize and discuss state-of-the-art HHG-based PES experiments. In order to keep this article compact and straightforward to understand, we are restricted to present limited amounts of aspects in the literature. For a possible incompleteness of our perspectives we apologize to the readers and would like to refer to materials in “**Further Reading**” for extended reading.

### Experimental Development

#### Overview

High-order harmonic generation (HHG) is a process to convert a number of low-energy photons to one high-energy photon in a strong laser electric field. It is not only most well known for experiments with gas media<sup>6–8</sup> but has also been extensively studied in solids<sup>9,10</sup> as well as at surfaces.<sup>11</sup> In a classical model of HHG in atoms, as illustrated in **Fig. 1**, a bound valence electron is ionized under the influence of a strong laser field from the distorted atomic potential by a tunneling process. This electron is then accelerated



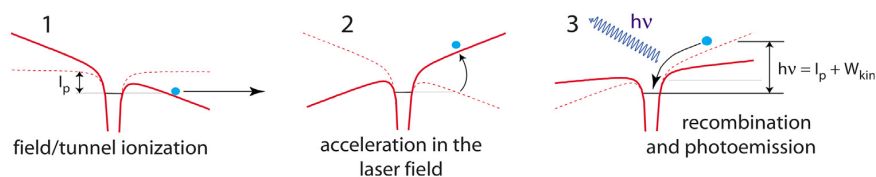


**Fig. 1** Three-step model for high-order harmonic generation (HHG) from atoms. Reprinted figure with permission from Winterfeldt, C.; Spielmann, C.; Gerber, G. Colloquium: optimal control of high-harmonic generation. *Rev. Mod. Phys.* **2008**, *80*, 117. Copyright (2017) by the American Physical Society.

in the laser electric field and recollides with its parent ion with a high kinetic energy ( $W_{\text{kin}}$ ).<sup>12,13</sup> The recollision can lead to emission of light with a photon energy ( $h\nu$ ) comparable to the sum of  $W_{\text{kin}}$  and the ionization potential ( $I_p$ ). Because  $W_{\text{kin}}$  can be high due to the ponderomotive acceleration in the laser field,  $h\nu$  can extend into the few keV regime.<sup>14–16</sup> The light generated from the single atom process in Fig. 1 adds up during its propagation in the medium<sup>17–20</sup> and is collected in far field with the corresponding vacuum-ultraviolet (VUV) optics for PES experiments.

A typical HHG setup consists of a generation chamber and a monochromator. For generation, setups with a free jet<sup>21,22</sup> or a fiber wave guide<sup>23,24</sup> are commonly employed. As a monochromator either a diffraction grating or band pass mirrors can be used, and they will be discussed in Sections “Photon Energy Range” and “Energy and Time Resolution.” In addition to laboratory setups, there are also large HHG user facilities available such as the existing Artemis<sup>25</sup> and the Extreme Light Infrastructure (ELI) in the future.<sup>26</sup>

### Photon Energy Range

HHG can provide photon energies beyond 1 keV.<sup>14–16</sup> For HHG-based PES experiments at surfaces as summarized in Fig. 2, lower photon energies from 10 to 100 eV have been used. The output photon energies from HHG depend on (1) the driven laser peak intensity, (2) the generation medium, as well as (3) the phase-matching conditions for the coherent sum of light emitted from single atoms. These dependencies have been thoroughly reviewed in the literature.<sup>7,8,11,27</sup> In addition, in HHG setups a metallic filter is usually used to block the driving laser field but allows the harmonics to transmit. An Al filter, for example, allows harmonics below 70 eV to pass through, whereas a Zr filter for harmonics above 70 eV.<sup>28,29</sup> These metallic filters limit the available photon energies in the PES experiments.

Moreover, in HHG-based PES experiments, a monochromator is often required for a reasonable energy resolution. Exceptions are time-resolved PES experiments using the reconstruction of attosecond beating by interference of two-photon transitions (RABBITT<sup>30–32</sup>), where an interference between photoexcitation by neighboring harmonics is required via an additional infrared excitation. Otherwise a monochromator, either consisting of gratings or dichroic mirrors, is used in HHG-based PES experiments. For a monochromator based on dichroic mirrors, only a fixed photon energy range can be selected.<sup>33–36</sup> In contrast, a grating monochromator allows experiments over a wide photon energy range and studies of a photon energy-dependent cross section of electronic states.<sup>37,38</sup>

### Energy and Time Resolution

Conventional electron spectrometers can have a high energy resolution better than few meV<sup>39–42</sup>; therefore the energy resolution in HHG-based PES experiments is mostly limited by the bandwidth of a single harmonic. In the very earlier experiments, Mathais et al. demonstrated an energy resolution of around 0.8 eV.<sup>43</sup> Nowadays the energy resolution has become better than 150 meV.<sup>44–46</sup> As an example, photoelectron spectra from the Shockley surface state on Cu(111) are compared in Fig. 3. With a HHG-based PES setup

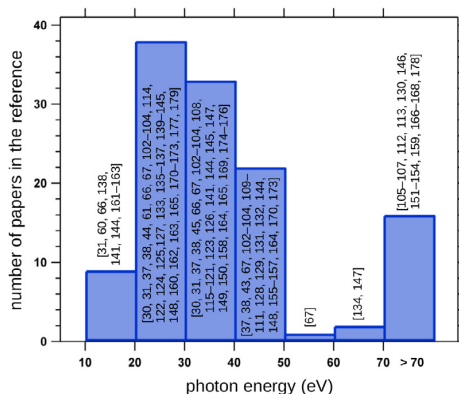


**Fig. 2** HHG-based PES experiments at surfaces sorted according to the applied photon energy. The numbers in References are indicated.

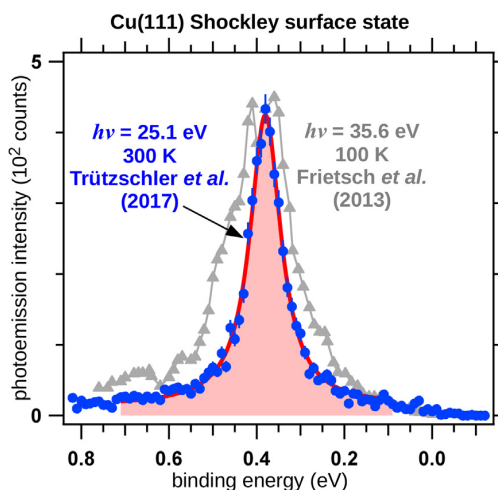


**Fig. 3** Photoelectron spectra from the Shockley surface state on Cu(111) at  $\bar{\Gamma}$ . *Blue* circles show spectrum from Trützscher et al. measured at a repetition rate of 0.7 MHz using a time-of-flight electron spectrometer.<sup>47</sup> The *red* curve shows a Lorentzian fit with a full-width-at-half-maximum (FWHM) of 86 meV. Provided that an intrinsic FWHM of 56 meV at 300 K is taken into account,<sup>48</sup> an upper bound of light band width of 65 meV is estimated. *Gray* triangles display the spectrum from Frietsch et al. measured at 100 K using HHG at 10 kHz and a hemispherical energy analyzer.<sup>45</sup> Due to the temperature dependence of the binding energy of the surface state,<sup>49</sup> their spectrum is shifted by +50 meV for comparison.

using a time-of-flight electron spectrometer, Trützscher et al. measured a linewidth of 86 meV. Taking the intrinsic linewidth at 300 K into account,<sup>48</sup> an upper bound of the light bandwidth of 65 meV can be estimated. The improvement in bandwidth can be clearly seen in comparison to an earlier work by Frietsch et al., where a 90-meV bandwidth of light at a higher photon energy was used.<sup>45</sup>

The temporal resolution in pump-probe HHG-based PES depends on several factors: (1) transform-limited bandwidth of the harmonics, (2) pulse stretching due to the monochromator, and (3) temporal broadening in focusing the harmonics onto the sample. A temporal width determined by factor (1) is about 18 fs for an energy bandwidth  $\Delta E$  of 100 meV for a single harmonic, and it scales reciprocally with  $\Delta E$ . Factor (2) is important for grating-based monochromators and has been intensively discussed in the literature.<sup>4,50–53</sup> This temporal broadening due to diffraction is proportional to the line density of the grating, but it can be compensated by a pair of identical gratings.<sup>54</sup>

Since the harmonics are usually focused by mirrors onto the sample in PES experiments, factor (3) can only have a significant influence for spherical mirrors due to the spherical aberration. For instance, a temporal broadening for a 3-mm beam diameter and a 25-mm focal length ( $f$ ) is 0.1 fs.<sup>55</sup> Because of its scaling with  $f^{-3}$ , this contribution should be negligible in practical HHG-based PES experiments with a long focal length of focusing mirrors. In addition to the temporal duration of the harmonics on the sample, the overall time resolution in the time-resolved pump-probe PES experiments includes the temporal overlap with the pump excitation (cross-correlation).

### Photon Flux and Repetition Rate

The photon flux as a function of the repetition rate of existing HHG light sources has been nicely reviewed in the literature.<sup>56–58</sup> In all optical experiments, the repetition rate of HHG can go beyond 100 MHz.<sup>59</sup> However, until now, repetition rates only up to 4 MHz have been used in static HHG-based PES experiments at surfaces.<sup>60</sup> Moreover, due to the requirement of a short, intense pump laser pulse in the pump-probe experiments, only a few hundred kilohertz repetition rates were demonstrated in time-resolved PES experiment.<sup>61</sup> Since the maximum number of photoelectrons generated from each HHG light pulse is limited by space charge effects,<sup>62,63</sup> there is still potential to increase the efficiency of HHG-based, time-resolved PES experiments by increasing the repetition rate into MHz range.<sup>64,65</sup> An overview for HHG-based PES at different repetition rates can be found in a previous publication.<sup>66</sup>

### Band Mapping

Due to the moderate bandwidth of harmonics, HHG-based PES has a lower energy and momentum resolution than conventional PES with discharge lamps or synchrotron radiation. Therefore, static band mapping using HHG-based PES is usually used only as a reference for time-resolved PES experiments where the momentum-resolved electron dynamics can be probed.

However, due to the widely tunable photon energy range, laboratory HHG-based PES allows to probe the crystal momentum perpendicular to the surface using photoexcitation transitions at different photon energies, which otherwise require synchrotron radiation. This has been utilized to distinguish a surface resonance on Pt(111) from bulk transitions.<sup>67</sup> Moreover, by selecting a specific photon energy, electronic states at a specific point in the three-dimensional (3D) Brillouin zone can be probed. This momentum selection is important for cases where the dynamics of excited electrons depends strongly on the 3D band dispersion of the final states.<sup>31</sup>

### Theory for Time-Dependent Photoemission Processes

The photoemission process has been formulated using diverse theoretical approaches in the literature. In view of several existing reviews,<sup>68–71</sup> only selected key ingredients will be discussed in the following. The photoemission intensity can be described in a simplified form<sup>69</sup>:

$$I(p_{surf}, s, E_f) \propto |\langle \Psi_f | \Delta | \Psi_i \rangle|^2 \delta(E_f^{total} - E_i^{total} - h\nu) \quad (1)$$

Here the quantum mechanical operator  $\Delta$  describes the interaction between the vector potential of the incident electromagnetic wave and the electron in solid via the single particle canonical momentum operator.  $p_{surf}$  is the momentum component of the photoelectron parallel to the surface, and  $s$  is its spin.  $\Psi_f$  and  $\Psi_i$  are the final and initial state wave functions of the whole system at energies  $E_f^{total}$  and  $E_i^{total}$ .  $\Psi_f$  includes the photoelectron in vacuum and the solid left behind with one photo-hole, whereas  $\Psi_i$  represents the system in the ground state before the photoexcitation.

If the lifetime of the photo-hole is neglected and the electrons in the solid are assumed to be independent from each other, Eq. (1) can be further simplified to a summation over all initial states of occupied single electron wave function and one electron final states that include the transport of the photoelectron away from the system.<sup>72</sup> For a realistic consideration on the transport, scattering processes have to be taken into account.<sup>73</sup> If the photoelectron and the rest of the system with a photo-hole is considered separately in the so-called sudden approximation,<sup>71,74,75</sup> the photoemission intensity can be rewritten as:

$$I(p_{surf}, s, E_f) \propto \sum_i |\langle \psi_f | \Delta | \psi_i \rangle|^2 A(E_i = E_f - h\nu) \quad (2)$$

Here  $A(E_i = E_f - h\nu)$  is the spectral function of the system with one photo-hole at the energy  $E_i$ . It describes the probability to create one photo-hole by the projection of the initial ground state of the whole system  $\Psi_i$  to the final state with one photo-hole. The summation  $i$  runs through all the occupied one-electron initial states  $\psi_i$ , and  $\psi_f$  is the one-electron final state at the energy  $E_f$ . By analyzing the photoelectron with the energy  $E_f$ , information regarding the system with one photo-hole as represented by  $A(E_i = E_f - h\nu)$  can be obtained.

In reality, the interaction between electrons in solids needs to be taken into account.<sup>76,77</sup> Furthermore, the time-dependent interaction between the photoelectron and the photo-hole as well as the lifetime of the photo-hole can have significant effects on the line shape of photoelectron spectra.<sup>78–80</sup> A more direct measurement of these dynamical processes is the time-resolved pump-probe PES experiments using high-order harmonics, whose theoretical description includes: (i) the macroscopic optical response of surfaces with the light field at the femtosecond time scale; (ii) the dynamics in the creation of the photoelectron; (iii) the microscopic time evolution of the system on the time scale of the photo-hole lifetime, within which the photoelectron can interact with the hole strongly; and (iv) the time-dependent propagation of the photoelectron away from the system. These aspects are summarized in Table 1, and a more thorough discussion can be found in the review by Pazourek et al.<sup>101</sup>

### Surfaces Investigated by HHG-Based PES

In the following sections, we summarize HHG-based PES experiments at surfaces in the literature and categorize them according to the systems investigated.

**Table 1** Overview of theoretical calculations for time-resolved PES

Theoretical description	Reference
Optical response at surfaces	81–85
Dynamics in the creation of photoelectrons	85–90
Photoelectron interacting with photo-hole/other electrons	88,90–95
Propagation of photoelectron	83–85,93,96–100

## 32 Angle-Resolved Photoelectron Spectroscopy at Surfaces With High-Order Harmonic Generation

**Table 2** Summary of HHG-based PES on adsorbate and molecular layers

Adsorbate system	Electronic state	Time scale (fs)	Reference
CO/Pt(111)	$1\pi$ , $4\sigma$ , $5\sigma$		37,102–104
I <sub>2</sub> /Cu	$ 4d_{3/2},  4d_{5/2}$		105
Iodo-phenylphenol/Si(100)	$ 4d_{3/2},  4d_{5/2}$	$0.5 \sim 5 \times 10^4$	106
Iodobenzoyloxy-functionalized resorc[4]arenes/Au/Ti/Si	$ 4d_{3/2},  4d_{5/2}$		107
In <sub>2</sub> S <sub>3</sub> /Ag/Si	$ 4d_{3/2},  4d_{5/2}$		108
O <sub>2</sub> /Pt(111)	$1\pi_g^*$	$550 \pm 140 \sim 5 \times 10^3$	109–111
O/Ni(111)	$0\ 2p$		103
W(CO) <sub>6</sub> /Si	$4\sigma$ , $4\pi$ , $5\sigma$		105
Xe/Pt(111)	Xe $4d$	$7.1 \pm 1.1$	112
Xe/Re(0001)	Xe $4d$ , Xe $5p$		113

**Adsorbates**

There are only a few adsorbate systems that have been studied by HHG-based PES (Table 2). Due to the high photon energies from HHG, photoelectrons in core levels of atoms and molecules can be excited. Therefore, photoelectrons from the adsorbates can be clearly identified apart from the substrate signals. Moreover, the energy of core levels depends sensitively on the environment, and the resultant chemical shifts provide information regarding the local structure at the surface. With pump–probe HHG-based PES, this information can be used to characterize optically excited relaxation pathways of surface chemistry on the femtosecond to picosecond time scales.<sup>106,109</sup>

**Two-Dimensional and Layered Materials**

The high photon energies from HHG also allow access to electronic states in the full Brillouin zone, in contrast to purely laser-based PES. Since the K points in the Brillouin zone of graphene are beyond the momentum range probed by PES using conventional ultraviolet laser sources, HHG-based time-resolved PES (tr-PES) gives a unique opportunity to study electron dynamics in graphene.<sup>114–120</sup> These studies are summarized in Table 3. Very similarly, HHG-based tr-PES allows to study electron dynamics at  $\Gamma$ , M, and K points in the Brillouin zone of other two-dimensional (2D) materials such as 1 T-TiSe<sub>2</sub> and 1 T-TaS<sub>2</sub>. These valuable investigations essentially elucidate different mechanisms behind the electronically driven metal-to-insulator phase transitions.<sup>127–129</sup> In Table 4 we summarize the HHG-based tr-PES experiments on these 2D materials.

**Metals**

With HHG-based tr-PES, even intriguing electron dynamics can be found in conventional metals. In Table 5 HHG-based PES studies on metals are summarized. By using the high photon energies of HHG, the attosecond time delays between photoemission processes from core and valence electrons in bulk Cu, Ni, and W<sup>30,31,159</sup> as well as in Mg/W(110) films<sup>151–153</sup> have been identified. The high photon energy makes it also possible to study spin dynamics of shallow core levels in rare earth ferromagnets Gd(0001) and Tb(0001). In these materials, it was discovered that the exchange splitting between electronic states can evolve transiently depending on their spatial localization and orbital angular momentum.<sup>149,150,158</sup>

**Table 3** Summary of HHG-based tr-PES on graphene

Graphene	Electronic state ( $h\nu_{pump}$ )	Time scale (fs)	Reference
$p$ -doped	$E_F$ near K (0.1 ~ 0.3 eV)	$135 \pm 35$	118
	$E_F$ near K (0.30 ~ 0.95 eV)	$13 \pm 4 \sim 860 \pm 50$	117
	$E_F$ near K (~0.95 eV)	$150 \sim 3 \times 10^3$	116,120,121
$n$ -doped	$E_F$ near K (~1.6 eV)	$25 \sim 2.8 \times 10^3$	114,115,119,122
	$E_F$ near K (0.1 ~ 0.4 eV)	$160 \sim 280$	123
	$E_F$ near K (1.6 eV)	$87 \sim 490$	114
Bilayer	$E_F$ near K (3.1 eV)	$\approx 400$	124
	$E_F$ near K (0.1 ~ 0.3 eV)	$150 \pm 20 \sim 2.8 \pm 0.6 \times 10^3$	118
	$E_F$ near K (0.8 eV)	$220 \pm 50 \sim 1.8 \pm 0.3 \times 10^3$	116
On Ni(111)	$E_F$ near K (1.6 eV)	$650 \sim 10^4$	125
	$\sigma$ , $\pi$ bands		38
	$E_F + 0.4 \sim 2$ eV		126

$h\nu_{pump}$ : excitation photon energy in an optical pump, HHG-probe experiment;  $E_F$ , Fermi level.

**Table 4** Summary of HHG-based tr-PES on two-dimensional (2D) materials besides graphene

System	Electronic state	Time scale (fs)	Reference
1 T-TiSe <sub>2</sub>	Se 3d <sub>3/2</sub> , Se 3d <sub>5/2</sub>	100~1.2 × 10 <sup>3</sup>	130
	Se 4p band	51 ± 15	44
	Se 4p band at M	20~110	127–129,131
	Ti 3d band	31 ± 3	44
	Ti 3d band near M	< 200	127
	Ti 3d band along ΓK	11 ± 10	132
	Ti 3d band along ΓM	81 ± 6	132
	VBM and CBM near M	70~7 × 10 <sup>3</sup>	133
	1 T-TaS <sub>2</sub>	Ta 4f <sub>7/2</sub>	460 ± 50~3 × 10 <sup>3</sup>
	Ta 5d bands near Γ	30 ± 300	135,136
	Ta 5d band at Γ (Mott gap)	< 20	128
	Ta 5d band near M (Peierls gap)	226 ± 38	128
Graphite	E <sub>F</sub> near H	100~10 <sup>4</sup>	137
1 T-TaSe <sub>2</sub>	Ta 5d bands	< 40~280	136
n-Doped Bi <sub>2</sub> Se <sub>3</sub>	Near CBM at Γ	160	138
MoS <sub>2</sub>	VBM, CBM along ΣK	~30	61
MoS <sub>2</sub> /Au(111)	VBM, CBM at K	50 ± 20	139
MoS <sub>2</sub> /graphene	VBM, CBM at K	40~5 × 10 <sup>4</sup>	140
2H-MoS <sub>2</sub>	VBM, CBM	1~3 × 10 <sup>3</sup>	141
WS <sub>2</sub> /Ag(111)	VBM, CBM near K	100 ± 50	142
2H-WSe <sub>2</sub>	VBM, CBM	0.1~1 × 10 <sup>4</sup>	141,143

VBM, valence band maximum; CBM, conduction band minimum; E<sub>F</sub>, Fermi level.

### Semiconductors

Electron dynamics in semiconductors has been studied since the 1980s using conventional tr-PES experiments with low photon energies. Nevertheless, these earlier experiments could only focus on the electronic states in the proximity of the band gap. With HHG-based PES, as one can clearly see in Table 6, shallow core levels at larger binding energies, such as the Ga and As 3d states, can be investigated, and it paves the way toward an element-specific identification of electron dynamics in compound semiconductors.<sup>164,168</sup>

**Table 5** Summary of HHG-based PES on metals

Metal	Electronic state	Time scale (fs)	Reference
Ag(001)	4d, 5sp bands		66,144
Ag(111)	4d PE delay	-0.2~0.2	145
Au(111)	5d PE delay	0~0.2	145
Au/Si(001)	Valence band	~0.07	146
Bi(001)	5d <sub>3/2</sub> , 5d <sub>5/2</sub>		147
Co/Cu(001)	Spin-resolved 3d		148
Cu(001)	3d space charge	1~2 × 10 <sup>6</sup>	148
Cu(111)	Shockley surface state		45,60
	3d, 4sp bands		43
	3d PE delay	-0.3~0.2	30
Gd/W(110)	Exchange-split Gd 5d	800 ± 100	149,150
	Magnetic dichroism at Gd 4f	14 ± 3 × 10 <sup>3</sup>	150
Mg/W(110)	Mg 2p versus conduction band PE delay	0~0.06	151,152
	Mg 2p versus W 4f PE delay	0.08~0.22	151
	Mg 2p versus plasmon satellite PE delay	0.06 ± 0.01	153
Ni(111)	3d bands		103
	3d Λ <sub>1</sub> versus Λ <sub>3</sub> PE delay	0~0.25	31
Pb	5d <sub>3/2</sub> , 5d <sub>5/2</sub>		108
Pt(110)	Near E <sub>F</sub>	< 100	154
Pt(111)	5d bands		37,67,102,103,112
	LAPE of PE from valence bands		155–157
	Near E <sub>F</sub>	260 ± 80	156
Tb/W(110)	Exchange-split Tb 5d	300~500	158
W(110)	4f <sub>3/2</sub> , 4f <sub>5/2</sub>		105
	4f versus conduction band PE delay	0.11 ± 0.07	159

PE, photoemission; LAPE, laser-assisted photoemission.



## 34 Angle-Resolved Photoelectron Spectroscopy at Surfaces With High-Order Harmonic Generation

**Table 6** Electron dynamics in semiconductors studied by HHG-based PES

Semiconductor	Electronic state	Time scale (fs)	Reference
10 nm Alq film	LUMO	$\sim 4 \times 10^5$	160
As-terminated Ge(111)	Unoccupied surface resonance at $\bar{M}$	$400 \sim 2 \times 10^3$	161
	As-derived surface state at $\bar{\Gamma}$	$1.5 \times 10^3 \sim 2 \times 10^5$	162,163
Ga(2 × 2)/Si(001)	Ga 3d	$\leq 1 \times 10^5$	164
GaAs(001)	Ga 3d, As 3d		105
	Valence band		165
p-doped GaAs(001)	Ga 3d	$\geq 1.5 \times 10^4, \leq 10^6$	166,167
	Ga 3d	$500 \sim 1.5 \times 10^4$	168
GaAs(110)	Ga 3d		108
Ge(110)	Valence band	$21 \pm 2 \times 10^3$	165
PCPDTBT polymer	$E_F - 0.2$ to $E_F + 2.3$ eV	$45 \sim 1.1 \pm 0.1 \times 10^3$	169

Alq, tris (8-hydroxy quinoline) aluminum; LUMO, lowest unoccupied molecular orbital.

**Table 7** Summary for HHG-based tr-PES on surfaces of oxides and strongly correlated materials

Oxide	Electronic state	Time scale (fs)	Reference
BaFe <sub>2</sub> As <sub>2</sub>	Near $E_F$	$60 \sim 1 \times 10^3$	170
Bi <sub>2</sub> Sr <sub>2</sub> CaCu <sub>2</sub> O <sub>8+<math>\delta</math></sub>	Nodal region	640	171
	Off-nodal region	150	171
	Antinodal region	$300 \sim 1.85 \times 10^3$	171
K <sub>0.3</sub> MO <sub>3</sub>	Near $E_F$	$0.6 \sim 1.3 \times 10^3$	172
HfO <sub>2</sub> /Si(001)	Near $E_F$	$\geq 2 \times 10^5$	173
$\alpha$ -SiO <sub>2</sub> (Quartz)	30 eV above CBM	$\sim 4 \times 10^4$	174,175
UO <sub>2</sub>	U 5f upper Hubbard band	$5 \sim 8 \times 10^3$	176
URu <sub>2</sub> Si <sub>2</sub>	Near $E_F$	20 ~ 301	177
VO <sub>2</sub> film	V 3p	~500	178
15 nm VO <sub>2</sub> /TiO <sub>2</sub> (001)	Near $E_F$	$3 \times 10^3$	179
20 nm WO <sub>3</sub> /Si(001)	Valence band	0.1	146

$E_F$ , Fermi level; CBM, conduction band minimum.

### Oxides and Strongly Correlated Materials

In strong contrast to the well-established studies on 2D materials, metals, and semiconductors, only few HHG-based tr-PES experiments have been realized on oxides as listed in Table 7. The superconducting electronic states in a high- $T_C$  superconductor Bi<sub>2</sub>Sr<sub>2</sub>CaCu<sub>2</sub>O<sub>8+ $\delta$</sub>  have been characterized in the time domain.<sup>171</sup> In addition, the strongly correlated oxide UO<sub>2</sub> was investigated, and the dynamics of correlated electrons in the Hubbard bands was revealed.<sup>176</sup>

### Summary

In this article we summarize the literature reporting photoelectron spectroscopy (PES) at surfaces using light sources that are based on high-order harmonic generation (HHG). These HHG-based PES experiments have established studies of surfaces dynamics and provide valuable information regarding relevant physical and chemical properties on the picosecond to femtosecond time scales. On the surfaces with adsorbates, or that of the two-dimensional materials, metals, semiconductors, and oxides, HHG-based PES reveals pathways of electronic excitation as well as relaxation, which can depend sensitively on the electron momentum coordinates. This information enables fundamental understanding of surfaces in the time domain, which in the future may pave a way toward ultrafast manipulation of the properties of solids at surfaces and interfaces.

### Acknowledgments

The author thanks K. Rossnagel, F. O. Schumann, A. Trützscher, M. Huth, and W. Widdra for critical reading of the manuscript. He also thanks A. Trützscher, M. Huth, and R. Kamrla for providing their PES data, as well as J. Kirschner and F. O. Schumann for supporting HHG-based coincidence PES. The stimulating ideas and long-term support from W. Widdra are gratefully acknowledged.

## References

- Siegbahn, K. Electron spectroscopy for chemical analysis (E.S.C.A.). *Phil. Trans. R. Soc. Lond. A: Math. Phys. Eng. Sci.* **1970**, *268*, 33–57.
- Bonzel, H.; Kleint, C. On the history of photoemission. *Prog. Surf. Sci.* **1995**, *49*, 107–153.
- Kolasinski, K. W. Surface photochemistry in the vacuum and extreme ultraviolet (VUV and XUV): high harmonic generation, H<sub>2</sub>O and O<sub>2</sub>. *J. Phys. Condens. Matter* **2006**, *18*, S1655.
- Bauer, M. Femtosecond ultraviolet photoelectron spectroscopy of ultrafast surface processes. *J. Phys. D: Appl. Phys.* **2005**, *38*, R253.
- Haight, R. Electron dynamics at surfaces. *Surf. Sci. Rep.* **1995**, *21*, 275–325.
- McPherson, A.; Gibson, G.; Jara, H.; et al. Studies of multiphoton production of vacuum-ultraviolet radiation in the rare gases. *J. Opt. Soc. Am. B* **1987**, *4*, 595–601.
- Winterfeldt, C.; Spielmann, C.; Gerber, G. Colloquium: optimal control of high-harmonic generation. *Rev. Mod. Phys.* **2008**, *80*, 117.
- Jaeglé, P. *Coherent Sources of XUV Radiation: Soft X-Ray Lasers and High-Order Harmonic Generation*, Springer: Berlin, Heidelberg Germany, 2006. ISBN 978-0-387-23007-8.
- Hohenleutner, M.; Langer, F.; Schubert, O.; et al. Real-time observation of interfering crystal electrons in high-harmonic generation. *Nature* **2015**, *523*, 572–575.
- Ghimire, S.; DiChiara, A. D.; Sistrunk, E.; et al. Observation of high-order harmonic generation in a bulk crystal. *Nat. Phys.* **2001**, *7*, 138–141.
- Teubner, U.; Gibbon, P. High-order harmonics from laser-irradiated plasma surfaces. *Rev. Mod. Phys.* **2009**, *81*, 445–479.
- Corkum, P. B. Plasma perspective on strong field multiphoton ionization. *Phys. Rev. Lett.* **1993**, *71*, 1994–1997.
- Lewenstein, M.; Balcou, P.; Ivanov, M. Y.; L'Huillier, A.; Corkum, P. Theory of high-harmonic generation by low-frequency laser fields. *Phys. Rev. A* **1994**, *49*, 2117–2132.
- Seres, E.; Seres, J.; Spielmann, C. X-ray absorption spectroscopy in the keV range with laser generated high harmonic radiation. *Appl. Phys. Lett.* **2006**, *89*, 181919.
- Seres, J.; Wobrauschek, P.; Strelli, C.; et al. Generation of coherent keV x-rays with intense femtosecond laser pulses. *New J. Phys.* **2006**, *8*, 251.
- Popmintchev, T.; Chen, M. C.; Popmintchev, D.; et al. Bright coherent ultrahigh harmonics in the keV x-ray regime from mid-infrared femtosecond lasers. *Science* **2012**, *336*, 1287–1291.
- Balcou, P.; L'Huillier, A. Phase-matching effects in strong-field harmonic generation. *Phys. Rev. A* **1993**, *47*, 1447–1459.
- Lewenstein, M.; Salières, P.; L'Huillier, A. Phase of the atomic polarization in high-order harmonic generation. *Phys. Rev. A* **1995**, *52*, 4747–4754.
- Kazamias, S.; Douillet, D.; Weihe, F.; et al. Global optimization of high harmonic generation. *Phys. Rev. Lett.* **2003**, *90*, 193901.
- Gaarde, M. B.; Tate, J. L.; Schafer, K. J. Macroscopic aspects of attosecond pulse generation. *J. Phys. B Atomic Mol. Phys.* **2008**, *41*, 132001.
- Li, X. F.; L'Huillier, A.; Ferray, M.; Lompré, L. A.; Mainfray, G. Multiple-harmonic generation in rare gases at high laser intensity. *Phys. Rev. A* **1989**, *39*, 5751–5761.
- Rothhardt, J.; Krebs, M.; Hdrich, S.; et al. Absorption-limited and phase-matched high harmonic generation in the tight focusing regime. *New J. Phys.* **2014**, *16*, 033022.
- Durfee, C. G.; Rundquist, A. R.; Backus, S.; et al. Phase matching of high-order harmonics in hollow waveguides. *Phys. Rev. Lett.* **1999**, *83*, 2187–2190.
- Rundquist, A.; Durfee, C. G.; Chang, Z.; et al. Phase-matched generation of coherent soft x-rays. *Science* **1998**, *280*, 1412–1415.
- Central Laser Facility, UK. <https://www.clf.stfc.ac.uk/Pages/Artemis.aspx>.
- ELI HHG beamline. <https://www.eli-beams.eu/en/research/x-ray-sources/high-order-harmonic-generation-hhg/> and Details of the ELI HHG beamline <https://www.eli-beams.eu/en/facility/experimental-halls/e1-material-and-biomolecular-applications/hhg-beam-line/>.
- Pfeifer, T.; Spielmann, C.; Gerber, G. Femtosecond x-ray science. *Rep. Prog. Phys.* **2006**, *69*, 443.
- Schultze, M.; Wirth, A.; Gruras, I.; et al. State-of-the-art attosecond metrology. *J. Electron Spectrosc. Relat. Phenom.* **2011**, *184*, 68–77.
- Chini, M.; Zhao, K.; Chang, Z. The generation, characterization and applications of broadband isolated attosecond pulses. *Nat. Photonics* **2014**, *8*, 178–186.
- Lucchini, M.; Castiglioni, L.; Kasmi, L.; et al. Light-matter interaction at surfaces in the spatiotemporal limit of macroscopic models. *Phys. Rev. Lett.* **2015**, *115*, 137401.
- Tao, Z.; Chen, C.; Szilvási, T.; et al. Direct time-domain observation of attosecond final-state lifetimes in photoemission from solids. *Science* **2016**, *353*, 62–67.
- Weber, S. J.; Manschwetus, B.; Billon, M.; et al. Flexible attosecond beamline for high harmonic spectroscopy and XUV/near-IR pump probe experiments requiring long acquisition times. *Rev. Sci. Instrum.* **2015**, *86*, 033108.
- Hofstetter, M.; Aquila, A.; Schultze, M.; et al. Lanthanum molybdenum multilayer mirrors for attosecond pulses between 80 and 130 eV. *New J. Phys.* **2011**, *13*, 063038.
- Suman, M.; Monaco, G.; Pelizzo, M. G.; Windt, D. L.; Nicolosi, P. Realization and characterization of an XUV multilayer coating for attosecond pulses. *Opt. Express* **2009**, *17*, 7922–7932.
- Kaiser, N.; Yulin, S.; Perske, M.; Feigl, T. High Performance EUV Multilayer. Proceeding SPIE 7101, Advances in Optical Thin Films III, 71010Z, 2008.
- Wonisch, A.; Neuhausler, U.; Kabachnik, N. M.; et al. Design, fabrication, and analysis of chirped multilayer mirrors for reflection of extreme-ultraviolet attosecond pulses. *Appl. Opt.* **2006**, *45*, 4147–4156.
- Haarlammer, T.; Golovin, A. V.; Zacharias, H. 1 $\pi$  resonance of CO on Pt(111) studied by angle-resolved ultraviolet photoelectron spectroscopy. *Phys. Rev. B* **2011**, *83*, 125435.
- Haarlammer, T.; Bignardi, L.; Winter, C.; et al. Final-state effects in photoemission experiments from graphene on Ni(111). *Eur. Phys. J. B* **2013**, *86*, 225.
- Hüfner, S. *Very high resolution photoelectron spectroscopy*, Springer: Berlin Heidelberg, Germany, 2007.
- Liu, G.; Wang, G.; Zhu, Y.; et al. Development of a vacuum ultraviolet laser-based angle-resolved photoemission system with a superhigh energy resolution better than 1 meV. *Rev. Sci. Instrum.* **2008**, *79*, 023105.
- Tamai, A.; Meevasana, W.; King, P. D. C.; et al. Spin-orbit splitting of the Shockley surface state on Cu(111). *Phys. Rev. B* **2013**, *87*, 075113.
- Yaji, K.; Harasawa, A.; Kuroda, K.; et al. High-resolution three-dimensional spin- and angle-resolved photoelectron spectrometer using vacuum ultraviolet laser light. *Rev. Sci. Instrum.* **2016**, *87*, 053111.
- Mathias, S.; Miaja-Avila, L.; Murnane, M. M.; et al. Angle-resolved photoemission spectroscopy with a femtosecond high harmonic light source using a two-dimensional imaging electron analyzer. *Rev. Sci. Instrum.* **2007**, *78*, 083105.
- Eich, S.; Stange, A.; Carr, A.; et al. Time- and angle-resolved photoemission spectroscopy with optimized high-harmonic pulses using frequency-doubled Ti:sapphire lasers. *J. Electron Spectrosc. Relat. Phenom.* **2014**, *195*, 231–236.
- Frietsch, B.; Carley, R.; Döbrich, K.; et al. A high-order harmonic generation apparatus for time- and angle-resolved photoelectron spectroscopy. *Rev. Sci. Instrum.* **2013**, *84*, 075106.
- Wernet, P.; Gaudin, J.; Godehusen, K.; Schwarzkopf, O.; Eberhardt, W. Femtosecond time-resolved photoelectron spectroscopy with a vacuum-ultraviolet photon source based on laser high-order harmonic generation. *Rev. Sci. Instrum.* **2011**, *82*, 063114.
- Trützscher, A. Photoemission und Doppelphotoemission an Metallen und Oxiden mittels Erzeugung hoher Harmonischer. PhD Thesis submitted to Martin-Luther-Universität Halle-Wittenberg, 2017.
- McDougall, B. A.; Balasubramanian, T.; Jensen, E. Phonon contribution to quasiparticle lifetimes in Cu measured by angle-resolved photoemission. *Phys. Rev. B* **1995**, *51*, 13891–13894.
- Paniago, R.; Matzdorf, R.; Meister, G.; Goldmann, A. Temperature dependence of Shockley-type surface energy bands on Cu(111), Ag(111) and Au(111). *Surf. Sci.* **1995**, *336*, 113–122.
- Nugent-Glandorf, L.; Scheer, M.; Samuels, D. A.; et al. A laser-based instrument for the study of ultrafast chemical dynamics by soft x-ray-probe photoelectron spectroscopy. *Rev. Sci. Instrum.* **2002**, *73*, 1875–1886.
- Frassetto, F.; Cacho, C.; Froud, C. A.; et al. Single-grating monochromator for extreme-ultraviolet ultrashort pulses. *Opt. Express* **2011**, *19*, 19169–19181.
- Poletto, L.; Miotti, P.; Frassetto, F.; et al. Double-configuration grating monochromator for extreme-ultraviolet ultrashort pulses. *Appl. Opt.* **2014**, *53*, 5879–5888.

## 36 Angle-Resolved Photoelectron Spectroscopy at Surfaces With High-Order Harmonic Generation

53. Ojeda, J.; Arrell, C. A.; Griji, J.; et al. Harmonium: a pulse preserving source of monochromatic extreme ultraviolet (30-110 eV) radiation for ultrafast photoelectron spectroscopy of liquids. *Struct. Dyn.* **2016**, *3*, 023602.
54. Igarashi, H.; Makida, A.; Ito, M.; Sekikawa, T. Pulse compression of phase-matched high harmonic pulses from a time-delay compensated monochromator. *Opt. Express* **2012**, *20*, 3725–3732.
55. Diels, J. C.; Rudolph, W., Eds.; *Ultrashort laser pulse phenomena, 2nd edition Edition*; Academic Press: Burlington, USA, 2006.
56. Heyl, C. M.; Arnold, C. L.; Couairon, A.; L'Huillier, A. Introduction to macroscopic power scaling principles for high-order harmonic generation. *J. Phys. B Atomic Mol. Phys.* **2017**, *50*, 013001.
57. Hädrich, S.; Rothardt, J.; Krebs, M.; et al. Single-pass high harmonic generation at high repetition rate and photon flux. *J. Phys. B Atomic Mol. Phys.* **2016**, *49*, 172002.
58. Emaury, F.; Diebold, A.; Saraceno, C. J.; Keller, U. Compact extreme ultraviolet source at megahertz pulse repetition rate with a low-noise ultrafast thin-disk laser oscillator. *Optica* **2015**, *2*, 980–984.
59. Jones, R. J.; Moll, K. D.; Thorpe, M. J.; Ye, J. Phase-coherent frequency combs in the vacuum ultraviolet via high-harmonic generation inside a femtosecond enhancement cavity. *Phys. Rev. Lett.* **2005**, *94*, 193201.
60. Chiang, C.-T.; Blättermann, A.; Huth, H.; et al. High-order harmonic generation at 4 MHz as a light source for time-of-flight photoemission spectroscopy. *Appl. Phys. Lett.* **2012**, *101*, 071116.
61. Wallauer, R.; Reimann, J.; Armbrust, N.; Güdde, J.; Höfer, U. Intervalley scattering in MoS<sub>2</sub> imaged by two-photon photoemission with a high-harmonic probe. *Appl. Phys. Lett.* **2016**, *109*, 162102.
62. Al-Obaidi, R.; Wilke, M.; Borgwardt, M.; et al. Ultrafast photoelectron spectroscopy of solutions: space-charge effect. *New J. Phys.* **2015**, *17*, 093016.
63. Oloff, L.-P.; Hanff, K.; Stange, A. Pump laser-induced space-charge effects in HHG-driven time- and angle-resolved photoelectron spectroscopy. *J. Appl. Phys.* **2016**, *119*, 225106.
64. Heyl, C. M.; Güdde, J.; L'Huillier, A.; Höfer, U. High-order harmonic generation with  $\mu\text{J}$  laser pulses at high repetition rates. *J. Phys. B Atomic Mol. Phys.* **2012**, *45*, 074020.
65. Puppini, M.; Deng, Y.; Prochnow, O.; et al. 500 KHz OPCPA delivering tunable sub-20 fs pulses with 15 W average power based on an all-ytterbium laser. *Opt. Express* **2015**, *23*, 1491–1497.
66. Chiang, C.-T.; Huth, M.; Trüttschler, A.; et al. Boosting laboratory photoelectron spectroscopy by megahertz high-order harmonics. *New J. Phys.* **2015**, *17*, 013035.
67. Tsilimis, G.; Fecher, G.; Braun, J.; Kutzner, J.; Zacharias, H. Observation of high-energy Pt(111) surface resonances excited by laser-generated XUV radiation. *Appl. Phys. A* **2004**, *78*, 177–181.
68. Smith, N. V. Photoemission properties of metals. *CRC Crit. Rev. Solid State Sci.* **1971**, *2*, 45–83.
69. Courths, R.; Hüfner, S. Photoemission experiments on copper. *Phys. Rep.* **1984**, *112*, 53.
70. Matzdorf, R. Investigation of line shapes and line intensities by high-resolution UV-photoemission spectroscopy some case studies on noble-metal surfaces. *Surf. Sci. Rep.* **1998**, *30*, 153–206.
71. Reinert, F.; Hüfner, S. Photoemission spectroscopy from early days to recent applications. *New J. Phys.* **2005**, *7*, 97.
72. Feibelman, P. J.; Eastman, D. E. Photoemission spectroscopy correspondence between quantum theory and experimental phenomenology. *Phys. Rev. B* **1974**, *10*, 4932–4947.
73. Pendry, J. B. Angular dependence of electron emission from surfaces. *J. Phys. C Solid State Phys.* **1975**, *8*, 2413.
74. Gadzuk, J. W. Many-body effects in photoemission. In *Photoemission and the electronic properties of surfaces*; Feuerbacher, B., Fitton, B., Willis, R. F., Eds.; John Wiley & Sons Ltd, 1981.
75. Hedin, L.; Lee, J. Sudden approximation in photoemission and beyond. *J. Electron Spectrosc. Relat. Phenom.* **2002**, *124*, 289–315.
76. Caroli, C.; Lederer-Rozenblatt, D.; Roulet, B.; Saint-James, D. Inelastic effects in photoemission: microscopic formulation and qualitative discussion. *Phys. Rev. B* **1973**, *8*, 4552–4569.
77. Wendin, G. *Breakdown of one-electron pictures in photoelectron spectra*, Springer: Berlin Heidelberg, Germany, 1981.
78. Doniach, S.; Sunjić, M. Many-electron singularity in x-ray photoemission and x-ray line spectra from metals. *J. Phys. C Solid State Phys.* **1970**, *3*, 285.
79. Gadzuk, J. W.; Sunjić, M. Excitation energy dependence of core-level x-ray-photoemission-spectra line shapes in metals. *Phys. Rev. B* **1975**, *12*, 524–530.
80. Hüfner, S.; Wertheim, G. K. Core-line asymmetries in the x-ray-photoemission spectra of metals. *Phys. Rev. B* **1975**, *11*, 678–683.
81. Borisov, A. G.; Sánchez-Portal, D.; Kazansky, A. K.; Echenique, P. M. Resonant and nonresonant processes in attosecond streaking from metals. *Phys. Rev. B* **2016**, *87*, 121110.
82. Borisov, A. G.; Echenique, P. M.; Kazansky, A. K. Attostreaking with metallic nano-objects. *New J. Phys.* **2012**, *14*, 023036.
83. Kazansky, A. K.; Echenique, P. M. One-electron model for the electronic response of metal surfaces to subfemtosecond photoexcitation. *Phys. Rev. Lett.* **2009**, *102*, 177401.
84. Liao, Q.; Thumm, U. Initial-state, mean-free-path, and skin-depth dependence of attosecond time-resolved IR-streaked XUV photoemission from single-crystalline magnesium. *Phys. Rev. A* **2014**, *89*, 033849.
85. Zhang, C.-H.; Thumm, U. Streaking and Wigner time delays in photoemission from atoms and surfaces. *Phys. Rev. A* **2011**, *84*, 033401.
86. Braun, J.; Rausch, R.; Potthoff, M.; Minár, J.; Ebert, H. One-step theory of pump-probe photoemission. *Phys. Rev. B* **2015**, *91*, 035119.
87. Lemell, C.; Tong, X.-M.; Krausz, F.; Burgdörfer, J. Electron emission from metal surfaces by ultrashort pulses: determination of the carrier-envelope phase. *Phys. Rev. Lett.* **2003**, *90*, 076403.
88. Freericks, J. K.; Krishnamurthy, H. R.; Pruschke, T. Theoretical description of time-resolved photoemission spectroscopy: application to pump-probe experiments. *Phys. Rev. Lett.* **2009**, *102*, 136401.
89. De Giovannini, U.; Brunetto, G.; Castro, A.; Walkenhorst, J.; Rubio, A. Simulating pump-probe photoelectron and absorption spectroscopy on the attosecond timescale with time-dependent density functional theory. *ChemPhysChem* **2013**, *14*, 1363–1376.
90. Pazourek, R.; Nagele, S.; Burgdörfer, J. Time-resolved photoemission on the attosecond scale: opportunities and challenges. *Faraday Discuss.* **2013**, *163*, 353–376.
91. Dahlström, J. M.; Carette, T.; Lindroth, E. Diagrammatic approach to attosecond delays in photoionization. *Phys. Rev. A* **2012**, *86*, 061402.
92. Baggesen, J. C.; Madsen, L. B. Secondary-electron cascade in attosecond photoelectron spectroscopy from metal. *Phys. Rev. A* **2009**, *80*, 030901.
93. Lemell, C.; Solleder, B.; Tökési, T.; Burgdörfer, J. Simulation of attosecond streaking of electrons emitted from a tungsten surface. *Phys. Rev. A* **2009**, *79*, 062901.
94. Matveev, O. P.; Shvaika, A. M.; Devereaux, T. P.; Freericks, J. K. Time-domain pumping a quantum-critical charge density wave ordered material. *Phys. Rev. B* **2016**, *94*, 115167.
95. Zhang, C.-H.; Thumm, U. Laser-assisted photoemission from adsorbate-covered metal surfaces: time-resolved core-hole relaxation dynamics from sideband profiles. *Phys. Rev. A* **2009**, *80*, 032902.
96. Krasovskii, E. E. Attosecond spectroscopy of solids: streaking phase shift due to lattice scattering. *Phys. Rev. B* **2011**, *84*, 195106.
97. Liao, Q.; Thumm, U. Attosecond time-resolved streaked photoemission from Mg-covered W(110) surfaces. *Phys. Rev. A* **2015**, *92*, 031401.
98. Liao, Q.; Thumm, U. Attosecond time-resolved photoelectron dispersion and photoemission time delays. *Phys. Rev. Lett.* **2014**, *112*, 023602.
99. Zhang, C.-H.; Thumm, U. Attosecond photoelectron spectroscopy of metal surfaces. *Phys. Rev. Lett.* **2009**, *102*, 123601.
100. Baggesen, J. C.; Madsen, L. B. Theory for time-resolved measurements of laser-induced electron emission from metal surfaces. *Phys. Rev. A* **2008**, *78*, 032903.
101. Pazourek, R.; Nagele, S.; Burgdörfer, J. Attosecond chronoscopy of photoemission. *Rev. Mod. Phys.* **2015**, *87*, 765–802.
102. Tsilimis, G.; Kutzner, J.; Zacharias, H. Photoemission study of clean and c(4x2)-2C0-covered Pt(111) using high-harmonic radiation. *Appl. Phys. A* **2003**, *76*, 743–749.

103. Tsilimis, G.; Benesch, C.; Kutzner, J.; Zacharias, H. Laser based soft-x-ray pulses for photoelectron spectroscopy of surfaces. *J. Opt. Soc. Am. B* **2003**, *20*, 246–253.
104. Tsilimis, G.; Kutzner, J.; Zacharias, H. Resonance in the  $1\pi$  photoemission cross-section of CO on Pt(111) measured by high harmonic radiation. *Surf. Sci.* **2003**, *528*, 171.
105. Drescher, M.; Siffalovic, P.; Spieweck, M.; Heinzmann, H. Applicability of monochromatized high harmonic extended ultraviolet radiation for inner-shell photoelectron spectroscopy. *J. Electron Spectrosc. Relat. Phenom.* **2002**, *127*, 103–108.
106. Dachraoui, H.; Michelswirth, M.; Siffalovic, P.; et al. Photoinduced reconfiguration cycle in a molecular adsorbate layer studied by femtosecond inner-shell photoelectron spectroscopy. *Phys. Rev. Lett.* **2011**, *106*, 107401.
107. Siffalovic, P.; Michelswirth, M.; Bartz, P.; et al. Large-scale homogeneous molecular templates for femtosecond time-resolved studies of the guest-host interaction. *J. Biotechnol.* **2004**, *112*, 139–149.
108. Haight, R.; Seidler, P. F. High resolution atomic core level spectroscopy with laser harmonics. *Appl. Phys. Lett.* **1994**, *65*, 517–519.
109. Bauer, M.; Lei, C.; Read, K.; et al. Direct observation of surface chemistry using ultrafast soft-x-ray pulses. *Phys. Rev. Lett.* **2001**, *87*, 025501.
110. Bauer, M.; Lei, C.; Tobey, R.; Murnane, M. M.; Kapteyn, H. C. Time-resolved UPS: a new experimental technique for the study of surface chemical reactions on femtosecond time-scales. *Surf. Sci.* **2003**, *532–535*, 1159–1165.
111. Lei, C.; Bauer, M.; Read, K.; et al. Hot-electron-driven charge transfer processes on  $O_2$ /Pt(111) surface probed by ultrafast extreme-ultraviolet pulses. *Phys. Rev. B* **2002**, *66*, 245420.
112. Miaja-Avila, L.; Saathoff, G.; Mathias, S.; et al. Direct measurement of core-level relaxation dynamics on a surface-adsorbate system. *Phys. Rev. Lett.* **2008**, *101*, 046101.
113. Magerl, E.; Neppi, S.; Cavalleri, A. L.; et al. A flexible apparatus for attosecond photoelectron spectroscopy of solids and surfaces. *Rev. Sci. Instrum.* **2011**, *82*, 063104.
114. Johannsen, J. C.; Ulstrup, S.; Crepaldi, A.; et al. Tunable carrier multiplication and cooling in graphene. *Nano Lett.* **2015**, *15*, 326–331.
115. Gierz, I.; Link, S.; Starke, U.; Cavalleri, A. Non-equilibrium Dirac carrier dynamics in graphene investigated with time- and angle-resolved photoemission spectroscopy. *Faraday Discuss.* **2014**, *171*, 311.
116. Gierz, I.; Mitrano, M.; Petersen, J. C.; et al. Population inversion in monolayer and bilayer graphene. *J. Phys. Condens. Matter* **2015**, *27*, 164204.
117. Gierz, I.; Petersen, J. C.; Mitrano, M.; et al. Snapshots of non-equilibrium Dirac carrier distributions in graphene. *Nat. Mater.* **2013**, *12*, 1119.
118. Gierz, I.; Mitrano, M.; Bromberger, H.; et al. Phonon-pump extreme-ultraviolet-photoemission probe in graphene: anomalous heating of Dirac carriers by lattice deformation. *Phys. Rev. Lett.* **2015**, *114*, 125503.
119. Gierz, I.; Calegari, F.; Aeschlimann, S.; et al. Tracking primary thermalization events in graphene with photoemission at extreme time scales. *Phys. Rev. Lett.* **2015**, *115*, 086803.
120. Johannsen, J. C.; Ulstrup, S.; Cilento, F.; et al. Direct view of hot carrier dynamics in graphene. *Phys. Rev. Lett.* **2013**, *111*, 027403.
121. Ulstrup, S.; Johannsen, J. C.; Crepaldi, A.; et al. Ultrafast electron dynamics in epitaxial graphene investigated with time- and angle-resolved photoemission spectroscopy. *J. Phys. Condens. Matter* **2015**, *27*, 164206.
122. Ulstrup, S.; Johannsen, J. C.; Cilento, F.; et al. Ramifications of optical pumping on the interpretation of time-resolved photoemission experiments on graphene. *J. Electron Spectrosc. Relat. Phenom.* **2015**, *200*, 340–346.
123. Pomarico, E.; Mitrano, M.; Bromberger, H.; et al. Enhanced electron-phonon coupling in graphene with periodically distorted lattice. *Phys. Rev. B* **2017**, *95*, 024304.
124. Someya, T.; Fukidome, H.; Ishida, Y. Observing hot carrier distribution in an n-type epitaxial graphene on a SiC substrate. *Appl. Phys. Lett.* **2014**, *104*, 161103.
125. Ulstrup, S.; Johannsen, J. C.; Cilento, F.; et al. Ultrafast dynamics of massive Dirac fermions in bilayer graphene. *Phys. Rev. Lett.* **2014**, *112*, 257401.
126. Bignardi, L.; Haarlammert, T.; Winter, C.; et al. Dual character of excited charge carriers in graphene on Ni(111). *Phys. Rev. B* **2014**, *89*, 075405.
127. Mathias, S.; Eich, S.; Urbancic, J.; et al. Self-amplified photo-induced gap quenching in a correlated electron material. *Nat. Commun.* **2016**, *7*, 12902.
128. Hellmann, S.; Rohwer, T.; Källäne, M.; et al. Time-domain classification of charge-density-wave insulators. *Nat. Commun.* **2012**, *3*, 1069.
129. Rohwer, T.; Hellmann, S.; Wiesenmayer, M.; et al. Collapse of long-range charge order tracked by time-resolved photoemission at high momenta. *Nature* **2011**, *471*, 490.
130. Dachraoui, H.; van der Laan, G.; Müller, N.; et al. Mapping spin-orbit activated interchannel coupling. *Europhys. Lett.* **2014**, *106*, 13001.
131. Rohde, G.; Rohwer, T.; Stange, A.; et al. Does the excitation wavelength affect the ultrafast quenching dynamics of the charge-density wave in 1 T-TaSe<sub>2</sub>? *J. Electron Spectrosc. Relat. Phenom.* **2014**, *195*, 244–248.
132. Rohde, T.; Rohwer, T.; Sohr, C.; et al. Tracking the relaxation pathway of photo-excited electrons in 1 T-TaSe<sub>2</sub>. *Eur. Phys. J. Spec. Topics* **2013**, *222*, 997–1004.
133. Monney, C.; Puppini, M.; Nicholson, C. W.; et al. Revealing the role of electrons and phonons in the ultrafast recovery of charge density wave correlations in 1 T-TaSe<sub>2</sub>. *Phys. Rev. B* **2016**, *94*, 165165.
134. Ishizaka, K.; Kiss, T.; Yamamoto, T.; et al. Femtosecond core-level photoemission spectroscopy on 1 T-TaS<sub>2</sub> using a 60-eV laser source. *Phys. Rev. B* **2011**, *83*, 081104.
135. Petersen, J. C.; Kaiser, S.; Dean, N.; et al. Clocking the melting transition of charge and lattice order in 1 T-TaS<sub>2</sub> with ultrafast extreme-ultraviolet angle-resolved photoemission spectroscopy. *Phys. Rev. Lett.* **2011**, *107*, 177402.
136. Sohr, C.; Stange, A.; Bauer, M.; Rosnagel, K. How fast can a Peierls-Mott insulator be melted? *Faraday Discuss.* **2014**, *171*, 243.
137. Stange, A.; Sohr, C.; Yang, L. X.; et al. Hot electron cooling in graphite: supercollision versus hot phonon decay. *Phys. Rev. B* **2015**, *92*, 184303.
138. Crepaldi, A.; Cilento, F.; Ressel, B.; et al. Evidence of reduced surface electron-phonon scattering in the conduction band of Bi<sub>2</sub>Se<sub>3</sub> by nonequilibrium ARPES. *Phys. Rev. B* **2013**, *88*, 121404.
139. Grubišić Čabo, A.; Miwa, J. A.; Grønberg, S. S.; et al. Observation of ultrafast free carrier dynamics in single layer MoS<sub>2</sub>. *Nano Lett.* **2015**, *15*, 5883–5887.
140. Ulstrup, S.; Čabo, A. G.; Miwa, J. A.; et al. Ultrafast band structure control of a two-dimensional heterostructure. *ACS Nano* **2016**, *10*, 6315–6322.
141. Rettenberger, A.; Leiderer, P.; Probst, M.; Haight, R. Ultrafast electron transport in layered semiconductors studied with femtosecond-laser photoemission. *Phys. Rev. B* **1997**, *56*, 12092–12095.
142. Ulstrup, S.; Čabo, A. G.; Biswas, D.; et al. Spin and valley control of free carriers in single-layer WS<sub>2</sub>. *Phys. Rev. B* **2017**, *95*, 041405.
143. Bertoni, R.; Nicholson, C. W.; Waldecker, L.; et al. Generation and evolution of spin-, valley-, and layer-polarized excited carriers in inversion-symmetric WSe<sub>2</sub>. *Phys. Rev. Lett.* **2016**, *117*, 277201.
144. Chiang, C.-T.; Huth, M.; Trützscher, A.; et al. Efficient and tunable high-order harmonic light sources for photoelectron spectroscopy at surfaces. *J. Electron Spectrosc. Relat. Phenom.* **2015**, *200*, 15–21.
145. Locher, R.; Castiglioni, L.; Lucchini, M. Energy-dependent photoemission delays from noble metal surfaces by attosecond interferometry. *Optica* **2015**, *2*, 405–410.
146. Okell, W. A.; Witting, T.; Fabris, D.; et al. Temporal broadening of attosecond photoelectron wavepackets from solid surfaces. *Optica* **2015**, *2*, 383–387.
147. Christensen, B.; Raarup, M.; Balling, P. Photoemission with high-order harmonics: a tool for time-resolved core-level spectroscopy. *Nucl. Instrum. Methods Phys. Res. A* **2010**, *615*, 114–126.
148. Plötzing, M.; Adam, R.; Weier, C.; et al. Spin-resolved photoelectron spectroscopy using femtosecond extreme ultraviolet light pulses from high-order harmonic generation. *Rev. Sci. Instrum.* **2016**, *87*, 043903.
149. Carley, R.; Döbrich, K.; Frietsch, B.; et al. Femtosecond laser excitation drives ferromagnetic gadolinium out of magnetic equilibrium. *Phys. Rev. Lett.* **2012**, *109*, 057401.
150. Frietsch, B.; Bowlan, J.; Carley, R.; et al. Disparate ultrafast dynamics of itinerant and localized magnetic moments in gadolinium metal. *Nat. Commun.* **2015**, *6*, 8262.
151. Neppi, S.; Ernstorfer, R.; Cavalleri, A. L. Direct observation of electron propagation and dielectric screening on the atomic length scale. *Nature* **2015**, *517*, 342.
152. Neppi, S.; Ernstorfer, R.; Bothschafter, E. M.; et al. Attosecond time-resolved photoemission from core and valence states of magnesium. *Phys. Rev. Lett.* **2012**, *109*, 087401.
153. Lemell, C.; Neppi, N.; Wachter, G.; et al. Real-time observation of collective excitations in photoemission. *Phys. Rev. B* **2015**, *91*, 241101.
154. Siffalovic, P.; Drescher, M.; Spieweck, M.; et al. Laser-based apparatus for extended ultraviolet femtosecond time-resolved photoemission spectroscopy. *Rev. Sci. Instrum.* **2011**, *72*, 30.

## 38 Angle-Resolved Photoelectron Spectroscopy at Surfaces With High-Order Harmonic Generation

155. Miaja-Avila, L.; Lei, C.; Aeschlimann, M.; et al. Laser-assisted photoelectric effect from surfaces. *Phys. Rev. Lett.* **2006**, *97*, 113604.
156. Saathoff, G.; Miaja-Avila, L.; Aeschlimann, M.; Murnane, M. M.; Kapteyn, H. C. Laser-assisted photoemission from surfaces. *Phys. Rev. A* **2008**, *77*, 022903.
157. Miaja-Avila, L.; Yin, J.; Backus, S.; et al. Ultrafast studies of electronic processes at surfaces using the laser-assisted photoelectric effect with long-wavelength dressing light. *Phys. Rev. A* **2009**, *79*, 030901.
158. Teichmann, M.; Frietsch, B.; Döbrich, K.; Carley, R.; Weinelt, M. Transient band structures in the ultrafast demagnetization of ferromagnetic gadolinium and terbium. *Phys. Rev. B* **2015**, *91*, 014425.
159. Cavalleri, A. L.; Müller, N.; Uphues, T. Attosecond spectroscopy in condensed matter. *Nature* **2007**, *449*, 1029.
160. Probst, M.; Haight, R. Unoccupied molecular orbital states of tris (8-hydroxy quinoline) aluminum: observation and dynamics. *Appl. Phys. Lett.* **1997**, *71*, 202–204.
161. Rettenberger, A.; Haight, R. Multivalley electron population dynamics on the Ge(111):As surface. *Phys. Rev. Lett.* **1996**, *76*, 1912–1915.
162. Haight, R.; Peale, D. R. Antibonding state on the Ge(111):As surface: spectroscopy and dynamics. *Phys. Rev. Lett.* **1993**, *70*, 3979–3982.
163. Rettenberger, A.; Haight, R. Electron spectroscopy and dynamics on the Ge(111):As 1x1 surface. *Surf. Sci.* **1998**, *414*, 197–208.
164. Melzer, A.; Kampa, D.; Wang, J.; Fauster, Th. Time-resolved photoemission at the Si(100)-Ga surface using a femtosecond higher-harmonic laser source. *Phys. Rev. B* **2009**, *80*, 205424.
165. Dakovski, G. L.; Li, Y.; Durakiewicz, T.; Rodriguez, G. Tunable ultrafast extreme ultraviolet source for time- and angle-resolved photoemission spectroscopy. *Rev. Sci. Instrum.* **2016**, *87*, 073108.
166. Oguri, K.; Tsunoi, T.; Kato, K.; et al. Dynamical observation of photo-dember effect on semi-insulating GaAs using femtosecond core-level photoelectron spectroscopy. *Appl. Phys. Express* **2015**, *8*, 022401.
167. Oguri, K.; Kato, K.; Nishikawa, T.; et al. Time-resolved surface photoelectron spectroscopy of photoexcited electron and hole dynamics on GaAs using 92 eV laser harmonic source. *Jpn. J. Appl. Phys.* **2012**, *51*, 072401.
168. Siffalovic, P.; Drescher, M.; Heinzmann, U. Femtosecond time-resolved core-level photoelectron spectroscopy tracking surface photovoltage transients on p-GaAs. *Europhys. Lett.* **2002**, *60*, 924.
169. Cappel, U. B.; Plogmaker, S.; Terschlusen, J. A.; et al. Electronic structure dynamics in a low bandgap polymer studied by time-resolved photoelectron spectroscopy. *Phys. Chem. Chem. Phys.* **2016**, *18*, 21921–21929.
170. Yang, L. X.; Rohde, G.; Rohwer, T.; et al. Ultrafast modulation of the chemical potential in BaFe<sub>2</sub>As<sub>2</sub> by coherent phonons. *Phys. Rev. Lett.* **2014**, *112*, 207001.
171. Dakovski, G. L.; Durakiewicz, T.; Zhu, J.-X.; et al. Quasiparticle dynamics across the full Brillouin zone of Bi<sub>2</sub>Sr<sub>2</sub>CaCu<sub>2</sub>O<sub>8+δ</sub> traced with ultrafast time and angle-resolved photoemission spectroscopy. *Struct. Dyn.* **2016**, *2*, 054501.
172. Liu, H. Y.; Gierz, I.; Petersen, J. C.; et al. Possible observation of parametrically amplified coherent phonons in K<sub>0.3</sub>MoO<sub>3</sub> using time-resolved extreme-ultraviolet angle-resolved photoemission spectroscopy. *Phys. Rev. B* **2013**, *88*, 045104.
173. Lim, D.; Haight, R. In situ photovoltage measurements using femtosecond pump-probe photoelectron spectroscopy and its application to metal-HfO<sub>2</sub>-Si structures. *J. Vacuum Sci. Technol. A: Vacuum Surf. Films* **2005**, *23*, 1698–1705.
174. Merdji, H.; Guizard, S.; Martin, P.; et al. Ultrafast electron relaxation measurements on α-SiO<sub>2</sub> using high-order harmonics generation. *Laser Part. Beams* **2000**, *18*, 489494.
175. Quéré, F.; Guizard, S.; Martin, P.; et al. Hot-electron relaxation in quartz using high-order harmonics. *Phys. Rev. B* **2000**, *61*, 9883–9886.
176. Gilbertson, S. M.; Durakiewicz, T.; Dakovski, G. L.; et al. Ultrafast photoemission spectroscopy of the uranium dioxide UO<sub>2</sub> Mott insulator: evidence for a robust energy gap structure. *Phys. Rev. Lett.* **2014**, *112*, 087402.
177. Dakovski, G. L.; Li, Y.; Gilbertson, S. M.; et al. Anomalous femtosecond quasiparticle dynamics of hidden order state in URu<sub>2</sub>Si<sub>2</sub>. *Phys. Rev. B* **2011**, *84*, 161103.
178. Dachraoui, H.; Müller, N.; Obermeier, G. Interplay between electronic correlations and coherent structural dynamics during the monoclinic insulator-to-rutile metal phase transition in VO<sub>2</sub>. *J. Phys. Condens. Matter* **2011**, *23*, 435402.
179. Yoshida, R.; Yamamoto, T.; Ishida, Y.; et al. Ultrafast photoinduced transition of an insulating VO<sub>2</sub> thin film into a nonrutile metallic state. *Phys. Rev. B* **2014**, *89*, 205114.

## Further Reading

- Haight, R.; Peale, D. R. Tunable photoemission with harmonics of subpicosecond lasers. *Rev. Sci. Instrum.* **1994**, *65*, 1853–1857.
- Yamamoto, T.; Ishida, Y.; Yoshida, R.; et al. Nonequilibrium electronic and phonon dynamics of Cu<sub>0.17</sub>Bi<sub>2</sub>Se<sub>3</sub> investigated by core-level and valence-band time-resolved photoemission spectroscopy. *Phys. Rev. B* **2015**, *92*, 121106.
- Schattke, W.; Van Hove, M. A. *Solid-State Photoemission and Related Methods: Theory and Experiment*, Wiley, 2003. ISBN 978-3-527-403349.
- Bovensiepen, U.; Petek, H.; Wolf, M. (Eds.). *Dynamics at Solid State Surfaces and Interfaces: Volume 1—Current Developments*. Wiley, ISBN: 978-3-527-633432, 2010.





## SiO<sub>2</sub>/Si(001) studied by time-resolved valence band photoemission at MHz repetition rates: Linear and nonlinear excitation of surface photovoltage

Robin Kamrla,<sup>1,2</sup> Andreas Trützschler,<sup>1,2</sup> Michael Huth,<sup>2</sup> Cheng-Tien Chiang,<sup>1,2,a)</sup>  
Frank O. Schumann,<sup>2</sup> and Wolf Widdra<sup>1,2,b)</sup>

<sup>1</sup>Institute of Physics, Martin-Luther-Universität Halle-Wittenberg, Von-Danckelmann-Platz 3, D-06120 Halle (Saale), Germany

<sup>2</sup>Max Planck Institute of Microstructure Physics, Weinberg 2, D-06120 Halle (Saale), Germany

(Received 19 November 2018; accepted 14 January 2019; published 1 February 2019)

The authors investigate the fluence and doping dependence of the surface photovoltage (SPV) shifts at SiO<sub>2</sub>/Si(001) interfaces by time-resolved photoelectron spectroscopy. Charge carriers are excited by pumping photon energies of  $h\nu_{\text{pump}} = 1.2$  and  $2.4$  eV and probed by high-order harmonics of  $h\nu_{\text{probe}} = 22.6$  eV at 0.2 and 0.7 MHz repetition rates. The authors observe SPV shifts of the non-bonding O<sub>2p</sub> state by 240 meV for SiO<sub>2</sub>/p-Si and by  $-140$  meV for SiO<sub>2</sub>/n-Si upon pumping with  $h\nu_{\text{pump}} = 1.2$  eV, and their decay rate is estimated from time-resolved measurements. Moreover, the authors observe a striking pumping fluence dependence of SPV at these interfaces, which indicates charge carrier generation by both linear and nonlinear optical excitations. *Published by the AVS.*  
<https://doi.org/10.1116/1.5082188>

### I. INTRODUCTION

Interface states and oxygen vacancies within the SiO<sub>2</sub> layer terminating a Si(001) substrate have been of great interest over the last decades due to their ability to trap charge carriers with a prolonged lifetime and the resultant speed limitations of microelectronics.<sup>1–5</sup> With fs light excitations, electron dynamics at these interfaces can be triggered by linear optical absorption, whereas at high excitation intensity, multiphoton processes can play an important role.<sup>6,7</sup>

With high-order harmonic generation (HHG) as an alternative light source to synchrotron radiation for time-resolved photoelectron spectroscopy (tr-PES), it is possible to resolve the dynamics of charge carrier excitation and recombination in the valence band of semiconductors and metals.<sup>8–14</sup> Since HHG-based tr-PES is sensitive to surfaces and interfaces, it is an ideal tool for studying charge dynamics at ultrathin semiconductor–insulator heterostructures under linear and nonlinear excitation conditions.<sup>15</sup> At the interface of these heterostructures, electron dynamics is associated with the time-dependent charge trapping and band bending upon optical pumping. As a result, the surface photovoltage (SPV) effect occurs and the energy levels of all electronic states undergo an electrostatic shift on a time scale ranging from several ps to few  $\mu\text{s}$ .<sup>5,8,10,16–27</sup>

Here, we report HHG-based tr-PES measurements of the SPV on SiO<sub>2</sub>/Si(001) driven by linear and nonlinear photoexcitation. We observe shifts of oxygen valence bands in SiO<sub>2</sub> pinned by the SPV at the interface. Moreover, we study its dependence on the doping of Si as well as the excitation density and photon energy. Our experiments reveal the important role of nonlinear optical excitations at semiconductor–insulator interfaces, which may provide insights for applications of nonlinear optoelectronic devices.

### II. EXPERIMENT

The experiments were driven by an ytterbium-fiber laser system (Impulse, Clark-MXR, Inc., USA), providing pulses of 1.2 eV photon energy at repetition rates between 0.2 and 1.0 MHz and an intensity full width at half maximum (FWHM) of 300 fs. By passing through a beamsplitter, the total output power was divided into pump and probe beam paths, which were overlapped on the sample in an ultrahigh vacuum chamber with a base pressure better than  $5 \times 10^{-10}$  mbar.

In the probe beam path, the laser output was used to drive HHG of vacuum-ultraviolet light between 14 and 42 eV.<sup>28,29</sup> To measure the valence band photoelectron spectra of SiO<sub>2</sub>/Si(001), the 19th harmonic at a photon energy of  $h\nu_{\text{probe}} = 22.6$  eV was selected via a toroidal diffraction grating and focused onto the sample. Due to the pulse front tilting at this diffraction geometry, we estimate the time resolution of the HHG beam to be about 2 ps.<sup>12</sup> To trigger SPV at the SiO<sub>2</sub>/Si(001) interface, we used pumping photon energies of  $h\nu_{\text{pump}} = 1.2$  or  $2.4$  eV. By varying the length of the pump beam path, time-resolved pump–probe measurements were performed at room temperature ( $T = 300$  K). The angle of incidence for pump and probe beams at the sample surface was  $-45^\circ$  and  $+45^\circ$ , respectively. Due to the  $90^\circ$  angle between pump and probe beams at the surface, the finite spatial beam size will impose a limit of temporal resolution due to the noncollinear geometry between the wave fronts. This aspect will be estimated later in Sec. III B. The photoelectrons were detected by a commercial time-of-flight spectrometer with  $\pm 15^\circ$  acceptance angle (Themis 1000, SPECS, Germany), which is aligned to the surface normal. The energy resolution of the experiments can be estimated by the band width of the high-order harmonics of around 70 meV.<sup>30</sup>

The *p*- and *n*-doped Si(001) samples with  $n_p = 2 \times 10^{15}$  cm<sup>-3</sup> boron and  $n_n = 5 \times 10^{15}$  cm<sup>-3</sup> phosphorus dopants were cleaned by Ar ion sputtering and heated up to 1100 K under UHV condition. The structure of the surfaces was

<sup>a)</sup>Electronic mail: cheng-tien.chiang@physik.uni-halle.de

<sup>b)</sup>Electronic mail: wolf.widdra@physik.uni-halle.de

checked by low energy electron diffraction, indicating a (2×1) surface reconstruction.<sup>31</sup> Furthermore, the stoichiometry of the surfaces was verified by Auger spectroscopy and x-ray photoelectron spectroscopy. Subsequently, the SiO<sub>2</sub>/*p*-Si and SiO<sub>2</sub>/*n*-Si interfaces were prepared by exposure to 100 L of oxygen at 900 K. According to previous studies by Pi *et al.*, this procedure results in 15 Å thick SiO<sub>2</sub> layers on top of the Si.<sup>32</sup>

The pump fluence absorbed by the sample was estimated from the measured pump power  $P$  and the two dimensional intensity profile of the pump beam. Since the spatial extent of the probe beam with  $d_{\text{FWHM}} = 60 \mu\text{m}$  is much smaller than the pump beam diameters of  $d_{\text{FWHM}} > 0.5 \text{ mm}$ , the absorbed pump fluence within the probed sample area is given by

$$\Phi = \frac{P}{f_{\text{Rep}} \cdot 2\pi\sigma_{\perp}\sigma_{\parallel}} \cdot (1 - R), \quad (1)$$

where  $f_{\text{Rep}}$  is the repetition rate,  $R$  is the reflectance, and  $\sigma = d_{\text{FWHM}}/\sqrt{8 \ln 2}$  is the standard deviation parallel ( $\sigma_{\parallel}$ ) and perpendicular ( $\sigma_{\perp}$ ) to the plane of incidence. For  $h\nu_{\text{pump}} = 1.2$  and  $2.4 \text{ eV}$ , we take the reflectance for *p*-polarized light at the 45° angle of incidence as  $R = 0.2$  and  $R = 0.3$ , respectively.<sup>33</sup>

### III. RESULTS

#### A. Doping dependence of SPV

Figure 1 shows the valence band photoelectron spectra in the energy range of the nonbonding O<sub>2p</sub> state of SiO<sub>2</sub> for *p*- and *n*-doped Si(001) measured with  $h\nu_{\text{probe}} = 22.6 \text{ eV}$  at a repetition rate of  $f_{\text{Rep}} = 0.7 \text{ MHz}$ .<sup>34</sup> Both samples are illuminated with  $h\nu_{\text{pump}} = 1.2 \text{ eV}$  at a fluence of  $71 \mu\text{J}/\text{cm}^2$  and probed at a delay of  $\Delta t = +350 \text{ ps}$ . Upon pumping, there is a clear shift of the spectra with its direction depending on the doping. For evaluation of the SPV shift, the spectra were fitted as indicated by the dotted curves. These fits correspond to the valence band edge positions of the O<sub>2p</sub> nonbonding states, and their shape is provided by numerical interpolation of the spectra without pumping as shown by the dotted curves for the gray data points in Figs. 1(a) and 1(b). The spectra measured with pumping (black) are fitted by these fit-curves with an additional energy shift as the fitting parameter. The analysis in Fig. 1 reveals an SPV shift of  $E_{\text{SPV}} = 240 \text{ meV}$  at SiO<sub>2</sub>/*p*-Si and  $-140 \text{ meV}$  at SiO<sub>2</sub>/*n*-Si. At this specific pumping fluence, the results are in quantitative agreement with previous studies at Si 2*p* core levels.<sup>25,35,36</sup>

#### B. Dependence of SPV on pump–probe delay

The observed  $E_{\text{SPV}}$  strongly depends on the time delay between the pump and probe excitations. For  $h\nu_{\text{pump}} = 1.2 \text{ eV}$  at  $f_{\text{Rep}} = 0.2 \text{ MHz}$  and  $h\nu_{\text{pump}} = 2.4 \text{ eV}$  at  $f_{\text{Rep}} = 0.7 \text{ MHz}$ , the measured  $E_{\text{SPV}}$  on SiO<sub>2</sub>/*p*-Si(001) is shown as a function of pump–probe delay in Figs. 2(a) and 2(b), respectively. Both datasets exhibit a monotonic increase of  $E_{\text{SPV}}$  at negative time delays  $\Delta t < 0$  followed by a plateau for  $\Delta t > 0$ . Due to the  $\pm 45^\circ$  angle of incidence and the pulse width

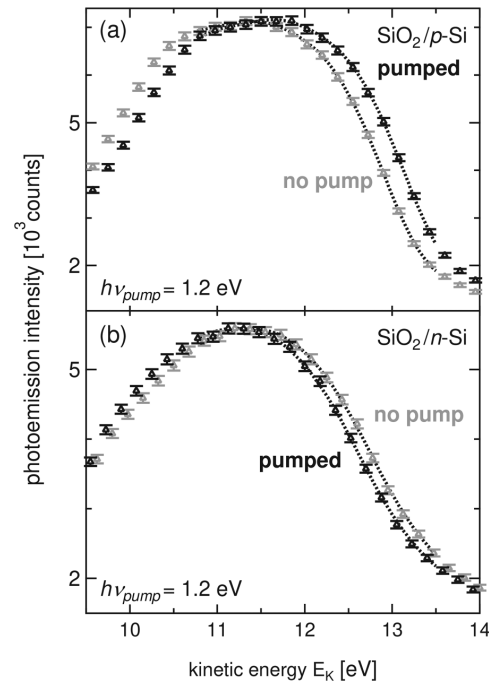


FIG. 1. Valence band photoelectron spectra of (a) SiO<sub>2</sub>/*p*-Si(001) and (b) SiO<sub>2</sub>/*n*-Si(001) with (black) and without (gray) pumping by  $h\nu_{\text{pump}} = 1.2 \text{ eV}$  at an absorbed fluence of  $71 \mu\text{J}/\text{cm}^2$ . The probe beam of  $h\nu_{\text{probe}} = 22.6 \text{ eV}$  was delayed from the pump by  $\Delta t = +350 \text{ ps}$ . Dotted curves show the fits for the quantitative evaluation of  $E_{\text{SPV}}$ .

of pump and probe beams, we can estimate a total time resolution of about 5 ps. Therefore, the slow increase at  $\Delta t < 0$  is not a result of limited time resolution as will be discussed below.

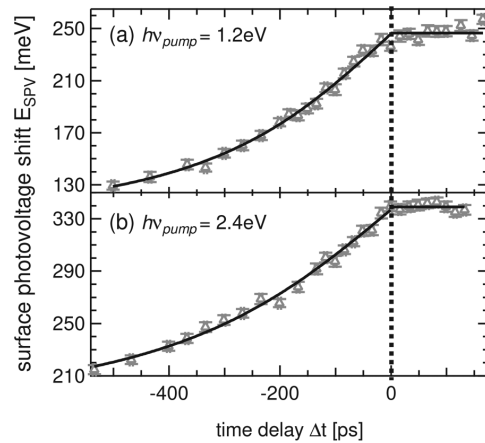


FIG. 2. Time dependence of the SPV at SiO<sub>2</sub>/*p*-Si(001) for excitation with (a)  $h\nu_{\text{pump}} = 1.2 \text{ eV}$  at a fluence of  $53 \mu\text{J}/\text{cm}^2$  and (b)  $h\nu_{\text{pump}} = 2.4 \text{ eV}$  at a fluence of  $2 \mu\text{J}/\text{cm}^2$ . Black curves at  $\Delta t < 0$  are fits according to Eq. (3) with  $E_{\text{max}} = 250 \text{ meV}$ ,  $E_{\text{min}} = 100 \text{ meV}$ ,  $r = 0.8 \text{ mm}$  in (a) and  $E_{\text{max}} = 340 \text{ meV}$ ,  $E_{\text{min}} = 180 \text{ meV}$ ,  $r = 0.9 \text{ mm}$  in (b), respectively.

The rise at negative delays can be explained in terms of a pump-induced dipole field at the surface of the sample.<sup>25</sup> This dipole field is generated by the SPV shift upon pumping, and its spatial extent depends on the pump beam radius  $r$ . The temporal change of the surface potential causes a time-varying electrostatic field that interacts with the photoelectrons that were already emitted into vacuum. The electrostatic field will accelerate or decelerate the photoelectrons according to Ref. 25

$$\Delta E_K(\Delta t) = E_{max} + (E_{max} - E_{min}) \cdot \frac{\Delta t}{\sqrt{r^2 + \Delta t^2}}, \quad (2)$$

where  $v$  is the velocity of the emitted photoelectrons.  $E_{min}$  and  $E_{max}$  represent the SPV before ( $\Delta t \rightarrow \infty$ ) and right at ( $\Delta t = 0$ ) the pump pulse. According to Eq. (2), the data in Figs. 2(a) and 2(b) for  $\Delta t < 0$  can be fitted as indicated by the black curves, using simplified circular pump beam diameters of  $r = 0.8$  and  $0.9$  mm, respectively. These values are in reasonable agreement with the measured FWHM of the pump beam Gaussian profile of  $0.6$  and  $0.7$  mm. The nearly constant  $E_{SPV}$  in Figs. 2(a) and 2(b) at positive delays  $\Delta t > 0$  is due to the low recombination rate of excited charge carriers on the  $\mu s$  time scale.<sup>36</sup>

### C. Intensity dependence of SPV

For pump photon energies of  $h\nu_{pump} = 1.2$  and  $2.4$  eV, the dependence of  $E_{SPV}$  on the pumping fluence is shown in Figs. 3(a) and 3(b), respectively. In both cases, various

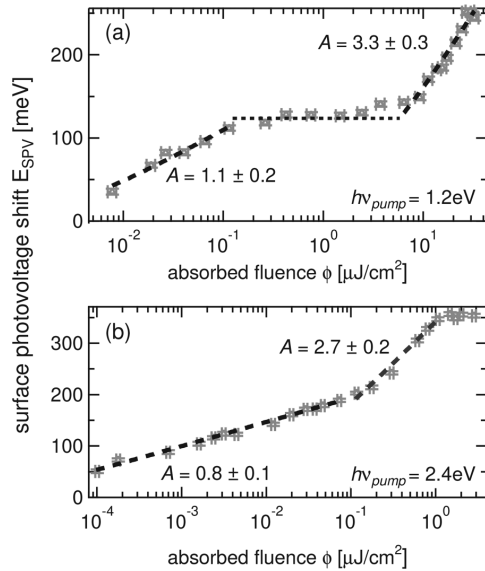


Fig. 3. Fluence dependence of  $E_{SPV}$  at SiO<sub>2</sub>/p-Si(001) for excitation with (a)  $h\nu_{pump} = 1.2$  eV at  $f_{rep} = 0.2$  MHz and (b)  $h\nu_{pump} = 2.4$  eV at  $f_{rep} = 0.7$  MHz. The probe beam is delayed by  $\Delta t = +150$  ps with respect to the pump. Black dashed curves are fits with Eq. (4). The horizontal dotted line in (a) marks the plateau at intermediate fluence.

regimes with linear dependences of  $E_{SPV}$  on  $\log(\Phi)$  having different slopes can be identified, as explained in the following in accordance with earlier studies.<sup>36,37</sup> Upon pumping, an additional charge carrier density  $\Delta p$  is induced in Si, resulting in a relative change of charge carrier density  $\Delta_p = \Delta p/n_p$  that is related to  $E_{SPV}$  at a limiting case of  $kT \ll E_{SPV} \ll V_0$  by<sup>37</sup>

$$\Delta_p = \frac{E_{SPV}}{kT} \cdot e^{E_{SPV}/kT} \cdot e^{-V_0/kT}, \quad (3)$$

where  $V_0$  is the equilibrium band bending and  $kT$  is the thermal energy at the sample temperature  $T$ . Due to the complicated dependence of  $\Delta_p$  on  $E_{SPV}$ ,  $E_{SPV}(\Delta_p)$  cannot be expressed analytically. Since  $kT \ll E_{SPV} \ll V_0$ , the linear term in Eq. (3) in front of the exponential functions can be neglected and  $E_{SPV}$  depends logarithmically on  $\Delta_p$ . By assuming the amount of excited charge carriers and a  $\Delta_p$  that has a power-law dependence on the absorbed pumping fluence  $\Phi$ ,<sup>38</sup>  $E_{SPV}(\Phi)$  can be approximated by<sup>36</sup>

$$E_{SPV}(\Phi) = AkT \cdot \ln(1 + B\Phi), \quad (4)$$

where  $A$  and  $B$  are fitting parameters. At low (high) excitation density, this formula ensures the linear (logarithmic) dependence of  $E_{SPV}$  on  $\Delta_p$  in Eq. (3).

The dashed lines in Fig. 3 are fits of  $E_{SPV}(\Phi)$  according to Eq. (4). For  $\Phi < 0.2 \mu J/cm^2$  at  $h\nu_{pump} = 1.2$  eV, the data in Fig. 3(a) can be well described with  $A = 1.1 \pm 0.2$  and  $B = 0.4 \pm 0.2 \text{ cm}^2/nJ$ , and for  $\Phi > 10 \mu J/cm^2$  with  $A = 3.3 \pm 0.3$  and  $B = 0.6 \pm 0.1 \text{ cm}^2/\mu J$ . In the intermediate fluence range,  $E_{SPV}$  stays nearly constant. In strong contrast,  $E_{SPV}$  triggered by  $h\nu_{pump} = 2.4$  eV in Fig. 3(b) only shows two regimes separated by  $\Phi = 0.1 \mu J/cm^2$  with  $A = 0.8 \pm 0.1$  ( $B = 120 \pm 30 \text{ cm}^2/nJ$ ) and  $A = 2.7 \pm 0.2$  ( $B = 120 \pm 40 \text{ cm}^2/\mu J$ ), which will be discussed in detail later. For  $\Phi$  above  $2 \mu J/cm^2$ , the  $E_{SPV}$  saturates at  $350$  meV and corresponds to a complete lifting of the band bending at the SiO<sub>2</sub>/p-Si(001) interface known as flat-band condition.<sup>25,35,36</sup>

## IV. DISCUSSION

### A. Doping dependence of SPV

The  $E_{SPV}$  on the  $p$ - and  $n$ -doped samples in Fig. 1 differs clearly in sign as well as in magnitude. This behavior can be explained according to previous experimental and theoretical studies on  $P_{b0}$  and  $P_{b1}$  states at the SiO<sub>2</sub>/Si interfaces.<sup>1-5</sup> These defect states result from Si dangling-bonds at the interface and are distributed in the lower and upper half of the Si bandgap, respectively.<sup>5</sup>

Following the analysis of Long *et al.* for time-resolved core level photoemission,<sup>37</sup> these interface states in the band gap of Si lead to a pinning of the Fermi level at the SiO<sub>2</sub>/Si interface. As a result, a space charge region is formed in Si near the interface, and bands are bent from the interior of Si toward the interface.<sup>39</sup> At  $300$  K, the Fermi level of bulk  $p$ - and  $n$ -Si is located approximately  $230$  meV above the valence band and  $230$  meV below the conduction band, respectively. Therefore, the Si bands at the SiO<sub>2</sub>/p-Si interface are bent toward lower energies and at SiO<sub>2</sub>/n-Si toward

higher energies. Upon illumination, photoexcited electron–hole pairs are generated and then separated within the space charge region.<sup>39</sup> Due to the band bending, the photoexcited minority charge carriers are accumulated at the interface whereas the majority charge carriers are accelerated into the bulk. This charge separation counteracts on the band bending and leads to a screening of the space charge potential by the photoexcited charge carriers. Finally, the band bending becomes lifted and the resultant electrostatic shift of the electronic states at the interface propagates into the SiO<sub>2</sub> overlayer. Because of this electrostatic shift of the electronic states in SiO<sub>2</sub>, the kinetic energies  $E_K$  of photoelectrons from the nonbonding O<sub>2p</sub> state are shifted to higher energies for SiO<sub>2</sub>/p-Si and to lower energies for SiO<sub>2</sub>/n-Si as displayed in Figs. 1(a) and 1(b), respectively. In addition, the differences in the magnitude of  $E_{SPV}$  for SiO<sub>2</sub>/p-Si and SiO<sub>2</sub>/n-Si can be related to an asymmetrically distributed interface state density, which has been pointed out by the work of Edwards.<sup>1</sup>

## B. Decay of SPV

Here, we discuss the quantitative evaluation of carrier decay time that can be extracted from the time-resolved SPV measurements in Fig. 2. Following the approach of Hecht,<sup>40</sup> the decay of  $E_{SPV}$  is governed by thermionic emission whose probability scales exponentially with  $E_{SPV}$  itself. This leads to a lifetime  $\tau$  depending on  $E_{SPV}$  as  $\tau(E_{SPV}) = \tau_\infty e^{-E_{SPV}/\alpha kT}$ .<sup>36,41</sup> In this formula,  $\tau_\infty$  describes the material dependent dark carrier lifetime and  $\alpha'$  is a phenomenological correction factor between 1 and 2, similar to the ideality factor of Schottky diodes.<sup>25,36,42,43</sup> By using  $\tau$ , a decay equation for  $\Delta_p$  can be formulated as

$$\frac{d\Delta_p(t)}{dt} = -\frac{\Delta_p(t)}{\tau(E_{SPV})} = -\frac{\Delta_p(t)}{\tau_\infty} \cdot e^{E_{SPV}/\alpha kT}. \quad (5)$$

In order to describe the time-resolved measurements in Sec. III B, the relation between  $\Delta_p$  and  $E_{SPV}$  in Eq. (3) is modified as

$$\Delta_p(E_{SPV}) = \frac{E_{SPV}}{\alpha kT} \cdot e^{E_{SPV}/\alpha kT} \cdot e^{-V_0/kT} \quad (6)$$

by adding a parameter  $\alpha$ , which plays a similar role as the fitting parameter  $A$  in Eq. (4). It has been shown in previous studies that one can describe the decay of  $E_{SPV}$  analytically by neglecting the linear term in Eq. (6) and formulate  $E_{SPV}(\Delta_p)$  similarly as in Eq. (4).<sup>36</sup> Here, we derive a solution of Eq. (5) with  $\alpha$  and  $\alpha'$  as independent parameters, since they may differ from each other and  $\alpha$  can be estimated from experiment similar to  $A$  in Eq. (4).

Assuming  $\Delta_p(E_{SPV})$  to be a continuous and monotonic function, one can derive a differential equation for the decay of  $E_{SPV}$  as

$$\frac{dE_{SPV}(t)}{dt} = \left( \frac{d\Delta_p(E_{SPV})}{dE_{SPV}} \right)^{-1} \cdot \frac{d\Delta_p(t)}{dt}. \quad (7)$$

Inserting the derivative of Eq. (6) with respect to  $E_{SPV}$  as well as the relation in Eq. (5) into Eq. (7), we arrive at

an analytical differential equation for the time dependence of  $E_{SPV}$

$$\frac{dE_{SPV}(t)}{dt} = -\frac{1}{\tau_\infty} \cdot \frac{E_{SPV}}{1 + E_{SPV}/\alpha kT} \cdot e^{E_{SPV}/\alpha kT}. \quad (8)$$

At a limiting case of  $E_{SPV} \gg \alpha kT$ , this differential equation can be solved as

$$E_{SPV}(t) = -\alpha' kT \cdot \ln \left( \frac{\alpha t}{\alpha' \tau_\infty} + e^{-E_{SPV,0}/\alpha kT} \right), \quad (9)$$

with a given initial condition  $E_{SPV}(t=0) = E_{SPV,0}$ .

From the measurements presented in Fig. 2, we find  $E_{SPV,0} = E_{max}$  at  $t=0$  and derive the value of SPV shift shortly before the subsequent laser pulse reaches the sample at  $t = f_{Rep}^{-1}$  as  $E_{SPV}(f_{Rep}^{-1}) \approx E_{min}$ . Inserting these conditions into Eq. (9),  $\tau_\infty$  can be expressed as

$$\tau_\infty = \alpha \cdot \left[ \alpha' f_{Rep} \cdot \left( e^{-E_{min}/\alpha kT} - e^{-E_{max}/\alpha kT} \right) \right]^{-1}. \quad (10)$$

In order to estimate  $\tau_\infty$  quantitatively from our experimental results, we assume  $\alpha = A$  for the measurements pumped by  $h\nu_{pump} = 1.2$  and 2.4 eV with  $A = 1.1$  and  $A = 0.8$ , respectively, which are extracted from Fig. 3 in the low fluence regime. The role of  $A$  at higher excitation densities will be discussed in Sec. IV C. In addition, we assume  $\alpha' = 2$  according to previous works,<sup>25,36</sup> and we obtain  $\tau_\infty = 18$  and 19  $\mu\text{s}$  for  $h\nu_{pump} = 1.2$  and 2.4 eV, respectively. These values are in agreement with time-resolved data measured by Shavorskiy *et al.*<sup>44</sup> on a 10 Å native oxide layer of  $\tau_\infty = 20 \mu\text{s}$  at  $E_{SPV,0} = 250$  meV. Using Eq. (9), we are also able to describe the time-dependent decay of  $E_{SPV}$  as measured on SiO<sub>2</sub>/p-Si by Bröcker *et al.*,<sup>36</sup> which is shown in Fig. 4. The fit to the experimental data leads to  $\tau_\infty \approx 19 \mu\text{s}$  in agreement with the data discussed above.

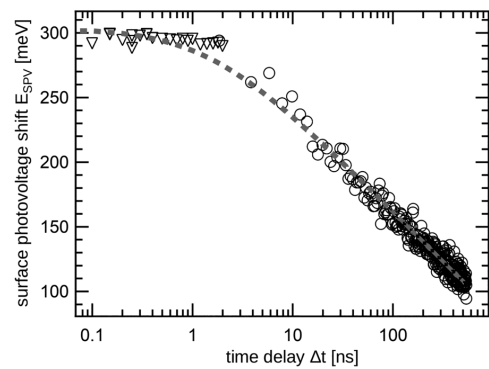


FIG. 4. Time dependence of the surface photovoltage  $E_{SPV}$  on pump–probe delay  $\Delta t$ . The gray dashed curve shows a fit according to Eq. (9) with  $E_{SPV,0} = 300$  meV,  $\alpha = 2$ ,  $\alpha' = 1.3$ , and  $\tau_\infty = 19 \mu\text{s}$ . Symbols are data for SiO<sub>2</sub>/p-Si(001) from Bröcker *et al.* (Ref. 36) with  $h\nu_{pump} = 2.3$  eV (data reproduced with permission from Ref. 36).

### C. Linear and nonlinear excitation of charge carriers

In order to explain the slopes of the fluence-dependent results in Fig. 3, we consider nonlinear absorption of  $m$  photons for photoexcitation of a single electron–hole pair, i.e.,  $\Delta_p \propto \Phi^m$ . Taking this nonlinear scaling explicitly into account, Eq. (3) can be approximated analogously to Eq. (4) as

$$E_{\text{SPV}}(\Phi) = m \cdot AkT \cdot \ln(1 + B\Phi). \quad (11)$$

Here, we assign the low fluence regimes of  $h\nu_{\text{pump}} = 1.2$  and 2.4 eV in Fig. 3 to linear excitation with one single photon ( $m = 1$ ) and the high fluence regime to nonlinear three-photon excitation with  $m = 3$ . In addition, we assume a constant  $A$  for different regimes. To describe the overall pump fluence dependence of SPV in Fig. 3, we estimate the pump-induced relative change of carrier density  $\Delta_p$  by the absorption length  $l_{\text{abs}}$  at  $h\nu_{\text{pump}}$  as<sup>36</sup>

$$\Delta_p = \frac{\gamma_1 \Phi + \gamma_3 \Phi^3}{n_p \cdot l_{\text{abs}} \cdot h\nu_{\text{pump}}}, \quad (12)$$

where  $n_p$  is the density of dopants and  $\gamma_1$  and  $\gamma_3$  are scaling factors corresponding to the cross section of linear and three-photon excitations.

In Fig. 5(a), the data from Fig. 3 are plotted versus  $\Delta_{p,\text{lin}}$  according to Eq. (12) with  $\gamma_3 = 0$  and  $\gamma_1 = 1$  for linear excitation. In comparison, the same data are shown in Fig. 5(b) according to Eq. (12) taking nonlinear excitation of charge carriers into account. For  $h\nu_{\text{pump}} = 1.2$  eV at low fluence, we assume  $\Delta_{p,\text{multi}} = \Delta_{p,\text{lin}}$ , because linear excitation dominates over the nonlinear one. Since  $E_{\text{SPV}}$  in Fig. 3(a) stays constant at intermediate fluence, we assume no further changes in  $\Delta_{p,\text{multi}}$  from linear charge carrier excitation whose origin will be explained later. At higher fluences for  $E_{\text{SPV},0} \geq 125$  meV,  $\Delta_{p,\text{multi}}$  is calculated from Eq. (12) by  $\gamma_1 = 0$  and  $\gamma_3 = 6.6 \cdot 10^{-4} \text{ cm}^4/\mu\text{J}^2$ . In Fig. 5(b) for  $h\nu_{\text{pump}} = 2.4$  eV, we use  $\gamma_1 = 1$  and  $\gamma_3 = 93 \text{ cm}^4/\mu\text{J}^2$ .

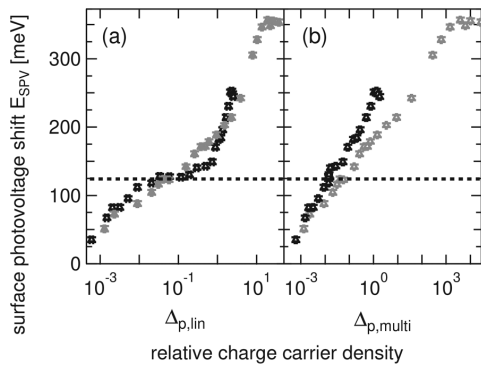


Fig. 5. Dependence of  $E_{\text{SPV}}$  at SiO<sub>2</sub>/p-Si(001) on the relative charge carrier density excited by linear and nonlinear optical absorption  $\Delta_{p,\text{lin}}$  (a) and  $\Delta_{p,\text{multi}}$  (b), respectively. Data points in black from Fig. 3(a) and in gray from Fig. 3(b) are scaled according to Eq. (12). The dashed horizontal line marks the plateau of  $E_{\text{SPV}} = 125$  meV for  $h\nu_{\text{pump}} = 1.2$  eV at intermediate excitation density.

As one can clearly see in Fig. 5(b), the SPV for both  $h\nu_{\text{pump}}$  is comparable when plotted as a function of  $\Delta_{p,\text{multi}}$ , indicating a well-defined general relation between the nonlinearly photoexcited carrier density and the SPV as formulated by Eq. (11).

For further analysis of the data shown in Fig. 5(a), the temporal relaxation of  $E_{\text{SPV}}$  discussed in Sec. IV B needs to be taken into account. Since the measurements with  $h\nu_{\text{pump}} = 1.2$  eV are performed at  $f_{\text{Rep}}^{-1} = 5 \mu\text{s}$ , at least five consecutive pumping pulses contribute to the measured SPV within the  $\tau_{\infty} \approx 20 \mu\text{s}$  that was derived before. Therefore, at  $\Delta_p \approx 0.2$ , the density of total excited charge carriers equals to the concentration of boron dopants within the Si bulk. As can be seen in Fig. 5(a), this estimated value lies within the plateau of  $E_{\text{SPV}}$ , and therefore we ascribe the nearly constant  $E_{\text{SPV}}$  for  $h\nu_{\text{pump}} = 1.2$  eV at the intermediate fluence to the complete excitation of all boron acceptor states. These states are located 45 meV above the Si valence band within the indirect bandgap  $E_{\text{gap}} = 1.15$  eV of Si. At room temperature, these states are occupied by electrons before the photoexcitation with  $h\nu_{\text{pump}} = 1.2$  eV.<sup>1</sup>

In the following, we will discuss the possible origin of the plateau. The boron acceptor states are localized in real space and consequently have a flat dispersion in the momentum space.<sup>45,46</sup> Therefore, optical excitation of electrons from the acceptor states into the conduction bands may not require phonons and could more efficiently generate charge carriers than the indirect transitions from the valence band to the conduction band of Si. However, due to the limited amount of dopants in Si, this contribution saturates at higher fluences when all electrons in the acceptor states are excited. Consequently,  $E_{\text{SPV}}$  does not further increase exponentially when  $\Delta_p$  is approaching 0.2. At much higher fluences for  $h\nu_{\text{pump}} = 1.2$  eV, the transition to  $m = 3$  is observed in Fig. 3. There, the three-photon energy of 3.6 eV is sufficient to trigger direct transitions from the valence to the conduction bands of Si across the direct bandgap of 3.4 eV.

## V. SUMMARY AND CONCLUSIONS

By using time-resolved photoelectron spectroscopy with a high-order harmonic light source working at megahertz repetition rates, we characterized the time, intensity, and doping dependence of surface photovoltage at the SiO<sub>2</sub>/Si(001) interface upon sub-bandgap and above bandgap photoexcitation. At the SiO<sub>2</sub>/p-Si interface, we observe an SPV shift of the nonbonding  $O_{2p}$  state of 240 meV toward higher energies upon illumination with  $h\nu_{\text{pump}} = 1.2$  eV, whereas at SiO<sub>2</sub>/n-Si, a shift of 140 meV toward lower energies is found. From the time-resolved measurements, we estimate the decay time of SPV at SiO<sub>2</sub>/p-Si of about 20  $\mu\text{s}$  for  $h\nu_{\text{pump}} = 1.2$  and 2.4 eV. Moreover, we observe the transition from linear to nonlinear excitations of SPV, which leads to distinctly different scaling of SPV on the pumping fluence. Whereas in the regime of low excitation density, linear photoexcitation of charge carriers dominates; at high fluences, nonlinear optical excitations can occur. Our observation emphasizes the importance of nonlinear photoexcitations at



SiO<sub>2</sub>/Si interfaces and may provide a deeper understanding of semiconductor–insulator heterostructures aiming at possible applications to nonlinear optoelectronic devices.

#### ACKNOWLEDGMENTS

The authors would like to gratefully acknowledge the valuable technical support from H. Menge, F. Helbig, F. Thiele, F. Weiß, and R. Kulla. This work is partially supported by the Deutsche Forschungsgemeinschaft through SFB 762 (B7, A3) and SFB/TRR 227 (A06).

- <sup>1</sup>A. H. Edwards, *Phys. Rev. B* **36**, 9638 (1987).  
<sup>2</sup>J. P. Campbell and P. M. Lenahan, *Appl. Phys. Lett.* **80**, 1945 (2002).  
<sup>3</sup>C. R. Helms and B. E. Deal, *The Physics and Chemistry of SiO<sub>2</sub> and the Si-SiO<sub>2</sub> Interface* (Plenum, New York, 1988).  
<sup>4</sup>E. Mehes and C. H. Patterson, *Phys. Rev. Mater.* **1**, 044602 (2017).  
<sup>5</sup>T. Tsuchiya and Y. Ono, *Jpn. J. Appl. Phys.* **54**, 04DC01 (2015).  
<sup>6</sup>T. Wang, N. Venkatram, J. Gosciniaik, Y. Cui, G. Qian, W. Ji, and D. T. H. Tan, *Opt. Express* **21**, 32192 (2013).  
<sup>7</sup>J. G. Mihaychuk, N. Shamir, and H. M. van Driel, *Phys. Rev. B* **59**, 2164 (1999).  
<sup>8</sup>P. Siffalovic, M. Drescher, and U. Heinzmann, *Europhys. Lett.* **60**, 924 (2002).  
<sup>9</sup>K. Oguri, K. Kato, T. Nishikawa, H. Gotoh, K. Tateno, T. Sogawa, and H. Nakano, *Jpn. J. Appl. Phys.* **51**, 072401 (2012).  
<sup>10</sup>K. Oguri, T. Tsunoi, K. Kato, H. Nakano, T. Nishikawa, K. Tateno, T. Sogawa, and H. Gotoh, *Appl. Phys. Express* **8**, 022401 (2015).  
<sup>11</sup>A. Melzer, D. Kampa, J. Wang, and T. Fauster, *Phys. Rev. B* **80**, 205424 (2009).  
<sup>12</sup>M. Bauer, *J. Phys. D Appl. Phys.* **38**, R253 (2005).  
<sup>13</sup>S. Hellmann *et al.*, *Nat. Commun.* **3**, 1069 (2012).  
<sup>14</sup>C. W. Nicholson, A. Lücke, W. G. Schmidt, M. Puppig, L. Rettig, R. Ermstorfer, and M. Wolf, *Science* **362**, 821 (2018).  
<sup>15</sup>J. V. Barth, G. Costantini, and K. Kern, *Nature* **437**, 671 (2005).  
<sup>16</sup>B. M. Marsh, M. E. Vaida, S. K. Cushing, B. R. Lamoureux, and S. R. Leone, *J. Phys. Chem. C* **121**, 21904 (2017).  
<sup>17</sup>B. F. Spencer *et al.*, *Faraday Discuss.* **171**, 275 (2014).  
<sup>18</sup>S. Grafström, *J. Appl. Phys.* **91**, 1717 (2002).  
<sup>19</sup>M. Moreno, M. Alonso, J. L. Sacedon, M. Hörické, R. Hey, K. Horn, and K. H. Ploog, *Phys. Rev. B* **61**, 16060 (2000).  
<sup>20</sup>M. H. Hecht, *Phys. Rev. B* **43**, 12102 (1991).  
<sup>21</sup>T. Watanabe, M. Hori, T. Tsuchiya, A. Fujiwara, and Y. Ono, *Jpn. J. Appl. Phys.* **56**, 011303 (2017).  
<sup>22</sup>M. Marsi *et al.*, *J. Electron. Spectrosc. Relat. Phenom.* **94**, 149 (1998).  
<sup>23</sup>C. Bandis and B. B. Pate, *Surf. Sci.* **345**, L23 (1996).  
<sup>24</sup>T. J. Šarapatka, *Surf. Sci.* **275**, 443 (1992).  
<sup>25</sup>W. Widdra *et al.*, *Surf. Sci.* **543**, 87 (2003).  
<sup>26</sup>R. Yukawa, S. Yamamoto, K. Akikubo, K. Takeuchi, K. Ozawa, H. Kumigashira, and I. Matsuda, *Adv. Mater. Interfaces* **3**, 1600527 (2016).  
<sup>27</sup>S. Tanaka, *J. Electron. Spectrosc. Relat. Phenomena* **185**, 152 (2012).  
<sup>28</sup>C.-T. Chiang, A. Blättermann, M. Huth, J. Kirschner, and W. Widdra, *Appl. Phys. Lett.* **101**, 071116 (2012).  
<sup>29</sup>C.-T. Chiang, M. Huth, A. Trüttschler, M. Kiel, F. Schumann, J. Kirschner, and W. Widdra, *New J. Phys.* **17**, 013035 (2015).  
<sup>30</sup>C.-T. Chiang, *Encyclopedia of Interfacial Chemistry*, edited by K. Wandelt (Elsevier, Oxford, 2018), pp. 28–38.  
<sup>31</sup>T. Tabata, T. Aruga, and Y. Murata, *Surf. Sci.* **179**, L63 (1987).  
<sup>32</sup>T.-W. Pi, J.-F. Wen, C.-P. Ouyang, R.-T. Wu, and G. Wertheim, *Surf. Sci.* **478**, L333 (2001).  
<sup>33</sup>M. A. Green, *Sol. Energy Mater. Sol. Cells* **92**, 1305 (2008).  
<sup>34</sup>F. G. Bell and L. Ley, *Phys. Rev. B* **37**, 8383 (1988).  
<sup>35</sup>M. Copuroglu, H. Sezen, R. L. Opila, and S. Suzer, *ACS Appl. Mater. Interfaces* **5**, 5875 (2013).  
<sup>36</sup>D. Bröcker, T. Gießel, and W. Widdra, *Chem. Phys.* **299**, 247 (2004).  
<sup>37</sup>J. P. Long, H. R. Sadeghi, J. C. Rife, and M. N. Kabler, *Phys. Rev. Lett.* **64**, 1158 (1990).  
<sup>38</sup>The corresponding power-law will be discussed in detail in Sec. IV B.  
<sup>39</sup>S. M. Sze and K. K. Ng, *Physics of Semiconductor Devices* (Wiley, New York, 2006).  
<sup>40</sup>M. H. Hecht, *Phys. Rev. B* **41**, 7918 (1990).  
<sup>41</sup>R. J. Hamers and D. G. Cahill, *J. Vac. Sci. Technol. B* **9**, 514 (1991).  
<sup>42</sup>W. Shockley and W. T. Read, *Phys. Rev.* **87**, 835 (1952).  
<sup>43</sup>M. A. Kroon and R. A. C. M. M. van Swaaij, *J. Appl. Phys.* **90**, 994 (2001).  
<sup>44</sup>A. Shavorskiy *et al.*, *Rev. Sci. Instrum.* **85**, 093102 (2014).  
<sup>45</sup>J. C. Inkson, *J. Phys. C Solid State Phys.* **14**, 1093 (1981).  
<sup>46</sup>D. M. Eagles, *J. Phys. Chem. Solids* **16**, 76 (1960).



## Electron pair emission detected by time-of-flight spectrometers: Recent progress

Michael Huth,<sup>1</sup> Cheng-Tien Chiang,<sup>1,2</sup> Andreas Trützscher,<sup>1,2</sup> Frank O. Schumann,<sup>1</sup> Jürgen Kirschner,<sup>1,2</sup> and Wolf Widdra<sup>2,1</sup>

<sup>1</sup>Max Planck Institute of Microstructure Physics, Weinberg 2, D-06120 Halle, Germany

<sup>2</sup>Institute of Physics, Martin-Luther-Universität Halle-Wittenberg, Von-Danckelmann-Platz 3, D-06120 Halle (Saale), Germany

(Received 11 December 2013; accepted 18 January 2014; published online 11 February 2014)

We present results for electron coincidence spectroscopy using two time-of-flight (ToF) spectrometers. Excited by electron impact, the energy and momentum distribution of electron pairs emitted from the Cu(111) surface are resolved and a spectral feature related to the Shockley surface state is identified. By combining the two ToF spectrometers with a high-order harmonic generation light source, we demonstrate double photoemission spectroscopy in the laboratory that required synchrotron radiation in the past. Utilizing this setup, we report results for  $(\gamma,2e)$  on NiO(001) on Ag(001) excited with light at 30 eV photon energy. © 2014 AIP Publishing LLC. [<http://dx.doi.org/10.1063/1.4864274>]

Electrons in a solid form an interacting many-particle system. This leads to the emergence of effects like superconductivity, metal-insulator transition, and long-range magnetic ordering.<sup>1,2</sup> Understanding the electron correlation in solids is a prerequisite for a complete description as well as the design of new functional materials.

The electron correlation can be literally divided into two parts. The first ingredient is that the wave function is antisymmetric with respect to exchange of the identical electrons with half-integer spin. The second component in the electron correlation originates from the Coulomb repulsion between electrons due to their charge. The combination of these two effects leads to a reduced probability of finding one electron in the vicinity of another one, which is termed as the exchange-correlation hole.<sup>3</sup> An exact description of a many-electron system has to include these ingredients and these have become the important topic for modern electron spectroscopy experiments.

Electron pair emission from surfaces can reveal directly the electron correlation. The emission of electron pairs upon the excitation by a single electron (e,2e) or a single photon  $(\gamma,2e)$  is only possible due to the existence of electron correlation.<sup>4</sup> Early experiments concentrated on atomic systems with few electrons like  $(\gamma,2e)$  from He and (e,2e) from H and showed characteristic energy and momentum distributions of the electron pairs.<sup>5-7</sup> Investigations with (e,2e) on solid systems started with the work of Kirschner *et al.* which showed that for a W(001) surface pair emission from valence electrons exists.<sup>8</sup> Later, Herrmann *et al.* reported first experiments on  $(\gamma,2e)$  from metal surfaces which revealed that the electrons in a pair are emitted with a preference for unequal energies.<sup>9</sup> In these reports, the energy distribution of electron pairs is characterized in detail, whereas the momentum degrees of freedom were not fully explored.

In this Letter, we present momentum-resolved experiments for (e,2e) from Cu(111) valence states and for  $(\gamma,2e)$  from NiO(001) using a laboratory time-of-flight coincidence spectroscopy. For  $(\gamma,2e)$  coincidence spectroscopy on solids, a pulsed light source with photon energies higher than 20 eV

is required and here we used a high repetition rate high-harmonic generation source in the laboratory.<sup>10</sup> Cu(111) is particularly interesting due to the formation of an electronic state near the surface with a parabolic dispersion. This Shockley surface state is one of the few systems where theoretical calculations for pair emission are available.<sup>11,12</sup> NiO is a 3d transition metal oxide and while theories using *local density approximation* can successfully describe electronic properties of metals they fail to describe NiO properly. The description can be improved by the introduction of an *U* parameter to treat electron correlation more refined. Thus, for NiO, a stronger correlation between localized *d*-electrons is expected. The emission of electron pairs from the 3d-bands by excitation with a single photon carries information about the correlation between the electrons.

The experiments were performed in an ultra high vacuum chamber with a base pressure below  $5 \times 10^{-10}$  millibar. The Cu(111) metal surface for the (e,2e)-experiment was prepared with Ar<sup>+</sup> ion sputtering and annealing up to 800 K. The chamber is equipped with two time-of-flight spectrometers (Themis 1000, SPECS<sup>13</sup>) in coplanar geometry inclined by  $\pm 45^\circ$  with respect to the sample normal. Each spectrometer has an acceptance angle of  $\pm 15^\circ$ . The detectors consist of a chevron mounted microchannel plate stack (MCP) from which the time-of-flight signal is retrieved and (x,y)-delay lines (Surface Concept) that allow to obtain the two-dimensional electron arrival position. The delay lines collect the electron cloud leaving the MCP and the charge flows to both ends of the anode. The difference of the arrival time at the ends of the anodes determines the hit position. Thus, the in-plane components of the momentum in any direction and the energy of the electrons are obtained. In the center between the spectrometers, the excitation source is mounted. Our signal processing is performed differently as compared to a typical time-of-flight photoemission spectroscopy setup that uses time-to-digital converters. The amplified time-of-flight signals are further processed to filter the coincident events on both detectors. They are fed to constant fraction discriminators for signal shaping and then to an AND logic unit that triggers data

acquisition when the time-of-flight signals arrive within a time interval of 100 ns. This logic triggers data acquisition only if coincident hits occurred. Data acquisition is carried out by a 12 channel digitizer (Aquiris DC282 ASbus2). The device samples synchronously at 2 GS/s all time-of-flight signals, the start time signal from the excitation source and both delay line detector signals. The sampled waveforms of the delay line pulses are evaluated with a dynamic threshold peak detection algorithm to calculate the hit position. The determination of the hit position is twice as successful as compared to a conventional time-to-digital converter with a fixed threshold due to the higher sensitivity. To retrieve momentum and energy of electrons, the software SIMION was used to calculate the electron trajectories in the spectrometer. This provides the conversion matrix for transformation of arrival location and time  $(x, y, t)$  to  $(k_x, k_y, E)$ . In coincidence, both spectrometers analyze the three dimensional coordinates of each detected electron of the acquired electron pair.

For coincidence spectroscopy from valence states, a ToF spectrometer setting with a wide energy range is favorable because it allows to investigate the energy sharing between the electrons in a pair. A lens setting with wide energy range and acceptance angle has a high transmission which is crucial for a reasonable high detection efficiency. Such setting is comparable to a high pass energy mode of a hemispherical analyzer that reduces energy resolution. Also the performance of a ToF spectrometer depends not only on the lens setting but also on an accurate model for the conversion from the hit coordinates  $(x, y, t)$  to  $(k_x, k_y, E)$ . For a reliable measurement, a precise calibration of the spectrometers for the anticipated operation mode is required. To obtain the resolution of the instrument, the excitation pulse length should be at least in the range of the time resolution of the MCP that is about 150 ps. Due to the lack of the availability of short-pulsed electron or light sources in the energy range between 25 eV and 50 eV, there were no reference data for the spectrometer performance available from the manufacturer. Here, we used the single-bunch mode at the BESSY II synchrotron radiation facility (beamline UE112-PGM1) to calibrate the angular and energy resolution of the spectrometers. As a reference feature, we analyzed photoelectrons from the Shockley surface state on a clean Cu(111) surface with a well defined dispersion.<sup>14</sup> With a photon energy of 17 eV, the ToF spectrometers could be set to identical settings as for coincidence measurements for valence bands. The inset in Fig. 1 shows the parallel momentum distribution of the Shockley surface state within an energy interval between  $E_F$  and  $E_F - 0.1$  eV. We obtained with our coincidence spectroscopy setup in a wide energy window from 6 eV to 18 eV a momentum and energy resolution of  $\Delta k_{\parallel} = 0.01 \text{ \AA}^{-1}$  and  $\Delta E = 180 \text{ meV}$ , respectively. A wide energy window results in a smaller ToF dispersion, therefore, these values are not representative of the ultimate resolution of the instrument. For the application of high-resolution photoemission, it has been shown that the spectrometer reaches an energy resolution better than  $4.7 \text{ meV}$ .<sup>13</sup>

After the calibration of our instrument, we performed coincidence spectroscopy in the laboratory. For excitation, a pulsed low energy electron gun (Kimball EGPS-1022C) was used that was driven by a pulse generator (HP 8131A) for

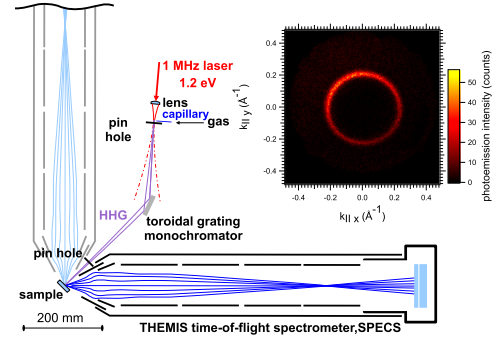


FIG. 1. Sketch of the experimental setup. The two ToF spectrometers are aligned coplanar  $\pm 45^\circ$  with respect to the sample normal. Here, for  $(\gamma, 2e)$ , the HHG light source is driven by a 1040 nm laser that is focused in a gas jet. The generated high-order harmonics passes through a monochromator for photon energy selection. Inset: Parallel momentum distribution of photoelectrons from the Shockley surface state as calibration of the ToF spectrometers.

electron pulses with 2 ns length at a repetition rate of 1 MHz. A primary electron energy ( $E_p$ ) of 27 eV was chosen and one expects the onset of emission at  $E_{sum} = E_p - \phi = 22.1 \text{ eV}$  with a work function  $\phi = 4.9 \text{ eV}$ . Hence, we chose a spectrometer setting with a wide energy range from 6 eV to 18 eV for each ToF. The primary flux was adjusted to give a count rate lower than 3000 counts/s on a single detector that results in a coincidence intensity of 2 counts/s. In Fig. 2, the energy distribution of the emitted electron pairs is displayed. The axes are the energies of individual electrons in a pair indicated as  $E_{left}$  and  $E_{right}$ . The sum energy of an electron pair is  $E_{sum} = E_{left} + E_{right}$  which is constant parallel to the dashed diagonal line in the plot. Three diagonal features at different  $E_{sum}$  and an onset in intensity indicated by the dashed lines can be distinguished. The onset corresponds to the maximum energy that an electron pair can have due to energy conservation which is located at  $E_{sum}^{max} = E_p - \phi$ , with  $E_p$  being the primary energy and  $\phi$  being the work function for a single electron. Events with higher energies are

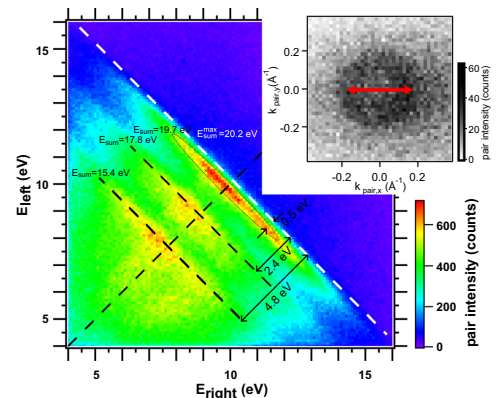


FIG. 2. 2D energy distribution obtained with  $E_p = 27 \text{ eV}$  on Cu(111). The dashed white line marks the onset of pair emission. Three features emerge at 0.5, 2.4, and 4.8 eV below the onset. The inset shows the parallel momentum distribution for pairs between  $E_{sum}^{max}$  and  $E_{sum}^{max} - 200 \text{ meV}$ . The corresponding state is marked with the dashed ellipse in the energy distribution.

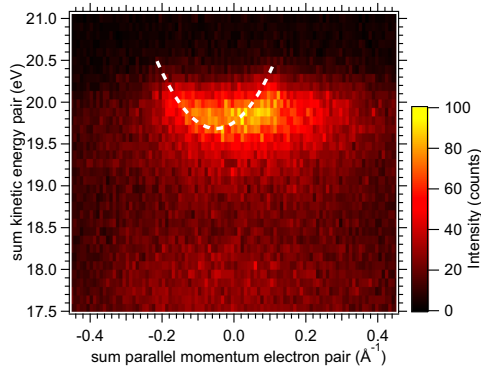
061602-3 Huth *et al.*Appl. Phys. Lett. **104**, 061602 (2014)

FIG. 3. Sum energy vs. sum momentum in  $k_x$  with  $\Delta k_y = 0.06 \text{ \AA}^{-1}$ . Directly below the emission onset, a feature with parabolic dispersion appears. The offset to zero in  $k_x$  is due to a small sample misalignment.

accidental coincidences where excitations from two or more primary electrons occur. Three intensity peaks can be distinguished at pair energies 0.5, 2.4, and 4.8 eV below  $E_{sum}^{max}$ . The intensity distribution shows a maximum if the energies of the electrons in a pair are equal. Our observation is in good agreement with results from Schumann *et al.* for (e,2e) on Cu(111) excited with 29.2 eV primary electrons where also three intensity peaks were observed.<sup>15,16</sup> It was concluded that a theoretical framework of (e,2e) on Cu(111) starting from an effective single-particle description of the valence states is a satisfactory description. The reproduction of this result proves that the instrument is capable of coincidence spectroscopy. With our energy resolution, we could also resolve the energy-momentum dispersion of these three features. While the states at 2.4 eV and 4.8 eV below  $E_{sum}^{max}$  appear flat, the feature 0.5 eV below the onset shows a parabolic dispersion as displayed in the sum energy ( $E_{sum}$ ) versus sum momentum ( $k_{sum,x}$ ) plot in Fig. 3. It has a similar shape and size as the well-known Shockley surface state. From theoretical calculations of Giebels *et al.* for (e,2e) on a single surface layer of Cu(111) with emission at a fixed angle of  $30^\circ$  and excited by electrons with 30 eV energy, three intensity peaks are expected at 0.5 eV, 2.5 eV, and 5.2 eV below the onset.<sup>11</sup> Thus, our results with a slightly different geometry and excitation energy reveal the predicted features qualitatively. Moreover, we were also able to resolve the parallel momentum distribution of the electron pairs. The momentum distribution of the pairs can be plotted as  $k_{sum,x}$  vs.  $k_{sum,y}$  with  $k_{sum} = k_{left} + k_{right}$ . The inset in Fig. 2 shows the two-dimensional momentum distribution of electron pairs for energies between  $E_{sum}^{max}$  and  $E_{sum}^{max} - 200 \text{ meV}$ , which shows a circular intensity distribution with an estimated radius of  $k_{\parallel} = 0.15 \text{ \AA}^{-1}$ .

For the ( $\gamma$ ,2e) experiment, we used a compact high-order harmonic generation (HHG) laboratory source for pulsed excitation with vacuum ultraviolet. The setup was described previously.<sup>10</sup> However, here we use alternatively an all-fiber-based laser (Clark-MXR Impulse) that delivers pulses at 1.2 eV with 200 fs pulse width and up to 14  $\mu\text{J}$  pulse energy. These pulses are focused in a 4 bar Ar or Xe gas jet in a vacuum chamber to generate light pulses with energies

between 13 eV and 45 eV. After the generation process, a toroidal monochromator allows to select the photon energy for excitation. The monochromator chamber has entry and exit pin holes that work as slits and allow differential pumping towards the photoemission chamber. The bandwidth of the generated light pulses is 150 meV and the repetition rate can be tuned between 200 kHz and 25 MHz.

In the past, only synchrotron radiation sources operated in single-bunch mode could provide pulsed light with sufficient high repetition rate. However, coincidence experiments require long acquisition times and beamtime at synchrotron radiation sources is limited. From this aspect, this HHG light source allows ToF-based ( $\gamma$ ,2e) spectroscopy in the laboratory. It is not suited for coincidence spectroscopy with hemispherical analyzers where for efficient spectroscopy the source repetition rate has to be in the range of the flight time dispersion of the electrons in the pair which is in the range of 10 ns. Therefore, a HHG light source with a repetition rate greater than 100 MHz would be required.<sup>15,17,18</sup> Here, we utilized the light source in combination with the ToF spectrometers to investigate ( $\gamma$ ,2e) from NiO(001). On a Ag(001) crystal, 15 monolayer thick NiO(001) films were prepared by evaporation of Ni in an  $\text{O}_2$  atmosphere of  $1 \times 10^{-6}$  millibar for 10 min.<sup>19</sup> The surface cleanliness and ordering were checked by Auger electron spectroscopy and low energy electron diffraction. The pulsed HHG light source was set to a photon energy of 30 eV,  $p$ -polarized, and at a repetition

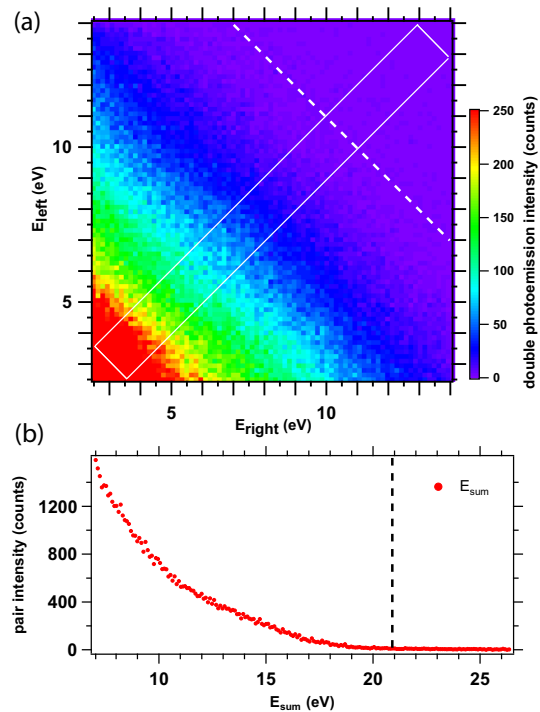


FIG. 4. (a) 2D energy distribution obtained with  $h\nu = 30 \text{ eV}$  on NiO(001). The diagonal dashed line marks the expected onset of pair emission. The intensity does not reproduce that but increases slowly towards lower pair energies. Also no preference for a specific energy sharing can be distinguished. (b) Intensity depending on  $E_{sum}$  along the white rectangle in (a).

rate of 1 MHz. The light intensity was tuned so that the count rate on a single detector was about 1000 counts/s. The coincidence count rate was 0.2 counts/s. The two dimensional energy distribution of the electron pairs is presented in Fig. 4. As for (e,2e), the axes are the energies of the single electrons  $E_{left}$  and  $E_{right}$  and parallel to the dashed diagonal line is the sum energy constant. From sum energies of 7 to 21 eV, the intensity monotonically decreases as shown by the line profile in Fig. 4. This is in strong contrast to the (e,2e) case from Cu(111) where an onset of intensity was observed. At a fixed sum energy, the intensity is constant independent of how the energy is shared between the two single electrons. The maximum sum energy for ( $\gamma$ ,2e) that an emitted pair can have is approximately  $E_{sum}^{max} = h\nu - 2\phi$  which is indicated by the dashed line. In addition, the energy of the pair is shared uniformly between the two single electrons. To understand the observed intensity distribution, further studies using different photon energy and geometry for angle-resolved measurement as well as support from theories would be required. In a simple picture, the ( $\gamma$ ,2e) spectrum could be approximated by the self-convoluted band structure which broadens intensity features strongly.

To summarize, we present a double ToF spectrometer setup for coincidence spectroscopy which was calibrated and applied for (e,2e) from Cu(111). The energy distribution of pair emission from Cu(111) shows three intensity peaks with a preference for equal energy sharing between two electrons. The electron pair momentum distribution shows a parabolic dispersion for the state 0.5 eV below the intensity onset. This is in agreement with previous (e,2e) studies on Cu(111) and demonstrates the capability of the instrument for coincidence spectroscopy. In combination with a high repetition rate HHG light source, we achieve ( $\gamma$ ,2e) experiments in the laboratory. Results for ( $\gamma$ ,2e) on NiO(001) excited with 30 eV photon energy are shown. The two dimensional energy

distribution of the electron pairs yields an increase in intensity towards lower sum energies and a broad and structureless energy sharing between electrons. Our work extends spectroscopy on electron pair emission with momentum resolution and initiates ( $\gamma$ ,2e) experiments in the laboratory.

We would like to thank H. Engelhardt, R. Neumann, F. Weiss, R. Kulla, and the BESSY II staff for valuable technical support. This work was partially funded by the DFG through SFB 762.

- <sup>1</sup>P. Monthoux, D. Pines, and G. G. Lonzarich, *Nature* **450**, 1177 (2007).
- <sup>2</sup>J. Berakdar, H. Gollisch, and R. Feder, *Solid State Commun.* **112**, 587 (1999).
- <sup>3</sup>J. C. Slater, *Rev. Mod. Phys.* **6**, 209 (1934).
- <sup>4</sup>J. Berakdar, *Phys. Rev. B* **58**, 9808 (1998).
- <sup>5</sup>C. Gazier and J. R. Prescott, *Phys. Lett. A* **32**, 425 (1970).
- <sup>6</sup>L. Avaldi and A. Huetz, *J. Phys. B: At., Mol. Opt. Phys.* **38**, S861 (2005).
- <sup>7</sup>L. Malegat, *Phys. Scr.* **T110**, 83 (2004).
- <sup>8</sup>F. O. Schumann, C. Winkler, and J. Kirschner, *Phys. Rev. Lett.* **98**, 257604 (2007).
- <sup>9</sup>R. Herrmann, S. Samarin, H. Schwabe, and J. Kirschner, *Phys. Rev. Lett.* **81**, 2148 (1998).
- <sup>10</sup>C. T. Chiang, A. Blättermann, M. Huth, J. Kirschner, and W. Widdra, *Appl. Phys. Lett.* **101**, 071116 (2012).
- <sup>11</sup>F. Giebels, H. Gollisch, and R. Feder, *J. Phys.: Condens. Matter* **21**, 355002 (2009).
- <sup>12</sup>H. Gollisch, N. v. Schwartzberg, and R. Feder, *Phys. Rev. B* **74**, 075407 (2006).
- <sup>13</sup>M. H. Berntsen, O. Götberg, and O. Tjernberg, *Rev. Sci. Instrum.* **82**, 095113 (2011).
- <sup>14</sup>S. Hüfner, *Photoelectron Spectroscopy* (Springer, Berlin, 2003).
- <sup>15</sup>F. O. Schumann, R. S. Dhaka, G. A. van Riessen, Z. Wei, and J. Kirschner, *Phys. Rev. B* **84**, 125106 (2011).
- <sup>16</sup>F. O. Schumann, C. Winkler, and J. Kirschner, *Phys. Rev. B* **88**, 085129 (2013).
- <sup>17</sup>M. Volkel and W. Sandner, *J. Phys. E: Sci. Instrum.* **16**, 456 (1983).
- <sup>18</sup>O. Kugeler, S. Marburger, and U. Hergenhahn, *Rev. Sci. Instrum.* **74**, 3955 (2003).
- <sup>19</sup>S. Grosser, C. Hagendorf, H. Neddermeyer, and W. Widdra, *Surf. Interface Anal.* **40**, 1741 (2008).



## Band-Resolved Double Photoemission Spectroscopy on Correlated Valence Electron Pairs in Metals

Andreas Trütschler,<sup>1,2</sup> Michael Huth,<sup>1</sup> Cheng-Tien Chiang,<sup>2,1,\*</sup> Robin Kamrta,<sup>2,1</sup>  
Frank O. Schumann,<sup>1</sup> Jürgen Kirschner,<sup>1,2</sup> and Wolf Widdra<sup>2,1,†</sup>

<sup>1</sup>Max-Planck-Institut für Mikrostrukturphysik, Weinberg 2, D-06120 Halle (Saale), Germany

<sup>2</sup>Institute of Physics, Martin-Luther-Universität Halle-Wittenberg, Von-Danckelmann-Platz 3, D-06120 Halle (Saale), Germany

(Received 26 September 2016; published 27 March 2017)

Correlated valence electrons in Ag and Cu are investigated using double photoemission spectroscopy driven by a high-order harmonic light source. Electron pairs consisting of two  $d$  electrons as well as pairs with one  $sp$  and one  $d$  electron are resolved in the two-dimensional energy spectrum. Surprisingly, the intensity ratio of  $sp-d$  to  $d-d$  pairs from Ag is 3 times higher than in the self-convoluted density of states. Our results directly show the band-resolved configurations of electron pairs in solids and emphasize a band-dependent picture for electron correlation even in these paradigmatic metals.

DOI: 10.1103/PhysRevLett.118.136401

Since the discovery of magnetism and superconductivity, studying electron correlation has become an indispensable field of physics [1,2]. Because of the central role of the electron-electron interaction in strongly correlated materials [3] as well as its impact on molecular and single-electron devices [4,5], varieties of spectroscopies have been devoted to measure correlated electrons in solids. Among them, double photoemission (DPE) experiments analyze pairs of interacting electrons directly and have been developed progressively over several decades [6,7].

Generally, DPE on solids is challenging due to the coincidence detection of two photoelectrons. This explicitly involves a reduced joint acceptance of two spectrometers and a compromised energy resolution due to a broad, simultaneously detected energy range up to few tens eV. Moreover, to suppress accidental coincident events, the incident photon flux must be kept low [7] and the measurement time becomes long, up to several days. With a laboratory high-order harmonic light source and a pair of time-of-flight spectrometers, we recently constructed a new DPE setup [Fig. 1(a), inset] [8,9]. It allows us to reveal the band-dependent signatures of the two-particle valence spectra of Ag and Cu. Pairs of interacting valence electrons are identified according to their sum kinetic energies ( $E_{\text{sum}}$ ) and specifically related to the number of participating  $d$  electrons. These two-electron  $E_{\text{sum}}$  features constitute a more intricate structure than the self-convoluted single-particle density of states and provide evidence for a distinctly band-dependent electron correlation even in these conventional metals. Because  $E_{\text{sum}}$  is a good quantum number for an electron pair instead of their individual energies, our DPE results provide valuable information regarding the electron pair configurations which go beyond the capabilities of single-particle spectroscopies.

DPE experiments were performed with  $s$ - and  $p$ -polarized light with photon energies ( $h\nu$ ) of 32.3 and 25.1 eV,

respectively. The photoelectron pairs were analyzed by a pair of TOF spectrometers, each having a  $\pm 15^\circ$  acceptance and oriented at  $\pm 45^\circ$  to the sample surface normal [8,9]. Figure 1(a) shows the raw two-particle DPE histogram from Ag(001) as a function of kinetic energies  $E_1$  and  $E_2$  of individual photoelectron within a pair. For each  $E_{1,2}$ , we integrate over the detected angular distribution of photoelectrons. To separate the true DPE signals from a background of accidental coincidence events, a second set of experiments with a 30 times higher photon flux is used. These reference spectra are dominated by the accidental events and serve as the background spectra. The raw and the background spectra are compared in Fig. 1(b) along  $E_{\text{sum}}$ , with the latter scaled down to the former in the region of  $E_{\text{sum}} > 29$  eV, where DPE is prohibited [10]. For clarity, only DPE spectra after this background subtraction are presented subsequently. A DPE cutoff at  $E_{\text{sum}}^{sp-d} = 18.9$  eV can be clearly seen in Fig. 1(b), which represents photoemission of the most energetic correlated electron pairs in Ag.

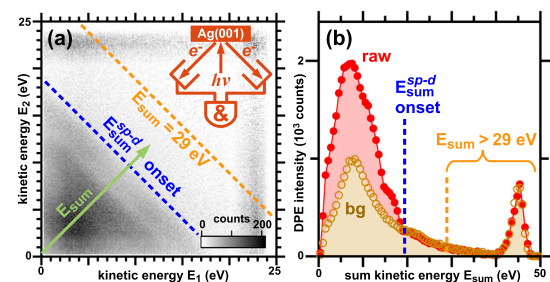


FIG. 1. (a) Histogram of two-electron photoemission coincidence events (raw data) on Ag(001) at  $h\nu = 32.3$  eV. The setup is shown schematically in the inset. (b) Raw and scaled background (bg)  $E_{\text{sum}}$  spectra.

The detailed energy hierarchy of correlated electron pairs is revealed in Figs. 2(a) and 2(b), which are derived from the raw data in Fig. 1 [11]. Below  $E_{\text{sum}}^{sp-d}$ , we observe two stepwise intensity increases at 14.7 ( $E_{\text{sum}}^{d-d}$ ) and 9.3 eV ( $E_{\text{sum}}^{d-d-d^*}$ ). Moreover, the DPE spectrum in Fig. 2(c) at  $h\nu = 25.1$  eV shows two steps at  $E_{\text{sum}}^{sp-d} = 12.0$  eV and  $E_{\text{sum}}^{d-d} = 7.3$  eV. Since both  $h\nu - E_{\text{sum}}^{sp-d}$  and  $h\nu - E_{\text{sum}}^{d-d}$  are  $h\nu$  independent within  $\pm 0.5$  eV [12], we assign  $E_{\text{sum}}^{sp-d}$  and  $E_{\text{sum}}^{d-d}$  as well as  $E_{\text{sum}}^{d-d-d^*}$  to features of occupied two-electron states that can be specified only by their total energy as a proper quantum number of a two-particle system.

As shown in Figs. 2(b) and 2(c), these two-electron features are located at pair binding energies  $E_{B,\text{sum}} = 4.6, 8.8,$  and  $14.2 \pm 0.7$  eV. These values are compatible with 1, 2, and 3 times the minimum binding energy of electrons within the Ag 4d bands of 4 eV [14]. Therefore, we attribute the first two energies to the onset of pair emission with  $sp-d$  and  $d-d$  electron-electron assignments, respectively. As an example, we illustrate in Fig. 2(d) the  $sp-d$  pair emission process with one  $sp$  electron from the Fermi-level ( $E_F$ ) and one  $d$  electron from the top of the  $d$  bands. This  $sp-d$  process results in the pairs with a maximum kinetic energy of  $E_{\text{sum}}^{sp-d}$  and is indicated by the dashed line in Figs. 2(c). In analogy, the emission of two electrons from the  $d$  bands has a maximum energy of  $E_{\text{sum}}^{d-d}$  (dashed-dotted line).

Moreover, the spectra in Figs. 2(a) and 2(b) have an intensity increase below  $E_{\text{sum}}^{d-d-d^*}$ , which corresponds to about 3 times the minimal binding energy of the Ag  $d$  bands. Therefore, we explain the marked area  $d-d-d^*$  as a lower bound for the emission process of a  $d-d$  pair accompanied by another  $d$  electron excited up to  $E_F$  ( $d^*$ ) as shown in Fig. 2(d). The labeled  $d-d-d^*$  intensity amounts to 40% of the  $d-d$  pairs, one order of magnitude larger than conventional shake-up satellites [15], and it overlays on a sizable background [16]. Both these properties are consistent with the known low-energy electron pairs in coincidence Auger spectra on metals, which result from decay processes with at least three valence electrons [17,18]. Because of the characteristic onset  $E_{\text{sum}}^{d-d-d^*}$ , it is possible to identify the  $d-d-d^*$  pairs from other underlying multielectron events. Here we also tentatively exclude  $d-d$  pairs with an atomically localized two-hole final state ( $d^{-2}$ ), since they would contribute a sharp spectrum with a narrow width of about 1 eV [19]. An alternative explanation for  $d-d-d^*$  pairs may be the excitation of transient excitons during the  $d-d$  pair emission [20,21].

In Fig. 3(a), we compare the DPE spectra of Ag with the self-convoluted density of states (cDOS, dashed line) [22], which is scaled to match the  $d-d$  pair intensity. The cDOS gives an estimation for the two-electron DOS as a function of the binding energy of the pairs ( $E_{B,\text{sum}}$ ) and is derived

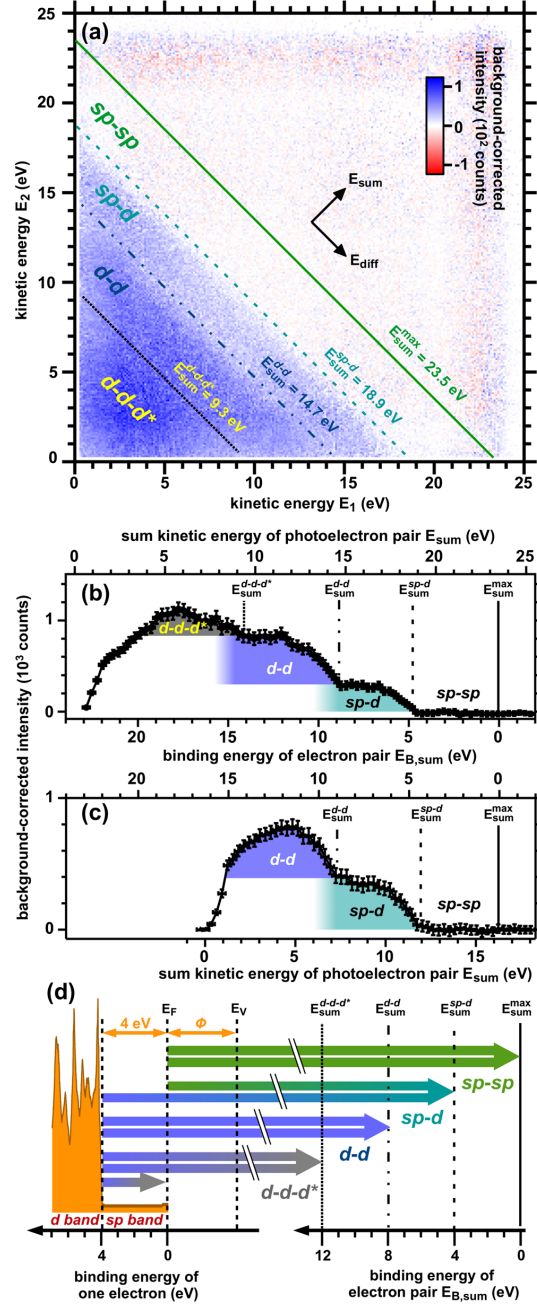


FIG. 2. (a) DPE data at  $h\nu = 32.3$  eV on Ag(001). (b)  $E_{\text{sum}}$  spectrum from (a) integrated over  $E_{\text{diff}} = \pm 1$  eV. (c) The same as (b) for  $h\nu = 25.1$  eV. (d) DOS of Ag [13] with DPE processes.  $E_V$  labels the vacuum level.

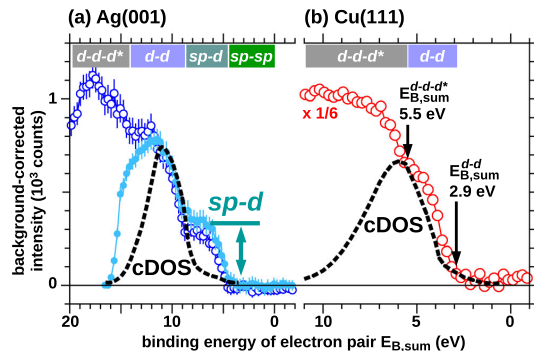


FIG. 3. Comparison of DPE spectra with the self-convoluted DOS adapted from Powell (cDOS) [22]. The constituents of electron pairs are labeled near the upper scale. (a) DPE spectra of Ag(001) at  $h\nu = 32.3(25.1)$  eV with empty (solid) symbols from Figs. 2(b) and 2(c). The threefold higher intensity of  $sp-d$  pairs compared to cDOS is highlighted. (b) DPE spectrum of Cu(111) with  $h\nu = 32.3$  eV integrated over all  $E_{diff}$  for better statistics.

from the Cini-Sawatzky model for two valence holes at the weak correlation limit [23,24]. As one can see, the clear DPE feature from  $sp-d$  pairs of Ag is surprising. First of all, its intensity amounts to a factor of 3 higher as compared to the cDOS at  $E_{B,sum} = 5-8$  eV. Second, with more than 20% variation in  $h\nu$ , this enhancement exists persistently. Therefore, significant  $h\nu$ -dependent final state effects acting only on  $sp-d$  or  $d-d$  pairs can be excluded. Possible candidates for such effects are pair diffraction and shake-off [25,26]. Furthermore, identical experiments on Cu(111) give the DPE spectrum in Fig. 3(b) in comparison with the cDOS. There, the  $sp-d$  pairs are merely visible, despite the  $d-d$  and  $d-d-d^*$  features that can be identified similarly as for Ag [27]. To explain all these observations qualitatively, either the two-particle DOS of  $sp-d$  electron pairs in Ag must be enhanced relative to the  $d-d$  pairs due to correlation, or the DPE matrix element for the  $sp-d$  pairs must be significantly larger than for the  $d-d$  pairs. Since the DPE matrix element is also linked to the strength of correlation [28–30], our results provide in either case an indication for significant electron correlation between the  $5sp$  and  $4d$  electrons in Ag.

Since an *ab initio* DPE calculation for Ag does not exist yet, we discuss qualitatively two aspects regarding the  $sp-d$  and  $d-d$  pairs. The first one is the existence of an electron correlation between  $sp$  and  $d$  electrons that is stronger in Ag than in Cu. The  $sp-d$  electron-electron interaction in transition metals has been postulated to explain itinerant magnetism [31] and the Kondo effect [32]. This interaction is strengthened in solids due the compression of the extended  $sp$  wave function towards the  $d$  electrons in atomic cores [33]. As a consequence of the larger volume fraction occupied by the  $4d$  electrons in comparison to the  $3d$  electrons [34], the  $sp-d$  interaction can be stronger in

Ag than in Cu, therefore explaining our observation of  $sp-d$  pairs in DPE only on Ag. Additionally, this stronger  $sp-d$  interaction in Ag also leads to a larger  $sp-d$  hybridization at  $E_F$  [35]. Moreover, the  $Ag^+ 4d^{10}$  shell has a significantly higher polarizability than the  $Cu^+ 3d^{10}$  shell [36]. As a result, the surrounding  $5sp$  electrons in Ag could influence the  $4d$  electrons more actively and lead to a significant DPE of  $5sp-4d$  electron pairs. This perspective is furthermore consistent with previous band structure calculations, where the different impact of electron correlation on  $sp$  electrons in Ag as compared to Cu was implied [37].

A second aspect is the lower strength of electron correlation between the  $d$  electrons in the detected  $d-d$  pairs than that between the  $sp$  and  $d$  electrons. Since the on-site Coulomb interaction  $U_{on\ site}$  between  $d$  electrons is usually large up to several eV [38,39], only interacting  $d$  electrons at different atomic sites may have a lower strength of correlation than that between the  $sp$  and  $d$  electrons near the same atom ( $U_{intersite} < 0.5U_{on\ site}$  for Ag [40]). This consideration suggests that the observed  $d-d$  pairs are a result of the interatomic correlation and leave two photoholes at separated atomic sites ( $d^{-1} + d^{-1}$ ). These  $d$  holes can propagate through the lattice with energy dispersion and give rise to a width in the  $E_{sum}$  spectrum comparable with the cDOS. It is, however, not straightforward to separate according to DPE spectra the on-site from the band correlation effects, with the latter conventionally assigned to a shift between experimental and theoretical band energies.

In the DPE spectra of both Ag and Cu in Fig. 3, we observe a generally dominant intensity of the  $d-d$  and  $d-d-d^*$  electron pairs. In strong contrast, vanishing DPE intensity is observed for pairs with both electrons from the bulk  $sp$  bands or from the  $sp$ -derived Shockley surface state [41]. The observation of electron pair emission as soon as  $d$  bands are considered clearly suggests that a band-resolved picture is required for electron correlation, in general, even for metals like Ag and Cu. The vanishing intensity of  $sp-sp$  pair is attributed to their low cDOS (Fig. 3) and the less dominant role of electron correlation in the electron gas of the  $sp$  electrons [42].

A closer look at Fig. 3(b) reveals a small but observable energy shift between the  $E_{sum}$  spectrum and the cDOS of Cu for  $d-d$  pairs. However, for Ag in Fig. 3(a), they coincide reasonably. We ascribe this difference to the influence of the stronger Coulomb interaction between  $d$  electrons in Cu than in Ag [38,39], which contributes to the repulsion between the two photoholes in the DPE final state and triggers the relaxation of the whole electronic system [43,44]. Because the itinerant nature of correlated valence electrons is unavoidably related to a site-dependent Coulomb interaction [19,45], the atomic models conventionally used for core-valence Auger decays may not be directly applicable to describe the shifted onset observed in our DPE experiments. Therefore, we consider the

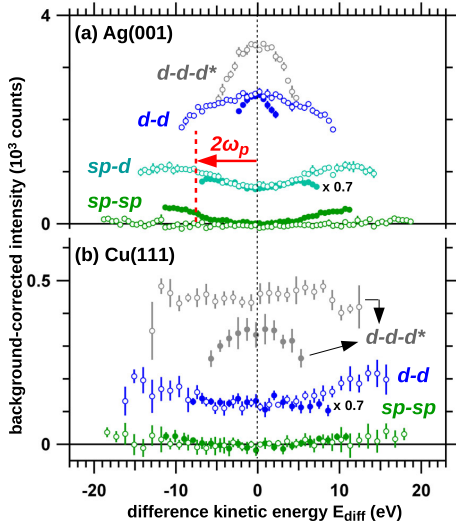


FIG. 4.  $E_{\text{diff}}$  spectra for (a) Ag(001) and (b) Cu(111) with empty (solid) symbols for  $h\nu = 32.3(25.1)$  eV. Each spectrum is integrated over  $E_{B,\text{sum}} = \pm 2$  eV for Ag and  $\pm 1$  eV for Cu centered at the indicated pair binding energy region in Figs. 2 and 3(b). The  $d-d-d^*$  spectra are centered at  $E_{B,\text{sum}}^{d-d-d^*} - 2$  eV, and the Cu  $sp-sp$  spectra at  $E_{B,\text{sum}}$  around 1.4 eV. For comparison, the  $sp-d$  pairs from Ag and the  $d-d$  pairs from Cu at  $h\nu = 25.1$  eV are scaled by a factor of 0.7.

difference between the observed Cu  $d-d$  onset from the cDOS as an upper bound for the correlation energy of the valence bands DPE process [46], which awaits theories including a refined exchange correlation for a quantitative comparison [33].

The pairs of interacting valence electrons not only have band-specific total energies but also share the exciting photon energy in distinct ways. This can be clearly quantified in terms of the experimentally accessible, kinetic energy difference ( $E_{\text{diff}}$ ), which corresponds to the intensity distribution perpendicular to  $E_{\text{sum}}$  direction in the DPE histogram as shown in Fig. 2(a). In Fig. 4, the  $E_{\text{diff}}$  spectra are shown, classified according to the pair configurations discussed above. The  $E_{\text{diff}}$  spectra for Ag  $d-d$  and  $d-d-d^*$  pairs show higher intensity at  $E_{\text{diff}} \approx 0$ . In contrast,  $sp-d$  pairs from Ag as well as  $d-d$  pairs from Cu are less favorable around  $E_{\text{diff}} \approx 0$  when compared to  $|E_{\text{diff}}| \gg 0$ . These results show a clear partition of  $h\nu$  over the two interacting electrons within a pair and its dependence on their valence band character. Moreover, going from  $d-d$  to  $d-d-d^*$  pairs measured at the same  $h\nu$ , we observe a more enhanced signal near  $E_{\text{diff}} \approx 0$  comparing to larger  $|E_{\text{diff}}|$  for both Ag and Cu, which reveals the influence of the additional  $d^*$  excitation to the energy distribution within the  $d-d$  pairs.

A closer look at the  $E_{\text{diff}}$  spectrum of  $sp-d$  pairs of Ag shows a roughly constant intensity beyond  $|E_{\text{diff}}| \geq 2\hbar\omega_p$ , with  $\hbar\omega_p \approx 3.8$  eV as the bulk Ag plasmon energy [47]. This observation implies that the electrons with otherwise equal energy in an  $sp-d$  pair may additionally exchange energy via a plasmon and end up as a pair with a larger  $|E_{\text{diff}}|$ . In contrast, the observed intensity of Cu  $d-d$  pairs increases up to a much higher  $|E_{\text{diff}}| \approx 10$  eV. This value is comparable to a broad plasmonlike energy-loss resonance [47] as well as to the on-site Coulomb repulsion  $U_{\text{on site}} \approx 9-11$  eV [48,49]. The former is excluded because an energy-loss process also alters the total energy ( $E_{\text{sum}}$ ) of an electron pair. Therefore, we attribute the latter as a possible origin for the increasing DPE intensity at larger  $|E_{\text{diff}}|$  for Cu  $d-d$  pairs, which involves an additional DPE pathway via a reconfiguration of the  $d$  shell related to  $U_{\text{on site}}$ .

In summary, DPE spectroscopy resolves band-specific electron pairs in Ag(001) and Cu(111). In spite of the isoelectronic single-particle band structure of Ag and Cu, they show remarkably different response in the two-particle spectrum. We identify distinct two-particle energy features in the pair sum kinetic energies and relate the energy thresholds according to the number of  $d$  electrons involved. Besides electron pairs consisting of  $sp-d$  and  $d-d$  electrons, we provide indications for processes with three  $d$  electrons. The emission of  $sp-d$  electron pairs is enhanced on Ag whereas barely observable on Cu due to the weaker  $sp-d$  interaction. Moreover, the energy sharing within a pair depends sensitively on the constituent valence electrons and provides hints of energy exchange between electrons via a plasmon in Ag or via the on-site Coulomb interaction in Cu. Our results reveal a clear band dependence in the pairs of mutually interacting electrons in solids, which may pave a way to systematically analyze quasiparticles by multidimensional photoelectron spectroscopy [50].

Technical support from H. Engelhard, F. Helbig, F. Weiß, H. Menge, and R. Kulla is gratefully acknowledged. This work is partially funded by the Deutsche Forschungsgemeinschaft through SFB 762.

\* Corresponding author.

cheng-tien.chiang@physik.uni-halle.de

† wolf.widdra@physik.uni-halle.de

- [1] C. Zener and R. R. Heikes, *Rev. Mod. Phys.* **25**, 191 (1953).
- [2] J. Bardeen, L. N. Cooper, and J. R. Schrieffer, *Phys. Rev.* **108**, 1175 (1957).
- [3] M. Imada, A. Fujimori, and Y. Tokura, *Rev. Mod. Phys.* **70**, 1039 (1998).
- [4] F. Schulz, M. Ijäs, R. Drost, S. K. Hämäläinen, A. Harju, A. P. Seitsonen, and P. Liljeroth, *Nat. Phys.* **11**, 229 (2015).
- [5] D. Goldhaber-Gordon, H. Shtrikman, D. Mahalu, D. Abusch-Magder, U. Meirav, and M. Kastner, *Nature (London)* **391**, 156 (1998).



- [6] G. Stefani, S. Iacobucci, A. Ruocco, and R. Gotter, *J. Electron Spectrosc. Relat. Phenom.* **127**, 1 (2002).
- [7] F. O. Schumann, C. Winkler, and J. Kirschner, *Phys. Status Solidi (b)* **246**, 1483 (2009).
- [8] M. Huth, C.-T. Chiang, A. Trützschler, F. O. Schumann, J. Kirschner, and W. Widdra, *Appl. Phys. Lett.* **104**, 061602 (2014).
- [9] C.-T. Chiang, M. Huth, A. Trützschler, F. O. Schumann, J. Kirschner, and W. Widdra, *J. Electron Spectrosc. Relat. Phenom.* **200**, 15 (2015).
- [10] J. Kirschner, O. M. Artamonov, and S. N. Samarin, *Phys. Rev. Lett.* **75**, 2424 (1995).
- [11] The error bars in Figs. 2–4 are derived from the electron counting statistics and error propagation due to the background subtraction.
- [12] The uncertainty for the absolute binding energy here is estimated by the energy resolution of the spectrometer (0.05 eV at 5 eV and 0.2 eV at 25 eV) and the bandwidth of light (0.1 eV) as well as the uncertainty for determining the work function (0.2 eV).
- [13] L. Pasquali, M. Sapet, E. Staiacu-Casagrande, P. Cortona, V. Esaulov, S. Nannarone, M. Canepa, S. Terreni, and L. Mattera, *Nucl. Instrum. Methods Phys. Res., Sect. B* **212**, 274 (2003).
- [14]  $E_{B,\text{sum}}$  is derived by assuming a DPE threshold equal to twice the work function ( $2\phi$ ) and starts at  $E_{\text{sum}} \approx h\nu - 2\phi$  as marked in Fig. 2 [7]. The experimentally observed deviations from integer multiples of 4 eV are given by  $\Delta E_{\text{Ag}}^{sp-d} = 0.6 \pm 0.7$ ,  $\Delta E_{\text{Ag}}^{d-d} = 0.8 \pm 0.7$ , and  $\Delta E_{\text{Ag}}^{d-d^*} = 2.2 \pm 0.7$  eV.
- [15] M. Iwan, F. J. Himpsel, and D. E. Eastman, *Phys. Rev. Lett.* **43**, 1829 (1979).
- [16] See Supplemental Material at <http://link.aps.org/supplemental/10.1103/PhysRevLett.118.136401> for an estimation for the low-energy electron pairs underlying the  $d-d^*$  signals.
- [17] E. Jensen, R. A. Bartynski, R. F. Garrett, S. L. Hulbert, E. D. Johnson, and C.-C. Kao, *Phys. Rev. B* **45**, 13636 (1992).
- [18] S. F. Mukherjee, K. Shastry, and A. H. Weiss, *Phys. Rev. B* **84**, 155109 (2011).
- [19] R. J. Cole, C. Verdozzi, M. Cini, and P. Weightman, *Phys. Rev. B* **49**, 13329 (1994).
- [20] W.-D. Schöne and W. Ekaradt, *Phys. Rev. B* **65**, 113112 (2002).
- [21] X. Cui, C. Wang, A. Argondizzo, S. Garrett-Roe, B. Gumhalter, and H. Petek, *Nat. Phys.* **10**, 505 (2014).
- [22] C. Powell, *Solid State Commun.* **26**, 557 (1978).
- [23] M. Cini, *Solid State Commun.* **24**, 681 (1977).
- [24] P. A. Bennett, J. C. Fuggle, F. U. Hillebrecht, A. Lenselink, and G. A. Sawatzky, *Phys. Rev. B* **27**, 2194 (1983).
- [25] Z. Wei, F. O. Schumann, R. S. Dhaka, and J. Kirschner, *Phys. Rev. B* **85**, 195120 (2012).
- [26] T. Schneider, P. L. Chocian, and J.-M. Rost, *Phys. Rev. Lett.* **89**, 073002 (2002).
- [27] The stepwise intensity increase at  $E_{B,\text{sum}}^{d-d} = 2.9$  eV and  $E_{B,\text{sum}}^{d-d^*} = 5.5$  eV are compatible with the doubled and tripled values of the minimum binding energy of Cu 3d bands of 2 eV [22]. Therefore, they correspond to the onset of  $d-d$  and  $d-d^*$  electron pairs.
- [28] J. Berakdar, *Phys. Rev. B* **58**, 9808 (1998).
- [29] B. D. Napitu and J. Berakdar, *Phys. Rev. B* **81**, 195108 (2010).
- [30] F. O. Schumann, Y. Aliaev, I. Kostanovskiy, G. Di Filippo, Z. Wei, and J. Kirschner, *Phys. Rev. B* **93**, 235128 (2016).
- [31] T. Kasuya, *Prog. Theor. Phys.* **16**, 45 (1956).
- [32] J. Kondo, *J. Appl. Phys.* **37**, 1177 (1966).
- [33] L. Hodges, R. E. Watson, and H. Ehrenreich, *Phys. Rev. B* **5**, 3953 (1972).
- [34] W. A. Harrison and S. Froyen, *Phys. Rev. B* **21**, 3214 (1980).
- [35] D. van der Marel and G. A. Sawatzky, *Phys. Rev. B* **37**, 10674 (1988).
- [36] J. Mitroy, M. S. Safronova, and C. W. Clark, *J. Phys. B* **43**, 202001 (2010).
- [37] Z. Yi, Y. Ma, M. Rohlfing, V. M. Silkin, and E. V. Chulkov, *Phys. Rev. B* **81**, 125125 (2010).
- [38] E. Şaşıoğlu, C. Friedrich, and S. Blügel, *Phys. Rev. B* **83**, 121101 (2011).
- [39] R. Nyholm, K. Helenelund, B. Johansson, and S.-E. Hömström, *Phys. Rev. B* **34**, 675 (1986).
- [40] C. Verdozzi and M. Cini, *Phys. Rev. B* **51**, 7412 (1995).
- [41] The DPE signal of  $sp-sp$  pairs for both Ag and Cu at  $h\nu = 32.3$  eV is below 1% of the total DPE signal. It amounts to 8% for Ag at  $h\nu = 25.1$  eV.
- [42] D. Pines, *Phys. Rev.* **92**, 626 (1953).
- [43] L. S. Cederbaum, F. Tarantelli, A. Sgamellotti, and J. Schirmer, *J. Chem. Phys.* **85**, 6513 (1986).
- [44] E. Antonides, E. C. Janse, and G. A. Sawatzky, *Phys. Rev. B* **15**, 1669 (1977).
- [45] D. R. Jennison, *Phys. Rev. B* **18**, 6996 (1978).
- [46] P.-O. Löwdin, *Int. J. Quantum Chem.* **55**, 77 (1995).
- [47] A. Alkauskas, S. D. Schneider, C. Hébert, S. Sagmeister, and C. Draxl, *Phys. Rev. B* **88**, 195124 (2013).
- [48] D. Chandessris, J. Lecante, and Y. Petroff, *Phys. Rev. B* **27**, 2630 (1983).
- [49] K. Nakamura, R. Arita, Y. Yoshimoto, and S. Tsuneyuki, *Phys. Rev. B* **74**, 235113 (2006).
- [50] R. Rausch and M. Potthoff, *New J. Phys.* **18**, 023033 (2016).



Supplemental material: Estimation for the background of  $d$ - $d$ - $d^*$  events on Ag

In Fig.S1a the simplified, model density of states (DOS) for  $sp$  and  $d$  electrons in Ag are shown, and in Fig.S1b to Fig.S1d the convoluted DOS (cDOS) for different combinations of  $sp$  and  $d$  electrons are derived.

In the total contribution from all the cDOS of  $sp$ - $d$ ,  $d$ - $d$  and  $d$ - $d$ - $d^*$  pairs ( $\Sigma cDOS$ , Fig.S2a), we multiply the cDOS of  $sp$ - $d$  pairs by a factor of 5.5 and that of the  $d$ - $d$ - $d^*$  pairs by 0.4. The former factor takes into account phenomenologically the enhanced  $sp$ - $d$  pair intensity relative to the  $d$ - $d$  pairs as discussed in the main text. Because of the simplified shape of DOS here, this value is larger than the factor 3 obtained from the comparison with a realistic cDOS (Fig.3a of the main text). As shown in Fig.S2b below, the weighted  $sp$ - $d$  and  $d$ - $d$  pairs in  $\Sigma cDOS$  reasonably estimate the double photoemission (DPE) spectrum at the photon energy  $h\nu = 25.1$  eV.

In Fig.S2c the DPE spectra at  $h\nu = 32.3$  eV is compared with the  $\Sigma cDOS$ , and a reasonable agreement ( $\Sigma cDOS$ +LEP) is reached when a smooth distribution of low-energy electron pairs (LEP) is added. In accordance with literature reporting large low-energy tails in coincidence core-valence electron pair spectra, we ascribe the LEP to excitation processes where at least three electrons are involved (Ref.[17,18] of the main text). Those reported low-energy tails in electron pair spectra are dominant below the onset of two-electron excitations, which is in qualitative agreement with the onset of LEP in Fig.S2c near the onset of the cDOS of  $d$ - $d$  pairs.

The  $d$ - $d$ - $d^*$  events here can be identified separately from the LEP due to its characteristic onset at around three times the minimal binding energy of the  $d$  bands.

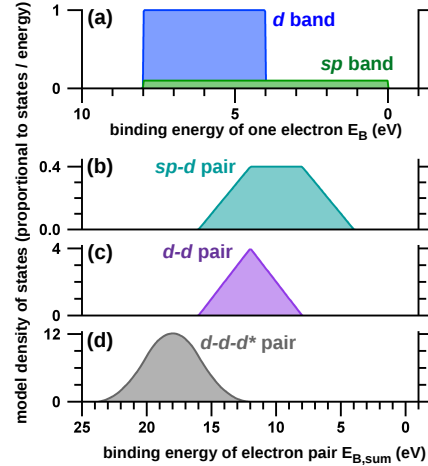


FIG. S1. (a) Model density of states (DOS) for  $sp$  and  $d$  electrons in Ag. Convoluted DOS (cDOS) of (b)  $sp$  and  $d$ , (c)  $d$  and  $d$ , as well as (d) three  $d$  electrons.

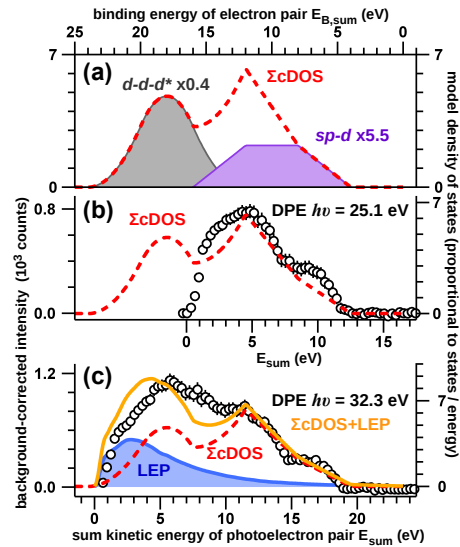


FIG. S2. (a) Weighted sum of cDOS from Fig. S1 (red dashed,  $\Sigma cDOS$ ) with the scaled cDOS of  $sp$ - $d$  and  $d$ - $d$ - $d^*$  pairs explicitly shown. (b,c) Comparison of DPE spectra (black circles) from Fig. 2 of the main text with  $\Sigma cDOS$ . In (c) an additional distribution of low-energy electron pairs (LEP, blue filled) is assumed for the comparison with  $\Sigma cDOS$ +LEP.



## Extended energy range analysis for angle-resolved time-of-flight photoelectron spectroscopy

Michael Huth,<sup>1</sup> Andreas Trützschler,<sup>1,2</sup> Cheng-Tien Chiang,<sup>1,2,a)</sup> Robin Kamrla,<sup>1,2</sup> Frank O. Schumann,<sup>1,b)</sup> and Wolf Widdra<sup>1,2,c)</sup>

<sup>1</sup>Max Planck Institute of Microstructure Physics, Weinberg 2, D-06120 Halle (Saale), Germany

<sup>2</sup>Institute of Physics, Martin-Luther-Universität Halle-Wittenberg, Von-Danckelmann-Platz 3, D-06120 Halle (Saale), Germany

(Received 15 July 2018; accepted 5 October 2018; published online 23 October 2018)

An approximation method for electrostatic time-of-flight (ToF) spectroscopy on photoelectrons distributed over a wide energy range is presented. This method is an extension of conventional analysis and aims at specific energy and angular regions, where distinctly different emission angles and energies are mapped to the same ToF and detector position by the spectrometer. The general formulation and the systematic errors are presented, and a practical example is demonstrated for photoelectrons from Ag(001) with kinetic energies of 0.5–25 eV. © 2018 Author(s). All article content, except where otherwise noted, is licensed under a Creative Commons Attribution (CC BY) license (<http://creativecommons.org/licenses/by/4.0/>). <https://doi.org/10.1063/1.5048515>

### I. INTRODUCTION

Time-of-flight (ToF) spectroscopy of charged particles allows the detection of many spectroscopic channels in parallel. In ion mass spectroscopy, a wide range of charge to mass ratio of ions is analyzed simultaneously,<sup>1,2</sup> and in electron spectroscopy, a large phase space of emission angle and kinetic energy can be acquired at the same time using angle-resolving detection.<sup>3,4</sup> Recently, due to the importance of angle-resolved photoelectron spectroscopy (ARPES) on studying electronic properties of novel materials, ToF spectroscopy of photoelectrons has been developed remarkably.<sup>5–12</sup>

In contrast to conventional hemispherical energy analyzers, in ToF-based ARPES, the two-dimensional (2D) emission angular distribution ( $\theta, \phi$ ) and the corresponding energy ( $E$ ) spectra are measured in a single experiment.<sup>3,4</sup> Generally, a ToF spectrometer acquires the hit position of an individual photoelectron ( $x, y$ ) on a 2D detector and its ToF from the sample to the detector ( $t$ ). In an ideal case, the spectrometer should perform a one-to-one mapping from  $(\theta, \phi, E)$  to  $(x, y, t)$ , which allows  $(\theta, \phi, E)$  to be retrieved from the detected  $(x, y, t)$  coordinates as shown in Fig. 1(a).

However, the one-to-one forward mapping can only be guaranteed in a limited energy and angular range,<sup>13,14</sup> beyond which the ToF spectrometer performs a many-to-one forward mapping from  $(\theta, \phi, E)$  to  $(x, y, t)$  such as in Fig. 1(b). The restricted energy range of the one-to-one mapping not only puts an upper bound for the efficiency of ToF spectroscopy but may also inhibit advanced experiments, where a wide energy range is especially desirable. An example for such experiments is coincidence photoelectron

spectroscopy,<sup>15–19</sup> where the total detection efficiency scales quadratically with that of the individual spectrometer.<sup>20</sup>

In this paper, we present a general extension of the conventional method to analyze the photoelectron events in a ToF-based spectrometer. This analysis includes the many-to-one forward mapping such as in Fig. 1(b) and allows one to extend the available angular and energy range. The method is based on assumptions for the distribution among the multiple  $(\theta_i, \phi_i, E_i)$  events that are mapped to the same  $(x, y, t)$  detector coordinates by the ToF spectrometer. The resultant systematic error in the retrieved emission coordinates of photoelectrons  $(\theta, \phi, E)$  can be quantified according to the imaging properties of the spectrometer. In the following, we describe this approximation and illustrate it with a commercial ToF spectrometer.<sup>21</sup> As an example, we apply this analysis to ARPES on a Ag(001) with photoelectrons distributed over a kinetic energy range from 0.5 to 25 eV.

### II. FORMULATION OF APPROXIMATION

In conventional analyses, the one-to-one mapping in Fig. 1(a) is considered as a transformation between an infinitesimal volume  $\Delta x \times \Delta y \times \Delta t$  around the detector coordinates  $(x, y, t)$  to a volume element  $\Delta\theta \times \Delta\phi \times \Delta E$  in the photoemission configuration space  $(\theta, \phi, E)$ . The analyses rely on a grid in the  $(x, y, t)$  space consisting of contours with constant  $\theta, \phi$ , and  $E$ , which are calculated beforehand by simulations of electron trajectories. For each individual photoelectron, the event detected with its  $(x, y, t)$  coordinates, an interpolation between the contours of the grid is performed in order to obtain the corresponding  $(\theta, \phi, E)$  values. The work flow of the conventional analysis is shown by the left side of Fig. 2 (black), and its precision can be estimated from experiments, where the resolutions of the spectrometers are examined in detail. Typical values of optimal resolutions can be better than 0.2° and 5 meV with spectrometer settings of low kinetic ( $E_{kin}$ ) and pass energies ( $E_{pass}$ ).<sup>4,11</sup> These

<sup>a)</sup>Electronic mail: cheng-tien.chiang@physik.uni-halle.de

<sup>b)</sup>Electronic mail: schumann@mpi-halle.de

<sup>c)</sup>Electronic mail: wolf.widdra@physik.uni-halle.de



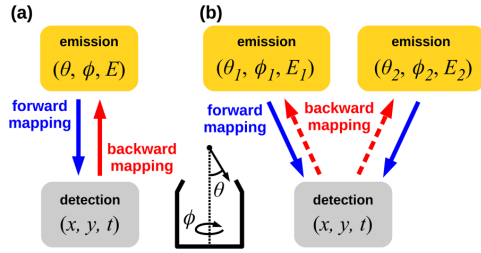


FIG. 1. (a) One-to-one mapping from the photoelectron emission angles ( $\theta$ ,  $\phi$ ) and kinetic energy ( $E$ ) to the hit position on the 2D detector ( $x$ ,  $y$ ) and ToF ( $t$ ). For small regions in the  $\theta$ - $\phi$ - $E$  configuration space, multiple  $\theta$ - $\phi$ - $E$  combinations lead to identical detection events as illustrated by the two-to-one mapping from  $(\theta, \phi, E)$  to  $(x, y, t)$  in (b). The approximated backward mapping is indicated by the dashed arrows. The inset exemplifies the polar ( $\theta$ ) and the azimuthal ( $\phi$ ) angles with respect to the spectrometer axis (dotted) in the case of a cylindrical ToF spectrometer.

settings are specifically chosen for high energy resolution whereas the available energy window is only of few eV wide. For wide energy applications, settings with a higher  $E_{pass}$  need to be applied, resulting in an inevitable trade-off to a lower energy resolution. In this paper, we will demonstrate an application of wide energy range, which will have an energy resolution of about 180 meV in the conventional analysis<sup>22</sup> and will be discussed in detail later.

Whereas conventional analyses do not introduce additional uncertainties formally, in practice their accuracies are limited by the precision of the electron trajectory simulations as well as the spatial and time resolutions of the

detector. For example, considering two individual events which are detected in proximity much closer than the spatial and time resolutions of the detector, their detector coordinates ( $x$ ,  $y$ ,  $t$ ) cannot be distinguished from each other despite of their distinctly different emission coordinates ( $\theta$ ,  $\phi$ ,  $E$ ). As a result, these two events are *apparently* related to the same detector coordinates due to the limited detector resolutions, as if they would be mapped by the spectrometer in a two-to-one forward mapping as in Fig. 1(b). Therefore, in spite of the formally well-defined boundary between the one-to-one and the many-to-one mappings as shown in Fig. 1, in practical analyses, this boundary is determined by the detector resolutions and the precision of the trajectory simulations.

For cases where the different  $(\theta, \phi, E)$  coordinates in a many-to-one mapping have only small discrepancies as compared to the spectrometer resolution, they can be evaluated without a significant degradation of the overall resolution. To perform such an evaluation, an assumption regarding the distribution among the different  $(\theta, \phi, E)$  coordinates in the many-to-one mapping is required. For clarity, we illustrate our approximation for the backward mapping of the two-to-one mapping in Fig. 1(b) as follows:

With weighting  $w_1$ :

$$\Delta x \times \Delta y \times \Delta t \rightarrow \Delta \theta_1 \times \Delta \phi_1 \times \Delta E_1$$

$$(x, y, t) \rightarrow (\theta_1, \phi_1, E_1).$$

With weighting  $w_2$ :

$$\Delta x \times \Delta y \times \Delta t \rightarrow \Delta \theta_2 \times \Delta \phi_2 \times \Delta E_2$$

$$(x, y, t) \rightarrow (\theta_2, \phi_2, E_2).$$

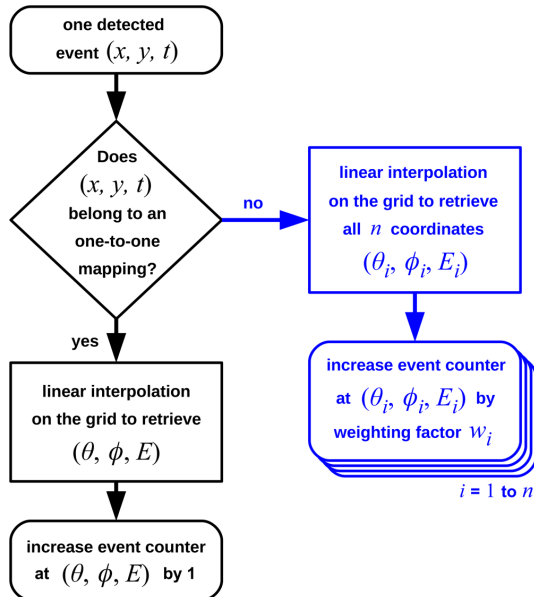


FIG. 2. Work flow of conventional analysis for one-to-one mapping (black) and the approximated method to analyze the many-to-one mapping (blue). Detected photoelectrons are registered in the photoelectron spectrum by the event counter.

In this approximation, we assign the detected event at  $(x, y, t)$  with a weighting factor  $w_1$  to the emission coordinates  $(\theta_1, \phi_1, E_1)$ , and with a factor  $w_2$  to  $(\theta_2, \phi_2, E_2)$ . Assumptions of factors  $w_1$  and  $w_2$  need to be made, which should not generate features only at some specific energy or angular coordinates. Moreover, these factors need to be normalized by  $w_1 + w_2 = 1$  since the number of events should be conserved in both the forward and the backward mappings. In a general case of an  $n$ -to-one forward mapping, where  $n$  different  $(\theta_i, \phi_i, E_i)$  with  $i = 1$  to  $n$  are mapped to the same  $(x, y, t)$ ,  $n$  different weighting factors are needed with a constraint  $\sum_{i=1}^n w_i = 1$ . In Fig. 2, this work flow for the many-to-one mapping is shown (blue).

The systematic error due to this approximation can be quantified by considering an incident photoelectron with emission coordinates  $(\theta_m, \phi_m, E_m)$  that arrives in the spectrometer at the detector coordinates  $(x, y, t)$ . In case  $(x, y, t)$  do not allow a one-to-one backward mapping, this event must stem from  $n$  different emission coordinates with  $n > 1$ . The approximated backward mapping will deliver these  $n$  different emission coordinates  $(\theta_i, \phi_i, E_i)$ , each with a corresponding weighting factor  $w_i$ . Since only one set of the  $n$  different  $(\theta_i, \phi_i, E_i)$  coordinates matches  $(\theta_m, \phi_m, E_m)$ , the difference between  $(\theta_m, \phi_m, E_m)$  and the other  $n-1$  sets of  $(\theta_i, \phi_i, E_i)$  leads to errors in the approximated backward

mapping. The resultant systematic error in energy and emission angles due to the approximated backward mapping can be evaluated as

$$\sigma_E = \sqrt{\sum_{i=1}^n w_i \times (E_i - E_{in})^2}, \quad (1)$$

$$\sigma_\theta = \sqrt{\sum_{i=1}^n w_i \times (\theta_i - \theta_{in})^2}.$$

Similarly, the systematic error for the emission angle  $\phi$  can be calculated. These errors have an upper bound as given by the maximum difference between the  $n$  different values of  $(\theta_i, \phi_i, E_i)$ . Take  $\sigma_E$  for the case of  $n = 2$  as an example, its upper bound is  $\sigma_E^{max} = E^{max} - E^{min}$  according to Eq. (1),<sup>23</sup> where  $E^{max}$  and  $E^{min}$  are the maximum and the minimum, respectively, among the two different values of  $E_i$ . Generally, the errors  $\sigma_E$ ,  $\sigma_\theta$ , and  $\sigma_\phi$  depend on  $w_i$ . Often the possible photoemission events that are mapped to the same  $(x, y, t)$  are rather close to each other in the  $(\theta_i, \phi_i, E_i)$  configuration space, and the formal ambiguity might introduce only a small error.

### III. PRACTICAL EXAMPLE

In the following, we demonstrate a practical example for the approximated backward mapping in Sec. II using a commercial ToF spectrometer.<sup>11,21</sup> The settings of the spectrometer are wide-angle-mode with a nominal kinetic energy ( $E_{kin}$ ) of 8 eV and a pass energy ( $E_{pass}$ ) of 60 eV. Due to the cylindrical symmetry with respect to the optical axis of the spectrometer, the three-dimensional (3D) emission coordinates  $(\theta, \phi, E)$  can be reduced to  $(\theta, E)$  and displayed on the 2D plane as shown in Fig. 3(a). Correspondingly, the 3D volume  $\Delta\theta \times \Delta\phi \times \Delta E$  is reduced to an area of a triangle  $\Delta\theta \times \Delta E/2$ . Here, we intentionally use a triangular grid

instead of a rectangular grid, since only a triangle can be mapped to the detector space in general without producing any additional crossing between its edges. As shown in Fig. 3(a), the triangles are defined by neighboring  $(\theta, E)$  points and cover the spectrometer acceptance range. In Fig. 3(a), a low resolution of  $\Delta\theta$  and  $\Delta E$  is selected for better visualization.

The emission coordinates  $(\theta, E)$  are connected to the detector coordinates  $(r, t)$  by the forward mapping according to the electrostatic model of the spectrometer.<sup>24</sup> Here, the radial position  $r$  appears instead of the 2D coordinates  $(x, y)$  due to the cylindrical symmetry, and its origin is located at the spectrometer axis.<sup>25</sup> As a consequence, the forward mapping transforms the  $(\theta, E)$  grid in Fig. 3(a) to the  $(r, t)$  grid in Fig. 3(b).

#### A. Two-to-one forward mapping

To illustrate a practical example of the two-to-one forward mapping as formally outlined in Fig. 1(b), we consider two triangular elements on the  $(\theta, E)$  plane in Fig. 3(a) (filled) and their corresponding triangles on the  $(r, t)$  plane in Fig. 3(b). As shown in the insets of Fig. 3(b), these two triangles have an overlap on the  $(r, t)$  plane. As a consequence, detected events in this overlapping  $(r, t)$  region can originate from either of the two triangles on the  $(\theta, E)$  plane. As an example, two independent events with different emission angles and energies are indicated by the blue dots in the inset of Fig. 3(a), which arrive at the same detector coordinates as indicated in the inset of Fig. 3(b). Consequently, a two-to-one forward mapping occurs within this overlapping  $(r, t)$  region and it corresponds to the formal situation in Fig. 1(b).

#### B. Error estimation

The error estimation in the approximated backward mapping is a crucial aspect to judge the usefulness of the

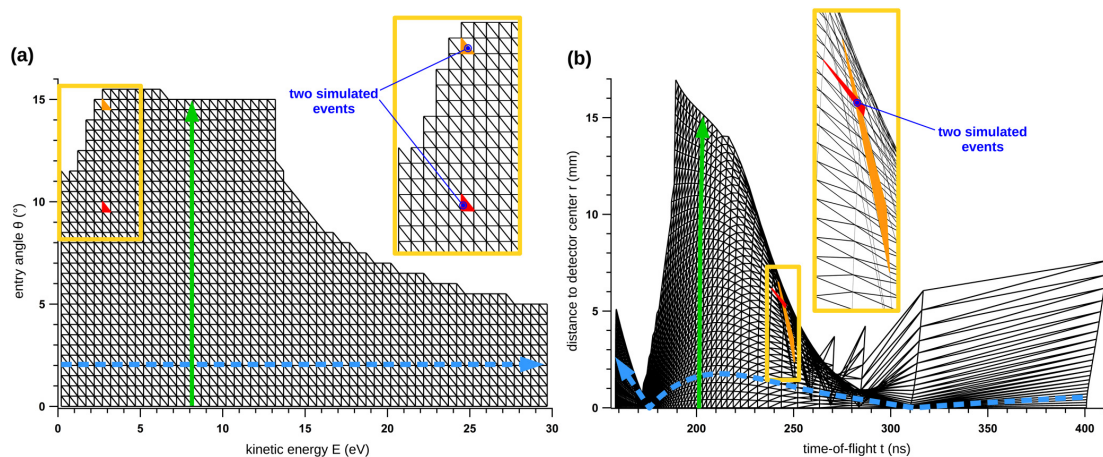


FIG. 3. (a) Grid of the  $(\theta, E)$  emission coordinates of photoelectrons entering the ToF-spectrometer<sup>21</sup> and (b) the corresponding grid of the  $(r, t)$  detector coordinates after the forward mapping. The insets (yellow boxes) show two simulated events (blue dots) with different  $(\theta, E)$  arriving at the same  $(r, t)$ . Such a two-to-one forward mapping is indicated by the overlapping region between the filled triangles (colored) in (b). Solid and dashed arrows indicate exemplary contours with a constant  $E$  and a constant  $\theta$ , respectively.

extended analysis. Ideally, the backward mapping should transform the detector coordinates  $(r, t)$  in Fig. 3(b) to the emission coordinates  $(\theta, E)$  in Fig. 3(a) without introducing any error. However, since in the forward mapping an  $n$ -to-one mapping with  $n > 1$  can occur as shown in Fig. 1(b) and described in Sec. III A, the approximated backward mapping as formulated in Sec. II is required. In Fig. 4(a), the order  $n$  for the spectrometer settings in Fig. 3 is shown. Note that in a practical application, mainly regions with  $n \leq 3$  will be used. In the approximated backward mapping, we assume a distribution of the weighting factor  $w_i$  proportional to the solid angle  $\Omega_i$  in the proximity of the  $(\theta, E_i)$  emission coordinates and inversely proportional to its corresponding area  $A_i$  on the  $(r, t)$  plane,

$$w_i = \frac{\Omega_i/A_i}{\sum_{i=1}^n \Omega_i/A_i}. \quad (2)$$

Here, the normalization condition  $\sum_{i=1}^n w_i = 1$  is fulfilled by the summation in the denominator. With this choice of  $w_i$ , the original distribution of photoelectrons can be retrieved if

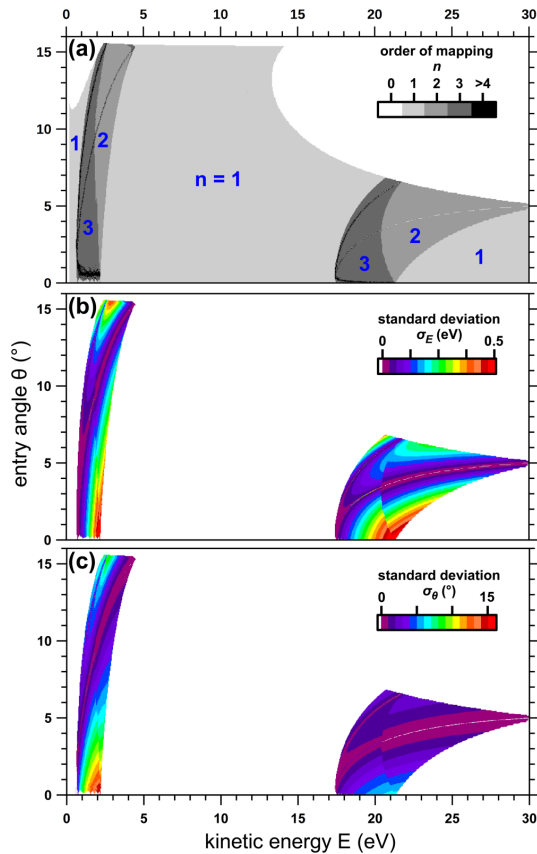


FIG. 4. (a) Order  $n$  of the forward mapping,<sup>21</sup> which transforms events from  $(\theta, E)$  in Fig. 3(a) to  $(r, t)$  in Fig. 3(b). In (b) and (c), the systematic error in energy ( $\sigma_E$ ) and angle ( $\sigma_\theta$ ) according to Eq. (1) due to the approximated backward mapping are shown, respectively. In conventional analysis, only regions with  $n = 1$  are considered.

it is homogeneous over the angular and energy range of the many-to-one mapping. For the same spectrometer settings as in Fig. 4(a), the systematic errors  $\sigma_E$  and  $\sigma_\theta$  are derived according to Eq. (1) and displayed in Figs. 4(b) and 4(c).

The maximum of the systematic error in energy  $\sigma_E$  for the specific spectrometer settings<sup>21</sup> in Fig. 4(b) is up to 0.45 eV in the region around 2 eV and around 22 eV for a small range of small emission angles. This value is only about a factor of 2 worse than the energy resolution in the conventional analysis of the spectrometer settings for a wide energy range,<sup>22</sup> which may be acceptable for experiments aiming only at a moderate energy resolution. The angular error  $\sigma_\theta$  in Fig. 4(c) is smaller than 7° except in the low energy region near  $E = 2$  eV or at large entry angles  $\theta \geq 14^\circ$ . The large  $\sigma_\theta$  in these regions can be understood by considering the focus of the ToF spectrometer, where photoelectrons with largely different emission angles are mapped onto a small area near the center  $r \approx 0$  of the 2D detector.<sup>26,27</sup>

For application to other energy ranges, a similar pattern as in Fig. 4(a) needs to be used according to the different kinetic ( $E_{kin}$ ) and pass energy ( $E_{pass}$ ) settings of the spectrometer.<sup>11,21</sup> When increasing  $E_{kin}$ , the middle  $n = 1$  region in Fig. 4(a) will shift towards higher energies. In addition, the ratio between its energetic extension to the value of  $E_{pass}$  will increase as the ratio  $E_{kin}/E_{pass}$  increases. As an example, the central  $n = 1$  region for  $(E_{kin}, E_{pass}) = (8, 60)$  eV has a width of about 15 eV at  $\theta = 0^\circ$  as can be seen in Fig. 4(a), and it expands to about 24 eV for the settings of  $E_{kin} = 16$  eV at the same  $E_{pass}$ . Accordingly, the many-to-one regions on the lower and higher energy sides will be shifted in energy. Moreover, as shown in Fig. 3(a), the many-to-one mapping occurs between  $(\theta, E)$  coordinates with comparable energies but different angles. Therefore, we may expect that  $\sigma_E$  in Fig. 4(b) would scale with the energy width of the many-to-one regions when varying  $E_{kin}$  and  $E_{pass}$ , whereas  $\sigma_\theta$  could remain sizable as in Fig. 4(c). As shown in Fig. 4(b), the maximum of  $\sigma_E$  for  $(E_{kin}, E_{pass}) = (8, 60)$  eV is about 0.45 eV at  $E \approx 2$  eV, and it increases up to about 1.3 eV at  $E \approx 7$  eV for the settings  $(E_{kin}, E_{pass}) = (16, 60)$  eV.

### C. Photoelectron spectroscopy (ARPES) on Ag(001)

The approximated backward mapping is demonstrated and compared with conventional one-to-one backward mapping in Fig. 5 for ARPES experiments on a Ag(001) surface. The photoelectrons are excited by a high-order harmonic light source<sup>28</sup> and analyzed by the ToF spectrometer presented in Secs. III A and III B. The settings of the spectrometer were a wide-angle-mode with a nominal kinetic energy ( $E_{kin}$ ) of 8 eV, a pass energy ( $E_{pass}$ ) of 60 eV. The corresponding energy and angular acceptance ranges are displayed by the grid in Fig. 3(a) as well as by the filled area in Fig. 4(a), having a central one-to-one mapping region within  $E = 9 \pm 4$  eV for  $\theta = \pm 15^\circ$ . The photon flux was estimated as  $3 \times 10^5$  photons/s, with a pulse duration of around 2 ps, an estimated bandwidth of 70 meV at the 32 eV photon energy, and a spot size measured on the sample of  $100 \pm 30 \mu\text{m}$ . The total acquisition time was 11 min. In Fig. 5(a), only photoelectron events at the  $(r, t)$  detector coordinates with a



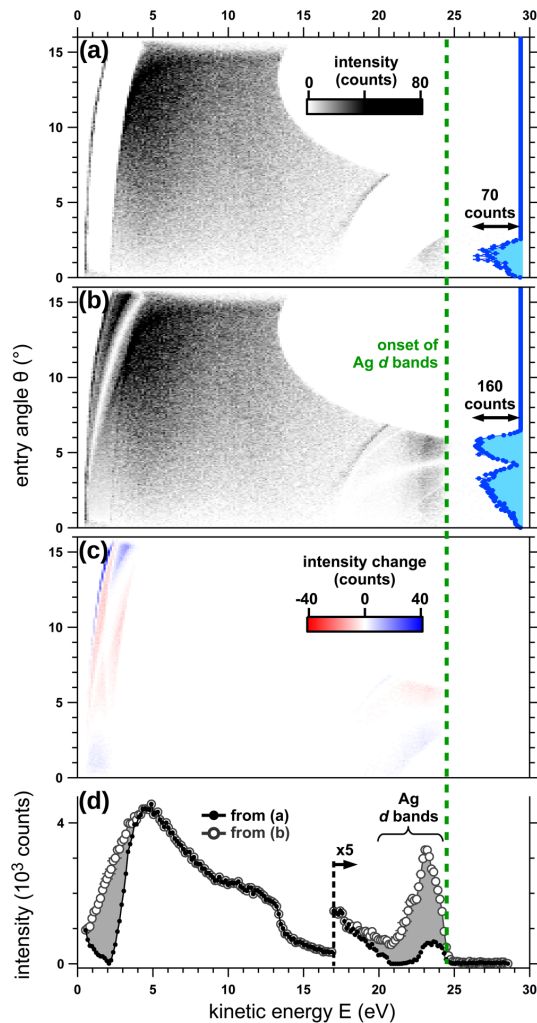


FIG. 5. Distribution of photoelectrons from Ag(001) excited by *s*-polarized light with 32 eV photon energy. Light incidence is parallel to the surface normal, and the entry angle  $0^\circ$  into the spectrometer corresponds to an emission angle of  $45^\circ$  from the surface normal. In (a), only the one-to-one backward mapping is used, and in (b) the approximated backward mapping is additionally applied. In (c), the change in the approximated backward mapping due to a more simplified weighting factor  $w_i = 1/n$  is shown. Angle-integrated spectra from (a) and (b) are shown in (d). The dashed line indicates the onset of emission from the Ag *d* bands about 4 eV below the Fermi-level. Filled spectra (blue) in (a) and (b) show the angular distribution integrated from 22 to 24 eV, with an error bar  $\sigma_\theta$  in (b) up to  $5^\circ$  according to Fig. 4(c).

one-to-one correspondence to the  $(\theta, E)$  emission coordinates are considered. In Fig. 5(b), the approximation method in Sec. II is additionally applied on the same measured dataset with the weighting factors in Eq. (2) in order to retrieve events from the *n*-to-one forward mapping by the spectrometer.

By comparing Figs. 5(a) and 5(b), we can clearly see that more photoelectron events are analyzed when the approximated backward mapping is used. More specifically, in the comparison in Fig. 5(d), a fourfold intensity increase

at the Ag *4d* bands can be clearly seen when using the approximated backward mapping. Therefore, the approximated backward mapping provides an opportunity to analyze more photoelectron events in an extended energy range as detected by the ToF-spectrometer.

In addition, the angular distributions of Ag *d* electrons from 22 to 24 eV are shown by the filled spectra in Figs. 5(a) and 5(b), with a corresponding error in Fig. 4(c) up to  $5^\circ$ . This sizable error is due to the focusing of electron trajectories with various emission angles near  $t = 170$  ns as can be seen in Fig. 3(b). Furthermore, in Fig. 5(c), we show the change in the case of more simplified weighting factors  $w_i = 1/n$  instead of Eq. (2). This change may be viewed as an estimation for the systematic error in the intensity.

Last but not least, we discuss the influence of the detector resolution to the spectra in Fig. 5(b). As an example, we consider the energy broadening ( $\Delta E$ ) due to the detector time resolution, which dominates over the contribution of the detector spatial resolution for our settings. From the forward mapping in Sec. III A, we can extract the dependence of the kinetic energy of electron ( $E$ ) on the time-of-flight ( $t$ ) as quantified by  $(\partial E/\partial t)_r$ . This quantity provides an estimation for the energy broadening due to a given resolution of the time-of-flight measurement. With an assumed time resolution  $\Delta t \approx 0.24$  ns in the experiments, we estimate an energy resolution by  $\Delta t(\partial E/\partial t)_r \approx 180$  meV at around 25 eV. This value is in agreement with our previous experiments with similar settings<sup>22</sup> and can be compared with the systematic energy error due to the approximated backward mapping in Fig. 4(b).

#### IV. SUMMARY

To summarize, we demonstrate an approximation method to extend the energy and angular range of photoelectrons that can be analyzed using time-of-flight (ToF) spectroscopy. Our approximation allows one to analyze photoelectron events whose emission coordinates  $(\theta, \phi, E)$  are mapped to the detector coordinates  $(x, y, t)$  in a many-to-one mapping. Conventionally, these events are detected in parallel with the events in the one-to-one mapping, but they are abandoned in the data analysis. In the approximation, we assume a given distribution among the multiple emission coordinates  $(\theta_i, \phi_i, E_i)$  that correspond to the same  $(x, y, t)$ . The resultant systematic errors in the retrieved energy and emission angles have upper bounds, and they are given by the maximum difference between the emission coordinates  $(\theta_i, \phi_i, E_i)$  that are mapped to the same detector coordinates  $(x, y, t)$  by the spectrometer. As a practical example, we measure photoelectrons from a Ag(001) surface using a commercial ToF spectrometer and analyze them with the approximated backward mapping. As a result, the photoelectrons distributed over a kinetic energy range from 0.5 to 25 eV can be analyzed in parallel. In combination with conventional ToF analysis, our approximation method assists to characterize photoelectrons more efficiently and is important for advanced spectroscopies with demanding statistics, such as coincidence electron spectroscopies at surfaces.<sup>22,29</sup> In addition, our method may be extended to spectrometers with non-cylindrical symmetries.

## ACKNOWLEDGMENTS

Technical support from R. Kulla, F. Helbig, and F. Weiss is gratefully acknowledged. The authors thank Professor J. Kirschner for his long-standing interest and support. This work is partially funded by the Deutsche Forschungsgemeinschaft through SFB-762 (B7, A3) and SFB/TRR-227 (A06).

<sup>1</sup>N. Mirsaleh-Kohan, W. D. Robertson, and R. N. Compton, *Mass Spectrom. Rev.* **27**, 237 (2008).

<sup>2</sup>A. Benninghoven, *Angew. Chem. Int. Ed.* **33**, 1023 (1994).

<sup>3</sup>G. Schönhense, K. Medjanik, and H.-J. Elmers, *J. Electron. Spectros. Relat. Phenomena* **200**, 94 (2015).

<sup>4</sup>D. Kühn, F. Sorgenfrei, E. Giangrisostomi, R. Jay, A. Musazay, R. Ovsyannikov, C. Strählmán, S. Svensson, N. Mårtensson, and A. Föhlisch, *J. Electron. Spectros. Relat. Phenomena* **224**, 45 (2018).

<sup>5</sup>K. Medjanik, O. Fedchenko, S. Chernov, D. Kutnyakhov, M. Ellguth, A. Oelsner, B. Schönhense, T. R. F. Peixoto, P. Lutz, C.-H. Min, F. Reinert, S. Däster, Y. Acremann, J. Viehhaus, W. Wurth, H. J. Elmers, and G. Schönhense, *Nat. Mater.* **16**, 615–621 (2017).

<sup>6</sup>C. Tusche, P. Goslawski, D. Kutnyakhov, M. Ellguth, K. Medjanik, H. J. Elmers, S. Chernov, R. Wallauer, D. Engel, A. Jankowiak, and G. Schönhense, *Appl. Phys. Lett.* **108**, 261602 (2016).

<sup>7</sup>D. Kutnyakhov, S. Chernov, K. Medjanik, R. Wallauer, C. Tusche, M. Ellguth, S. A. Nepijko, M. Krivenkov, J. Braun, S. Borek, J. Minár, H. Ebert, H. J. Elmers, and G. Schönhense, *Sci. Rep.* **6**, 29394 (2016).

<sup>8</sup>U. B. Cappel, S. Plogmaker, J. A. Terschlüsen, T. Leitner, E. M. J. Johansson, T. Edvinsson, A. Sandell, O. Karis, H. Siegbahn, S. Svensson, N. Mårtensson, H. Rensmo, and J. Söderström, *Phys. Chem. Chem. Phys.* **18**, 21921 (2016).

<sup>9</sup>C. Strählmán, R. Sankari, M. Lundqvist, G. Öhrwall, R. Ovsyannikov, S. Svensson, N. Mårtensson, and R. Nyholm, *J. Phys. Conf. Ser.* **425**, 092011 (2013).

<sup>10</sup>P. D. C. King, R. C. Hatch, M. Bianchi, R. Ovsyannikov, C. Lupulescu, G. Landolt, B. Slomski, J. H. Dil, D. Guan, J. L. Mi, E. D. L. Rienks, J. Fink, A. Lindblad, S. Svensson, S. Bao, G. Balakrishnan, B. B. Iversen, J. Osterwalder, W. Eberhardt, F. Baumberger, and P. Hofmann, *Phys. Rev. Lett.* **107**, 096802 (2011).

<sup>11</sup>M. H. Berntsen, O. Götzberg, and O. Tjemberg, *Rev. Sci. Instrum.* **82**, 095113 (2011).

<sup>12</sup>A. Oelsner, O. Schmidt, M. Schicketanz, M. Klais, G. Schönhense, V. Mergel, O. Jagutzki, and H. Schmidt-Boecking, *Rev. Sci. Instrum.* **72**, 3968 (2001).

<sup>13</sup>R. Ovsyannikov, P. Karlsson, M. Lundqvist, C. Lupulescu, W. Eberhardt, A. Föhlisch, S. Svensson, and N. Mårtensson, *J. Electron Spectros. Relat. Phenomena* **191**, 92 (2013).

<sup>14</sup>B. Wannberg, *Nuclear Instrum. Methods Phys. Res. A* **601**, 182 (2009).

<sup>15</sup>A. Trüttschler, M. Huth, C.-T. Chiang, R. Kamrla, F. O. Schumann, J. Kirschner, and W. Widdra, *Phys. Rev. Lett.* **118**, 136401 (2017).

<sup>16</sup>T. Arion and U. Hergenbahn, *J. Electron Spectros. Relat. Phenomena* **200**, 222 (2015).

<sup>17</sup>F. O. Schumann, C. Winkler, and J. Kirschner, *Phys. Status Solidi (b)* **246**, 1483 (2009).

<sup>18</sup>G. Stefani, S. Iacobucci, A. Ruocco, and R. Gotter, *J. Electron Spectrosc. Relat. Phenom.* **127**, 1 (2002).

<sup>19</sup>M. Hattass, T. Jahnke, S. Schössler, A. Czasch, M. Schöffler, L. P. H. Schmidt, B. Ulrich, O. Jagutzki, F. O. Schumann, C. Winkler, J. Kirschner, R. Dörmer, and H. Schmidt-Böcking, *Phys. Rev. B* **77**, 165432 (2008).

<sup>20</sup>This simplified argument is valid for cases where the angular acceptance does not strongly depend on the energy, and it can be refined by considering the energy dependent joint acceptance.

<sup>21</sup>Themis 1000, SPECS Surface Nano Analysis GmbH, Berlin, Germany.

<sup>22</sup>M. Huth, C.-T. Chiang, A. Trüttschler, F. O. Schumann, J. Kirschner, and W. Widdra, *Appl. Phys. Lett.* **104**, 061602 (2014).

<sup>23</sup> $\sigma_E^{max}$  occurs when, for example,  $w_1 = 1$ ,  $w_2 = 0$ ,  $E_1 = E_{max}$ , and  $E_m = E_2 = E_{min}$ .

<sup>24</sup>The spectrometer model is provided by the manufacturer,<sup>21</sup> and the trajectories of photoelectrons are calculated by the commercial program: SIMION, version 8, Scientific Instrument Services, Inc., USA.

<sup>25</sup>In experiments, the position of  $r = 0$  can be estimated by the focusing of electron trajectories with various emission angles  $\theta$  at a given time-of-flight  $t$ , for example, near  $t = 170$  ns in Fig. 3(b).

<sup>26</sup>T. Mulvey and M. J. Wallington, *Rep. Prog. Phys.* **36**, 347 (1973).

<sup>27</sup>A. B. El-Kareh and J. C. J. El-Kareh, *Electron Beams, Lenses, and Optics* (Academic Press, 1970), pp. 185–245.

<sup>28</sup>C.-T. Chiang, M. Huth, A. Trüttschler, F. O. Schumann, J. Kirschner, and W. Widdra, *J. Electron Spectros. Relat. Phenomena* **200**, 15 (2015).

<sup>29</sup>C. Lupulescu, T. Arion, U. Hergenbahn, R. Ovsyannikov, M. Förstel, G. Gavrilă, and W. Eberhardt, *J. Electron Spectros. Relat. Phenomena* **191**, 104 (2013).

# Bibliography

- [1] H. P. Bonzel and Ch. Kleint. [On the history of photoemission](#). *Prog. Surf. Sci.* **49**, 107 (1995).
- [2] F. Reinert and S. Hüfner. [Photoemission spectroscopy-from early days to recent applications](#). *New J. Phys.* **7**, 97 (2005).
- [3] F. J. Himpsel. [Photoemission from solids](#). *Nucl. Instr. Meth. Phys. Res. B* **208**, 753 (1983).
- [4] G. Schönhense, K. Medjanik, and H.-J. Elmers. [Space-, time- and spin-resolved photoemission](#). *J. Electron Spectrosc. Relat. Phenomena* **200**, 94 (2015).
- [5] L. H. Hall, J. Bardeen, and F. J. Blatt. [Infrared absorption spectrum of germanium](#). *Phys. Rev.* **95**, 559 (1954).
- [6] R. Braunstein and E. O. Kane. [The valence band structure of the III-V compounds](#). *J. Phys. Chem. Solids* **23**, 1423 (1962).
- [7] J. C. Phillips. [Band structure of silicon, germanium, and related semiconductors](#). *Phys. Rev.* **125**, 1931 (1962).
- [8] B. R. Cooper, H. Ehrenreich, and H. R. Philipp. [Optical properties of noble metals. II](#). *Phys. Rev.* **138**, A494 (1965).
- [9] M. Cardona. [Optical properties and band structure of SrTiO<sub>3</sub> and BaTiO<sub>3</sub>](#). *Phys. Rev.* **140**, A651 (1965).
- [10] D. Shoenberg. [The de Haas-van Alphen effect and the electronic structure of metals](#). *Proc. Phys. Soc.* **79**, 1 (1962).
- [11] S. J. Williamson, S. Foner, and M. S. Dresselhaus. [de Haas-van Alphen Effect in pyrolytic and single-crystal graphite](#). *Phys. Rev.* **140**, A1429 (1965).
- [12] J. B. Ketterson and L. R. Windmiller. [de Haas-van Alphen effect in platinum](#). *Phys. Rev. B* **2**, 4813 (1970).
- [13] B. Gregory, J. Arthur, and G. Seidel. [Measurements of the Fermi surface of SrTiO<sub>3</sub>:Nb](#). *Phys. Rev. B* **19**, 1039 (1979).
- [14] A. I. Coldea. [Quantum oscillations probe the normal electronic states of novel superconductors](#). *Phil. Trans. R. Soc. A* **368**, 3503 (2010).
- [15] E. O. Kane. [Implications of crystal momentum conservation in photoelectric emission for band-structure measurements](#). *Phys. Rev. Lett.* **12**, 97 (1964).
- [16] F. J. Himpsel. [Angle-resolved measurements of the photoemission of electrons in the study of solids](#). *Adv. Phys.* **32**, 1 (1983).
- [17] R. Courths and S. Hüfner. [Photoemission experiments on copper](#). *Phys. Rep.* **112**, 53 (1984).
- [18] G. Schönhense. [Spin-dependent effects in photoemission](#). *Vacuum* **41**, 506 (1990).
- [19] C. M. Schneider and J. Kirschner. [Spin- and angle-resolved photoelectron spectroscopy from solid surfaces with circularly polarized light](#). *Cri. Rev. Solid Stat.* **20**, 179 (1995).

- [20] P. D. Johnson. [Spin-polarized photoemission](#). *Rep. Prog. Phys.* **60**, 1217 (1997).
- [21] A. Damascelli, Z. Hussain, and Z.-X. Shen. [Angle-resolved photoemission studies of the cuprate superconductors](#). *Rev. Mod. Phys.* **75**, 473 (2003).
- [22] J. H. Dil. [Spin and angle resolved photoemission on non-magnetic low-dimensional systems](#). *J. Phys.: Condens. Matter* **21**, 403001 (2009).
- [23] R. Matzdorf. [Investigation of line shapes and line intensities by high-resolution UV-photoemission spectroscopy - Some case studies on noble-metal surfaces](#). *Surf. Sci. Rep.* **30**, 153 (1998).
- [24] P. Heimann, J. Hermanson, H. Miosga, and H. Neddermeyer. [d-like surface-state bands on Cu\(100\) and Cu\(111\) observed in angle-resolved photoemission spectroscopy](#). *Phys. Rev. B* **20**, 3059 (1979).
- [25] M. Pessa, P. Heimann, and H. Neddermeyer. [Photoemission and electronic structure of iron](#). *Phys. Rev. B* **14**, 3488 (1976).
- [26] R. Haight. [Electron dynamics at surfaces](#). *Surf. Sci. Rep.* **21**, 275 (1995).
- [27] R. Haight and D. R. Peale. [Tunable photoemission with harmonics of subpicosecond lasers](#). *Rev. Sci. Instrum.* **65**, 1853 (1994).
- [28] A. McPherson, G. Gibson, H. Jara, U. Johann, T. S. Luk, I. A. McIntyre, K. Boyer, and C. K. Rhodes. [Studies of multiphoton production of vacuum-ultraviolet radiation in the rare gases](#). *J. Opt. Soc. Am. B* **4**, 595 (1987).
- [29] M. Ferray, A. L'Huillier, X. F. Li, L. A. Lompré, G. Mainfray, and C. Manus. [Multiple-harmonic conversion of 1064 nm radiation in rare gases](#). *J. Phys. B: At. Mol. Opt. Phys.* **21**, L31 (1988).
- [30] C. Winterfeldt, C. Spielmann, and G. Gerber. [Colloquium: Optimal control of high-harmonic generation](#). *Rev. Mod. Phys.* **80**, 117 (2008).
- [31] C. Corder, P. Zhao, J. Bakalis, X. Li, M. D. Kershish, A. R. Muraca, M. G. White, and T. K. Allison. [Ultrafast extreme ultraviolet photoemission without space charge](#). *Struct. Dyn.* **5**, 054301 (2018).
- [32] B. Frietsch, R. Carley, K. Döbrich, C. Gahl, M. Teichmann, O. Schwarzkopf, Ph. Wernet, and M. Weinelt. [A high-order harmonic generation apparatus for time- and angle-resolved photoelectron spectroscopy](#). *Rev. Sci. Instrum* **84**, 075106 (2013).
- [33] Private communication with [Prof. Michael Bauer](#) and Gerald Rohde, Institut für Experimentelle und Angewandte Physik, Christian-Albrechts-Universität zu Kiel, Germany (2012).
- [34] S. H. Chew, F. Süßmann, C. Späth, A. Wirth, J. Schmidt, S. Zherebtsov, A. Guggenmos, A. Oelsner, N. Weber, J. Kapaldo, A. Gliserin, M. I. Stockman, M. F. Kling, and U. Kleineberg. [Time-of-flight-photoelectron emission microscopy on plasmonic structures using attosecond extreme ultraviolet pulses](#). *Appl. Phys. Lett.* **100**, 051904 (2012).
- [35] T. Rohwer, S. Hellmann, M. Wiesenmayer, C. Sohrt, A. Stange, B. Slomski, A. Carr, Y. Liu, L. M. Avila, Ma. Kalläne, S. Mathias, L. Kipp, K. Rossnagel, and M. Bauer. [Collapse of long-range charge order tracked by time-resolved photoemission at high momenta](#). *Nature* **471**, 490 (2011).
- [36] G. L. Dakovski, Y. Li, T. Durakiewicz, and G. Rodriguez. [Tunable ultrafast extreme ultraviolet source for time- and angle-resolved photoemission spectroscopy](#). *Rev. Sci. Instrum.* **81**, 073108 (2010).
- [37] A. Mikkelsen, J. Schwenke, T. Fordell, G. Luo, K. Klünder, E. Hilner, N. Anttu, A. A. Zakharov, E. Lundgren, J. Mauritsson, J. N. Andersen, H. Q. Xu, and A. L'Huillier. [Photoemission electron microscopy using extreme ultraviolet attosecond pulse trains](#). *Rev. Sci. Instrum.* **80**, 123703 (2009).
- [38] A. L. Cavalieri, N. Müller, Th. Uphues, V. S. Yakovlev, Baltuška, B. A. Horvath, B. Schmidt, L. Blümel, R. Holzwarth, S. Hendel, M. Drescher, U. Kleineberg, P. M. Echenique, R. Kienberger, F. Krausz, and U. Heinzmann. [Attosecond spectroscopy in condensed matter](#). *Nature* **449**, 1029 (2007).

- 
- [39] M. Bauer. [Femtosecond ultraviolet photoelectron spectroscopy of ultra-fast surface processes](#). *J. Phys. D: Appl. Phys.* **38**, R253 (2005).
- [40] J. Graf, S. Hellmann, C. Jozwiak, C. L. Smallwood, Z. Hussain, R. A. Kaindl, L. Kipp, K. Rossnagel, and A. Lanzara. [Vacuum space charge effect in laser-based solid-state photoemission spectroscopy](#). *J. Appl. Phys.* **107**, 014912 (2010).
- [41] S. Hellmann, K. Rossnagel, M. Marczynski-Bühlow, and L. Kipp. [Vacuum space-charge effects in solid-state photoemission](#). *Phys. Rev. B* **79**, 035402 (2009).
- [42] G. Schönhense, A. Oelsner, O. Schmidt, G. H. Fecher, V. Mergel, O. Jagutzki, and H. Schmidt-Böcking. [Time-of-flight photoemission electron microscopy – a new way to chemical surface analysis](#). *Surf. Sci.* **480**, 180 (2001).
- [43] P. S. Kirchmann, L. Rettig, D. Nandi, U. Lipowski, M. Wolf, and U. Bovensiepen. [A time-of-flight spectrometer for angle-resolved detection of low energy electrons in two dimensions](#). *Appl. Phys. A* **91**, 211 (2008).
- [44] M. H. Berntsen, O. Götberg, and O. Tjernberg. [An experimental setup for high resolution 10.5 eV laser-based angle-resolved photoelectron spectroscopy using a time-of-flight electron analyzer](#). *Rev. Sci. Instrum.* **82**, 095113 (2011).
- [45] G. Öhrwall, P. Karlsson, M. Wirde, M. Lundqvist, P. Andersson, D. Ceolin, B. Wannberg, T. Kachel, H. Dürr, W. Eberhardt, and S. Svensson. [A new energy and angle resolving electron spectrometer – First results](#). *J. Electron Spectrosc. Relat. Phenomena* **183**, 125 (2011).
- [46] R. Ovsyannikov, P. Karlsson, M. Lundqvist, C. Lupulescu, W. Eberhardt, A. Föhlisch, S. Svensson, and N. Mårtensson. [Principles and operation of a new type of electron spectrometer – ArTOF](#). *J. Electron Spectrosc. Relat. Phenomena* **191**, 92 (2013).
- [47] C. Tusche, A. Krasnyuk, and J. Kirschner. [Spin resolved bandstructure imaging with a high resolution momentum microscope](#). *Ultramicroscopy* **159**, 520 (2015).
- [48] B. Krömker, M. Escher, D. Funnemann, D. Hartung, H. Engelhard, and J. Kirschner. [Development of a momentum microscope for time resolved band structure imaging](#). *Rev. Sci. Instrum.* **79**, 053702 (2008).
- [49] M. Kotsugi, W. Kuch, F. Offi, L. I. Chelaru, and J. Kirschner. [Microspectroscopic two-dimensional Fermi surface mapping using a photoelectron emission microscope](#). *Rev. Sci. Instrum.* **74**, 2754 (2003).
- [50] S. Förster, K. Meinel, R. Hammer, Martin Trautmann, and W. Widdra. [Quasicrystalline structure formation in a classical crystalline thin-film system](#). *Nature* **502**, 215 (2013).
- [51] S. Förster, J. I. Flege, E. M. Zollner, F. O. Schumann, R. Hammer, A. Bayat, K.-M. Schindler, J. Falta, and W. Widdra. [Growth and decay of a two-dimensional oxide quasicrystal: High-temperature \*in situ\* microscopy](#). *Annalen der Physik* **529**, 1600250 (2017).
- [52] J. Friedel. [Do metallic quasicrystals and associated Frank and Kasper phases follow the Hume Rothery rules?](#) *Helv. Phys. Acta* **61**, 538 (1988).
- [53] A.-P. Tsai. [A test of Hume-Rothery rules for stable quasicrystals](#). *J. Non-Cryst. Solids* **334-335**, 317 (2004).
- [54] C. Caroli, D. Lederer-Rozenblatt, B. Roulet, and D. Saint-James. [Inelastic effects in photoemission: Microscopic formulation and qualitative discussion](#). *Phys. Rev. B* **8**, 4552 (1973).
- [55] W. L. Schaich and N. W. Ashcroft. [Model calculations in the theory of photoemission](#). *Phys. Rev. B* **3**, 2452 (1971).
- [56] P. J. Feibelman and D. E. Eastman. [Photoemission spectroscopy - Correspondence between quantum theory and experimental phenomenology](#). *Phys. Rev. B* **10**, 4932 (1974).



- [57] B. Feuerbacher and R. F. Willis. [Photoemission and electron states at clean surfaces](#). *J. Phys. C: Solid State Phys.* **9**, 169 (1976).
- [58] L. Hedin and J. D. Lee. [Sudden approximation in photoemission and beyond](#). *J. Electron Spectrosc. Relat. Phenomena* **124**, 289 (2002).
- [59] G. Borstel. [Theoretical aspects of photoemission](#). *Appl. Phys. A* **38**, 193 (1985).
- [60] L. F. Wagner, Z. Hussain, C. S. Fadley, and R. J. Baird. [Angular-dependent XPS valence-band spectra from single-crystal copper](#). *Solid State Commun.* **21**, 453 (1977).
- [61] Y. Takata, Y. Kayanuma, S. Oshima, S. Tanaka, M. Yabashi, K. Tamasaku, Y. Nishino, M. Matsunami, R. Eguchi, A. Chainani, M. Oura, T. Takeuchi, Y. Senba, H. Ohashi, S. Shin, and T. Ishikawa. [Recoil effect of photoelectrons in the Fermi edge of simple metals](#). *Phys. Rev. Lett.* **101**, 137601 (2008).
- [62] A. X. Gray, C. Papp, S. Ueda, B. Balke, Y. Yamashita, L. Plucinski, J. Minár, J. Braun, E. R. Ylvisaker, C. M. Schneider, W. E. Pickett, H. Ebert, K. Kobayashi, and C. S. Fadley. [Probing bulk electronic structure with hard x-ray angle-resolved photoemission](#). *Nat. Mater.* **10**, 759 (2011).
- [63] J. Minár, J. Braun, and H. Ebert. [Recent developments in the theory of HARPES](#). *J. Electron Spectrosc. Relat. Phenomena* **190**, 159 (2013).
- [64] M. Sperlich, C. König, G. Güntherodt, A. Sekiyama, G. Funabashi, M. Tsunekawa, S. Imada, A. Shigemoto, K. Okada, A. Higashiya, M. Yabashi, K. Tamasaku, T. Ishikawa, V. Renken, T. Allmers, M. Donath, and S. Suga. [Intrinsic correlated electronic structure of CrO<sub>2</sub> revealed by hard x-ray photoemission spectroscopy](#). *Phys. Rev. B* **87**, 235138 (2013).
- [65] J. B. Pendry and J. F. L. Hopkinson. [Theory of photoemission](#). *J. Phys. Colloques* **39**, C4–142 (1978).
- [66] J. B. Pendry. [Angular dependence of electron emission from surfaces](#). *J. Phys. C: Solid State Phys.* **8**, 2413 (1975).
- [67] G. D. Mahan. [Theory of photoemission in simple metals](#). *Phys. Rev. B* **2**, 4334 (1970).
- [68] J. Anderson and G. J. Lapeyre. [Chemisorption-induced surface umklapp processes in angle-resolved synchrotron photoemission from W\(001\)](#). *Phys. Rev. Lett.* **36**, 376 (1976).
- [69] A. Tamai, W. Meevasana, P. D. C. King, C. W. Nicholson, A. de la Torre, E. Rozbicki, and F. Baumberger. [Spin-orbit splitting of the Shockley surface state on Cu\(111\)](#). *Phys. Rev. B* **87**, 075113 (2013).
- [70] F. O. Schumann, Y. Aliaev, I. Kostanovskiy, G. Di Filippo, Z. Wei, and J. Kirschner. [Electron pair emission from surfaces: Intensity relations](#). *Phys. Rev. B* **93**, 235128 (2016).
- [71] R. Herrmann, S. Samarin, H. Schwabe, and J. Kirschner. [Two electron photoemission in solids](#). *Phys. Rev. Lett.* **81**, 2148 (1998).
- [72] F. O. Schumann, C. Winkler, G. Kerherve, and J. Kirschner. [Mapping the electron correlation in two-electron photoemission](#). *Phys. Rev. B* **73**, 041404 (2006).
- [73] F. O. Schumann, C. Winkler, and J. Kirschner. [Correlation effects in two electron photoemission](#). *Phys. Rev. Lett.* **98**, 257604 (2007).
- [74] M. Hattass, T. Jahnke, S. Schössler, A. Czasch, M. Schöffler, L. Ph. H. Schmidt, B. Ulrich, O. Jagutzki, F. O. Schumann, C. Winkler, J. Kirschner, R. Dörner, and H. Schmidt-Böcking. [Dynamics of two-electron photoemission from Cu\(111\)](#). *Phys. Rev. B* **77**, 165432 (2008).
- [75] The angular acceptance is estimated as  $25^\circ \times 0.3^\circ$ , private communications with Prof. Felix Baumberger, Department of Quantum Matter Physics, University of Geneva, Switzerland (2019).
- [76] T. A. Carlson. [Double electron ejection resulting from photo-ionization in the outermost shell of He, Ne, and Ar, and its relationship to electron correlation](#). *Phys. Rev.* **156**, 142 (1967).

- [77] F. W. Byron and C. J. Joachain. [Multiple ionization processes in helium](#). *Phys. Rev.* **164**, 1 (1967).
- [78] R. Wehlitz, F. Heiser, O. Hemmers, B. Langer, A. Menzel, and U. Becker. [Electron-energy and -angular distributions in the double photoionization of helium](#). *Phys. Rev. Lett.* **67**, 3764 (1991).
- [79] O. Schwarzkopf, B. Krässig, J. Elmiger, and V. Schmidt. [Energy- and angle-resolved double photoionization in helium](#). *Phys. Rev. Lett.* **70**, 3008 (1993).
- [80] T. Schneider, P. L. Chocian, and J.-M. Rost. [Separation and identification of dominant mechanisms in double photoionization](#). *Phys. Rev. Lett.* **89**, 073002 (2002).
- [81] Y. Hikosaka, T. Aoto, P. Lablanquie, F. Penent, E. Shigemasa, and K. Ito. [Experimental investigation of core-valence double photoionization](#). *Phys. Rev. Lett.* **97**, 053003 (2006).
- [82] E. P. Møansson, D. Guénot, C. L. Arnold, D. Kroon, S. Kasper, J. M. Dahlström, E. Lindroth, A. S. Kheifets, A. L’Huillier, S. L. Sorensen, and M. Gisselbrecht. [Double ionization probed on the attosecond timescale](#). *Nat. Phys.* **10**, 207 (2014).
- [83] R. Wehlitz. [Double photoionization of hydrocarbons and aromatic molecules](#). *J. Phys. B: At. Mol. Opt. Phys.* **49**, 222004 (2016).
- [84] P. A. Carpeggiani, E. V. Gryzlova, M. Reduzzi, A. Dubrouil, D. Faccialá, M. Negro, E. Lindroth, K. Ueda, S. M. Burkov, F. Frassetto, F. Stienkemeier, Y. Ovcharenko, O. Plekan, P. Finetti, K. C. Prince, C. Callegari, A. N. Grum-Grzhimailo, and G. Sansone. [Complete reconstruction of bound and unbound electronic wavefunctions in two-photon double ionization](#). *Nat. Phys.* **15**, 170 (2019).
- [85] J. L. Robins. [A review of Auger photoelectron coincidence spectroscopy](#). *Prog. Surf. Sci.* **48**, 167 (1995).
- [86] G. Stefani, R. Gotter, A. Ruocco, F. Offi, F. Da Pieve, S. Iacobucci, A. Morgante, A. Verdini, A. Liscio, H. Yao, and R. A. Bartynski. [Photoelectron-Auger electron coincidence study for condensed matter](#). *J. Electron Spectrosc. Relat. Phenomena* **141**, 149 (2004).
- [87] R. Gotter, M. Sbroscia, M. Caminale, S. R. Vaidya, E. Perfetto, R. Moroni, F. Bisio, S. Iacobucci, G. Di Filippo, F. Offi, A. Ruocco, G. Stefani, L. Mattera, and M. Cini. [Monitoring antiferromagnetism via angle-resolved Auger photoelectron coincidence spectroscopy: The case of NiO/Ag\(001\)](#). *Phys. Rev. B* **88**, 094403 (2013).
- [88] G. Di Filippo, F. O. Schumann, S. Patil, Z. Wei, G. Stefani, G. Fratesi, M. I. Trioni, and J. Kirschner. [Electron coincidence studies of sulfur-overlayers on Cu\(001\) and Ni\(001\) surfaces](#). *J. Electron Spectrosc. Relat. Phenomena* **211**, 32 (2016).
- [89] Z. Wei, F. O. Schumann, C. H. Li, L. Behnke, G. Di Filippo, G. Stefani, and J. Kirschner. [Dynamic screening probed by core-resonant double photoemission from surfaces](#). *Phys. Rev. Lett.* **113**, 267603 (2014).
- [90] R. Gotter, G. Fratesi, R. A. Bartynski, F. Da Pieve, F. Offi, A. Ruocco, S. Ugenti, M. I. Trioni, G. P. Brivio, and G. Stefani. [Spin-dependent on-site electron correlations and localization in itinerant ferromagnets](#). *Phys. Rev. Lett.* **109**, 126401 (2012).
- [91] M. Cini, E. Perfetto, R. Gotter, F. Offi, A. Ruocco, and G. Stefani. [Insight on hole-hole interaction and magnetic order from dichroic Auger-photoelectron coincidence spectra](#). *Phys. Rev. Lett.* **107**, 217602 (2011).
- [92] R. Gotter, F. Offi, F. Da Pieve, A. Ruocco, G. Stefani, S. Ugenti, M. I. Trioni, and R. A. Bartynski. [Electronic and magnetic properties of thin films probed by Auger photoelectron coincidence spectroscopy \(APECS\)](#). *J. Electron Spectrosc. Relat. Phenomena* **161**, 128 (2007).
- [93] W. S. M. Werner, W. Smekal, H. Störi, H. Winter, G. Stefani, A. Ruocco, F. Offi, R. Gotter, A. Morgante, and F. Tommasini. [Emission-depth-selective Auger photoelectron coincidence spectroscopy](#). *Phys. Rev. Lett.* **94**, 038302 (2005).
- [94] F. O. Schumann, C. Winkler, and J. Kirschner. [Sensing the electron–electron correlation in solids via double photoemission](#). *phys. status solidi (b)* **246**, 1483 (2009).

- [95] F. O. Schumann. [Studying the electron-electron correlation by pair emission from surfaces](#). Habilitation, Martin-Luther-Universität Halle-Wittenberg (2012).
- [96] J. Berakdar. [Emission of correlated electron pairs following single-photon absorption by solids and surfaces](#). *Phys. Rev. B* **58**, 9808 (1998).
- [97] N. Fominykh, J. Henk, J. Berakdar, P. Bruno, H. Gollisch, and R. Feder. [Theory of two-electron photoemission from surfaces](#). *Solid State Commun.* **113**, 665 (2000).
- [98] N. Fominykh, J. Berakdar, J. Henk, and P. Bruno. [Spectroscopy of the electron-electron interaction in solids](#). *Phys. Rev. Lett.* **89**, 086402 (2002).
- [99] Y. Pavlyukh, M. Schüler, and J. Berakdar. [Single- or double-electron emission within the Keldysh nonequilibrium Green's function and Feshbach projection operator techniques](#). *Phys. Rev. B* **91**, 155116 (2015).
- [100] M. Protopapas, C. H. Keitel, and P. L. Knight. [Atomic physics with super-high intensity lasers](#). *Rep. Prog. Phys.* **60**, 389 (1997).
- [101] T. Brabec and F. Krausz. [Intense few-cycle laser fields: Frontiers of nonlinear optics](#). *Rev. Mod. Phys.* **72**, 545 (2000).
- [102] F. Krausz and M. Ivanov. [Attosecond physics](#). *Rev. Mod. Phys.* **81**, 163 (2009).
- [103] M. Hohenleutner, F. Langer, O. Schubert, M. Knorr, U. Huttner, S. W. Koch, M. Kira, and R. Huber. [Real-time observation of interfering crystal electrons in high-harmonic generation](#). *Nature* **523**, 572 (2015).
- [104] M. Sivilis, M. Taucer, G. Vampa, K. Johnston, A. Staudte, A. Y. Naumov, D. M. Villeneuve, C. Ropers, and P. B. Corkum. [Tailored semiconductors for high-harmonic optoelectronics](#). *Science* **357**, 303 (2017).
- [105] S. Y. Kruchinin, F. Krausz, and V. S. Yakovlev. [Colloquium: Strong-field phenomena in periodic systems](#). *Rev. Mod. Phys.* **90**, 021002 (2018).
- [106] L. V. Keldysh. [Ionization in the field of a strong electromagnetic wave](#). *Sov. Phys. JETP* **20**, 1307 (1965).
- [107] P. B. Corkum. [Plasma perspective on strong field multiphoton ionization](#). *Phys. Rev. Lett.* **71**, 1994 (1993).
- [108] H. R. Reiss. [Effect of an intense electromagnetic field on a weakly bound system](#). *Phys. Rev. A* **22**, 1786 (1980).
- [109] T. F. Gallagher. [Above-threshold ionization in low-frequency limit](#). *Phys. Rev. Lett.* **61**, 2304 (1988).
- [110] J. L. Krause, K. J. Schafer, and K. C. Kulander. [High-order harmonic generation from atoms and ions in the high intensity regime](#). *Phys. Rev. Lett.* **68**, 3535 (1992).
- [111] A. L'Huillier, M. Lewenstein, P. Salières, Ph. Balcou, M. Yu. Ivanov, J. Larsson, and C. G. Wahlström. [High-order harmonic-generation cutoff](#). *Phys. Rev. A* **48**, R3433 (1993).
- [112] M. Lewenstein, Ph. Balcou, M. Yu. Ivanov, A. L'Huillier, and P. B. Corkum. [Theory of high-harmonic generation by low-frequency laser fields](#). *Phys. Rev. A* **49**, 2117 (1994).
- [113] T. Popmintchev, M.-C. Chen, P. Arpin, M. M. Murnane, and H. C. Kapteyn. [The attosecond nonlinear optics of bright coherent X-ray generation](#). *Nat. Photonics* **4**, 822 (2010).
- [114] A. L'Huillier, K. J. Schafer, and K. C. Kulander. [Higher-order harmonic generation in xenon at 1064 nm: The role of phase matching](#). *Phys. Rev. Lett.* **66**, 2200 (1991).
- [115] M. Lewenstein, P. Salières, and A. L'Huillier. [Phase of the atomic polarization in high-order harmonic generation](#). *Phys. Rev. A* **52**, 4747 (1995).

- [116] A. L'Huillier, P. Balcou, S. Candel, K. J. Schafer, and K. C. Kulander. [Calculations of high-order harmonic-generation processes in xenon at 1064 nm](#). *Phys. Rev. A* **46**, 2778 (1992).
- [117] A. L'Huillier and Ph. Balcou. [High-order harmonic generation in rare gases with a 1-ps 1053-nm laser](#). *Phys. Rev. Lett.* **70**, 774 (1993).
- [118] P. Salières, A. L'Huillier, and M. Lewenstein. [Coherence Control of High-Order Harmonics](#). *Phys. Rev. Lett.* **74**, 3776 (1995).
- [119] A. Rundquist, C. G. Durfee, Z. Chang, C. Herne, S. Backus, M. M. Murnane, and H. C. Kapteyn. [Phase-matched generation of coherent soft x-rays](#). *Science* **280**, 1412 (1998).
- [120] C. G. Durfee, A. R. Rundquist, S. Backus, C. Herne, M. M. Murnane, and H. C. Kapteyn. [Phase matching of high-order harmonics in hollow waveguides](#). *Phys. Rev. Lett.* **83**, 2187 (1999).
- [121] C. M. Heyl, J. Gädde, A. L'Huillier, and U. Höfer. [High-order harmonic generation with  \$\mu\$ J laser pulses at high repetition rates](#). *J. Phys. B: At. Mol. Opt. Phys.* **45**, 074020 (2012).
- [122] C. M. Heyl, C. L. Arnold, A. Couairon, and A. L'Huillier. [Introduction to macroscopic power scaling principles for high-order harmonic generation](#). *J. Phys. B: At. Mol. Opt. Phys.* **50**, 013001 (2016).
- [123] C. M. Heyl, H. Coudert-Alteirac, M. Miranda, M. Louisy, K. Kovacs, V. Tosa, E. Balogh, K. Varjú, A. L'Huillier, A. Couairon, and C. L. Arnold. [Scale-invariant nonlinear optics in gases](#). *Optica* **3**, 75 (2016).
- [124] J. Rothhardt, M. Krebs, S. Hädrich, S. Demmler, J. Limpert, and A. Tünnermann. [Absorption-limited and phase-matched high harmonic generation in the tight focusing regime](#). *New J. Phys.* **16**, 033022 (2014).
- [125] C.-G. Wahlström, J. Larsson, A. Persson, T. Starczewski, S. Svanberg, P. Salières, Ph. Balcou, and A. L'Huillier. [High-order harmonic generation in rare gases with an intense short-pulse laser](#). *Phys. Rev. A* **48**, 4709 (1993).
- [126] M. Schnürer, Z. Cheng, M. Hentschel, G. Tempea, P. Kálmán, T. Brabec, and F. Krausz. [Absorption-limited generation of coherent ultrashort soft-x-ray pulses](#). *Phys. Rev. Lett.* **83**, 722 (1999).
- [127] S. Kim, J. Jin, Y.-J. Kim, I.-Y. Park, Y. Kim, and S.-W. Kim. [High-harmonic generation by resonant plasmon field enhancement](#). *Nature* **453**, 757 (2008).
- [128] M. Sivis, M. Duwe, B. Abel, and C. Ropers. [Nanostructure-enhanced atomic line emission](#). *Nature* **485**, E1 (2012).
- [129] M. Sivis, M. Duwe, B. Abel, and C. Ropers. [Extreme-ultraviolet light generation in plasmonic nanostructures](#). *Nat. Phys.* **9**, 304 (2013).
- [130] M. B. Raschke. [High-harmonic generation with plasmonics: feasible or unphysical?](#) *Ann. Phys* **525**, A40 (2013).
- [131] I.-Y. Park, S. Kim, J. Choi, D.-H. Lee, Y.-J. Kim, M. F. Kling, M. I. Stockman, and S.-W. Kim. [Plasmonic generation of ultrashort extreme-ultraviolet light pulses](#). *Nat. Photonics* **5**, 677 (2011).
- [132] G. Vampa, B. G. Ghamsari, S. Siadat Mousavi, T. J. Hammond, A. Olivieri, E. Lisicka-Skrek, A. Yn Naumov, D. M. Villeneuve, A. Staudte, P. Berini, and P. B. Corkum. [Plasmon-enhanced high-harmonic generation from silicon](#). *Nat. Phys.* **13**, 659 (2017).
- [133] T. Saule, S. Heinrich, J. Schötz, N. Lilienfein, M. Högner, O. deVries, M. Plötner, J. Weitenberg, D. Esser, J. Schulte, P. Russbuehdt, J. Limpert, M. F. Kling, U. Kleineberg, and I. Pupeza. [High-flux ultrafast extreme-ultraviolet photoemission spectroscopy at 18.4 MHz pulse repetition rate](#). *Nat. Comm.* **10**, 458 (2019).
- [134] A. K. Mills, S. Zhdanovich, M.X. Na, F. Boschini, E. Razzoli, M. Michiardi, A. Sheyerman, M. Schneider, T. J. Hammond, V. Süß, C. Felsner, A. Damascelli, and D. J. Jones. [Cavity-enhanced high harmonic generation for XUV time-resolved ARPES](#). *arXiv:1902.05997* (2019).

- [135] C. W. Nicholson, A. Lücke, W. G. Schmidt, M. Puppín, L. Rettig, R. Ernstorfer, and M. Wolf. [Beyond the molecular movie: Dynamics of bands and bonds during a photoinduced phase transition](#). *Science* **362**, 821 (2018).
- [136] M. Puppín, Y. Deng, C. W. Nicholson, J. Feldl, N. B. M. Schröter, H. Vita, P. S. Kirchmann, C. Monney, L. Rettig, M. Wolf, and R. Ernstorfer. [Time- and angle-resolved photoemission spectroscopy of solids in the extreme ultraviolet at 500 kHz repetition rate](#). *Rev. Sci. Instrum.* **90**, 023104 (2019).
- [137] I. Pupeza, S. Holzberger, T. Eidam, H. Carstens, D. Esser, J. Weitenberg, P. Rußbüldt, J. Rauschenberger, J. Limpert, Th. Udem, A. Tünnermann, T. W. Hänsch, A. Apolonski, F. Krausz, and E. Fill. [Compact high-repetition-rate source of coherent 100 eV radiation](#). *Nat. Photonics* **7**, 608 (2013).
- [138] S. Hädrich, M. Krebs, J. Rothhardt, H. Carstens, S. Demmler, J. Limpert, and A. Tünnermann. [Generation of  \$\mu\$ W level plateau harmonics at high repetition rate](#). *Opt. Express* **19**, 19374 (2011).
- [139] J. Bouillet, Y. Zaouter, J. Limpert, S. Petit, Y. Mairesse, B. Fabre, J. Higuët, E. Mével, E. Constant, and E. Cormier. [High-order harmonic generation at a megahertz-level repetition rate directly driven by an ytterbium-doped-fiber chirped-pulse amplification system](#). *Opt. Lett.* **34**, 1489 (2009).
- [140] A. Damm, J. Gütde, P. Feulner, A. Czasch, O. Jagutzki, H. Schmidt-Böcking, and U. Höfer. [Application of a time-of-flight spectrometer with delay-line detector for time- and angle-resolved two-photon photoemission](#). *J. Electron Spectrosc. Relat. Phenomena* **202**, 74 (2015).
- [141] D. Kühn, F. Sorgenfrei, E. Giangrisostomi, R. Jay, A. Musazay, R. Ovsyannikov, C. Strählman, S. Svensson, N. Mårtensson, and A. Föhlisch. [Capabilities of angle resolved time of flight electron spectroscopy with the 60° wide angle acceptance lens](#). *J. Electron Spectrosc. Relat. Phenomena* **224**, 45 (2018).
- [142] MBS M-1 VUV monochromator, [MB Scientific AB](#), Uppsala, Sweden.
- [143] [Impulse](#), Clark-MXR, Inc., Dexter, United States of America.
- [144] Time-of-flight spectrometer [THEMIS 1000](#), SPECS GmbH, Berlin, Germany.
- [145] R. Wehlitz, L. S. Pibida, J. C. Levin, and I. A. Sellin. [Angle-resolving electron-electron coincidence setup](#). *Rev. Sci. Instrum.* **70**, 1978 (1999).
- [146] M. G. White, R. A. Rosenberg, G. Gabor, E. D. Poliakoff, G. Thornton, S. H. Southworth, and D. A. Shirley. [Time-of-flight photoelectron spectroscopy of gases using synchrotron radiation](#). *Rev. Sci. Instrum.* **50**,(10) 126 (1979).
- [147] R. Haight, J. A. Silberman, and M. I. Lilie. [Novel system for picosecond photoemission spectroscopy](#). *Rev. Sci. Instrum.* **59**, 1941 (1988).
- [148] M. Schicketanz, A. Oelsner, J. Morais, V. Mergel, H. Schmidt-Böcking, and G. Schönhense. [Electron-TOF-analyser for complete momentum analysis in photoemission from surfaces](#). *Nucl. Instrum. Methods Phys. Res. A* **467-468**, 1519 (2001).
- [149] J. Ullrich, R. Moshhammer, A. Dorn, R. Dörner, L. Ph. H. Schmidt, and H. Schmidt-Böcking. [Recoil-ion and electron momentum spectroscopy: reaction-microscopes](#). *Rep. Prog. Phys.* **66**, 1463 (2003).
- [150] B. Wannberg. [Electron optics development for photo-electron spectrometers](#). *Nucl. Instrum. Methods Phys. Res. A* **601**, 182 (2009).
- [151] A. Oelsner, O. Schmidt, M. Schicketanz, M. Klais, G. Schönhense, V. Mergel, O. Jagutzki, and H. Schmidt-Böcking. [Microspectroscopy and imaging using a delay line detector in time-of-flight photoemission microscopy](#). *Rev. Sci. Instrum.* **72**, 3968 (2001).
- [152] D. F. Förster, B. Lindenau, M. Leyendecker, F. Janssen, C. Winkler, F. O. Schumann, J. Kirschner, K. Hollmack, and A. Föhlisch. [Phase-locked MHz pulse selector for x-ray sources](#). *Opt. Lett.* **40**, 2265 (2015).



- [153] C. Tusche, P. Goslawski, D. Kutnyakhov, M. Ellguth, K. Medjanik, H. J. Elmers, S. Chernov, R. Wallauer, D. Engel, A. Jankowiak, and G. Schönhense. [Multi-MHz time-of-flight electronic bandstructure imaging of graphene on Ir\(111\)](#). *Appl. Phys. Lett.* **108**, 261602 (2016).
- [154] The model of the spectrometer in Ref. [144] is implemented in the numerical simulations of electron trajectories by the program [SIMION](#), version 8, Scientific Instrument Services, Inc., United States of America.
- [155] W. L. Wiese and J. R. Fuhr. [Accurate atomic transition probabilities for hydrogen, helium, and lithium](#). *J. Phys. Chem. Ref. Data* **38**, 565 (2009).
- [156] A. Trützscher. [Photoemission und Doppelphotoemission an Metallen und Oxiden mittels Erzeugung hoher Harmonischer](#). Dissertation, Martin-Luther-Universität Halle-Wittenberg (2017).
- [157] F. Roth, T. Arion, H. Kaser, A. Gottwald, and W. Eberhardt. [Angle resolved Photoemission from Ag and Au single crystals: Final state lifetimes in the attosecond range](#). *J. Electron Spectrosc. Relat. Phenomena* **224**, 84 (2018).
- [158] F. Roth, C. Lupulescu, E. Darlatt, A. Gottwald, and W. Eberhardt. [Angle resolved photoemission from Cu single crystals: Known facts and a few surprises about the photoemission process](#). *J. Electron Spectrosc. Relat. Phenomena* **208**, 2 (2016).
- [159] F. Emaury, A. Diebold, C. J. Saraceno, and U. Keller. [Compact extreme ultraviolet source at megahertz pulse repetition rate with a low-noise ultrafast thin-disk laser oscillator](#). *Optica* **2**, 980 (2015).
- [160] F. Lindner, W. Stremme, M. G. Schätzel, F. Grasbon, G. G. Paulus, H. Walther, R. Hartmann, and L. Strüder. [High-order harmonic generation at a repetition rate of 100 kHz](#). *Phys. Rev. A* **68**, 013814 (2003).
- [161] I. Velchev, W. Hogervorst, and W. Ubachs. [Precision VUV spectroscopy of Ar I at 105 nm](#). *J. Phys. B: At. Mol. Opt. Phys.* **32**, L511 (1999).
- [162] E. B. Saloman. [Energy levels and observed spectral lines of xenon, Xe I through Xe LIV](#). *J. Phys. Chem. Ref. Data* **33**, 765 (2004).
- [163] X. F. Li, A. L’Huillier, M. Ferray, L. A. Lompré, and G. Mainfray. [Multiple-harmonic generation in rare gases at high laser intensity](#). *Phys. Rev. A* **39**, 5751 (1989).
- [164] M. V. Ammosov, N. B. Delone, and V. P. Krainov. [Tunnel ionization of complex atoms and of atomic ions in an alternating electromagnetic field](#). *Sov. Phys. JETP* **64**, 1191 (1986).
- [165] L. V. Keldysh. [Ionization in the field of a strong electromagnetic wave](#). *Sov. Phys. JETP* **20**, 1307 (1965).
- [166] A. Cabasse, Ch. Hazera, L. Quintard, E. Cormier, S. Petit, and E. Constant. [Collection and spectral control of high-order harmonics generated with a 50 W high-repetition rate ytterbium femtosecond laser system](#). *J. Phys. B: At. Mol. Opt. Phys.* **49**, 085601 (2016).
- [167] J.-F. Hergott, M. Kovacev, H. Merdji, C. Hubert, Y. Mairesse, E. Jean, P. Breger, P. Agostini, B. Carré, and P. Salières. [Extreme-ultraviolet high-order harmonic pulses in the microjoule range](#). *Phys. Rev. A* **66**, 021801 (2002).
- [168] P. H. Bucksbaum, R. R. Freeman, M. Bashkansky, and T. J. McIlrath. [Role of the ponderomotive potential in above-threshold ionization](#). *J. Opt. Soc. Am. B* **4**, 760 (1987).
- [169] S. Eich, A. Stange, A.V. Carr, J. Urbancic, T. Popmintchev, M. Wiesenmayer, K. Jansen, A. Ruffing, S. Jakobs, T. Rohwer, S. Hellmann, C. Chen, P. Matyba, L. Kipp, K. Rossnagel, M. Bauer, M. M. Murnane, H.C. Kapteyn, S. Mathias, and M. Aeschlimann. [Time- and angle-resolved photoemission spectroscopy with optimized high-harmonic pulses using frequency-doubled Ti:Sapphire lasers](#). *J. Electron Spectrosc. Relat. Phenomena* **195**, 231 (2014).

- [170] P. Wernet, J. Gaudin, K. Godehusen, O. Schwarzkopf, and W. Eberhardt. [Femtosecond time-resolved photoelectron spectroscopy with a vacuum-ultraviolet photon source based on laser high-order harmonic generation](#). *Rev. Sci. Instrum* **82**, 063114 (2011).
- [171] E. Magerl, S. Neppl, A. L. Cavalieri, E. M. Bothschafter, M. Stanislowski, Th. Uphues, M. Hofstetter, U. Kleineberg, J. V. Barth, D. Menzel, F. Krausz, R. Ernstorfer, R. Kienberger, and P. Feulner. [A flexible apparatus for attosecond photoelectron spectroscopy of solids and surfaces](#). *Rev. Sci. Instrum.* **82**, 063104 (2011).
- [172] S. Mathias, L. Miaja-Avila, M. M. Murnane, H. Kapteyn, M. Aeschlimann, and M. Bauer. [Angle-resolved photoemission spectroscopy with a femtosecond high harmonic light source using a two-dimensional imaging electron analyzer](#). *Rev. Sci. Instrum.* **78**, 083105 (2007).
- [173] G. Tsilimis, J. Kutzner, and H. Zacharias. [Resonance in the  \$1\pi\$  photoemission cross-section of CO on Pt\(111\) measured by high harmonic radiation](#). *Surf. Sci.* **528**, 171 (2003).
- [174] P. Siffalovic, M. Drescher, M. Spieweck, T. Wiesenthal, Y. C. Lim, R. Weidner, A. Elizarov, and U. Heinzmann. [Laser-based apparatus for extended ultraviolet femtosecond time-resolved photoemission spectroscopy](#). *Rev. Sci. Instrum.* **72**, 30 (2001).
- [175] D. Riedel, J. L. Hernandez-Pozos, R. E. Palmer, S. Baggott, K. W. Kolasinski, and J. S. Foord. [Tunable pulsed vacuum ultraviolet light source for surface science and materials spectroscopy based on high order harmonic generation](#). *Rev. Sci. Instrum.* **72**, 1977 (2001).
- [176] H. L. Skriver and N. M. Rosengaard. [Surface energy and work function of elemental metals](#). *Phys. Rev. B* **46**, 7157 (1992).
- [177] N. D. Lang and W. Kohn. [Theory of metal surfaces: work function](#). *Phys. Rev. B* **3**, 1215 (1971).
- [178] A. Klein. [Interface properties of dielectric oxides](#). *J. Am. Ceram. Soc.* **99**, 369 (2016).
- [179] J. Robertson and S. J. Clark. [Limits to doping in oxides](#). *Phys. Rev. B* **83**, 075205 (2011).
- [180] S. D. Ha and S. Ramanathan. [Adaptive oxide electronics: a review](#). *J. Appl. Phys.* **110**, 071101 (2011).
- [181] T. Südmeyer, S. V. Marchese, S. Hashimoto, C. R. E. Baer, G. Gingras, B. Witzel, and U. Keller. [Femtosecond laser oscillators for high-field science](#). *Nat. Photon.* **2**, 599 (2008).
- [182] Th. Schmidt, A. Sala, H. Marchetto, E. Umbach, and H.-J. Freund. [First experimental proof for aberration correction in XPEEM: Resolution, transmission enhancement, and limitation by space charge effects](#). *Ultramicroscopy* **126**, 23 (2013).
- [183] A. Locatelli, T. O. Montes, M. Á. Niño, and E. Bauer. [Image blur and energy broadening effects in XPEEM](#). *Ultramicroscopy* **111**, 1447 (2011).
- [184] X. J. Zhou, B. Wannberg, W. L. Yang, V. Brouet, Z. Sun, J. F. Douglas, D. Dessau, Z. Hussain, and Z.-X. Shen. [Space charge effect and mirror charge effect in photoemission spectroscopy](#). *J. Electron Spectrosc. Relat. Phenomena* **142**, 27 (2005).
- [185] S. Passlack, S. Mathias, O. Andreyev, D. Mittnacht, M. Aeschlimann, and M. Bauer. [Space charge effects in photoemission with a low repetition, high intensity femtosecond laser source](#). *J. Appl. Phys.* **100**, 024912 (2006).
- [186] L.-P. Oloff, K. Hanff, A. Stange, G. Rohde, F. Diekmann, M. Bauer, and K. Rossnagel. [Pump laser-induced space-charge effects in HHG-driven time- and angle-resolved photoelectron spectroscopy](#). *J. Appl. Phys.* **119**, 225106 (2016).
- [187] G. Schönhense, K. Medjanik, C. Tusche, M. de Loos, B. van der Geer, M. Scholz, F. Hieke, N. Gerken, J. Kirschner, and W. Wurth. [Correction of the deterministic part of space-charge interaction in momentum microscopy of charged particles](#). *Ultramicroscopy* **159**, 488 (2015).
- [188] R. Z. Bachrach, F. C. Brown, and S. B. M. Hagström. [Photoelectron spectroscopy by time-of-flight technique using synchrotron radiation](#). *J. Vac. Sci. Tech.* **12**, 309 (1975).

- [189] F. Reinert, G. Nicolay, S. Schmidt, D. Ehm, and S. Hüfner. [Direct measurements of the L-gap surface states on the \(111\) face of noble metals by photoelectron spectroscopy](#). *Phys. Rev. B* **63**, 115415 (2001).
- [190] S.V. Chernov, K. Medjanik, C. Tusche, D. Kutnyakhov, S.A. Nepijko, A. Oelsner, J. Braun, J. Minár, S. Borek, H. Ebert, H.J. Elmers, J. Kirschner, and G. Schönhense. [Anomalous  \$d\$ -like surface resonances on Mo\(110\) analyzed by time-of-flight momentum microscopy](#). *Ultramicroscopy* **159**, 453 (2015).
- [191] Y. Ishida, H. Kanto, A. Kikkawa, Y. Taguchi, Y. Ito, Y. Ota, K. Okazaki, W. Malaeb, M. Mulazzi, M. Okawa, S. Watanabe, C.-T. Chen, M. Kim, C. Bell, Y. Kozuka, H. Y. Hwang, Y. Tokura, and S. Shin. [Common origin of the circular-dichroism pattern in angle-resolved photoemission spectroscopy of SrTiO<sub>3</sub> and Cu<sub>x</sub>Bi<sub>2</sub>Se<sub>3</sub>](#). *Phys. Rev. Lett.* **107**, 077601 (2011).
- [192] H. Eckardt, L. Fritsche, and J. Noffke. [Self-consistent relativistic band structure of the noble metals](#). *J. Phys. F: Metal Physics* **14**, 97 (1984).
- [193] R. L. Benbow and N. V. Smith. [Photoemission spectra and band structures of  \$d\$ -band metals. X. Relativistic momentum matrix elements](#). *Phys. Rev. B* **27**, 3144 (1983).
- [194] J. A. Knapp, F. J. Himpsel, and D. E. Eastman. [Experimental energy band dispersions and lifetimes for valence and conduction bands of copper using angle-resolved photoemission](#). *Phys. Rev. B* **19**, 4952 (1979).
- [195] M. Ossiander, J. Riemensberger, S. Nepl, M. Mittermair, M. Schäffer, A. Duensing, M. S. Wagner, R. Heider, M. Wurzer, M. Gerl, M. Schnitzenbaumer, J. V. Barth, F. Libisch, C. Lemell, J. Burgdörfer, P. Feulner, and R. Kienberger. [Absolute timing of the photoelectric effect](#). *Nature* **561**, 374 (2018).
- [196] Z. Tao, C. Chen, T. Szilvási, M. Keller, M. Mavrikakis, H. Kapteyn, and M. Murnane. [Direct time-domain observation of attosecond final-state lifetimes in photoemission from solids](#). *Science* **353**, 62 (2016).
- [197] M. Lucchini, L. Castiglioni, L. Kasmi, P. Kliuiev, A. Ludwig, M. Greif, J. Osterwalder, M. Hengsberger, L. Gallmann, and U. Keller. [Light-matter interaction at surfaces in the spatiotemporal limit of macroscopic models](#). *Phys. Rev. Lett.* **115**, 137401 (2015).
- [198] B. A. McDougall, T. Balasubramanian, and E. Jensen. [Phonon contribution to quasiparticle lifetimes in Cu measured by angle-resolved photoemission](#). *Phys. Rev. B* **51**, 13891 (1995).
- [199] M. Çopuroğlu, H. Sezen, R. L. Opila, and S. Suzer. [Band-bending at buried SiO<sub>2</sub>/Si interface as probed by XPS](#). *ACS Applied Materials & Interfaces* **5**, 5875 (2013).
- [200] L. Kronik and Y. Shapira. [Surface photovoltage phenomena: theory, experiment, and applications](#). *Surf. Sci. Rep.* **37**, 1 (1999).
- [201] D. Bröcker, T. Gießel, and W. Widdra. [Charge carrier dynamics at the SiO<sub>2</sub>/Si\(100\) surface: a time-resolved photoemission study with combined laser and synchrotron radiation](#). *Chem. Phys.* **299**, 247 (2004).
- [202] W. Widdra, D. Bröcker, T. Gießel, I. V. Hertel, W. Krüger, A. Liero, F. Noack, V. Petrov, D. Pop, P. M. Schmidt, R. Weber, I. Will, and B. Winter. [Time-resolved core level photoemission: surface photovoltage dynamics of the SiO<sub>2</sub>/Si\(100\) interface](#). *Surf. Sci.* **543**, 87 (2003).
- [203] Zs. Bor and B. Rácz. [Group velocity dispersion in prisms and its application to pulse compression and travelling-wave excitation](#). *Opt. Comm.* **54**, 165 (1985).
- [204] H. Igarashi, A. Makida, M. Ito, and T. Sekikawa. [Pulse compression of phase-matched high harmonic pulses from a time-delay compensated monochromator](#). *Opt. Express* **20**, 3725 (2012).
- [205] M. Ito, Y. Kataoka, T. Okamoto, M. Yamashita, and T. Sekikawa. [Spatiotemporal characterization of single-order high harmonic pulses from time-compensated toroidal-grating monochromator](#). *Opt. Express* **18**, 6071 (2010).

- [206] C. Gazier and J. R. Prescott. [Pairs of photoemitted electrons from potassium](#). *Phys. Lett. A* **32**, 425 (1970).
- [207] J. Kirschner, O. M. Artamonov, and S. N. Samarin. [Angle resolved energy correlated coincidence electron spectroscopy of solid surfaces](#). *Phys. Rev. Lett.* **75**, 2424 (1995).
- [208] L. Pasquali, M.C. Sapet, E.M. Staicu-Casagrande, P. Cortona, V.A. Esaulov, S. Nannarone, M. Canepa, S. Terreni, and L. Mattera. [Ag\(100\) surface density of states probed by metastable deexcitation spectroscopy: A comparison between experiment and theory](#). *Nucl. Instr. and Meth. in Phys. Res. B* **212**, 274 (2003).
- [209] K. Giesen, F. Hage, F. J. Himpsel, H. J. Riess, W. Steinmann, and N. V. Smith. [Effective mass of image-potential states](#). *Phys. Rev. B* **35**, 975 (1987).
- [210] P.-O. Löwdin. [The historical development of the electron correlation problem](#). *Int. J. Quantum Chem.* **55**, 77 (1995).
- [211] L. S. Cederbaum, F. Tarantelli, A. Sgamellotti, and J. Schirmer. [On double vacancies in the core](#). *J. Chem. Phys.* **85**, 6513 (1986).
- [212] M. Iwan, F. J. Himpsel, and D. E. Eastman. [Two-electron resonance at the 3p threshold of Cu and Ni](#). *Phys. Rev. Lett.* **43**, 1829 (1979).
- [213] C. J. Powell. [Solid-state and atomic features in the valence-band Auger spectra of copper, silver, and gold](#). *Solid State Commun.* **26**, 557 (1978).
- [214] M. T. Butterfield, R. A. Bartynski, and S. L. Hulbert. [Pd  \$M\_{45}VV\$  Auger spectrum determined by Auger-photoelectron coincidence spectroscopy: Intrinsic line shape and Coster-Kronig transitions](#). *Phys. Rev. B* **66**, 115115 (2002).
- [215] D. E. Ramaker. [The past, present, and future of Auger line shape analysis](#). *Crit. Rev. Solid State Mater. Sci.* **17**, 211 (1991).
- [216] P. A. Bennett, J. C. Fuggle, F. U. Hillebrecht, A. Lenselink, and G. A. Sawatzky. [Electronic structure of Ni and Pd alloys. III. Correlation effects in the Auger spectra of Ni alloys](#). *Phys. Rev. B* **27**, 2194 (1983).
- [217] G. Treglia, M. C. Desjonqueres, F. Ducastelle, and D. Spanjaard. [Correlation effects on Auger spectra in unfilled d band metals](#). *J. Phys. C: Solid State Phys* **14**, 4347 (1981).
- [218] M. Cini. [Two hole resonances in the XVV Auger spectra of solids](#). *Solid State Commun.* **24**, 681 (1977).
- [219] G. A. Sawatzky. [Quasiatomic Auger spectra in narrow-band metals](#). *Phys. Rev. Lett.* **39**, 504 (1977).
- [220] W. A. Harrison and S. Froyen. [Universal linear-combination-of-atomic-orbitals parameters for d-state solids](#). *Phys. Rev. B* **21**, 3214 (1980).
- [221] J. Mitroy, M. S. Safronova, and C. W. Clark. [Theory and applications of atomic and ionic polarizabilities](#). *J. Phys. B* **43**, 202001 (2010).
- [222] B. D. Napitu and J. Berakdar. [Two-particle photoemission from strongly correlated systems: A dynamical mean-field approach](#). *Phys. Rev. B* **81**, 195108 (2010).
- [223] F. O. Schumann, L. Behnke, C. H. Li, J. Kirschner, Y. Pavlyukh, and J. Berakdar. [Electron pair emission from a highly correlated material](#). *Phys. Rev. B* **86**, 035131 (2012).
- [224] N. F. Mott and R. Peierls. [Discussion of the paper by de Boer and Verwey](#). *Proc. Phys. Soc.* **49**, 72 (1937).
- [225] J. Zaanen, G. A. Sawatzky, and J. W. Allen. [Band gaps and electronic structure of transition-metal compounds](#). *Phys. Rev. Lett.* **55**, 418 (1985).

- [226] V. I. Anisimov, J. Zaanen, and O. K. Andersen. [Band theory and Mott insulators: Hubbard U instead of Stoner I](#). *Phys. Rev. B* **44**, 943 (1991).
- [227] S. Hüfner. [Electronic structure of NiO and related 3d-transition-metal compounds](#). *Adv. Phys.* **43**, 183 (1994).
- [228] A. Fujimori, T. Yoshida, K. Okazaki, T. Tsujioka, K. Kobayashi, T. Mizokawa, M. Onoda, T. Katsufuji, Y. Taguchi, and Y. Tokura. [Electronic structure of Mott–Hubbard-type transition-metal oxides](#). *J. Electron Spectrosc. Relat. Phenomena* **117-118**, 277 (2001).
- [229] J. Kuneš, V. I. Anisimov, S. L. Skornyakov, A. V. Lukoyanov, and D. Vollhardt. [NiO: correlated band structure of a charge-transfer insulator](#). *Phys. Rev. Lett.* **99**, 156404 (2007).
- [230] D. N. Basov, R. D. Averitt, D. van der Marel, M. Dressel, and K. Haule. [Electrodynamics of correlated electron materials](#). *Rev. Mod. Phys.* **83**, 471 (2011).
- [231] G. Witte, P. Senet, and J. P. Toennies. [Helium-atom-scattering study of the structure and phonons of the NiO\(100\) and CoO\(100\) surfaces](#). *Phys. Rev. B* **58**, 13264 (1998).
- [232] K. Gillmeister, M. Kiel, and W. Widdra. [Image potential states at transition metal oxide surfaces: A time-resolved two-photon photoemission study on ultrathin NiO films](#). *Phys. Rev. B* **97**, 085424 (2018).
- [233] Z.-X. Shen, R. S. List, D. S. Dessau, B. O. Wells, O. Jepsen, A. J. Arko, R. Bartlett, C. K. Shih, F. Parmigiani, J. C. Huang, and P. A. P. Lindberg. [Electronic structure of NiO: Correlation and band effects](#). *Phys. Rev. B* **44**, 3604 (1991).
- [234] M. Taguchi, M. Matsunami, Y. Ishida, R. Eguchi, A. Chainani, Y. Takata, M. Yabashi, K. Tamasaku, Y. Nishino, T. Ishikawa, Y. Senba, H. Ohashi, and S. Shin. [Revisiting the valence-band and core-level photoemission spectra of NiO](#). *Phys. Rev. Lett.* **100**, 206401 (2008).
- [235] T. M. Schuler, D. L. Ederer, S. Itza-Ortiz, G. T. Woods, T. A. Callcott, and J. C. Woicik. [Character of the insulating state in NiO: A mixture of charge-transfer and Mott-Hubbard character](#). *Phys. Rev. B* **71**, 115113 (2005).
- [236] O. Tjernberg, G. Chiaia, U. O. Karlsson, and F. M. F. de Groot. [Resonant photoelectron spectroscopy on CoO](#). *J. Phys. Condens. Matter* **9**, 9863 (1997).
- [237] M. T. Greiner, L. Chai, M. G. Helander, W.-M. Tang, and Z.-H. Lu. [Transition metal oxide work functions: The influence of cation oxidation state and oxygen vacancies](#). *Adv. Funct. Mater.* **22**, 4557 (2012).
- [238] S. Sindhu, M. Heiler, K.-M. Schindler, W. Widdra, and H. Neddermeyer. [Growth mechanism and angle-resolved photoemission spectra of cobalt oxide \(CoO\) thin films on Ag\(100\)](#). *Surf. Sci.* **566-568**, 471 (2004).
- [239] F. Reinert, P. Steiner, S. Hüfner, H. Schmitt, J. Fink, M. Knupfer, P. Sandl, and E. Bertel. [Electron and hole doping in NiO](#). *Z. Phys. B* **97**, 83 (1995).
- [240] Y. Fukuda, S. Mochizuki, and N. Sanada. [Soft x-ray appearance potential spectroscopy study of NiO and CoO single crystal surfaces](#). *J. Appl. Phys.* **106**, 023701 (2009).
- [241] A. Freitag, V. Staemmler, D. Cappus, C.A. Ventrice, K. Al Shamery, H. Kühlenbeck, and H.-J. Freund. [Electronic surface state of NiO \(100\)](#). *Chem. Phys. Lett.* **210**, 10 (1993).
- [242] A. Gorschlüter and H. Merz. [Localized d-d excitations in NiO\(100\) and CoO\(100\)](#). *Phys. Rev. B* **49**, 17293 (1994).
- [243] B. Fromme, C. Bethke, M. Möller, Th. Anschutz, and E. Kisker. [Electron-exchange processes in bulk and surface d-d excitations in transition-metal oxides](#). *Vacuum* **48**, 225 (1997).
- [244] M. Magnuson, S. M. Butorin, A. Agui, and J. Nordgren. [Resonant soft x-ray Raman scattering of NiO](#). *J. Phys.: Condens. Matter* **14**, 3669 (2002).



- [245] K. Satitkovitchai, Y. Pavlyukh, and W. Hübner. *Ab initio* embedded cluster study of optical second-harmonic generation below the gap of a NiO(001) surface. *Phys. Rev. B* **67**, 165413 (2003).
- [246] G. W. Pratt and R. Coelho. Optical Absorption of CoO and MnO above and below the Néel Temperature. *Phys. Rev.* **116**, 281 (1959).
- [247] J. van Elp, J. L. Wieland, H. Eskes, P. Kuiper, G. A. Sawatzky, F. M. F. de Groot, and T. S. Turner. Electronic structure of CoO, Li-doped CoO, and LiCoO<sub>2</sub>. *Phys. Rev. B* **44**, 6090 (1991).
- [248] F. C. Zhang and T. M. Rice. Effective Hamiltonian for the superconducting Cu oxides. *Phys. Rev. B* **37**, 3759 (1988).
- [249] J. Kuneš, V. I. Anisimov, A. V. Lukoyanov, and D. Vollhardt. Local correlations and hole doping in NiO: A dynamical mean-field study. *Phys. Rev. B* **75**, 165115 (2007).
- [250] R. Eder, A. Dorneich, and H. Winter. Single-particle spectra of charge-transfer insulators by cluster perturbation theory: The correlated band structure of NiO. *Phys. Rev. B* **71**, 045105 (2005).
- [251] J. Bala, A. M. Oleś, and J. Zaanen. Origin of band and localized electron states in photoemission of NiO. *Phys. Rev. B* **61**, 13573 (2000).
- [252] J. Bala, A. M. Oleś, and J. Zaanen. Zhang-Rice localization, quasiparticle dispersions, and the photoemission of NiO. *Phys. Rev. Lett.* **72**, 2600 (1994).
- [253] Q. Yin, A. Gordienko, X. Wan, and S. Y. Savrasov. Calculated momentum dependence of Zhang-Rice states in transition metal oxides. *Phys. Rev. Lett.* **100**, 066406 (2008).
- [254] L. Hozoi, S. Nishimoto, G. Kalosakas, D. B. Bodea, and S. Burdin. Nonlocal interactions in doped cuprates: Correlated motion of Zhang-Rice polarons. *Phys. Rev. B* **75**, 024517 (2007).
- [255] S. Schenk, S. Förster, K. Meinel, R. Hammer, B. Leibundgut, M. Paleschke, J. Pantzer, C. Dresler, F. O. Schumann, and W. Widdra. Observation of a dodecagonal oxide quasicrystal and its complex approximant in the SrTiO<sub>3</sub>-Pt(111) system. *J. Phys.: Condens. Matter* **29**, 134002 (2017).
- [256] W. Di, K. E. Smith, and S. D. Kevan. Angle-resolved photoemission study of the clean and hydrogen-covered Pt(111) surface. *Phys. Rev. B* **45**, 3652 (1992).
- [257] E. Frantzeskakis, S. Pons, A. Crepaldi, H. Brune, K. Kern, and M. Grioni. Ag-coverage-dependent symmetry of the electronic states of the Pt(111)-Ag-Bi interface: The ARPES view of a structural transition. *Phys. Rev. B* **84**, 245443 (2011).
- [258] H. J. Herrera-Suárez, A. Rubio-Ponce, and D. Olgún. Electronic band structure of the Pt(111) surface: An *ab initio* and tight-binding study – I. *Comput. Mater. Sci.* **56**, 141 (2012).
- [259] Y. S. Kim, S. H. Jeon, A. Bostwick, E. Rotenberg, P. N. Ross, A. L. Walter, Y. J. Chang, V. R. Stamenkovic, N. M. Markovic, T. W. Noh, S. Han, and B. S. Mun. Role of preferential weak hybridization between the surface-state of a metal and the oxygen atom in the chemical adsorption mechanism. *Phys. Chem. Chem. Phys.* **15**, 19019 (2013).
- [260] A. Dal Corso. Clean Ir(111) and Pt(111) electronic surface states: A first-principle fully relativistic investigation. *Surf. Sci.* **637-638**, 106 (2015).
- [261] E. W. Plummer and J. W. Gadzuk. Surface states on tungsten. *Phys. Rev. Lett.* **25**, 1493 (1970).
- [262] S.-L. Weng, T. Gustafsson, and E. W. Plummer. Three surface resonances on the (100) face of W and Mo: An angle-resolved synchrotron photoemission study. *Phys. Rev. Lett.* **39**, 822 (1977).
- [263] S. Muff, N. Pilet, M. Fanciulli, A. P. Weber, C. Wessler, Z. Ristić, Z. Wang, N. C. Plumb, M. Radović, and J. H. Dil. Influence of ferroelectric order on the surface electronic structure of BaTiO<sub>3</sub> films studied by photoemission spectroscopy. *Phys. Rev. B* **98**, 045132 (2018).
- [264] P. Lutz, S. Moser, V. Jovic, Y. J. Chang, R. J. Koch, S. Ulstrup, J. S. Oh, L. Moreschini, S. Fatale, M. Grioni, C. Jozwiak, A. Bostwick, E. Rotenberg, H. Bentmann, and F. Reinert. Volatile two-dimensional electron gas in ultrathin BaTiO<sub>3</sub> films. *Phys. Rev. Mater.* **2**, 094411 (2018).

- [265] G. Berner, M. Sing, H. Fujiwara, A. Yasui, Y. Saitoh, A. Yamasaki, Y. Nishitani, A. Sekiyama, N. Pavlenko, T. Kopp, C. Richter, J. Mannhart, S. Suga, and R. Claessen. [Direct  \$k\$ -space mapping of the electronic structure in an oxide-oxide interface](#). *Phys. Rev. Lett.* **110**, 247601 (2013).
- [266] C. Cancellieri, M. L. Reinle-Schmitt, M. Kobayashi, V. N. Strocov, P. R. Willmott, D. Fontaine, Ph. Ghosez, A. Filippetti, P. Delugas, and V. Fiorentini. [Doping-dependent band structure of  \$\text{LaAlO}\_3/\text{SrTiO}\_3\$  interfaces by soft x-ray polarization-controlled resonant angle-resolved photoemission](#). *Phys. Rev. B* **89**, 121412 (2014).
- [267] S. M. Walker, F. Y. Bruno, Z. Wang, A. de la Torre, S. Ricco, A. Tamai, T. K. Kim, M. Hoesch, M. Shi, M. S. Bahramy, P. D. C. King, and F. Baumberger. [Carrier-density control of the  \$\text{SrTiO}\_3\$  \(001\) surface 2D electron gas studied by ARPES](#). *Adv. Mater.* **27**, 3894 (2015).
- [268] A. P. Smith and N. W. Ashcroft. [Pseudopotentials and quasicrystals](#). *Phys. Rev. Lett.* **59**, 1365 (1987).
- [269] R. D. Werkman, P. J. Schurer, I. Vincze, and F. van der Woude. [Are quasicrystals Hume-Rothery alloys?](#) *Hyperfine Interact.* **45**, 409 (1989).
- [270] G. Trambly de Laissardiere, D. Mayou, and D. Nguyen Manh. [Electronic structure of transition atoms in quasi-crystals and Hume-Rothery alloys](#). *Europhys. Lett.* **21**, 25 (1993).
- [271] U. Mizutani, T. Takeuchi, and H. Sato. [Interpretation of the Hume-Rothery rule in complex electron compounds:  \$\gamma\$ -phase  \$\text{Cu}\_5\text{Zn}\_8\$  Alloy, FK-type  \$\text{Al}\_{30}\text{Mg}\_{40}\text{Zn}\_{30}\$  and MI-type  \$\text{Al}\_{68}\text{Cu}\_7\text{Ru}\_{17}\text{Si}\_8\$  1/1-1/1-1/1 approximants](#). *Prog. Mater. Sci.* **49**, 227 (2004).
- [272] S. W. Robey, L. T. Hudson, V. E. Henrich, C. Eylem, and B. Eichhorn. [Resonant photoelectron spectroscopy studies of  \$\text{BaTiO}\_3\$  and related mixed oxides](#). *J. Phys. Chem. Solids* **57**, 1385 (1996).
- [273] R. E. Cohen and H. Krakauer. [Electronic structure studies of the differences in ferroelectric behavior of  \$\text{BaTiO}\_3\$  and  \$\text{PbTiO}\_3\$](#) . *Ferroelectrics* **136**, 65 (1992).
- [274] P. Pertosa and F. M. Michel-Calendini. [X-ray photoelectron spectra, theoretical band structures, and densities of states for  \$\text{BaTiO}\_3\$  and  \$\text{KNbO}\_3\$](#) . *Phys. Rev. B* **17**, 2011 (1978).
- [275] ˘. Ellialtıođlu and T. Wolfram. [Surface electronic properties of  \$d\$ -band perovskites: Study of the  \$\pi\$  bands](#). *Phys. Rev. B* **18**, 4509 (1978).
- [276] A. Stuck, J. Osterwalder, T. Greber, S. Hufner, and L. Schlapbach. [Partial densities of states of alloys measured with x-ray-photoelectron diffraction:  \$\text{AuCu}\_3\(001\)\$](#) . *Phys. Rev. Lett.* **65**, 3029 (1990).
- [277] Ch. Sondergaard, Ch. Schultz, M. Schonning, S. Lizzit, A. Baraldi, S. Agergaard, M. B. Nielsen, H. Li, and Ph. Hofmann. [Symmetry-resolved density of states from valence band photoelectron diffraction](#). *Phys. Rev. B* **64**, 245110 (2001).
- [278] E. Tamura, W. Piepke, and R. Feder. [Spin-resolved photoemission from \(111\) surfaces of Pd, Ir and Pt by circularly polarised light: theory and comparison with experiment](#). *J. Phys.: Condens. Matter* **1**, 6469 (1989).
- [279] J. L. Wang, A. Pancotti, P. Jegou, G. Niu, B. Gautier, Y. Y. Mi, L. Tortech, S. Yin, B. Vilquin, and N. Barrett. [Ferroelectricity in a quasiamorphous ultrathin  \$\text{BaTiO}\_3\$  film](#). *Phys. Rev. B* **84**, 205426 (2011).
- [280] D. Ehre, H. Cohen, V. Lyahovitskaya, and I. Lubomirsky. [X-ray photoelectron spectroscopy of amorphous and quasiamorphous phases of  \$\text{BaTiO}\_3\$  and  \$\text{SrTiO}\_3\$](#) . *Phys. Rev. B* **77**, 184106 (2008).
- [281] R. E. Cohen. [Origin of ferroelectricity in perovskite oxides](#). *Nature* **358**, 136 (1992).
- [282] M. Greif, L. Castiglioni, A. P. Seitsonen, S. Roth, J. Osterwalder, and M. Hengsberger. [Photoelectron diffraction in the x-ray and ultraviolet regime: Sn-phthalocyanine on  \$\text{Ag}\(111\)\$](#) . *Phys. Rev. B* **87**, 085429 (2013).

- [283] J. W. Gadzuk. [Surface molecules and chemisorption. II. Photoemission angular distributions.](#) *Phys. Rev. B* **10**, 5030 (1974).
- [284] N. A. Cherepkov and G. Schönense. [Linear dichroism in photoemission from oriented molecules.](#) *Europhys. Lett.* **24**, 79 (1993).
- [285] N. Niizeki and H. Mitani. [Two-dimensional dodecagonal quasilattices.](#) *J. Phys. A: Math. Gen.* **20**, L405 (1987).
- [286] S. Schenk, S. Förster, and W. Widdra, in preparation (2019).
- [287] E. Rotenberg, W. Theis, K. Horn, and P. Gille. [Quasicrystalline valence bands in decagonal AlNiCo.](#) *Nature* **406**, 602 (2000).
- [288] V. A. Rogalev, O. Gröning, R. Widmer, J. H. Dil, F. Bisti, L. L. Lev, T. Schmitt, and V. N. Strocov. [Fermi states and anisotropy of Brillouin zone scattering in the decagonal Al–Ni–Co quasicrystal.](#) *Nat. Comm.* **6**, 8607 (2015).
- [289] S. J. Ahn, P. Moon, T.-H. Kim, H.-W. Kim, H.-C. Shin, E. H. Kim, H. W. Cha, S.-J. Kahng, P. Kim, M. Koshino, Y.-W. Son, C.-W. Yang, and J. R. Ahn. [Dirac electrons in a dodecagonal graphene quasicrystal.](#) *Science* **361**, 782 (2018).
- [290] E. Rotenberg, W. Theis, and K. Horn. [Model simulations of momentum-resolved photoemission from quasicrystals.](#) *J. Alloys Compd.* **342**, 348 (2002).
- [291] J. Voit, L. Perfetti, F. Zwick, H. Berger, G. Margaritondo, G. Grüner, H. Höchst, and M. Grioni. [Electronic structure of solids with competing periodic potentials.](#) *Science* **290**, 501 (2000).
- [292] F. O. Schumann, C. Winkler, J. Kirschner, F. Giebels, H. Gollisch, and R. Feder. [Spin-resolved mapping of spin contribution to exchange-correlation holes.](#) *Phys. Rev. Lett.* **104**, 087602 (2010).
- [293] C. Tusche. [Spin blocking in the correlated double-electron capture from metal surfaces.](#) *Phys. Rev. Lett.* **115**, 027602 (2015).
- [294] S. Samarin, O. Artamonov, and J. Williams. [Emission of correlated electron pairs from surfaces induced by photons, positrons and ions.](#) chapter 4, page 203. Springer International Publishing (2018).
- [295] J. C. Slater. [The electronic structure of metals.](#) *Rev. Mod. Phys.* **6**, 209 (1934).
- [296] E. Wigner. [On the interaction of electrons in metals.](#) *Phys. Rev.* **46**, 1002 (1934).
- [297] E. Wigner and F. Seitz. [On the constitution of metallic sodium.](#) *Phys. Rev.* **43**, 804 (1933).
- [298] J. C. Slater. [A simplification of the Hartree-Fock method.](#) *Phys. Rev.* **81**, 385 (1951).
- [299] L. Hedin. [New method for calculating the one-particle Green's function with application to the electron-gas Problem.](#) *Phys. Rev.* **139**, A796 (1965).
- [300] W. Kohn and L. J. Sham. [Self-consistent equations including exchange and correlation effects.](#) *Phys. Rev.* **140**, A1133 (1965).
- [301] O. Gunnarsson and B. I. Lundqvist. [Exchange and correlation in atoms, molecules, and solids by the spin-density-functional formalism.](#) *Phys. Rev. B* **13**, 4274 (1976).
- [302] R. O. Jones and O. Gunnarsson. [The density functional formalism, its applications and prospects.](#) *Rev. Mod. Phys.* **61**, 689 (1989).
- [303] J. P. Perdew. [Generalized gradient approximations for exchange and correlation: A look backward and forward.](#) *Physica B* **172**, 1 (1991).
- [304] J. P. Perdew, K. Burke, and Y. Wang. [Generalized gradient approximation for the exchange-correlation hole of a many-electron system.](#) *Phys. Rev. B* **54**, 16533 (1996).

- 
- [305] J. P. Perdew, W. Yang, K. Burke, Z. Yang, E. K. U. Gross, M. Scheffler, G. E. Scuseria, T. M. Henderson, I. Y. Zhang, A. Ruzsinszky, H. Peng, J. Sun, E. Trushin, and A. Görling. [Understanding band gaps of solids in generalized Kohn-Sham theory](#). *Proc. Natl. Acad. Sci. U.S.A.* **114**, 2801 (2017).
- [306] S. Sharma, E. K. U. Gross, A. Sanna, and J. K. Dewhurst. [Source-free exchange-correlation magnetic fields in density functional theory](#). *J. Chem. Theory Comput* **14**, 1247 (2018).
- [307] R. Rausch and M. Potthoff. [Multiplons in the two-hole excitation spectra of the one-dimensional Hubbard model](#). *New J. Phys.* **18**, 023033 (2016).
- [308] R. Rausch and M. Potthoff. [Filling-dependent doublon dynamics in the one-dimensional Hubbard model](#). *Phys. Rev. B* **95**, 045152 (2017).
- [309] R. Rausch and M. Potthoff. [Pump-probe Auger-electron spectroscopy of Mott insulators](#). *Phys. Rev. B* **99**, 205108 (2019).





# Lebenslauf

## Dr. CHENG-TIEN CHIANG

Institut für Physik, Martin-Luther-Universität Halle-Wittenberg  
Von-Danckelmann-Platz 3, Halle (Saale), D-06120, Germany  
+49-345-552-5368, cheng-tien.chiang@physik.uni-halle.de

Geburtsdatum:	26.06.1984	Geburtsort:	Taipeh, Taiwan
Geschlecht:	männlich	Familienstand:	verheiratet, eine Tochter (2015)
Staatsangehörigkeit:	Taiwan		

### Wissenschaftliche Ausbildung

09.2002 – 06.2005     **Bachelor of Science, Physik**  
National Taiwan University, Taipeh, Taiwan

09.2005 – 06.2007     **Master of Science, Physik**  
National Taiwan University, Taipeh, Taiwan  
Masterarbeit:   Morphology, electronic and magnetic structure of Mn/Cu<sub>3</sub>Au(100)  
studied by scanning tunneling microscopy and spectroscopy  
Arbeitsgruppe:   Prof. Minn-Tsong Lin

07.2007 – 01.2011     **Doctor rerum naturalium, Physik**  
Max-Planck-Institut für Mikrostrukturphysik und  
Martin-Luther-Universität Halle-Wittenberg, Halle (Saale), Germany  
Dissertation:   Spin and magnetization dependent two-photon photoemission  
from ultrathin ferromagnetic cobalt films  
Abteilung:       Prof. Jürgen Kirschner

### Wissenschaftliche Tätigkeit

07.2010 – 03.2016     **Wissenschaftlicher Mitarbeiter (postdoc)**  
Arbeitsgruppe:   Max-Planck-Fellow Gruppe von Prof. Wolf Widdra  
Max-Planck-Institut für Mikrostrukturphysik, Halle (Saale), Germany

seit 04.2016           **Wissenschaftlicher Mitarbeiter (postdoc)**  
Fachgruppe:     Prof. Wolf Widdra  
Martin-Luther-Universität Halle-Wittenberg, Halle (Saale), Germany

Cheng-Tien Chiang  
Halle (Saale), 24.06.2019



## **Erklärung an Eides statt**

hiermit erkläre ich, die vorliegende Habilitationsschrift

### **Advanced laboratory-based photoelectron spectroscopies on metal and oxide surfaces**

selbständig und ohne fremde Hilfe verfasst und keine anderen als die von mir angegebenen Quellen und Hilfsmittel benutzt zu haben. Die den benutzten Werken wörtlich oder inhaltlich entnommenen Stellen sind als solche kenntlich gemacht.

Cheng-Tien Chiang

Halle (Saale), 24.06.2019



## Note after submission

After the submission of this thesis, some parts of this Habilitation work have been published in the following two articles:

Electronic band structure of a two-dimensional oxide quasicrystal

Cheng-Tien Chiang, Martin Ellguth, Florian O. Schumann, Christian Tusche, Richard Kraska, Stefan Förster, and Wolf Widdra

Phys. Rev. B **100**, 125149 (2019)

<https://journals.aps.org/prb/abstract/10.1103/PhysRevB.100.125149>

Laser-based double photoemission spectroscopy at surfaces

Cheng-Tien Chiang, Andreas Trützscher, Michael Huth, Robin Kamrla, Frank O. Schumann, and Wolf Widdra

Prog. Surf. Sci. (in press, available online 2 April 2020)

<https://doi.org/10.1016/j.progsurf.2020.100572>





# Acknowledgement

During this Habilitation work I was constantly receiving tremendous help from the colleagues in Halle as well as from other researchers worldwide. Specifically I would like to thank:

**Prof. Wolf Widdra** for allowing me to start in his Surface Science Group immediately after I submitted my PhD thesis. In Wolf's group I have been learning not only science, but also the open-minded attitude toward the world. Especially I would like to thank Wolf for showing me how to be humble and nice while remaining scientifically professional.

**Prof. Jürgen Kirschner** for suggesting me to join Wolf's group, as well as the long-term support and interest in my work.

**PD Dr. Frank O. Schumann** for stimulating discussions, suggestions as well as brainstorming and critical thinking. Especially I have enjoyed a few moments very much, when I tried to convince Frank with my mostly immature and hand-waving scientific ideas.

**Dr. Michael Huth** and **Dr. Andreas Trützscher** for their invaluable support and company in the big lab as well as in the basement lab. Michael's professional programming skills together with Andreas' critical insights are of critical importance for the DPE experiments. **Dr. Alexander Blättermann** for his talented experimental skills and theoretical modelling, which contributed significantly to the first HHG setup in Halle. **Dr. Stefan Förster** for introducing me the beauty of oxides as well as the talent of scientific management when building up a group. **PD Dr. Michael Schindler** for chemistry lessons during lunch breaks.

**Robin Kamrla** for Robin's unprecedented patience and tolerance for my picky attitude toward numerous aspects, especially toward scientific presentation. **Mathias Augstein** and **Maximilian Paleschke** for their constant support in the laser lab as well as their questions, which often helped me to uncover my insufficient understanding in many aspects of optics and solid state physics.

**Ralf Kulla**, **Frank Weiß**, **Frank Helbig** as well as the **MLU and MPI Mechanical and Electronic Workshops** for the excellent technical assistance. **Tina Bourguignon**, **Aline Leuchtenberger** as well as the **Colleagues in the Dean's Office (Dekanat)** for numerous administrative supports. **Matthias Hädrich** in the Gustav-Mie lecture hall for the support of my Probevorlesung. I also thank all the other **Colleagues in Wolf's Surface Science Group**, whose names are not mentioned explicitly here due to the limited page, for providing a very positive and encouraging environment for science.

**Prof. Jens Güdde** in Philipps-Universität Marburg for sharing with us the insights into HHG setups.

Last but not least, I would like to thank **my Family** for their endless support regardless of the actual spatial distance between us.

